DESIGN AND COMPARATIVE PERFORMANCE EVALUATION OF NOVEL MOBILE HANDSET ANTENNAS AND THEIR RADIATIVE EFFECTS ON USERS

PETROS K. PANAYI

Ph.D. 2000

Design and Comparative Performance Evaluation of Novel Mobile Handset Antennas and their Radiation Effects on Users

Petros K. Panayi

A thesis submitted in partial fulfilment of the requirements of the University of Glamorgan for the degree of Doctor of Philosophy

October 2000

University of Glamorgan

DECLARATION

I declare that this thesis has not been, nor is currently being, submitted for the award of any other degree or similar qualification.

Signed: 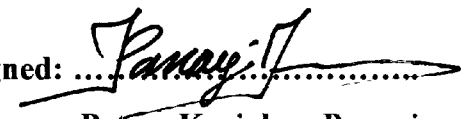

Petros Kyriakou Panayi

To my parents Kyriakos and Froso...

ACKNOWLAGEMENTS

I would like to thank my Director of Studies, Professor Miqdad Al-Nuaimi for his continued interest, encouragement and support throughout my project. His feedback has been a continuous source of inspiration, which had as a result the in-depth continuation and completion of this project.

I gratefully acknowledge my second supervisor Dr. Leonida Ivrissimtzis for his constructive criticism and his valuable suggestions that were giving the kick-start for novel ideals some of which have been used in this project.

Finally, I would like to thank and dedicate this thesis to my family and in particular to my parents that have been an inspiration and support for me during the time I was working on this project.

Abstract

The beginning of the 21st century is characterised, among others, by the evolution in telecommunications. The rapid growth of mobile communications and the variety of applications proposed for the third generation (3G) systems require long operation time, low weight and cost for terminals, as well as improved link quality.

For this reason a good efficiency and low profile antennas with low absorption losses by the user are desirable. The Planar Inverted-F Antenna (PIFA) is shown to result into low SAR values and high efficiency when operating in the proximity of the user. Despite these advantages, PIFA is also characterised by narrow bandwidth that limits its practical use. The first part of this work is dedicated to the measurements and evaluation of the radiation characteristics of the PIFA and other wire antennas both in the near and far fields. In addition, novel methods of PIFA tuning are presented. These include the repositioning of the shorting pin and modification of its capacitance. By using these techniques, the effective bandwidth of the PIFA can be increased to satisfy the GSM900 and DCS1800 system bandwidth requirements. Dual-band and electronically tuned PIFA prototypes are also included.

The effects of the handset size on the mass averaged Specific Absorption Rate (SAR), and antenna efficiency are investigated. The appropriate choice of handset can result in up to 30%-reduced peak SAR. The computed SAR values from PIFA are compared with those resulting from the use of a handset equipped with quarter-wavelength monopole antenna. A new measure referred to as the 3dB SAR volume is proposed. This measure provides better understanding of the absorbed power distribution in the operator's head.

Results obtained in the course of study show that low profile handset antennas, such as the PIFA, present in addition to dual resonance and low reflection losses, reduced SAR values, high efficiency and low 3dB SAR volume.

Finally, SAR and 3dB SAR volume values from simulations on 5- and 10- years old child head models are compared with their equivalents for adult models from which appropriate conclusions are drawn.

Table of Contents

Chapter / Sections. **Page**

List of Figures

List of Tables

Abbreviations:

AM[1]	Amplitude Modulation
AMPS[1]	Advance Mobile Phone System
AR	Axial ratio
ASK[1]	Amplitude-Shift Keying
BTS[1]	Base Transceiver Station
CDMA[1]	Code-Division Multiple Access
CEPT[1]	Comite Europeen des Postes et Telecommunications
CELENEC[7]	European committee of electrotechnical standardisation
DFT[2]	Discrete Fourier transform
DUT[4]	Device Under Test
DS-CDMA	Direct sequence CDMA
Emf[2]	Electromotive force
EMF[7]	Electromagnetic fields
ERC [1]	European Radiocommunications Office
ETSI[1]	European Telecommunication Standards Institute
FCC[7]	Federal Communication Commission
FDD[1]	Frequency Division Duplex
FDMA/TDMA[1]	Frequency Division Multiple Access/Time Division multiple Access
FDTD[1][2]	Finite Difference Time Domain
FM[1]	Frequency Modulation
FSK[1]	Frequency-Shift Keying
FSL[4]	Free space loss
FS-PIFA[3]	Full-short circuit planar inverted-F antenna
GMSK[1]	Gaussian Minimum-Shift Keying
GSM[1]	Groupe Spéciale Mobile
IMT-2000[1]	International Mobile Telecommunications-2000
IMTS[1]	Improved Mobile Telephone Service
ISDN[1]	Integrated Services Digital Network
ISO/OSI[1]	International Standards Organization/Open System Interconnection
JDC[1]	Japanese Digital Cellular
LAN[1]	Local Area Networks
MoM[1][2]	Method of Moments
MPE[3]	Maximum permissible exposure
MS[1]	Mobile Station

MSK[1]	Minimum-Shift Keying
MSS[1]	Mobile Satellite Services
MTE[7]	Mobile Communication Equipment
MTS[1]	Mobile Telephone Service
NADC [1]	North America Digital Cellular
NEC[2]	Numerical Electromagnetic Code
NMT[1]	Nordic Mobile Telephony
NRPB[7]	National Radiological Protection Board
OQPSK[1]	Offset Quadrature Phase-Shift Keying
PC[2]	Personal computer
PCS[1]	Personal Commination Services
PDC[1]	Personal Digital Cellular
PEC[5]	Perfect Electromagnetic Conductor
PIFA[1][3]	Planar Inverted-F Antenna
PLF[2]	Polarization loss factor
PM[1]	Phase Modulation
PN[1]	Pseudonoise
PSK[1]	Phase-Shift Keying
QPSK[1]	Quadrature Phase-Shift Keying
RCDLA[3]	Radiation-coupled dual-L antenna
RCS[2]	Radar cross-section
RPSD[4]	Radiowave Propagation and System Design group
SAR[1]	Specific Absorption Rates
SDMA[1]	Space Division Multiple Access
SSN7[1]	Signaling System No. 7
TACS[1]	Total Access Communication System
TD-CDMA[1]	Time Division – CDMA
TDMA[1]	Time-Division Multiple Access
TDD[1]	Time Division Duplex
TEM[2]	Transverse Electromagnetic
UMTS[1]	Universal Mobile Communication System
UTRA[1]	UMTS Terrestrial Radio Access
VNA[4]	Vector Spectrum Analyser
VSWR[4]	Voltage Standing-Wave Ratio
W-CDMA[1]	Wideband CDMA

1. INTRODUCTION

The ability to communicate with precision is probably the most important quality that characterises human beings and differentiates humans from other known forms of life. Starting from oral and moving to written communications, information is exchanged and shared throughout the eras of human existence. Methods of communication have been developed through the years with the main objectives always being: speed, accuracy, reliability, volume of information shared and lower costs.

Telegraph has been the first means of electronic information sent through a wire. The first telegraphic message was sent in the USA in 1844. Telegraphic messages were sent using "Morse code" transmitted as electric pulses. The pulses were translated back into text using an operator at each side of the wire connecting the locations. This method was considered to be efficient, fast replacing the mail service where the message was considered to be urgent.

A more natural method, not requiring decoding, is to send voice signals through transmission lines. Alexander Graham Bell introduced this method in 1875. Since then, the telephone service has grown and spread enormously as the telephone has become widely used by millions of people throughout the world. A new era in telephony followed recently with the introduction of mobile telephone systems, accelerated by further developments in digital telecommunication networks.

1.1 Mobile communications and GSM.

Thanks to Guglielmo Marconi who utilised Heinrich Rudolf Herz electromagnetic waves based methods, wireless communications became feasible in 1897. In the beginning this technology was available for military use only. In 1914 radio, a wireless form of electronic communications, was used for practical purposes in World War I. Following the end of the war, radio was used for the first commercial radio broadcasts in the 1920s. The first commercial television programme was broadcast in the 1940s. The first public mobile telephony, like the Mobile Telephone

Service (MTS) and Improved Mobile Telephone Service (IMTS) appeared in the 1960s. In the 1970s and 1980s cellular technology was developed firstly in North America where the Advance Mobile Phone System (AMPS) standard was introduced in 1979. The cellular system (see Fig. 1.1) was assigned frequencies in the 800 MHz band. The Personal Communination Services (PCS) standard followed in 1994. In the U.K. Total Access Communication System (TACS), which was based on the AMPS standard with some special adaptations in bandwidth e.g. utilising the 900 MHz band, was introduced as the analogue mobile telephony system in Europe. Another system referred as the Nordic Mobile Telephony (NMT) i.e. the NMT450/NMT900 was introduced in Scandinavian countries. These systems added to the variety of analogue systems available around the world during the first half of 1990s.

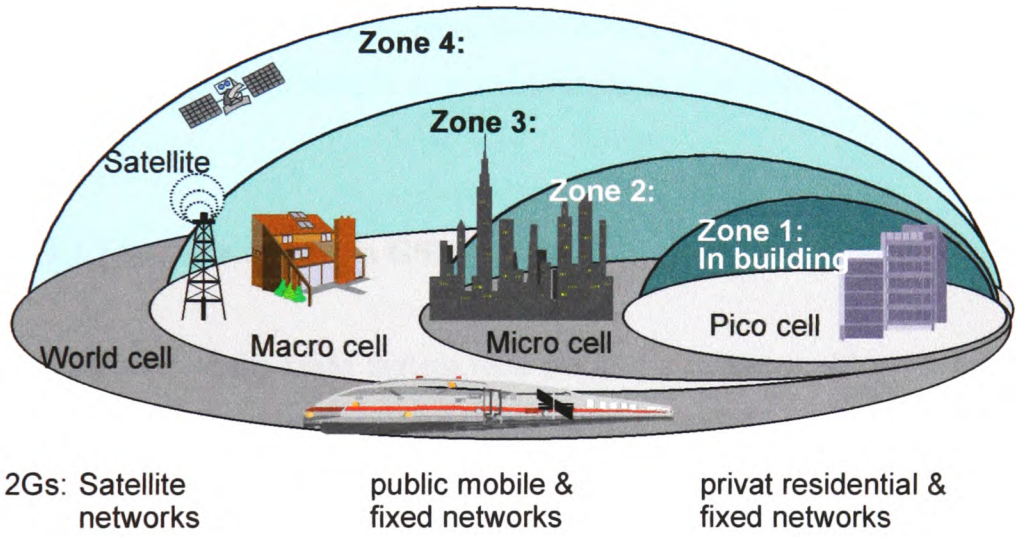

Fig. 1.1 *Cell classification in mobile and wireless communication.*
2nd generation network (GSM) implement zone 3 (Macro Cell) [1.2].

1.1.1 History of GSM.

The increased demand for mobile communications has soon led to saturation in the frequency bandwidth available for analogue telephony. In addition to this, analogue radio transmission has the effect of directly passing physical influences and interference in radio transmission link to the receiver. A new technology was needed

to improve the communication quality and capacity. Digital radio systems have the potential of performing significantly better than analogue systems under critical and more difficult reception conditions, e.g. low signal-to-noise ratio, multipath interference, and signal fading. In addition, more value-added services can be realised using digital technology. Global standards are also advantageous in radio communications, even though, regulatory authorities and radio spectrum management problems have once again led to variability of the standards within national and regional scale. In the U.S. the North American Digital Cellular (NADC) system, or simply the Time-Division Multiple-Access (TDMA) system has been formulated. In Japan, the Japanese Digital Cellular (JDC) or Personal Digital Cellular (PDC) system has been proposed. In Europe, the Groupe Spéciale Mobile (GSM) was formed and became active. Today the GSM standard has become widely accepted, having formed the basis of mobile service with over 200 million customers throughout the world connected to more than 320 mobile phone networks. The GSM systems refer to digital mobile phone systems implementing the GSM standards.

1.1.2 Services offered in GSM system.

The development of the GSM system took place in two phases. Phase 1 had been developed in the early years providing the most value services. Phases 2 and 2+ were designed and introduced to add supplementary services. These services are comparable with the Integrated Services Digital Network (ISDN) but the bit rate is limited to 13 kbps for speech and 9600 bps for bearer services. Tables 1.1 and 1.2 summarize the services available in the two GSM development phases [1.1].

Services Category	Services	Comment
Teleservices	Telephony (speech)	So-called full rate, 13 kbps
	Emergency Calls (speech)	
	Short-Message Services (SMS): point-to-point and point-to-multipoint (cell broadcast)	Alphanumeric information: user-to-user and network to all users.
	Telefax	Group 3
Bearer Services	Asynchronous data	300-9600 bps,
	Synchronous data	300-9600 bps
	Asynchronous PAD (packet-switched, packet assembler/disassembler) access	300-9600 bps
	Alternate speech and data	300-9600 bps
Supplementary services	Call forwarding	For example, subscriber busy not reachable or does not answer.
	Call barring	For example, all calls, international calls, incoming calls.

Table 1.1 *GSM Phase 1 Services.*

Services Category	Services	Comment
Teleservices	Telephony (speech)	Half rate, 6.5 kbps.
	Short-message services	General Improvements.
Bearer Services	Synchronous dedicated packed data access	2,400-9,600 bps.
Supplementary services	Calling/connected line identity presentation	Displays calling party's directory number before/after call connection.
	Calling/connected line identity restriction	Restricts the display of the calling party's number at called party's side before/after call connection.
	Call waiting	Informs the user about a second (incoming) call and allows to answer it.
	Call hold	Puts an active call on hold in order to answer or originate another (second) call.
	Multiparty communication	Conference calls.
	Closed user group	Establishment of groups with limited access.
	Advice of charge	Online charge information.
	Unstructured supplementary services data	Offers an open communications link for use between networks and user for operator-defined services.
	Operator-determined barring	Restriction of different services, call types by the operator.

Table 1.2 *Services added through GSM Phase 2 Services.*

1.1.3 The GSM physical layer.

The GSM system makes use of Signaling System No. 7 (SSN7) which has been borrowed from the ISDN. This is described using the International Standards Organization/Open System Interconnection (ISO/OSI) layer model shown in Table 1.3 [1.1].

Layer 7	APPLICATION	Application protocols, user-oriented provision of communication media
Layer 6	PRESENTATION SESSION	Application-specific format transfer
Layer 5	SESSION	Collection of application processes, billing
Layer 4	TRANSPORT	Flow control of point-to-point connections
Layer 3	NETWORK	Connection and switching of communication links
Layer 2	DATA LINK	Control of signaling links, block transfer of signaling data
Layer 1	PHYSICAL	Physical transmission, coding error correction, modulation, etc.

Table 1.3 *The seven layers of the ISO/OSI model.*

Interest here, however, is centred on Layer 1. The physical layer mechanics include modulation, power control coding, timing, and all the other procedures required to establish a reliable link between the Mobile Station (MS) and the Base Transceiver Station (BTS). The GSM system uses Frequency-Division Multiple-Access/Time-Division Multiple-Access (FDMA/TDMA) methods. Time division access is by means of eight time slots each of which is allocated to a different user sharing the

channel. A GSM time slot is thus 577 μs long in every 4.615 ms. As in all cellular systems (analogue and digital) GSM utilizes, in addition, Space Division Multiple Access (SDMA) a method which allows frequency reuse. Using SDMA might cause co-channel interference if the distance separating two transmitters using the same frequency is not sufficient.

Frequency spectrum is considered to be a very valuable asset in wireless communications. Frequencies are allocated to services by regulation authorities in each country. The characteristics of the propagation channel depend on the channel frequency. The antennas required for receiving or transmitting the signal are also related to the frequency band used. For this reason frequency bandwidth for the GSM system is limited to 70 MHz. The following table (Table 1.4) gives how this frequency band is allocated within the system. The DCS1800 (PCN in the United Kingdom) has been introduced after GSM, aiming at solving the increased channel demand. This system has the same specifications as the GSM900 but higher frequency band is used.

	GSM900	**PCN or DCS1800**
Up-Link (MS-to-BTS)	890-915 MHz	1710-1785 MHz
Down-Link (BTS-to-MS)	935-960 MHz	1805-1880 MHz
Duplex Spacing	45 MHz	95 MHz
Channel No	125 (0 used as guard band)	374
Channel BW	200 kHz	200 kHz

Table 1.4 *GSM900 and DCS1800 frequency allocation [1.1].*

The power required for a reliable link is dependent on the distance and the propagation path of the channel. For this reason maximum power transmission is not continuously required. Power management is beneficial for the mobile station operation time and in minimising potential risks from the extensive exposure to radiation. For this reason, the maximum radiation power is limited with mobile device types as shown in Table 1.5 and in radiation power classes to which each device can switch according to channel requirements. The power levels for GSM and DCS are given in Table 1.6 and 1.7 respectively.

Mobile Station Type	Maximum Output Power (W)
Fixed mobile stations permanently installed in a car.	20
Portable units (bag phones).	8
Hand-portable units.	2

Table 1.5 *Maximum output power for mobile stations in cellular networks [1.1].*

Power Class	Maximum power of a mobile station	Maximum power of a base station
1	20W	320W
2	8W	160W
3	5W	80W
4	2W	40W
5	0.8W	20W
6		10W
7		5W
8		2.5W

Table 1.6 *Power levels in the GSM System [1.1].*

Power Class	Maximum power of a mobile station	Maximum power of a base station
1	1 W	20 W
2	2.5 W	10 W
3		5 W
4		2.5 W

Table 1.7 *Power levels in the DCS1800 System [1.1].*

The channel bandwidth of 200 kHz, used in GSM, is wider than the analogue channels of 12.5 kHz and 30 kHz. Using TDMA, as mentioned above, a single channel is used by eight mobile stations simultaneously. The mobile station transmits

a burst every 4.615 ms creating an underlined frequency of 216.6 Hz. This frequency is within the audible range and can cause problems to electronics devices. Receive and transmit signals are separated by three time slots. Due to the TDMA method used, the mobile station must be within 28 μs achieve a dynamic range of 70 dB and remains in this power level for 542.8 μs to transmit the information. To achieve these requirements a power ramp of 36 dBm is used during power on and power off. This method is used also in the base stations if only certain time slots of the physical channel are used. Due to the distance between the base station and the mobile terminal, signals do not arrive at a specified time. For this reason, mobiles farthest from the base station are given a head start (timing advantage). Data sent during communication does not contain only voice information. Burst of data, sent during the time allocated to a given mobile station, contains in addition to voice data error correction codes and additional information that are used by both the MS and the BTS.

Human hearing of audio signal, in telephony, is limited to frequency components below 4 kHz. According to the sampling frequency, then, sampling signal of 8 kHz must be used. If the signal is quantized by 13 bit (2^{13} = 8,192 quantization levels) for good sound quality, 104 kbs must be sent during conversation. This is by far above the 13 kbs of the GSM system. Sophisticated compression methods, based on voice signal properties, are used to reduce the data by a factor of eight but maintaining the good quality of communications. These methods are described in detail in [1.1].

All signals, transmitted using free space as propagation medium, are modulated. Modulation offers some advantages over sending information at its original frequency, some of which are listed below:

i. A single medium, like the air, can be shared by different applications (i.e. TV, radio and mobile communication systems).
ii. The required power for transmitting a signal over a given distance is reduced due to radiowave properties at a given frequency.
iii. The size of the receiver and its antenna can be controlled by the carrier frequency. For this reason, high frequency radio terminals can be small and efficient but their communication distance in urban areas is short.

iv. Application requirements can be controlled by the carrier frequencies properties. For instance, space diversity is better applied if high frequencies are used. On the other hand, long distance communications can be achieved by low carrier frequencies.

We can send digital information on a carrier signal by altering any of the carrier characteristics such as its amplitude resulting in amplitude modulation (AM), its frequency FM, or phase PM, in accordance with the information. To reflect the binary on-off nature of digital modulation various modulation methods, which are called keying methods, are used: Amplitude-Shift Keying (ASK), Frequency-Shift Keying (FSK), and Phase-Shift Keying (PSK). If two bits are represented by a 90° phase change of the carrier the method is called Quadrature Phase-Shift Keying (QPSK). Offset Quadrature Phase-Shift Keying (OQPSK) refers to QPSK where only one of the two bits is allowed to change for every phase change.

In GSM, Gaussian Minimum-Shift Keying (GMSK) modulation method is used. This is a Minimum-Shift Keying (MSK) modulation where a Gaussian low-pass filter is used to smooth the phase transition from one bit time to the next. In MSK the odd and even bits of a data sequence are used to generate two new data sequences (the "odd bits" and the "even bits") as shown in Fig. 1.2. For instance, when anyone of the odd numbered bits (1,3,5,7,...) is high then the "odd bits" sequence is high and when it is low the "odd bits" sequence is low. The same is done for the even numbered bits. MSK signal is the result of combining two frequencies using information from the "odd bits" and the "even bits" as shown in Table 1.8.

Digital Input		MSK Output	
Bit Value		Frequency	Sense
Odd Bit	Even Bit	High or Low	+ or -
1	1	High	+
-1	1	Low	-
1	-1	Low	+
-1	-1	High	-

Table 1.8 *MSK truth table.*

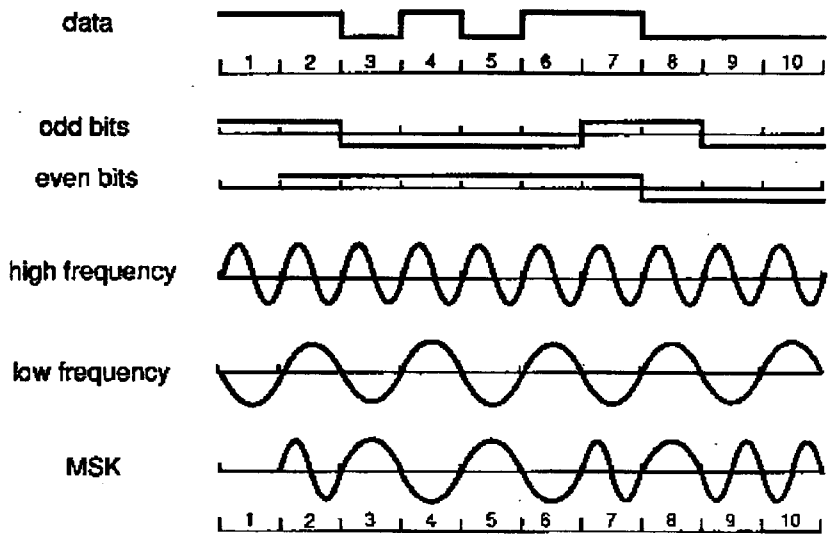

Fig. 1.2 *Generating minimum-shift keying [1.1].*

1.2 UMTS/ITM2000 and 3rd generation of mobile communications.

The data rate of GSM based communication systems is limited to 13 kbs which allows good quality voice communication but relatively low rate of data transfer. Moreover, additional capacity, that GSM may not be able to support in the near future, will be required. The need for high data rate and increased capacity can be satisfied by the introduction of the 3rd generation of mobile communications. This technology will provide data rates from 384 kbs up to 2 Mbs. The main objectives, as described by the Universal Mobile Communication System (UMTS) forum [1.2], are summarized below.

- New and better services, i.e. multimedia and high-speed data services that are easy to use, and can be customised in order to address individual users' needs and preferences.
- Terminals and other "customer facing" equipment which allows fast and easy access to these services.
- User costs, which are low enough to ensure a global mass market - prices which are competitive.

- Similarly, a wide range of available terminals, with sufficiently low prices and mass market appeal, that will support the advanced capabilities of UMTS.
- Coverage in all environments through both terrestrial and satellite components, and through a radio technology with high spectral efficiency and service quality, allowing global and seamless roaming.

The UMTS is a member of the International Mobile Telecommunications-2000 (IMT-2000) global family of "third-generation" (3G) mobile communication system and is mainly active in Europe. One of the main responsibilities of UMTS is to design and drive European counties into the 3rd generation of mobile telephony. Table 1.9 gives the proposed schedule for UMTS. Similar organisations worldwide are working on the standards and on frequency allocation which will satisfy the bandwidth and capacity requirements which will harmonically coexist with the existing wireless systems. In Fig. 1.3 the world-wide spectrum allocation is shown. In general in all Comite Europeen des Postes et Telecommunications (CEPT) countries, the entire UMTS/IMT-2000 spectrum, except 15 MHz, which is already used in DECT, is designated for UMTS/IMT-2000. The bands for terrestrial UMTS are 1900 - 1980 MHz, 2010 - 2025 MHz, and 2110 - 2170 MHz. This gives 155 MHz in total. The Mobile Satellite Services (MSS) allocations at 2 GHz frequency bands that are identified for UMTS/IMT-2000 satellite component are 1980 – 2010 MHz and 2170 – 2200 MHz, which give a total of 60 MHz for UMTS/IMT-2000 satellite services. A total of 15 CEPT countries have by the 10th of Oct. 1998 signed up to this ERC (European Radiocommunications Office) decision. It is anticipated that more countries will sign the decision in the future.

Task name	19 96	19 97	19 98	19 99	20 00	2001	2002	2003	2004	2005
UMTS revised vision										
Co-operative research: ACTS										
UMTS Forum report no 1										
ERC spectrum decision										
EU UMTS decision										
National licence conditions										
National license decision										
ITU Framework standards										
Basic standards studies										
Detailed freezing UMTS standards										
UMTS System development										
Pre-operational trials										
UMTS Planning, deployment										
UMTS: Commercial operation										

Table 1.9 *UMTS Schedule for Europe [1.2].*

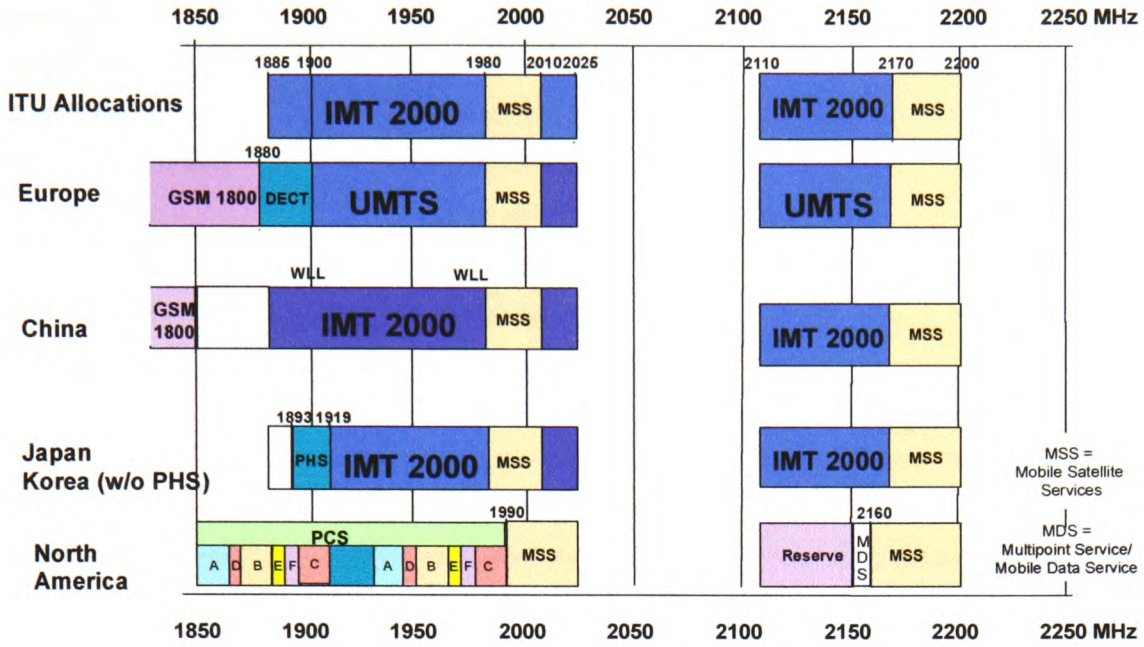

Fig. 1.3 *Spectrum identified for IMT-2000 [1.2].*

At least two 40 MHz blocks should be made available to operators by the beginning of year 2002 and all 155 MHz could be made available for terrestrial UMTS/IMT-2000 by year 2005 subject to market demand.

The market for UMTS comprises a wide area of applications. These are converted into six main service classes for this analysis. These services as given in [1.2] are summarised in Table 1.10. The first three services are seen as logical extensions of 2nd generation mobile market and the last three are addressing the new mobile multimedia market.

The bit rates, asymmetry factors and switching modes (circuit/packet switched) of the six service classes are derived from the market analysis given in Table 1.11.

Speech (S): (symmetric)	• Simple one to one and one to many voice (teleconferencing) services • Voicemail
Simple Messaging (SM): (asymmetric)	• SMS (short message delivery) and paging • Email delivery • Broadcast and public information messaging • Ordering/payment (for simple electronic commerce)
Switched Data (SD): (symmetric)	• Low speed dial-up LAN access • Internet/Intranet access • Fax Legacy services - mainly using radio modems such as PCMCIA cards, are not expected to be very significant by 2005.
Medium Multimedia (MMM): (asymmetric)	Asymmetric services which tend to be 'bursty' in nature, require moderate data rates, and are characterised by a typical file size of 0.5 Mbytes, with a tolerance to a range of delays. They are classed as packet switched services. • LAN and Intranet/Internet access • application sharing (collaborative working) • interactive games • lottery and betting services • sophisticated broadcast and public information messaging • simple online shopping and banking (electronic commerce) services
High Multimedia (HMM): (asymmetric)	Asymmetric services which also tend to be 'bursty' in nature, require high bit rates. These are characterised by a typical file size of 10 Mbytes, with a tolerance to a range of delays. They are classed as packet switched services. Applications include: • fast LAN and Intranet/Internet access • video clips on demand • audio clips on demand • online shopping
High Interactive Multimedia (HIMM): (symmetric)	Symmetric services which require reasonably continuous and high-speed data rates with a minimum of delay. Applications include: • video telephony and video conferencing • collaborative working and telepresence

Table 1.10 *UMTS applications.*

		Bit rate	Asymm. Factor	Switch Mode
HIMM	High Interactive Multimedia	128 kbps	1/1	circuit
HMM	High Multimedia	2000	0,005/1	packet
MMM	Medium Multimedia	384	0,026/1	packet
SD	Switched Data	14	1/1	circuit
SM	Simple Messaging	14	1/1	packet
S	Speech	16	1/1	circuit

Table 1.11 *Service characteristics.*

1.2.1 Physical layer for the 3rd generation.

The UMTS has been standardised by the European Telecommunication Standards Institute (ETSI) in the IMT-2000 framework, in co-operation with other regional and national standardisation bodies around the world to produce the detailed standards to satisfy growing market needs for global roaming and services availability. The ETSI decision in January 1998 on the radio access technique for UMTS combined two technologies into one common standard. These are:

1. W-CDMA (Wideband- CDMA) for paired spectrum bands and
2. TD-CDMA (Time Division – CDMA) for unpaired bands.

This powerful approach ensures an optimum solution for all the different operating environments and services needs. Comparison of the two modes is given in Table 1.12. In the W-CDMA referred to as Frequency Division Duplex (FDD), separate parts of the spectrum are used for the uplink and the downlink. On the other hand, for the TD-CDMA referred to as time-division duplex one frequency is used for both transmitting and receiving.

As mentioned above, the transmission rate capability of UMTS will provide at least 144 kbs for full mobility applications in all environments; 384 kbs for limited applications in the macro and micro cellular environments and 2.048 Mbs for low mobility applications particularly in the micro and pico cellular environments. The

2.048 Mbs rate may also be available for short range or packet applications in the macro cellular environment, depending on deploying strategies, radio network planning and spectrum availability. In later phases of UMTS development there will be a convergence with even higher data rate systems using mobile wireless Local Area Networks (LAN) technologies (microwave or infrared) providing data rates of for example 155 Mbs indoor environments.

Code-Division Multiple Access (CDMA) is a spread-spectrum communication system in which multiple users have access to the same frequency band. In DS-CDMA (direct sequence CDMA), spread spectrum refers to power spreading over a given transmission bandwidth. This is accomplished by spreading the base-band binary data by means of a high-speed pseudonoise (PN) code (called the chip rate). The composite high-speed data signaling are then modulated and transmitted over the air. In the North-American DS-CDMA standard (IS-95), the rate of the PN sequence was chosen to be 1.228 MHz and the transmission bandwidth to be 1.25 Mhz [1.3]. The CDMA offers the following advantages:

i. Capacity increase of 8 to 10 times compared to the AMPS analogue system and 4 to 5 times compared to GSM system.
ii. Improved call quality, being better and more consistent as compared to AMPS systems.
iii. Enhanced privacy.
iv. Improved coverage characteristics, allowing for the possibility of fewer cell sites.
v. Increased talk time for portables.
vi. Bandwidth on demand.

W-CDMA allows even higher data rates of up to 2 Mbs. This is achieved by providing multiple spreading factors that allow spreading over the channel bandwidth of 5 MHz and allowing multi-code operation.

Feature or Parameters	FDD mode	TDD mode
Radio access technology	Wideband CDMA (W-CDMA)	Hybrid TDMA/CDMA (TD-CDMA)
Typical deployment scenario	Wide area coverage	Local area coverage
Maximum data rate (in typical deployment scenario)	384 kbs	2Mbs
Service flexibility	High	High
Technical features and services	Support efficient packet access Soft and softer handover Adaptive antennas, advanced receiver structures and transmitter diversity Handover to GSM and TDD	Aggregate asymmetric services Joint detection Handover to GSM and FDD
CDMA chip rates	4.096 Mchip/s (expandable to 8.192 Mchip/s and 16.384 Mchip/s)	4.096 Mchip/s
Duplex operation	Frequency Division Duplex (FDD) Variable duplex spacing 130 – 190 MHz	Time Division Duplex (TDD)
Frame Duration	10msec	10msec
Slots per frame	16	16
Code spreading	Orthogonal variable spreading factor codes (4, 8, 16, 64, 128, 256)	Up to 10 spreading codes per slot Variable spreading factor (2, 4, 8, &16)
Error control method	½ and 1/3 rate convolutional coding Turbo coding	½ and 1/3 rate convolutional coding Turbo coding

Table 1.12 *The proposed modes for the UMTS.*

1.3 Research project objectives.

Having outlined the current and future technologies for personal communication systems within the GSM and UMTS standards, it is clear that there is both scope and continued interest in research of mobile communication systems. Table 1.13 shows mobile phone penetration in European countries (source: European electronic market forecast 1999). The percentage numbers are predicted to be increased in the next few years with the introduction of UMTS.

Country	Percentage penetration
Italy	35%
Germany	18%
UK	22%
France	19%
Spain	18%
Nordic Countries	47%
Benelux	20%
Rest of the W. Europe	24%

Table 1.13 *Mobile phone penetration by region.*

The tremendous popularity of PCS has been accompanied by health related concerns, which have been extensively publicized both in the technical literature and through the popular media. In the absence of clear evidence, hitherto of potential health risks to users associated with the use of mobile phones, methods of reducing EM wave radiation towards the operator's head are desirable. The Specific Absorption Rate (SAR) is a measure of the energy absorbed by dielectric materials when placed near a source of electromagnetic waves. SAR has been assigned standard maximum values by regulatory bodies aiming to constrain the exposure of users to radiowave radiation. These are applicable to uncontrolled exposure conditions such as those arising from the use of mobile phones. In addition, methods for increased mobile phone radiation efficiency, which may result in lower SAR, can lead to an extended use of the handset.

Low profile handsets are seen as more aesthetically attractive and hence more desirable by both service operators and users. The size of a handset can be related mostly to the size of the battery and the type of the antenna used. Low profile built-in antennas, like the Planar Inverted-F antenna (PIFA), result in both low SAR and low profile handsets. In Chapter 3, a summary of research carried out in recent years on both the SAR and PIFA is presented prior to the analytical formulation of our research work, and it also serves as a useful background to the research described in this thesis. The aims of this research are firstly to improve the bandwidth of PIFA so that it can be used for the GSM systems and secondly to carry out investigation of SAR arising in the user head and methods to reduce it. From literature, it is known that the PIFA result in lower SAR and higher efficiency compared to wire antennas used today in mobile telephony but suffers from narrow bandwidth. The objectives of this research are listed below:

1. Consideration and study into both the near and far fields of antennas operating in free space and in the proximity of operator's head/shoulder model using numerical methods, and in particular the Method of Moments and FDTD. Measurements, also, of the far-field radiation patterns of typical antennas used in mobile telephone handsts both in free space and under realistic operational conditions.
2. Detailed study of the PIFA antenna, including the relation of short pin position to its resonance frequency, and introduction of novel methods to increase PIFA's effective bandwidth, which will make it suitable for use in the GSM band.
3. Development of methods for obtaining double resonance PIFA that can be used in multi-band handsets.
4. Computation of the specific absorption rate using the FDTD method and investigation of the mass-averaged peak SAR values for head models of adults and those of 10- and 5-year-old children. Comparative results covering antennas like the monopole, helix and PIFA are included and techniques for reducing the SAR values and increasing the efficiency of the handset are discussed. This is achieved with a study into the relationship between the handset size and operator's head volume on the one hand and SAR values on the other.

1.4 Interim conclusions.

A brief overview of the history of telecommunication systems from the telegraph to UMTS has been presented in the introductory chapter of this thesis. It is evident that there is a continuous evolution in this technology with huge economic benefits for both companies and countries involved. From telegraph pulses to the CDMA of the UMTS communication, methods have undergone a tremendous evolution. An important role in wireless communication advances is the antennas. These have evolve and taken on numerous design forms since the "kite-antenna" Marconi used in the first transatlantic telecommunication experiment. PIFA is a low profile and aesthetically attractive alternative to wire antennas used in today's mobile phones which is characterized by high efficiency when operating near the user's head.

The two objectives of the research are addressed. The first relates to the study of a novel design of low profile antennas, such as the PIFA, and comparative evaluation of its performance. The second objective is directed to the problem of absorption of radiated electromagnetic energy by users of mobile handsets. Distribution of SAR in the user's head and methods to constrain it are studied. Results and analysis using numerical methods are presented in the following chapters.

2. ELECTROMAGNETIC THEORY UNDERLYING NUMERICAL SOLUTION METHODS

Electromagnetic science is evident in modern technology pervading everyday life. From the heaviest and most powerful motors to the smallest transistors, used in today's microchip circuits, electromagnetic science plays an important role in human's technological history. Electromagnetics have their roots in the sixth century B.C. in ancient Greece where Thales of Miletus noted that amber (electron in Greek) rubbed with a dry wood produced sparks and attracted light particles. He also noted the attraction between natural magnetic rocks found in an area called Magnesia. Twenty-two centuries later William Gilbert in a more scientific than philosophical approach invented the electroscope for measuring electrostatic effects and he described the earth as a huge magnet. Many scientists worked on different properties of electricity and magnetism in the years following. James C. Maxwell combined all the theories in a unified electromagnetic theory and formulated his well known equations which are unaffected by the radical changes resulting from Albert Einstein's relativity theory and quantum physics in the beginning of the 20^{th} century. Maxwell's equations predicted the existence of electromagnetic waves, the nature of light as a form of electromagnetic waves and the propagation speed of light.

In the following sections, Maxwell's equations are briefly discussed as these are used in the development of the Finite-Difference Time-Domain (FDTD) method, which is essentially a numerical solution of the differential form of Maxwell's equations implemented in discrete form. The description of the method of moments, which normally refers to the numerical solution of the integral form of Maxwell's equations concludes the chapter.

2.1 Gradient, Divergence and Curl.

In contrast to scalars, which have only magnitude, vector quantities have both magnitude and direction. Vectors are extensively used in analytical electromagnetics. In engineering mathematics it is useful to consider the rate of change of vectors. The

differential form of vectors is expressed mathematically using gradient, divergence, and curl, which are given below in the rectangular coordinates system.

The *gradient* of a scalar quantity f is a vector given by

$$gradf = \nabla f = \hat{x}\frac{\partial f}{\partial x} + \hat{y}\frac{\partial f}{\partial y} + \hat{z}\frac{\partial f}{\partial z} \tag{2.1}$$

where $\hat{x}, \hat{y}$ and $\hat{z}$ are unit vectors in the x, y and z directions respectively.

The *divergent* of a vector $\overline{A}$, on the other hand, is a scalar given by

$$div \cdot \overline{A} = \nabla \cdot \overline{A} = \frac{\partial A_x}{\partial x} + \frac{\partial A_y}{\partial y} + \frac{\partial A_z}{\partial z} \tag{2.2}$$

Finally, the *curl* of a vector $\overline{A}$ is a vector and is given by

$$curl \times \overline{A} = \nabla \times \overline{A} = \hat{x}(\frac{\partial A_z}{\partial y} - \frac{\partial A_y}{\partial z}) + \hat{y}(\frac{\partial A_x}{\partial z} - \frac{\partial A_z}{\partial x}) + \hat{z}(\frac{\partial A_y}{\partial x} - \frac{\partial A_x}{\partial y}) = \begin{vmatrix} \hat{x} & \hat{y} & \hat{z} \\ \frac{\partial}{\partial x} & \frac{\partial}{\partial y} & \frac{\partial}{\partial z} \\ A_x & A_y & A_z \end{vmatrix} \tag{2.3}$$

The gradient, divergence and curl can also be expressed in cylindrical and spherical coordinates as shown in Appendix A.

2.2 Maxwell's equations and electromagnetic theory.

Maxwell has done for electric and magnetic forces what Albert Einstein tried and failed to do many years later for all the forces of nature. Maxwell succeeded in using the laws attributed to Gauss, Amperè and Faraday in formulating a unified electromagnetic theory. His theory has maintained its validity even after the introduction of the relativity theory in the beginning of the 20th century and enabled explanation and prediction of many natural phenomena like the existence of electromagnetic waves in the form of radiowaves and light. These equations are summarised in this chapter and their discrete form is outlined. The latter can conveniently be used to solve electromagnetic problems numerically on digital computers.

2.2.1 Maxwell's equations from Gauss's law for electric fields.

The *electric flux density* $\overline{D}$ and the *electric field intensity* $\overline{E}$ are vectors in the same direction. This is true for all isotropic media, i.e. media whose properties do not change with direction. Gauss's law states that the electric field flux through any closed surface equals the charge enclosed. This can be expressed as:

$$\oint_s \overline{D} \cdot d\overline{s} = \oint_\upsilon \rho d\upsilon = \oint_\upsilon \nabla \cdot \overline{D} d\upsilon = Q \tag{2.4}$$

where $\oint_s$ is integration over closed surface s, $\oint_\upsilon$ is integration over closed volume υ, ρ is the *charge density* and Q is the *charge*. The divergence of the flux density gives the free space charge density at a point.

$$\nabla \cdot \overline{D} = \frac{\partial D_x}{\partial x} + \frac{\partial D_y}{\partial y} + \frac{\partial D_z}{\partial z} = \rho \tag{2.5}$$

Maxwell's divergence theorem from Gauss's law for electric fields states that the integral of the normal component of a vector function over a closed surface, s, equals the integral of the divergence of that vector throughout the volume, υ, enclosed by the surface s. Consequently $\nabla \cdot \overline{D}$ has a value whenever a charge is present.

2.2.2 Maxwell's equations from Gauss's law for magnetic fields.

Jean Baptiste Biot and Felix Savart have shown that current passing in a wire element ΔL produces a magnetic field given by (*Biot-Savart law*):

$$d\overline{B} = \frac{\mu}{4\pi} \frac{I\overline{R} \times \Delta\overline{L}}{\left|\overline{R}^3\right|} \tag{2.6}$$

$$\text{or } dB = \frac{\mu}{4\pi} \frac{IdL\sin\theta}{r^2} \tag{2.7}$$

where μ is the *permeability* of medium, and I is the *current* in the conductor of length L. The *magnetic flux* is given by

$$\psi_m = \oint_s \overline{B} \cdot d\overline{s} \tag{2.8}$$

and according to Gauss the integral of *magnetic flux density* $(\overline{B})$ over a closed surface is zero.

$$\oint_s \overline{B} \cdot d\overline{s} = 0 \tag{2.9}$$

and $$\nabla \cdot \overline{B} = 0 \tag{2.10}$$

This is the Maxwell's equation derived from Gauss's law for magnetic fields.

2.2.3 Maxwell's equations from Ampère's law.

The *magnetic field* $\overline{H}$ is a vector that has the same direction as the flux density $\overline{B}$ and is given by

$$\overline{H} = \frac{\overline{B}}{\mu} \tag{2.11}$$

Ampère's law states that the line integral of $\overline{H}$ around a single closed path is equal to the current enclosed.

$$\oint \overline{H} \cdot d\overline{L} = \oint_s \overline{J} \cdot d\overline{s} = I \tag{2.12}$$

To get the current density at a point the curl equation is used.

$$curl\overline{H} = \nabla \times \overline{H} = \overline{J} + \frac{\partial \overline{D}}{\partial t} \tag{2.13}$$

$\nabla \times \overline{H}$ has a value whenever a current is present.

2.2.4 Maxwell's equation from Faraday's law.

If the flux changes with time then an *electromotive force* (emf) in induced. From Faraday's law this is

$$V = -\frac{d\psi_m}{dt} = \oint \overline{E} \cdot d\overline{L} - \int_s \frac{\partial \overline{B}}{\partial t} \cdot d\overline{s} \tag{2.14}$$

where ψ_m is the total flux of an open-circuited loop. In differential form the electric field intensity can be written as

$$\nabla \times \overline{E} = -\frac{\partial \overline{B}}{\partial t} \tag{2.15}$$

This is the Maxwell's equation from Faraday's law in differential form.

Table 2.1 is a summary of Maxwell's equations in both their integral and differential forms.

No.	Integral	Differential	Description
1	$\oint_s \overline{D} \cdot d\overline{s} = \oint_u \rho du = \oint_u \nabla \cdot \overline{D} du = Q$	$\nabla \cdot \overline{D} = \rho$	**Maxwell's equation from Gauss's law for electric field.** Gauss's law states that the electric field flux D through any closed surface equals the charge enclosed.
2	$\Psi = \oint_s \overline{B} \cdot d\overline{s} = 0$	$\nabla \cdot \overline{B} = 0$	**Maxwell's equation from Gauss's law for magnetic fields.** According to Gauss the integral of magnetic flux density over a closed surface is zero.
3	$V = -\frac{d\psi_m}{dt} = \oint \overline{E} \cdot d\overline{L} = -\int_s \frac{\partial \overline{B}}{\partial t} \cdot d\overline{s}$	$\nabla \times \overline{E} = -\frac{\partial \overline{B}}{\partial t}$	**Maxwell's equation from Faraday's law.** If the magnetic flux changes with time then an emf in induced.
4	$\oint \overline{H} \cdot d\overline{L} = \oint_s \frac{\partial \overline{D}}{\partial t} \cdot d\overline{s} = I$	$\nabla \times \overline{H} = \frac{\partial \overline{D}}{\partial t}$	**Maxwell equation from Ampère's law.** Ampère's law states that the line integral of $\overline{H}$ is equal to the current enclosed.

Table 2.1 *Maxwell's equations in integral and differential form for free space [2.1].*

2.3 Waves theory.

Maxwell's equations can be used in solving electromagnetic problems. In electromagnetic waves, a changing electric field produces a changing magnetic field, which in turn generates an electric field. Electromagnetic waves thus propagate and energy is transferred in free space at the speed of light. In a transverse electromagnetic (TEM) wave, the electric and magnetic fields are orthogonal to each other, and both are orthogonal to the direction of propagation.

In a non-conductive medium, the Maxwell's curl equation from Ampère's law is reduced to

$$\nabla \times \overline{H} = \frac{\partial \overline{D}}{\partial t} \tag{2.16}$$

Using rectangular coordinates for an electromagnetic wave propagating in the x direction, with an electric field vector aligned with the y-axis the magnetic field vector pointing in the z direction may be expressed as:

$$\frac{\partial H_z}{\partial x} = -\varepsilon \frac{\partial E_y}{\partial t} \tag{2.17}$$

where ε is the permittivity of the medium. Similarly, from Faraday's law

$$\nabla \times \overline{E} = -\frac{\partial \overline{B}}{\partial t} \tag{2.18}$$

and which in this case reduces to

$$\frac{\partial E_y}{\partial x} = -\mu \frac{\partial H_z}{\partial t} \tag{2.19}$$

where μ is the permeability of the medium. Differentiating 2.17 and 2.19 with respect to time and space, wave equations for the electric and magnetic fields can be obtained. These are:

$$\frac{\partial^2 E_y}{\partial t^2} = \frac{1}{\mu\varepsilon} \frac{\partial^2 E_y}{\partial x^2} \tag{2.20}$$

and

$$\frac{\partial^2 H_z}{\partial t^2} = \frac{1}{\mu\varepsilon} \frac{\partial^2 H_z}{\partial x^2} \tag{2.21}$$

The constant $\frac{1}{\mu\varepsilon}$ on the R.H.S. of 2.20 and 2.19 represents

$$\upsilon^2 = \frac{1}{\mu\varepsilon} \tag{2.22}$$

where υ^2 is the velocity of propagation of the wave in the medium. A solution of equations 2.20 and 2.19 is of the following form:

$$E_y = E_0 \cos(\omega t \pm \beta x) \tag{2.23}$$

where β is a constant. This solution indicates a sinusoidal wave travelling in the direction of x.

2.4 Maxwell's equations solutions.

The Finite-Difference Time-Domain or FDTD is a convenient numerical method for solving Maxwell's equations in the time domain. The FDTD technique offers many advantages as a tool for electromagnetic modeling, simulation, and analysis. These capabilities according to [2.2] include:

- Broadband response prediction centered about the system resonances.
- Arbitrary three-dimension (3D) model geometies.
- Interaction of EM waves with an object of specific conductivity.
- Capability for modeling materials with frequency-dependent EM properties i.e. μ, ε, and σ.
- Different response type including near and far-field solutions.

The FDTD method was introduced by Yee [2.3] in 1966. In this classic paper Yee stated: "solutions to the time-dependent Maxwell's equations in general form are unknown except for few special cases. The difficulty is mainly due to the imposition of the boundary conditions." One of the main problems in 1966 was the limited memory available to digital computers. Today, thirty-four years later, advances in personal computer (PC) have resulted in considerably increase in computer processing power and memory capacity. Most of the simulations presented in this thesis using FDTD have been run on a relatively low-cost personal computer equipped with 256 Mbytes of memory.

In FDTD the differential form of Maxwell's equations is used to determine the electric and magnetic fields. For a linear isotropic material

$$\overline{D} = \varepsilon \overline{E} \tag{2.24}$$

$$\overline{B} = \mu \overline{H} \tag{2.25}$$

The total electric and magnetic fields can be expressed as the sum of the incident and scattered fields

$$\overline{E} = \overline{E}^{total} = \overline{E}^{incident} + \overline{E}^{scattered} \tag{2.26}$$

$$\overline{H} = \overline{H}^{total} = \overline{H}^{incident} + \overline{H}^{scattered} \tag{2.27}$$

Since electric and magnetic losses can dissipate energy as heat in materials the magnetic and electric currents, J_m and J_e respectively, can be written as

$$\overline{J}_m = \rho' \overline{H} \tag{2.28}$$

$$\overline{J}_e = \sigma \overline{E} \tag{2.29}$$

Here ρ' is an equivalent *magnetic resistivity* in ohms per meter and σ is the *electric conductivity* in Siemens per meter (S/m). The two curl Maxwell's equations can be then written as

$$\frac{\partial \overline{H}}{\partial t} = -\frac{1}{\mu} \nabla \times \overline{E} - \frac{\rho'}{\mu} \overline{H} \tag{2.30}$$

$$\frac{\partial \overline{E}}{\partial t} = \frac{1}{\varepsilon} \nabla \times \overline{H} - \frac{\sigma}{\varepsilon} \overline{E} \tag{2.31}$$

Rewriting the two Maxwell's curl equations in terms of incident and scattered fields, we get

$$\nabla \times (\overline{E}^{inc} + \overline{E}^{scat}) = -\frac{\mu \partial (\overline{H}^{inc} + \overline{H}^{scat})}{\partial t} - \rho' (\overline{H}^{inc} + \overline{H}^{scat}) \tag{2.32}$$

$$\nabla \times (\overline{H}^{inc} + \overline{H}^{scat}) = \varepsilon \frac{\partial (\overline{E}^{inc} + \overline{E}^{scat})}{\partial t} + \sigma (\overline{E}^{inc} + \overline{E}^{scat}) \tag{2.33}$$

The free space incident fields due to the absence of any material are

$$\nabla \times \overline{E}^{inc} = -\frac{\mu_0 \partial \overline{H}^{inc}}{\partial t} \tag{2.34}$$

$$\nabla \times \overline{H}^{inc} = \varepsilon_0 \frac{\partial \overline{E}^{inc}}{\partial t} \tag{2.35}$$

and the scattered fields in a medium is given if we substitute the incident fields above in the total field equations.

$$\nabla \times \overline{E}^{scat} = -\mu \frac{\partial \overline{H}^{scat}}{\partial t} - \rho' \overline{H}^{scat} - \left[(\mu - \mu_0) \frac{\partial \overline{H}^{inc}}{\partial t} + \rho' \overline{H}^{inc} \right] \tag{2.36}$$

$$\nabla \times \overline{H}^{scat} = \varepsilon \frac{\partial \overline{E}^{scat}}{\partial t} + \sigma \overline{E}^{scat} + \left[(\varepsilon + \varepsilon_0) \frac{\partial \overline{E}^{inc}}{\partial t} + \sigma \overline{E}^{inc} \right] \tag{2.37}$$

Outside the scattered field, the total field equations become

$$\nabla \times \overline{E}^{total} = -\mu_0 \frac{\partial \overline{H}^{total}}{\partial t} \tag{2.38a}$$

or

$$\nabla \times (\overline{E}^{inc} + \overline{E}^{scat}) = -\mu_0 \frac{\partial (\overline{H}^{inc} + \overline{H}^{scat})}{\partial t} \tag{2.38b}$$

$$\nabla \times \overline{H}^{total} = \varepsilon_0 \frac{\partial \overline{E}^{total}}{\partial t} \tag{2.39a}$$

or

$$\nabla \times (\overline{H}^{inc} + \overline{H}^{scat}) = \varepsilon_0 \frac{\partial (\overline{E}^{inc} + \overline{E}^{scat})}{\partial t} \tag{2.39b}$$

and the scattered fields in free space can be expressed as

$$\nabla \times \overline{E}^{scat} = -\mu_0 \frac{\partial \overline{H}^{scat}}{\partial t} \tag{2.40}$$

$$\nabla \times \overline{H}^{scat} = \varepsilon_0 \frac{\partial \overline{E}^{scat}}{\partial t} \tag{2.41}$$

In computing the scattered fields, however, only equations 2.36 and 2.37 are needed. Inside the scatterer μ, ε, ρ' and σ are used. Outside $\rho' = \sigma = 0, \mu = \mu_0$ and $\varepsilon = \varepsilon_0$ are used. These equations can be rearranged so that the time derivative of the field is expressed as a function of the remaining terms for ease in generating the appropriate differential equations, namely:

$$\frac{\partial \overline{H}^{scat}}{\partial t} = -\frac{\rho'}{\mu} \overline{H}^{scat} - \frac{\rho'}{\mu} \overline{H}^{inc} - \frac{(\mu - \mu_0)}{\mu} \frac{\partial H^{inc}}{\partial t} - \frac{1}{\mu} (\nabla \times \overline{E}^{scat}) \tag{2.42}$$

$$\frac{\partial \overline{E}^{scat}}{\partial t} = -\frac{\sigma}{\varepsilon} \overline{E}^{scat} - \frac{\sigma}{\varepsilon} \overline{E}^{inc} - \frac{(\varepsilon - \varepsilon_0)}{\varepsilon} \frac{\partial \overline{E}^{inc}}{\partial t} + \frac{1}{\varepsilon} (\nabla \times \overline{H}^{scat}) \tag{2.43}$$

In a finite-difference representation, derivatives are replaced with differences i.e.

$$\frac{\partial f}{\partial t} = \lim_{\Delta t \to 0} \frac{f(x,t_2) - f(x,t_1)}{\Delta t} \approx \frac{f(x,t_2) - f(x,t_1)}{\Delta t} \tag{2.44}$$

for time derivatives and

$$\frac{\partial f}{\partial x} = \lim_{\Delta x \to 0} \frac{f(x_2,t) - f(x_1,t)}{\Delta x} \approx \frac{f(x_2,t) - f(x_1,t)}{\Delta x} \tag{2.45}$$

for space derivatives.

The FDTD method divides the modelled space into cells. The size of Δt and Δx must be limited in order for the system to be stable. Each cell (Yee cell) must be sufficiently small with dimensions fixed at smaller than $\lambda/10$. This is to enable accurate results at the highest frequency of interest. On the other hand, the cell size must be large enough to keep the computing requirements at manageable levels. The materials presence also affects the cell size. The greater the permittivity or conductivity, the shorter the wavelength at a given frequency and the smaller the cell size required. The Yee cell is shown in Fig. 2.1.

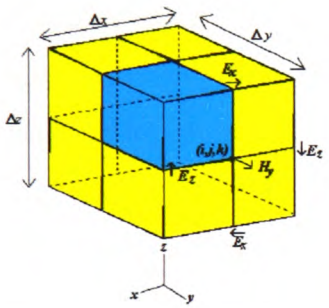

Fig. 2.1 *Yee cell used in the FDTD method.*

The time step for stability must satisfy Courant's stability criteria, namely:

$$\Delta t \leq \frac{1}{c\sqrt{\frac{1}{(\Delta x)^2} + \frac{1}{(\Delta y)^2} + \frac{1}{(\Delta z)^2}}} = \frac{\Delta}{c\sqrt{3}} \tag{2.46}$$

where on the RHS $\Delta x = \Delta y = \Delta z = \Delta$. Smaller time steps are permissible, but do not generally result in improvements to computational accuracy. For conductive materials, stable calculations require time steps smaller than the Courant limit. The same is valid for non-linear materials.

From the Yee cell diagram in Fig. 2.1 it can be seen that the magnetic field, in this method, has an offset of a half-cell. Then, the scattered electric field can be written as

$$E^{s,n} = \left(\frac{\varepsilon}{\varepsilon + \sigma\Delta t}\right)E^{s,n-1} - \left(\frac{\sigma\Delta t}{\varepsilon + \sigma\Delta t}\right)E^{i,n} - \left(\frac{(\varepsilon - \varepsilon_0)\Delta t}{\varepsilon + \sigma\Delta t}\right)E^{i,n} + \left(\nabla \times H^{s,n-\frac{1}{2}}\right)\left(\frac{\Delta t}{\varepsilon + \sigma\Delta t}\right) \tag{2.47}$$

For high conductivity values the equation above becomes:

$$E^{scat} = -E^{inc} \tag{2.48}$$

In a similar way, the corresponding equation for updating the other electric and magnetic fields can be obtained. Equation 2.47 can be readily solved [2.2].

2.4.1 Computer resources for FDTD.

Computer resources such as memory size and computation time are important factors in establishing an FDTD model. Before the design of a numerical model, the size of the required memory must be calculated using the following equation.

$$Storage = N \times \left[6\frac{Components}{Cell} \times 4\frac{Bytes}{Components} + 6\frac{IDs}{Cell} \times 1\frac{Byte}{ID} \right] = 30 \times N \tag{2.49}$$

This equation is used assuming that the material information is stored in 1-byte arrays, with both dielectric and magnetic materials considered. N is the total number of cells in the problem. For instance, if a numerical model consists of $153 \times 118 \times 120$ or 2,166,480 cells, 65 Mbytes of RAM is required. For the head/shoulders model used in this research, consisting of the same cell dimensions as mentioned above, a minimum of 96 Mbytes are used. The number of time steps (T) required in a simulation is given approximately by

$$T \cong 10 \times \sqrt{3} N^{1/3} \tag{2.50}$$

and the number of floating point operations is approximately given by

$$Operations = 10\sqrt{3} N^{4/3} \times 6\frac{Components}{Cell} \times 10\frac{Operations}{Component} \tag{2.51}$$

2.4.2 Far zone transformation.

As pointed out in previous sections the main limitations for FDTD are the available computer resources. These limitations become more severe in far-field calculations. The far-field region relation to a scatterer may be taken to start at distance R given by [2.4]

$$R = \frac{2D^2}{\lambda} \tag{2.52}$$

where D is the largest dimension of the scatterer. Both the memory requirements and the number of operations are dramatically increased if far field quantities are directly computed. The procedure for calculating the far field from near field data is straightforward for single frequency excitations. The near-to-far field transformation can be established if the complex time-harmonic electric and magnetic currents flowing on a closed surface surrounding the scattering object are stored during the simulation. If these complex fields or currents are written to disk then in post-processing, the far-zone radiation or the scattered fields can be determined. For multiple frequencies a hybrid approach is available which uses pulsed excitation for FDTD calculations. This gives the far field results in the frequency domain. For each frequency of interest a running discrete Fourier transform (DFT) of time harmonic tangential fields on a closed surface surrounding the FDTD geometry is updated at each time step.

If the scattering or radiating object is surrounded by a closed surface S' and if $\hat{n}$ is the local surface unit vector, then vector time-harmonic equivalent scattered surface currents $\bar{J}_s(\omega) = \hat{n} \times \bar{H}(\omega)$ and $\bar{M}_s(\omega) = -\hat{n} \times \bar{E}(\omega)$ exist on the surface, where $\bar{H}(\omega)$ and $\bar{E}(\omega)$ are the scattered magnetic and electric fields at the surface. The time harmonic vector-potentials $\bar{N}(\omega)$ and $\bar{L}(\omega)$ are defined as

$$\bar{N}(\omega) = \int_{s'} \bar{J}_s(\omega) e^{(jk\bar{r}' \cdot \hat{r})} ds' \tag{2.53}$$

$$\bar{L}(\omega) = \int_{s'} \bar{M}_s(\omega) e^{(jk\bar{r}' \cdot \hat{r})} ds' \tag{2.54}$$

where k is the wave number, $\hat{r}$ is the unit vector to the far zone field point, $\bar{r}'$ is the vector to the source point of integration, and S' is the closed surface surrounding the scatterer. The time harmonic far zone electric fields are related to

$$E_\theta = je^{(-jkR)} \frac{(-\eta N_\theta + L_\phi)}{2\lambda R} \tag{2.55}$$

$$E_\phi = je^{(-jkR)} \frac{(-\eta N_\phi + L_\theta)}{2\lambda R} \tag{2.56}$$

where η is the characteristic impedance of medium, and R is the distance from the origin to the far zone field point. In order to develop the corresponding time domain far zone transformation we need to take the inverse Fourier transformation of the

above. In a simplified notation, the inverse Fourier transformation process, the time harmonic vector potentials equals

$$W(\omega) = j\omega e^{\left(-\frac{j\omega R}{c}\right)} \frac{N(\omega)}{4\pi Rc} \tag{2.57}$$

$$U(\omega) = j\omega e^{\left(-\frac{j\omega R}{c}\right)} \frac{L(\omega)}{4\pi Rc} \tag{2.58}$$

where $k = \frac{2\pi f}{c} = \frac{\omega}{c}$. The corresponding equations for the far zone electric fields have no frequency dependence and can be written as

$$E_\theta = -\eta W_\theta - U_\phi \tag{2.59}$$

$$E_\phi = -\eta W_\phi - U_\theta \tag{2.60}$$

We can transform $W(\omega)$ and $U(\omega)$ into time-domain to obtain the vector potentials $W(t)$ and $U(t)$ as

$$W(t) = \frac{1}{4\pi Rc}\frac{\partial}{\partial t}\left(\int_{s'} J_s(t + \frac{(\bar{r}'\cdot\hat{r})}{c} - \frac{R}{c})ds'\right) \tag{2.61}$$

$$U(t) = \frac{1}{4\pi Rc}\frac{\partial}{\partial t}\left(\int_{s'} M_s(t + \frac{(\bar{r}'\cdot\hat{r})}{c} - \frac{R}{c})ds'\right) \tag{2.62}$$

where $J_s = \hat{n} \times H(t)$ and $M_s(t) = -\hat{n} \times E(t)$ are the time-domain electric and magnetic scattered currents on the closed surface surrounding the scatterer.

2.4.3 Antenna simulations with FDTD.

FDTD has been applied recently to antenna radiation and other related problems such as shielding and radar cross-section (RCS). The source, in antenna simulations, is typically driven by a single applied electric field in one FDTD cell. The advantage of the FDTD method over other methods is its ability to calculate far-field radiation patterns over a wide frequency band with a single program execution. Compared to method of moments, FDTD requires more computation time and more memory. However, due to the Cartesian nature of FDTD spirally shaped antennas, like the helix, are difficult to simulate requiring very small cell sizes. In most cases this is impractical.

The steady-state input power at an antenna at each frequency is given by

$$P_{in}(\omega) = \mathrm{Re}\left[V_1(\omega) I_1^*(\omega)\right] \tag{2.63}$$

where $V_1(\omega)$ and $I_1(\omega)$ are the Fourier transforms of the input potential ($V_1(t)$) and the input current ($I_1(t)$) respectively. The steady-state dissipated power equals

$$P_{diss} = \int_v \sigma \left|E_z(\omega)\right|^2 dv \tag{2.64}$$

where the σ is the material *conductivity* and the gain of a lossless isotropic antenna in the θ, ϕ directions is given by

$$Gain(\theta,\phi) = \frac{\left|E_F(\omega,\theta,\phi)\right| / \eta_0}{P_{in} / 4\pi} \tag{2.65}$$

where $E_F = (\omega,\theta,\phi)$ is the Fourier transform of the transient far zone time domain electric field radiation in the θ, ϕ directions, and η_0 is the characteristic impedance of free space. The efficiency of the antenna expressing the ratio of radiated power to total power will then given by

$$Efficiency = \frac{P_{in} - P_{diss}}{P_{in}} \tag{2.66}$$

In this study the FDTD is extensively used for the evaluation of the SAR arising in a human head tissue due to the use of mobile phone handset. For antennas operating in free space and made exclusively by conductive material the method of moments is much faster compared to FDTD. The method of moments principles are summarised in the next section.

2.5 The Method of Moments.

The Method of Moments (MoM) is one of the established and most extensively used numerical methods for solving antenna and a wide range of electromagnetic problems [2.7]. The method has been initially and successfully implemented for solving electromagnetic field problems involving wire antennas, scattering and radiation from structures that could be modelled by a wire grid mesh. It has been

extended and implemented in studing radiation and scattering from conductive or lossy flat plate structures.

In the MoM an electric and magnetic integral equation is transformed into a set of simultaneous linear algebraic equations (or matrix equations), which can be directly solved by standard numerical techniques. An outline of the technique is given below.

From basic electromagnetics the electric potential V of a point P at a distance r due to a charge Q is given by

$$V = \frac{Q}{4\pi\varepsilon r} \tag{2.67}$$

From a line with linear charge density $\rho_L(Qm^{-1})$ the potential at a point is given by the integral

$$V = \frac{1}{4\pi\varepsilon}\int_0^l \frac{\rho_L(x)}{r}dx \tag{2.68}$$

where l is the line length and $\rho(x)$ is the charge per unit of length of line. If $\rho(x)$ is available as a function of x, then equation 2.68 can be readily integrated. However, if $\rho(x)$ is not known, equation 2.68 represents an integral equation with the problem being to find a solution for $\rho(x)$, subject to given boundary conditions. The linear charge distribution can be approximated by segments with uniform charge density namely

$$Q_n = \overline{\rho}_L(x)_n \Delta x_n, \qquad n = 1,2,3....N \tag{2.69}$$

and the total charge on the wire is now given by

$$Q = \sum_{n=1}^{N} Q_n \tag{2.70}$$

Equation 2.68 can then be written as

$$\sum_{n=1}^{N} l_{mn} Q_n = V_m \tag{2.71}$$

Taking the case of a rod

$$l_{mn} = \frac{1}{4\pi\varepsilon r_{mn}}, \qquad m = 1,2,3,4.....M \tag{2.72}$$

$$r_{mn} = \sqrt{\alpha^2 + (x - x')} \tag{2.73}$$

where α is the rod radius, x is the axial distance of observation and x' is the axial distance of source point at middle of segment n. The above equation can be written in matrix form as

$$[l_{mn}][Q_n]=[V_m] \tag{2.74}$$

This matrix can be solved numerically on a digital computer. The more the segments in the model the more accurate the results. The number of segments used, as in the case of FDTD, is limited by the available computer resources.

The Numerical Electromagnetic Code (NEC) [2.8-2.10] is a widely used MoM software programme that has been compiled for many operating systems. The NEC and its predecessor AMP have been used successfully to model a wide range of antennas including complex structures, e.g. ships. Simulation with the MoM requires that the structure is modelled with a mesh of electrically small segments or flat plates or combination of the two. Proper choice of the segments and patches for a model is one of the most critical steps in obtaining accurate results. The number of segments is chosen to be the minimum required for acceptable accuracy, since the program running time and memory requirements increase rapidly as this number increases. There are several rules for wire-grid modeling of antennas:

- The length of the wire should be at least 1/10 of the wavelength at the desired frequency.
- Segments may not overlap since the division of current between two overlapping segments is undetermined.
- A large radius change between connected segments may decrease accuracy.
- A segment is required at each point where a network connection or voltage source is located.
- The number of wires joining at a single junction cannot exceed 30. This limitation, however, is due to an array dimension definition in NEC which can be altered by increasing this number in the source code
- When wires are parallel and very close together, the segments should be aligned to avoid incorrect current perturbation from an offset match point and a segment junction.

In NEC data is entered in the program as cards. Cards must be identified by their names. For instance, GW identifies a string of segments representing a straight wire. The start and stop coordinates, the number of segments, and the wire properties are some of the entries of this card. Cards for helix structures, patches, transmission lines and simulation properties (i.e frequency) are also available. The cards available in NEC2 are described in details in [2.10].

Despite its fast computational time advantage, some of the limitations of the NEC make it inappropriate for practical types of electromagnetic problems such a treatment of non-uniform structures. This is due to the increased memory and computational time requirements that the numerical solution of a 3D volume integral equation would involved.

2.6 Interim conclusions.

In this chapter the basic Maxwell's equations have been presented. The numerical solution of these equations can be used in computer programmes to solve accurately electromagnetic problems such as the radiation fields from antennas. The FDTD and MoM are two of these electromagnetic numerical methods. Results from the two methods on mobile phone antennas will be presented and compared later in this report. Some of the numerical results, like SAR predictions, are difficult to verify by measurements, making the numerical methods the only solution to the problem.

In Chapter 3 an overview of published literature on both the methods for improving PIFA's bandwidth and SAR is presented .

3. LITERATURE REVIEW

The commercial need for low cost and low profile antennas for mobile phones has drawn the interest of many researchers. While wire antennas, like the small helix and quarter-wavelength monopole, are predominantly used in mobile communication terminal applications, patch antennas are still the subject of research. Among the built-in antennas, the Planar Inverted-F Antenna is one of the most promising designs for handset applications due to its low profile, high efficiency and radiation characteristics, as well as the low SAR values resulting from the use of this antenna. Its narrow bandwidth, however, and the poor performance when the operator's hand is placed very closed to the radiating element have, prevented extensive application in mobile phones. Methods to increase the effective bandwidth and to reduce the size of PIFA, as well as recent research on the SAR are summarised in the following sections.

3.1 The Planar Inverted-F Antenna.

The performance of a PIFA for an 800 MHz band portable radio unit is reported in [3.1]. In this paper T. Taga and K. Tsunekawa state that the "PIFA exhibits sensitivity to both vertically and horizontally polarised radiowaves and therefore is suitable for use with portable radio equipment in which antenna orientation is not fixed." The authors describe the PIFA consisting "of a rectangular planar radiating element, a short pin between the radiation element and the surface of the case, and a feed line. The input impedance of PIFA elements including the metal case can be matched to the impedance of the inner circuit by selecting an appropriate distance between the feed point on the radiation element and the short pin." Both computed and measured characteristics of the PIFA for three antenna configurations are given. In particular, the PIFA is placed on the top, back and left sides of the handset as shown in Fig. 3.1. In the simulations, where a grid modelling method is used, the short pin is not modelled, because of method limitations. In the radiation pattern study, the most effective parameter is the length of the radio case. The longer this length, the more the E_Θ component patterns in the yz-plane face slightly downward. If the antenna is placed on the top of the handset the bandwidth increases with

distance from the conductive case. In particular, the relative bandwidth changes from 2% to 11.5% as the antenna distance from the handset increases from 0.02 to 0.09 wavelengths. This antenna displacement, however, results in an increase of the overall antenna volume. Finally, a PIFA in a two-antenna diversity configuration where the two antennas are mounted on two opposite sides of the handset is proposed.

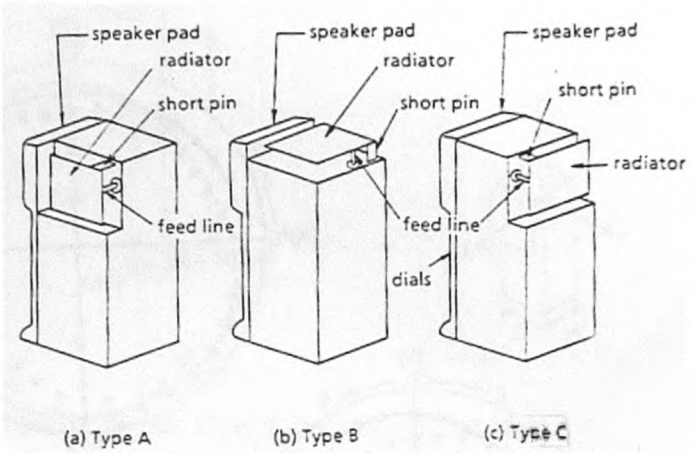

Fig. 3.1 *The Planar Inverted-F antenna in three different configurations.*

A Full Short circuit PIFA (FS-PIFA) is investigated in [3.2] by G. F. Pedersen and J. B. Andersen. This antenna, shown in Fig. 3.2, consists of a rectangular planar element, ground plane, coaxial feed, and a short-circuit plate of much narrower width than that of the side which is shorted. This configuration concentrates the current on the handset near the antenna, and has a relatively higher gain directed away from the user's head thereby reducing losses in the human body. This is important from the point of view of both efficiency and the reduction of possible health risks arising from exposure to microwave radiation. The bandwidth of this antenna can satisfy the GSM band requirements. Due to the absorption, losses in the plastic casing and shadowing, the integrated antenna has a smaller gain than the dipole by about 2dB. This gain is stated to be smaller inside a car and higher inside buildings. The influence of the head, however, is much reduced for the integrated antenna with less radiation toward the head.

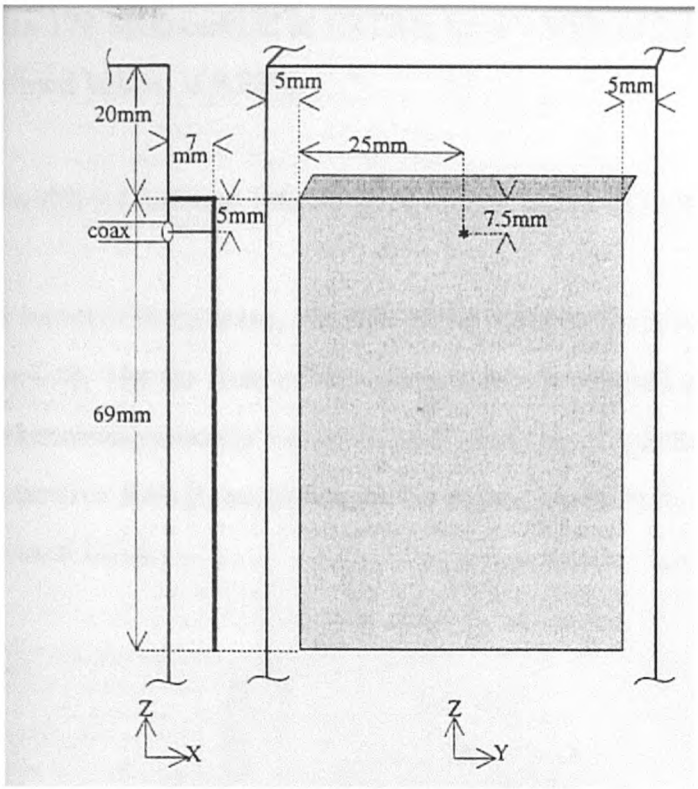

Fig. 3.2 *The Full Short circuit Planar Inverted-F Antenna.*

As already pointed out the PIFA is normally characterised by narrow bandwidth, which is one of its main limitations for commercial applications. In [3.3] C. R. Rowell and R. D. Murch introduced the capacitively loaded PIFA to overcome this problem. The proposed antenna is based on a PIFA design but it incorporates a capacitive load and feed. The capacitive load is formed by folding the open end of the PIFA towards the ground plane and adding a plate (parallel to the ground plane) to produce a parallel plate capacitor for the load. The capacitive feed is constructed by terminating the inner conductor of the coaxial cable to a conducting plate. This conducting plate is electromagnetically coupled to the radiating top plane. The antenna geometry is shown in Fig. 3.3. Different configurations have been studied in order to tune the antenna to the desired frequency band and in particular to the DCS1800 band. The authors state that "it can be observed that as the capacitive load increases (increasing w_{cap}/d_{cap} in Fig. 3.3), the resistive and reactance peaks contract, thereby decreasing the bandwidth of the structure. From these results it is realised that the capacitive load reduces the resonance frequency but at the expense of bandwidth and good matching." The introduction of the capacitive feed has resulted in improved impedance characteristics of the proposed antenna. Finally, with the proper antenna size, load and feed dimensions the bandwidth of the proposed antenna

can be increased to 178 MHz centred at 1.8 GHz for a VSWR of 2:1. The percentage bandwidth, as defined below, is 9.88%.

Percentage Bandwidth = (Antenna Bandwidth/Center Frequency) ×100% (3.1)

In addition to the bandwidth increase, the size of the antenna is reduced from λ/4, for a typical PIFA, to λ/8. The far field of the antenna has "remained unaffected by the addition of the electromagnetically coupled feed" and the efficiency due to current flow from the capacitive feed is, according to the paper, likely to be slightly less than that of a conventional PIFA.

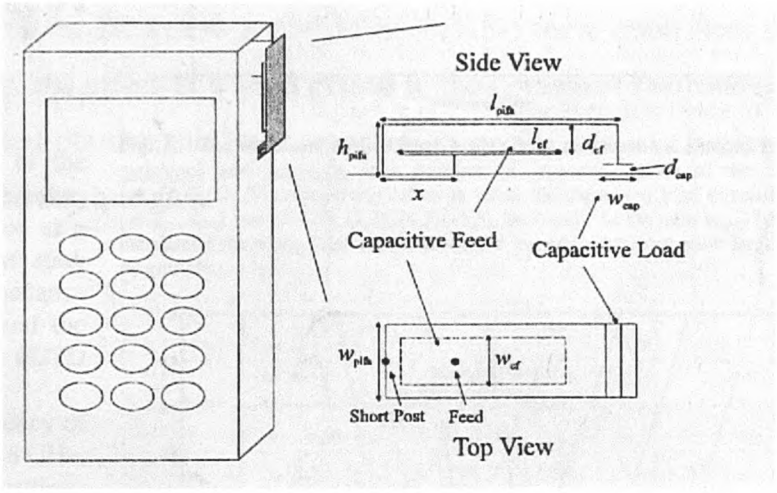

Fig. 3.3 *The capacitively loaded PIFA.*

Dual frequency planar inverted-F antenna, which operates at 0.9 GHz and 1.8 GHz bands, has been proposed by Z. D. Liu, P. S. Hall, and D. Wake in [3.4] and [3.5]. In the two-input-port configuration, shown in Fig. 3.4, the antenna "consists of two separated radiating elements, with the rectangular radiating element for 1.8 GHz and the L-shaped radiating element for 0.9 GHz. The dual-band antenna has almost the same size as a single-band planar inverted-F antenna operating at 0.9 GHz." The size of a typical PIFA can be determined approximately using [3.4]:

$$f_r = \frac{c}{4(a+b)} \qquad (3.2)$$

where c is the velocity of light, a and b are the width and length of radiating element and f_r is the operating frequency. The antenna impedance can be easily matched to 50Ω by appropriate choice of shorting pins and the feed-point position. Measurements and analysis using FDTD have shown that the antenna resonates near 0.9 GHz and 1.8 GHz if the right patch size and pin position are used. Mutual coupling does exist between the two patches causing some power to flow to the neighbouring patch but this has been measured at less than –17 dB. If the middle top corners of the two patches are electrically shorted and the feed and the shorting pins are placed in the middle of the antenna, a one-port antenna is obtained. Results from computations have shown that this antenna presents sufficient decoupling between the two radiating elements. The bandwidth for the GSM900 band operation is 63 MHz (7%) and for DCS1800 is 110 MHz (6.11%) for a return loss of less than –10dB. Further, the effect of a hand placed at the bottom of the handset is discussed and it is pointed out that this has a small effect on the mutual coupling between the patches and the antenna gain.

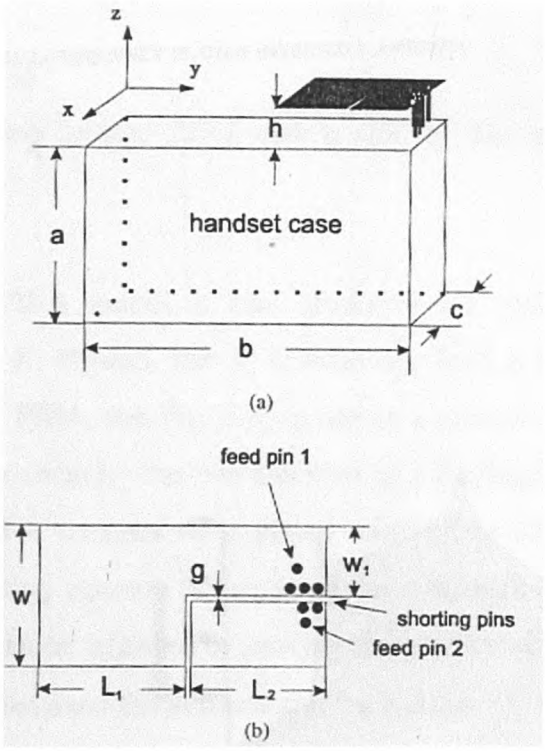

Fig. 3.4 *The Dual frequency PIFA [3.4].*

A dual-band capacitively loaded PIFA, using the designs outlined in the two previous papers, is presented in [3.7]. In this publication, C. R. Rowell and R. D. Murch used

the capacitively loaded PIFA with a slot as shown in Fig. 3.5a. It is shown that for every 5mm increase in the slot length the resonance frequency approximately decreases by 3%. With the introduction of a low-loss dielectric material ($\varepsilon_0 = 2.1$) between the top and ground planes the resonance frequency decreases to 940 MHz. If the same technique described in [3.2] and [3.3] were used, the result would be a dual-band PIFA resonating at 910 MHz and 1790 MHz. This antenna is shown in Fig. 3.5b.

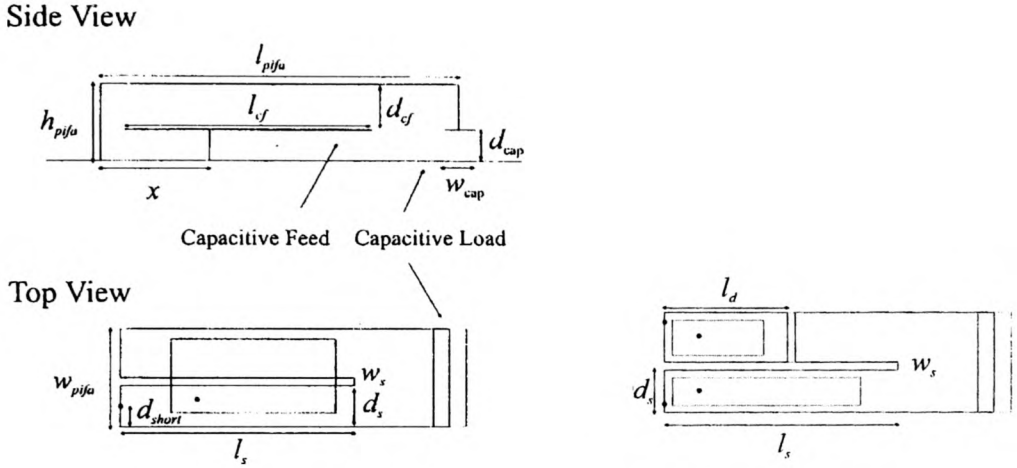

Fig. 3.5 *a) Capacitively loaded PIFA with a slot. b) The dual-band capacitively loaded PIFA.*

The low profile of PIFA makes it also attractive for mobile antenna diversity applications. In [3.7] K. Ogawa and T. Uwano use both a top-loaded short whip antenna and a built-in PIFA, see Fig. 3.6, to obtain a correlation coefficient of 0.26 between the signals received by the two antennas in a Rayleigh propagation channel. In this paper, the PIFA consists of a planar conducting element on a dielectric substrate. The conducting element is grounded via a through-hole at its corner. The matching impedance can be adjusted by moving the position of the feed point. Due to the dielectric element between the antenna and the handset f_r is approximately given by:

$$f_r = \frac{1}{4} \frac{c}{\alpha\sqrt{\varepsilon_r}(a+b+-\pi d)} \tag{3.3}$$

where ε_r is the relative permittivity of the substrate and α is a compensation coefficient, which is set to 0.9 for the proposed antenna. Measurements on this structure yielded –3.5dBd and –3.8dBd gains for the whip antenna and built-in antenna, respectively, where dBd denotes the gain relative to a half-wave dipole.

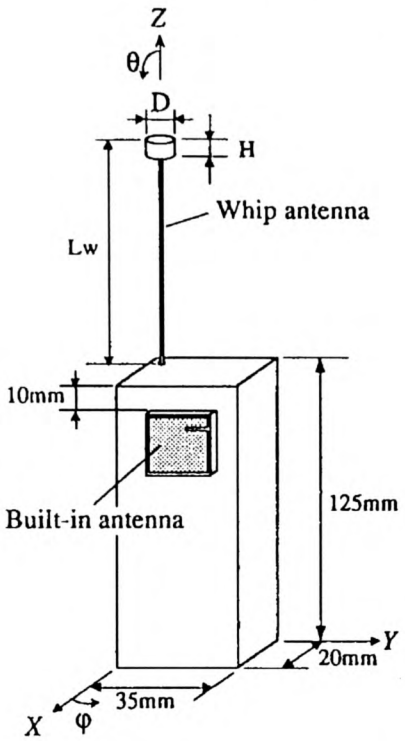

Fig. 3.6 *A top-loaded short whip antenna and a build-in PIFA in a diversity configuration.*

C. R. Rowell and R. D. Murch in [3.8] use two capacitively loaded PIFA for antenna diversity. Both antennas are designed for DCS1800 systems and are placed at the sides of a 80×40×10mm handset. The handset was then placed next to the operator's head. The correlation coefficient of the two received signals was computed for twenty-one different configurations and two inclinations of the handset (0° and 60°). Minimum correlation that also results in the highest diversity gain is achieved when the antennas are placed on the top and bottom of the handset on opposite sides. In this configuration, the antennas have also the highest physical separation.

Another low profile internal antenna, is the radiation-coupled dual-L antenna (RCDLA) which has been studied and introduced in [3.9] by J. Fuhl, P. Nowak, and E. Bonek. The antenna consists of two narrow metal plates that form an "L" shape. The elements are arranged in parallel with a narrow slot in between, as shown in Fig.

3.7. The feed point is placed in the middle of the antenna but is connected only on one section of the L-shaped patch. The antenna is mounted on the backside of the hand-held terminal, making use of the metallic housing as a shielding structure. From the simulations performed, it has been observed that the antenna has similar performance to that of the FS-PIFA in terms of shielding and radiation characteristics. In terms of bandwidth, the RCDLA outperforms the FS-PIFA giving satisfactory coverage of the GSM900 band. Despite the wide bandwidth obtained with the RCDLA, the results in [3.9] are based only on simulations using the MoM.

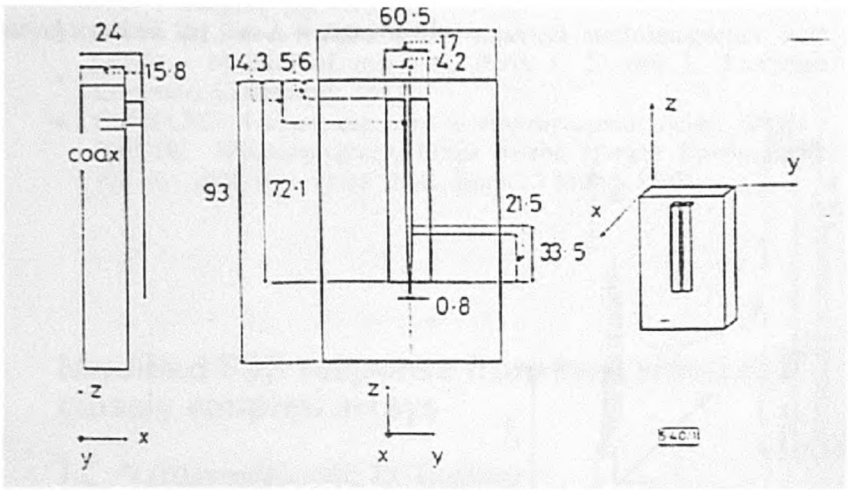

Fig. 3.7 *The dual-L antenna (RCDLA).*

As stated before, the electric properties of the antenna, such as the input impedance the radiation pattern, the efficiency and gain are significantly affected by the size of the conductive bodies next to the antenna such as the handset chassis, as well as its mounting positions. In particular, the efficiency of a $\lambda/4$ monopole on a handset can be lower than 40% in the presence of an operator, mainly due to radiation absorption by the human tissue. In [3.10] a new antenna is proposed, called the N-antenna (Fig. 3.8), which gives better performance under various operational conditions. "The antenna comprises two parallel narrow plates of different lengths where one terminal of the parallel plates is shorted and the other terminal in opened." The advantages of this type of antenna according to the authors (S.-G. Pan, T. Becks, A. Bahrwas and I. Wolff) are:

a) It is a double resonant structure and a wide bandwidth can be achieved by optimising its geometrical parameters.

b) Maximum radiation occurs in the horizontal direction and change little within the operating bandwidth of the antenna.

c) The antenna is a "non-symmetric structure," which means that the antenna gives the option for near-field design.

Both numerical and experimental methods for evaluating the performance of the N-antenna are used resulting in good agreement. The bandwidth of the antennas is reported to be 25-30 % (500 MHz) at DCS1800. Finally, from simulations in the proximity of the operator using FDTD, the efficiency has been found to increase to 87% compared to 40% for the λ/4 monopole.

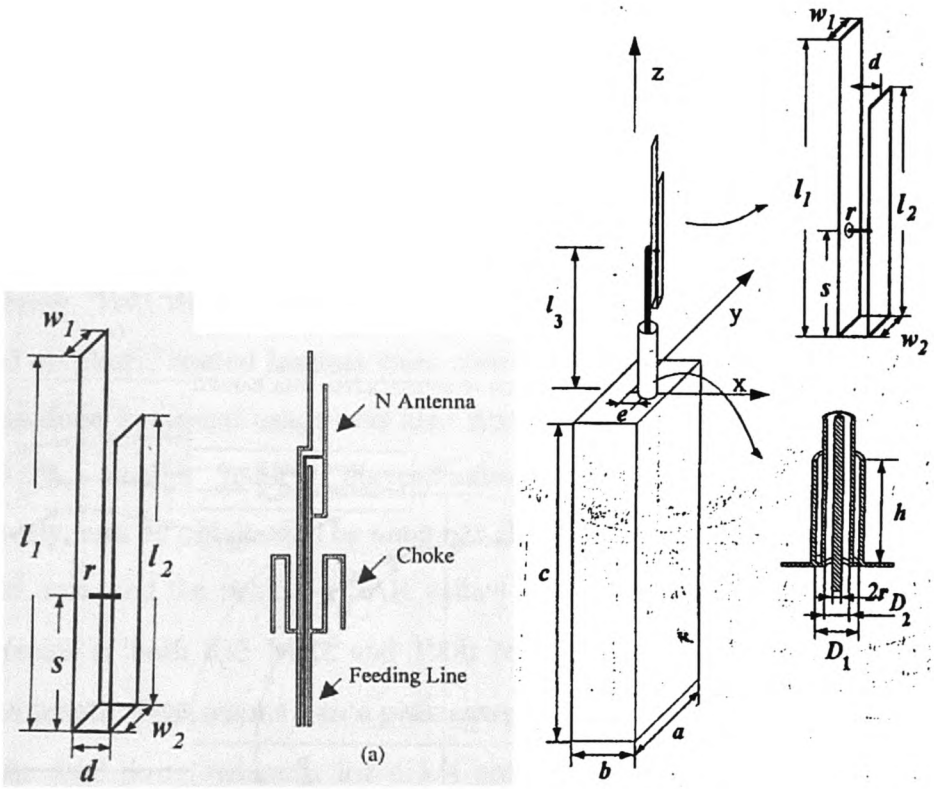

a) b) c)

Fig. 3.8 *a) The N-Antenna, b) The N-Antenna with a high frequency choke, c) N-Antenna and terminal configuration.*

3.2 Electromagnetic absorption and SAR.

The widespread use of cellular terminals and, in general, mobile wireless communication systems has consequently increased public concern about possible health hazards associated with microwave radiation. Safety guidelines on maximum permissible exposure (MPE) in mass-normalised Specific Absorption Rates (SAR) have been set by organisations worldwide. Some of the main research carried out on this subject is presented here.

A study of the electromagnetic absorption by the human head and neck caused by mobile telephones at 835 MHz and 1900 MHz is reported in [3.11]. The authors, O. P. Gandhi, G. Lazzi, and C. M. Furse, used the FDTD to calculate the electromagnetic energy coupled to the head from a mobile phone. For this reason, a millimetre-resolution anatomically based model of the human body consisting of 15 different tissue types was used. In particular, the model has a resolution of 1.875 mm for the two orthogonal axes in the cross-sectional planes and 3mm along the height of the body. Two different lengths of monopole antennas, namely $\lambda/4$ and $3\lambda/8$, mounted on plastic coated handset were considered. The effect of tilting the handset by 30^{o} as done in typical usage was also studied. By scaling the models by 21.77% and 36.5%, smaller models corresponding to 10- and 5-year-old children, respectively, can be obtained. The antennas showed that the powers absorbed by the head and neck and the peak 1-g SAR values were lower for $3\lambda/8$ antennas than the $\lambda/4$ antennas at both 835 MHz and 1900 MHz frequencies, due to differences in electrical length. That results into a peak current region for the $3\lambda/8$ antenna to be $\lambda/8$ above the feed point, whereas for a $\lambda/4$ antenna this region is at the base of the antenna, and, hence closer to the ear. Similar results were reported for the tilted antenna configurations. For the scaled models it was noted that even though the peak 1-g SAR values were fairly similar for the three models at 1900 MHz, the 1-g SAR values were considerably higher for the smaller head sizes at 835 MHz. There is also a larger in-depth penetration of SAR values for the models of 10- and 5-year-old children as compared to those for the adult model. Truncated head models in the term of half and third head sections were used to reduce simulation times, where good

agreement was achieved between the full model results and these obtained from the truncated models.

J. Toftgård, S. N. Hornsleth, and J. B. Andersen [3.12] present the user's effect on portable antennas. In this study, the hand and head were modelled as pure muscle with dielectric properties $\varepsilon_r = 50.5$ and $\sigma = 1.2(S/m)$ for 900 MHz and $\varepsilon_r = 49$ and $\sigma = 1.6(S/m)$ for 1900 MHz. The head was represented by a 90 mm sphere and the hand was modelled to be 100 mm wide and 20 mm thick and was wrapped around the lower part of the telephone on the side turning away from the head using a 5×5×5 mm^3 Yee cell, simulations and measurements of the far-field radiation patterns were shown to give good agreement in the dominant Θ-polarisation but not in the Φ-polarisation. This was probably due to the reflections in the anechoic chamber and difficulties with precise alignment of the antenna. Further, less power, by approximately 2dB is radiated in the direction of the operator's head due to shadowing. The resonance frequency of the λ/4 antenna is lower when it operates in the proximity of the user. The efficiency of the antenna also drops to 55%, whilst 96% of the total absorbed power was lost in the head and the remaining 4% in the hand. As expected, the efficiency increased as the terminal was held farther away from the head. Similar results are reported for a 1900 MHz centred band.

V. Hombach, K. Meier, M. Burkhardt, E. Kühn, and N. Kuster studied the dependence of EM energy absorbed on human head modelling at 900 MHz [3.13]. In this paper, both calculated and measured results are presented. Calculated results are obtained using FDTD, and in particular a commercially available code called MAFIA. On the other hand, measurements are done with a phantom head and a robotic arm. The SAR distribution is determined by measuring the electric field with miniaturised E-field probes inside shell phantoms filled with tissue simulating liquids. For dosimetric assessments of RF-sources close to the head, the following measurements strategy is implemented: The E-field probe first scans over a large area inside the head to roughly localise the maximum SAR value. Subsequently, SAR-measurements are done along a fine grid within a 35-g cubically shaped volume around this maximum value. This cube is large enough to provide sufficient data to evaluate the spatial peak SAR. Three different phantoms, for numerical and

experimental, tests have been used. From study of the electromagnetic phenomena, it was concluded that:

a) The region with high absorption values in all head phantoms is small and close to the feedpoint of the dipole.
b) Two SAR maxima can be identified in each of the phantoms, with one situating on the skin's surface and the other on the brain's surface. SAR values induced in the bone tissue are considerably lower.
c) The SAR distribution differs between the phantoms.

Further more, it has been reported that, 70% of the antenna input power is absorbed by the head and that the spatial peak SAR is affected by the size and shape of the human head for electromagnetic sources at a defined distance from the human head.

In [3.14], M. Okoniewski and M. A. Stuchly published further, primarily computational, research on the handset antenna and human body interaction. The antennas used are the monopole and dipole mounted on a metal box, along with three cubical models of the head, three similar spherical models, and three anatomically based models. The far-field radiation patterns have been calculated with and without the operator's hand. For the former case, the box representing the head nearly entirely blocks the radiation in the head direction. In the case of the sphere, there is a less dramatic albeit significant reduction in power radiated towards the half-space where the head is located.

The antenna patterns are to a lesser degree affected by the quality of the head model and other geometrical factors. The box models of the head at close distance to the phone give lower antenna efficiency and higher absorbed power in the head, which results in a higher SAR. Spherical models, which have resulted in better efficiency and less power absorbed by the head, are in reasonably good agreement with relatively low resolution anatomically accurate head models. An important factor on the results is the ear on the side of the handset. Finally, the importance of the hand in the numerical results is pointed out as a factor, which can reduce the antenna efficiency by as much as 16%!

The FDTD method is also used by S. Watanabe, M. Taki, T. Nojima and O. Fujiwara in [3.15] to study the characteristics of the SAR distribution in a head exposed to

electromagnetic fields radiated by a hand-held portable radio. A heterogeneous and realistic numerical head model, next to a λ/4 monopole and λ/2 dipole has been used. For result optimisation, input power has been set to 1 W. During exposure from the λ/2 dipole, a large amount of power is absorbed in the occipitotemporal area (upper back of the head) and in the area behind the auricle. With the exposure to the λ/4 monopole, on the other hand, the large SAR appears in the cheek and in the area behind the auricle. This implies that the SAR distribution on the surface of the head is strongly affected by the current distribution on the antenna and the conducting chassis of the radio terminal. No "hot spot" deep in the head is evident. The absorption in the eye of the head is greater for the λ/4 monopole than for the λ/2 dipole. The maximum local SAR values at 1.5 GHz are larger than those at 900 MHz, and this difference is due to the higher penetration depth at 1.5 GHz. For the exposure at 900 MHz, the maximum local SAR values are lower when the λ/2 dipole antenna because the position of the maximum current on the dipole antenna is farther from the head than that on the λ\4 monopole antenna. For antennas longer than 3/8λ, the maximum local SAR values decrease. Finally, the authors conclude that:

a) The maximum local SAR is lower in a head model without auricles.
b) When the radio is located in the vicinity of the head, the maximum local SAR values in the homogeneous head model agree well with those in the heterogeneous model.
c) The maximum local SAR values in the head do not depend on the position of the hand holding the radio as long as the hand does not shield the antenna.

S. V. Amos, M. S. Smith and D. Kitchener in [3.16] report their work on SAR evaluation with maximum continued power of 600 mW. Both the whip and PIFA with and without the ear were studied. It has been reported that the maximum 1-g mass averaged SAR is higher for the monopole antenna, compared to the PIFA. A decrease of SAR was recorded when the ear was removed. That is considered to be due to the averaging process. When placed next to the ear, the radiation is localised in one region, the ear. When the ear is removed, the radiation is distributed over a larger area and thus the average over a mass of 1g decreases. For the PIFA, the results indicate that the main consideration should be the position of the feed on the

element. Very low SAR values in the eye have been recorded and for this reason no extra recommendations are required. The authors conclude that:

a) The ear is an important parameter in the design model used in simulations. A standard model among different studies would be beneficial so that reliable comparisons can be drawn.
b) Parameters, such as the amount of shielding, the feed position and the electrical parameters of tissues, may all have significant effects on the resulting SAR.
c) Increased distance between the radiating element and head can significantly reduce SAR. This can be achieved through back-mounted PIFA or profiling of the handset.

3.3 Interim conclusions.

A brief summary of the literature research has been presented in this chapter. The first part covers alternative handset antennas for mobile terminals and, in particular, work on the PIFA is summarised. It becomes obvious that the main problem concerning the commercial application of PIFA is the narrow bandwidth that characterises the antenna. This is a limiting factor not only for the desirable dual-band use of the antenna but also its use in the GSM900 single band. Despite substantial previous work on the subject the problem of narrow bandwidth and its multiple resonances in the commercial bands remains. If a narrow bandwidth antenna, like the PIFA, is placed next to the operator's head or waist the resonance frequency will be shifted causing high reflections at frequencies outside the new bandwidth where the return loss is high. For this reason, not only the antenna bandwidth must be made equal to that required by the system bandwidth but it must also allow a guard band to ensure low VSWR under all possible operational conditions. This will be discussed with the introduction of the fine-tuned-PIFA later in Chapter 6.

The study of EM energy absorption, when a mobile phone is used in the proximity of the operator and results from various research investigations are summarised in the second section of this chapter. Even though SAR investigation covers a plethora of user-terminal configurations investigation is concentrated on the centre frequencies

of the GSM900 and DCS1800 bands. This gives the value of SAR at the specific frequencies but does not amount to a full understanding of SAR's behaviour with frequency. In addition, the effect of the handset size on the radiation properties of different antenna types has not been considered in detail. Furthermore, little attention has been given to the efficiency of the antenna under coupling conditions. In the following chapters, the SAR, antenna efficiency and a newly introduced concept of the 3dB SAR volume for different handset dimensions and head model sizes are studied and discussed.

4. FAR FIELD NUMERICAL EVALUATION AND MEASUREMENTS OF HANDHELD ANTENNAS

The problem of antenna radiation normally involves either analytical or numerical solution of Maxwell's equations. For the analysis of such problems the Green's functions can be used [2.4]. The complexities of the analytical methods, however, make them impractical for complex problems such as those encountered in antenna analysis. Hence, numerical methods, like the MoM and the FDTD outlined earlier, can be employed to provide an approximate solution to such problems. To verify the accuracy of numerical simulations, appropriate measurements can be performed. However, experimental investigation of antenna parameters suffer from a number of drawbacks too. Some of these, that affect our measurements, according to [2.4] are:

a) Unwanted reflections from the ground and walls of the anechoic chamber to sufficienty small levels, especially at low frequencies.
b) Ancillary equipment used (e.g. the tripod and the turn table) form part of the system under test and they may affect the overall result of the measurements, especially for electrically small radiators. The effect of the support structure is also difficult to compensate via calibration or simulation.

Both experimental and numerical results have been obtained in this study. In the next section, some basic antenna deffinitions are outlined as a useful background to the antenna measurements and numerical simulations. This will be helpful also in interpritation and assesment of the results.

4.1 Introduction to antennas.

Antenna is a device, which is used to receive and transmit electromagnetic waves efficiently. An antenna also serves as a directional device in addition to a probing device. In most of the cases an antenna is a metallic structure. Many types of antennas are known. Each of these antenna types, including dipoles, monopoles, loop and helix antennas, serves a specific application. Standard definitions and terms for antennas can be found in [2.4-2.6] and these have been agreed by international regulatory bodies such as the IEEE. Standardisation of the antenna glossary terms

helps in providing designers and engineers with a common terminology for antennas. In the following subsections, basic definitions and equations related to antennas, and in particular those designed and used as part of this research, are outlined.

4.1.1 Antenna types.

Antennas can be classified as follows.

1. *Wire Antennas:* These are simple antennas consisting of wire, whose shape and length define their radiation characteristics and operational frequency. There are various shapes of wire antennas including dipole, monopole, loop and helix, rectangular and square.
2. *Aperture Antennas:* Aperture antennas are more common at microwave frequencies. These include the pyramidal horn, conical horn, and rectangular waveguide.
3. *Microstrip Antennas:* Microstrip antennas are conductive patches, normally etched on dielectric substrates. The patches have different shapes and a plethora of techniques are used for achieving good radiation characteristics. The microstrip antennas are low profile, conformal to planar and nonplanar surfaces. They are simple and inexpensive to fabricate using modern printed-circuit technology. They can be mechanically robust when mounted on rigid surfaces and versatile in terms of resonance frequency, polarisation, pattern, and impedance.
4. *Array Antennas:* In an array antenna more than one antenna are used in various configurations. The distance between the array antenna elements, the phase, and amplitude of the individual antenna signals define the radiation characteristics of an array antenna.
5. *Reflector Antennas:* Reflector antennas are used for high directivity and gain where this is required. Main use is in the satellite communication and terrestrial point-to-point microwave relay links.
6. *Lens Antennas.* These antennas are used to collimate incident divergent energy to prevent it from spreading in undesired directions.

4.1.2 Antenna definitions and parameters.

This section presents basic antenna definitions, which are used in the following chapters. These definitions are described in more detail in [2.4-2.6].

The *radiation pattern* of an antenna is a mathematical function or a graphical representation of its radiation properties as a function of space coordinates. In most cases, the radiation pattern is determined in the far-field region and represented as a function of the directional coordinates. Radiation properties include power flux density, radiation intensity, field strength or polarisation.

An *isotropic antenna* is a hypothetical lossless antenna having equal radiation in all directions. A *directional antenna* is the antenna having the property of radiating or receiving electromagnetic waves more effectively in some directions than others. This term is usually applied to an antenna whose maximum directivity is significantly greater than that of a half-wave dipole. An *Omnidirectional Antenna* is an antenna having an essentially nondirectional pattern in a given plane and a directional pattern in any other direction. A simple example of an omnidirectional antenna is the half-wave dipole.

The space surrounding an antenna can be divided in to three regions. The *reactive near-field region* is that portion of the near-field region immediately surrounding the antenna wherein the reactive field predominates. For most antennas, the outer boundary of this region is commonly taken to lie at a distance R given by:

$$R = 0.62\sqrt{\frac{D^3}{\lambda}} \qquad (4.1)$$

from the antennas surface, where D is the largest dimension of the antenna. To be valid, D must also be larger compared to the wavelength. The *radiation near-field (Fresnel) region* is that region of the field of an antenna between the reactive near-field and the far-field region wherein radiation fields predominate and wherein the angular field distribution is dependent upon the distance from the antenna. Finally, the *far-field (Fraunhofer) region* is defined as that region of the field of an antenna where the angular field distribution is essentially independent of the distance from the antenna. The far-field region is commonly taken to exist at distances greater than

$$R = \frac{2D^2}{\lambda} \tag{4.2}$$

from the antenna.

Radiation intensity is the power radiated from an antenna per unit solid angle. The radiation intensity at a distance r is a far-field parameter and is given by

$$U = r^2 S_{rad} \tag{4.3}$$

where S_{rad} is the Poynting vector. The above equation can be also written , in terms of the electric field components, as

$$U(\theta,\phi) = \frac{r^2}{2\eta}\left|\overline{E}(r,\theta,\phi)\right|^2 \approx \frac{r^2}{2\eta}\left[\left|E_\theta(r,\theta,\phi)\right|^2 + \left|E_\phi(r,\theta,\phi)\right|^2\right] \tag{4.4}$$

where η is the intrinsic impedance of the medium. The *total power radiated* is then

$$P_{rad} = \oint_\Omega U d\Omega = \int_0^{2\pi}\int_0^{\pi} U \sin\theta d\theta d\phi \tag{4.5}$$

For an isotropic source the radiation intensity is simply given by

$$U_0 = \frac{P_{rad}}{4\pi} \tag{4.6}$$

Directivity of an antenna is the ratio of the radiation intensity in a given direction to the radiation intensity averaged over all directions. The averaged radiation intensity is equal to the total power radiated by the antenna divided by 4π. For a nonisotropic source the definition is equal to the ratio of its radiation intensity in a given direction over that of an isotropic source.

$$D = \frac{U}{U_0} = \frac{4\pi U}{P_{rad}} \tag{4.7}$$

The *total directivity* is the sum of the *partial directivities* for any two orthogonal polarisation.

$$D_0 = D_\theta + D_\phi \tag{4.8}$$

where

$$D_\theta = \frac{4\pi U_\theta}{(P_{rad})_\theta + (P_{rad})_\phi} \tag{4.9a}$$

and

$$D_\theta = \frac{4\pi U_\phi}{(P_{rad})_\theta + (P_{rad})_\phi} \tag{4.9b}$$

The directivity of a half-wavelength dipole is $D = 1.67\sin^3\theta$ and for an isotropic source is 1.

The *absolute gain* of an antenna is defined as the ratio of the intensity, in a given direction, to the radiation intensity that would be obtained if the power accepted by the antenna were radiated isotropically.

$$G = 4\pi \frac{radiation\_intensity}{total\_input(accepted)\_power} = 4\pi \frac{U(\theta,\phi)}{P_{in}} \tag{4.10}$$

On the other hand, the *relative gain* is the ratio of the power gain in a given direction to the power gain of a reference antenna in its referenced direction. The total *radiated power* is related to the input power by

$$P_{rad} = e_{cd} P_{in} \tag{4.11}$$

where e_{cd} is the antenna *radiation efficiency*. The gain is related to directivity by

$$G(\theta,\phi) = e_{cd} D(\theta,\phi) \tag{4.12}$$

and similarly to partial directivity case the total gain is the sum of the partial gains for any two orthogonal polarisation.

$$G_0 = G_\theta + G_\phi \tag{4.13}$$

where

$$G_\theta = \frac{4\pi U_\theta}{P_{in}} \tag{4.14a}$$

and

$$G_\phi = \frac{4\pi U_\phi}{P_{in}} \tag{4.14b}$$

The *antenna efficiency* is the product of the *reflection efficiency* (e_r), *conduction efficiency* (e_c) and the *dielectric efficiency* (e_d)

$$e_0 = e_r e_c e_d \tag{4.15}$$

The *bandwidth* of an antenna is defined as the frequency range within which the performance of the antenna, with respect to some characteristics, conforms to a

specified standard. For handheld antennas, described in the following chapters, a bandwidth corresponding to VSWR < 2:1 is used. For this case, the *reflection coefficient* is $|\rho| = \frac{1}{3}$ which means that $\frac{2}{3}$ of the total power from the transmitter is radiated.

Polarisation of an antenna in a given direction is the polarization of the wave transmitted (radiated) by the antenna. When the direction is not stated, the polarization is taken to be the polarization in the direction of the maximum gain.

Polarization loss factor (PLF) is the loss due to polarization mismatch between the receiving antenna and the electromagnetic wave. If the incoming wave is $\overline{E}_i = \hat{\rho}_w E_i$ where $\hat{\rho}_w$ is the unit vector of the wave, and the polarization of the electric field of the receiving antenna is $\overline{E}_a = \hat{\rho}_a E_a$ where $\hat{\rho}_a$ is its unit vector the polarization loss factor is

$$PLF = |\hat{\rho}_w + \hat{\rho}_a|^2 = |\cos\psi_p|^2 \tag{4.16}$$

where ψ_p is the angle between the two unit vectors.

The *input impedance* of an antenna is defined as the impedance presented by an antenna at its terminals or the ratio of the voltage to current at a pair of terminals or the ratio of the appropriate components of the electric to magnetic fields at a point. Antenna input impedance can be written as

$$Z_A = R_A + jX_A \tag{4.17}$$

where R_A is the antenna resistance and X_A is the antenna reactance. The resistance consists of two components: the *radiation resistance* (R_r) and the *loss resistance* (R_L).

$$R_A = R_r + R_L \tag{4.18}$$

4.1.3 Free-space propagation.

In the absence of any reflections or multipath the free propagation equation is

$$\frac{P_r}{P_t} = G_r G_t \left(\frac{\lambda}{4\pi R}\right) \tag{4.19}$$

where

P_r is the received power in watts,

P_t is the transimitted power in watts,

G_r is the transimiter antenna gain,

G_t is the receiver antenna gain,

λ is the wavelength and,

R is the distance between the receive and transmit antennas.

In logarithmic form eq. (4.19) can be written as

$$P_r(dBW) = P_t(dbW) + G_t(dBi) + G_r(dBi) + 20\log_{10}\left(\frac{\lambda}{4\pi}\right) - 20\log_{10}(R) \tag{4.20}$$

The free space loss (FSL) then can be defined as

$$FSL = 20\log_{10}\left(\frac{\lambda}{4\pi R}\right) \tag{4.21}$$

4.2 Antenna measurement facilities and methods.

The anechoic chamber of the Radiowave Propagation and System Design (RPSD) research group has been used for measurements of radiation patterns in the far field. For all far-field radiation pattern measurements, the distance between the antennas is 1 m, which meets the far-field radiation criterion in eq. 4.2. The size and shape of the anechoic chamber are depicted in Fig. 4.1.a. and the coordinates system used in this report is shown in Fig. 4.1.b. The walls of the anechoic chamber are covered by 90mm high pyramid absorbers, which were previously selected for measurements at frequencies greater than 10 GHz. These absorbers are small, compared to those required for measurements in the GSM frequency bands, allowing small amounts of reflections.

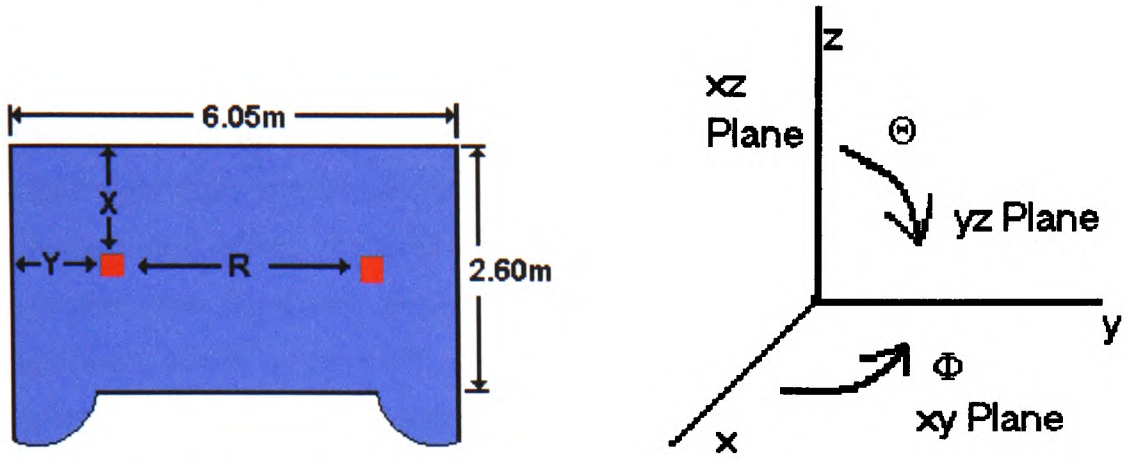

a) b)

Fig. 4.1 *a) The anechoic chamber of the RPSD research group, b) Coordinates system used in both the measurements and simulations.*

4.2.1 Measurement methods for handheld antennas.

Reflection coefficient and radiation measurements have been mainly carried out with the use of the Vector Spectrum Analyser (VNA HP8714c 300MHz-3GHz RF Network Analyser). In particular, some functions of the VNA that were systematically used are:

- *Reflection coefficient measurements*: Using this option, the input impedance and as a consequence VSWR or return-loss (S_{11}) of an antenna can be measured directly. The analyser computes the reflection using the following formula:

$$\textit{Reflection coefficient } (dB) = 10\log\left(\frac{P_{refl}}{P_{inc}}\right) \qquad (4.22)$$

  where P_{refl} is the power of the signal reflected from the device and P_{inc} is the incident power. "One-Port" calibration is needed in advance of the measurements.

- *Transmission coefficient measurements:* This function is used to measure the CW radiation pattern of antennas or to evaluate the absolute gain versus frequency. A "response" calibration is performed for this kind of measurement.

Measurement calibration is a process that improves accuracy of VNA measurements by using error correction arrays to compensate for systematic measurement errors.

Measurement errors are classified as random, drift, and systematic errors. *Random errors* such as noise from connectors that are non-repeatable and as such they can not removed by measurement calibration. *Drift errors*, such as frequency and temperature drift, are also non-repeatable and so not removable by calibration. To eliminate drift errors, the instrument must operate for at least one hour before measurements. *Systematic errors*, such as tracking and crosstalk, are the most significant errors in most RF measurements. Fortunately systematic errors are repeatable and for the most part can be corrected. However, small residual errors may remain.

Repeatable systematic errors are due to system frequency response, isolation between the signal paths, and mismatch and leakage in the test setup. *Frequency response errors* are errors that are a function of frequency. *Isolation errors* result from energy leakage between signal paths. In transmission measurements, this leakage results into crosstalk. In reflection measurements, it is due to impedance directivity. Finally, *mismatch errors* results from differences between the Device Under Test (DUT) port impedance and the instrument used port impedance.

For reflection measurements, *"one-port" calibration* is used. A one-port calibration prompts you to connect three measurement standards: an open circuit, a short circuit and a matched load (50Ω). The analyser measures each standard across the frequency band defined, using the number of points defined. The measurements of these standards are used to remove systematic errors caused by directivity, source match and frequency response. For transmission measurements *"response" calibration* is used. In a response calibration the VNA prompts the user to connect a *through cable* as the calibration standard, and then measures it across the frequency band defined and for the number of points defined. This measurement is used to correct systematic frequency response errors. Calibration is performed every time the instrument is used and every time one of the settings changes.

In Fig. 4.2.a block diagrams for reflection and transmission measurements are shown. It can be seen that for reflection measurements only one port of the VNA is used and for this reason the cable between the instrument and the antenna can be short in length. On the other hand, in transmission measurements both ports of the

VNA are used and longer cables are needed mainly due to the distance between the two antennas. In practice, mobile phone antenna reflection measurements can be done outside an anechoic chamber if the antenna is placed at a reasonably long distance from other surrounding objects. The cable used, then, can be short (i.e. 30cm). This is not the case for transmission measurements where the antennas must be in the anechoic chamber and the total cable length exceeds 6m. A photograph of the VNA, the standard loads used for "one-port" calibration and some of the antennas tested are shown in Fig. 4.2.b.

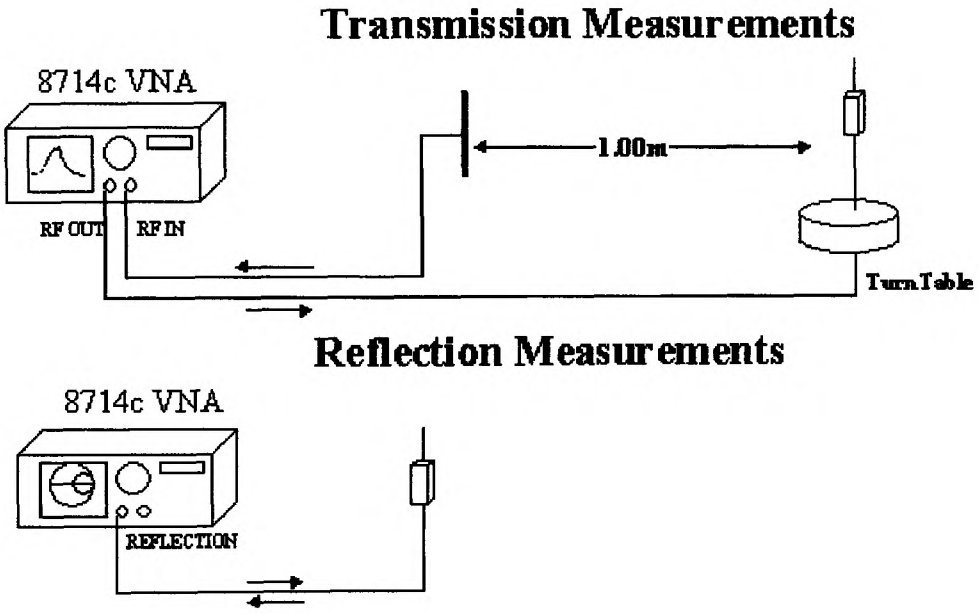

a)

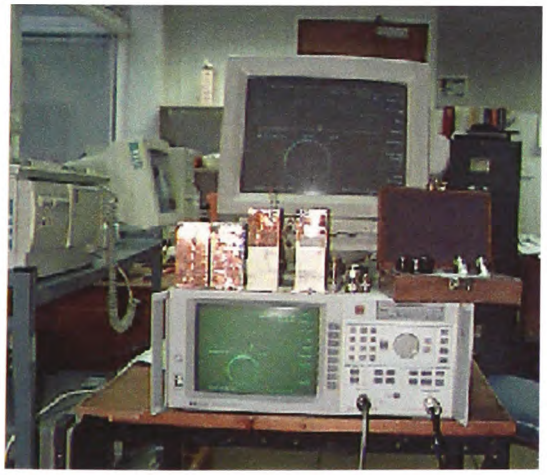

b)

Fig. 4.2 *a) Transmission and reflection measurements geometry. b) The Vector Network Analyser HP8714c 300MHz-3000MHz.*

4.3 Antenna reflection and input impedance measurements.

In the investigation carried out on mobile antennas, four different antenna types, three of which are shown in Fig. 4.3, have been built and tested, namely:

a) a half-wavelength dipole (two similar dipoles are used as the reference antenna),
b) a monopole antenna,
c) a small helix antenna, and
d) a Planar Inverted-F Antenna (PIFA).

These antennas have been designed to operate at a centre frequency of 945 MHz. This frequency is repeatedly used for measurements and simulations of antennas designed for the GSM900 system. In Fig. 4.4 the measured VSWRs of the four antennas are shown. It can be seen that the helix and the PIFA antennas have lower VSWR compared to the monopole and the dipole antennas but their bandwidth (VSWR < 2:1) is narrower. Therefore, reflection efficiency is better for these antennas at the operational frequency. No matching elements have been used in order to keep the antennas simple. The Smith chart in Fig. 4.5 shows that the dipole and the PIFA antennas have capacitive impedance. On the other hand, the helix and the monopole antenna are characterised by inductive impedance in their resonance frequency.

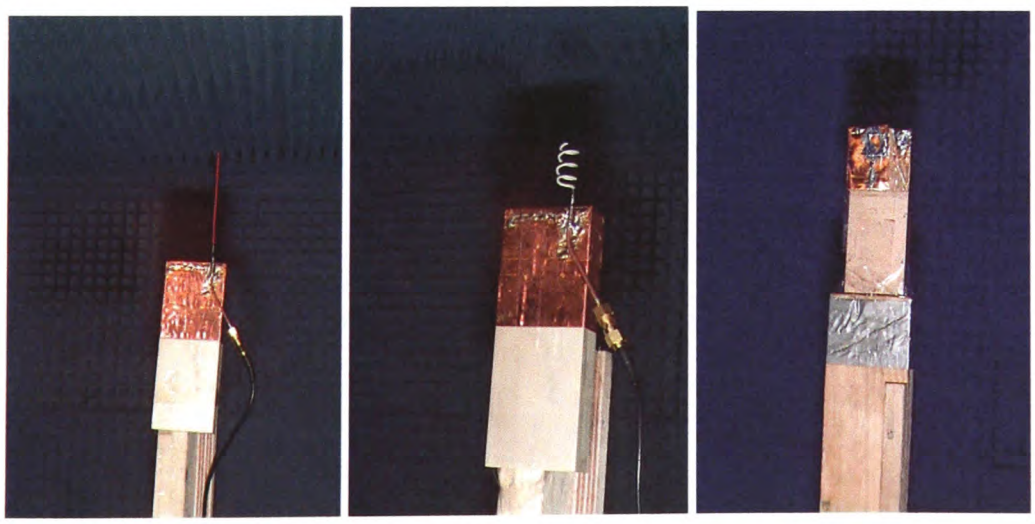

Fig. 4.3 *The three handheld portable phone antennas.*

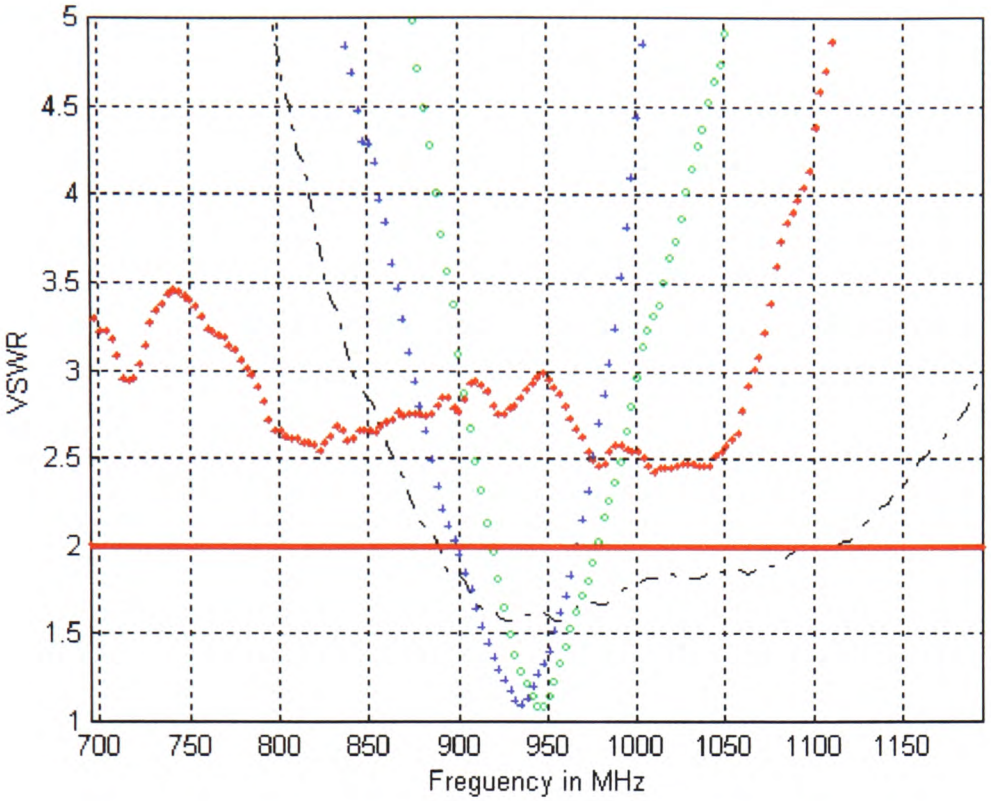

Fig. 4.4 *The VSWR of the four antennas. -- Dipole, ** Monopole, ++ Helix, and oo PIFA*

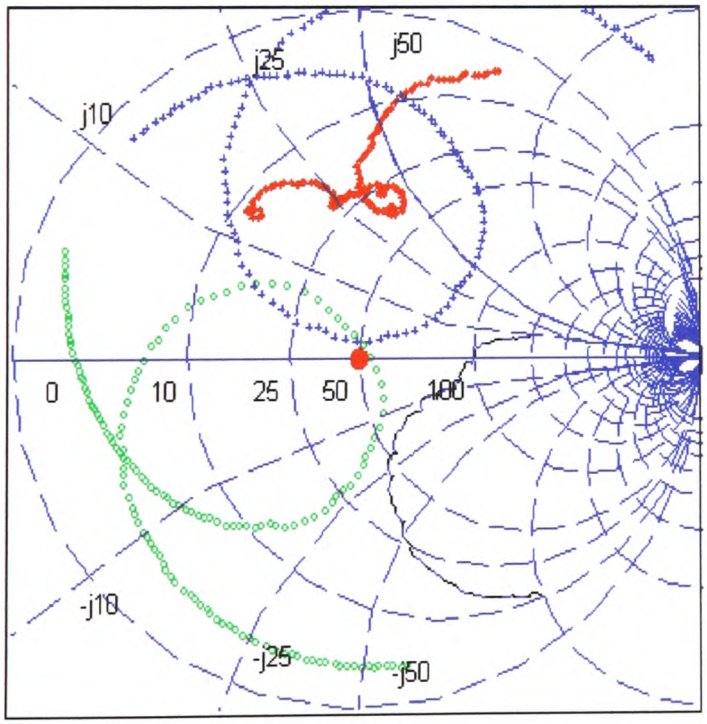

Fig. 4.5 *The Smith chart of the four antennas under test. -- Dipole, ** Monopole, ++ Helix, and oo PIFA*

4.4 Antenna absolute gain measurements using the 3-antenna method.

A convenient method to measure the absolute gain of the four antennas investigated is due to the U.S. National Bureau of Standards, which utilises a 3-antenna measurement method. An alternative method, with two instead of three antennas, is described in [2.7].

In the three-method model the free space propagation equations can be written as

$$\frac{P_1}{P_2} = G_1 G_2 \left(\frac{\lambda}{4\pi R}\right) \tag{4.23}$$

$$\frac{P_1}{P_3} = G_1 G_3 \left(\frac{\lambda}{4\pi R}\right) \tag{4.24}$$

$$\frac{P_2}{P_3} = G_2 G_3 \left(\frac{\lambda}{4\pi R}\right) \tag{4.25}$$

After measuring the ratio between the transmitted and received signal $\left(\frac{P_a}{P_b}\right)$ using the VNA and keeping R constant, the antennas gain can be found by solving the set of equations 4.23-4.25.

In Fig. 4.6, the wide-band boresight antenna gain measured for the dipole, helix and PIFA antennas, using the three-antenna method is plotted. The PIFA performance is superior to that of the other three antennas. This is due to the small directivity of the PIFA towards the boresight and its good efficiency. Relatively low gain has been measured for the dipole and helix antennas. The low gain of the dipole, compared to its theoretical value, as well as the ripple on the wide-band boresight gain plots is due to reflections from the walls and the ground of the anechoic chamber which have been reduced but not sufficiently eliminated by the absorbers.

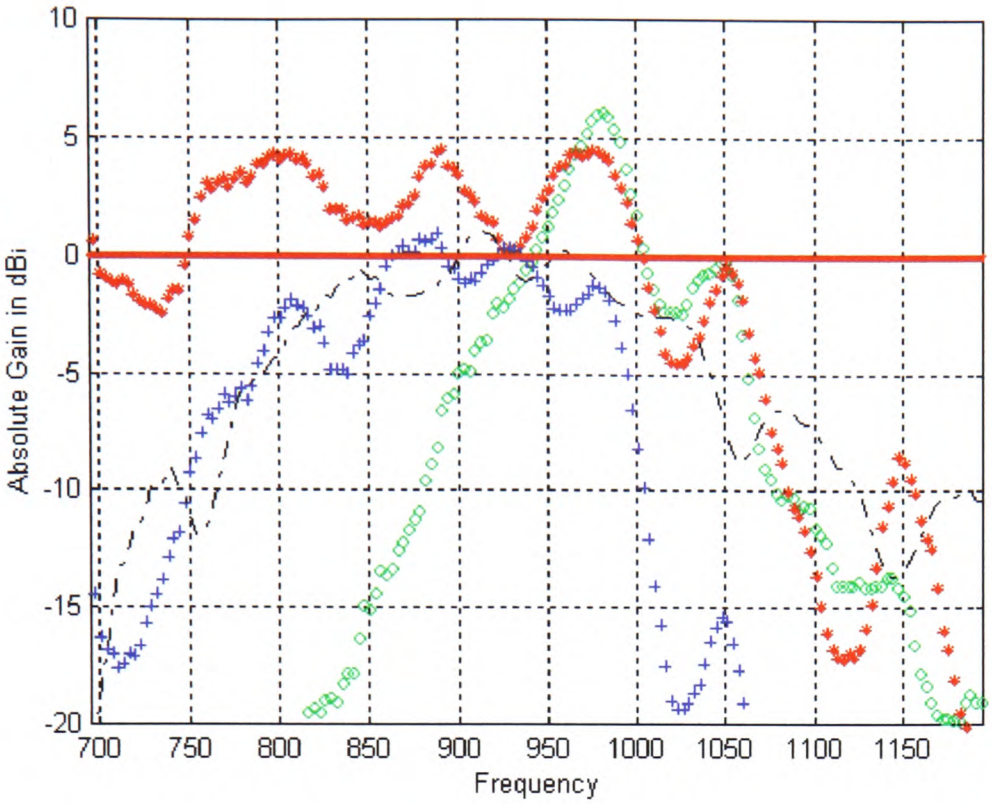

Fig. 4.6 *Absolute gain of the four antennas. -- Dipole, ** Monopole, ++ Helix, and oo PIFA*

4.5 Far-field radiation pattern simulations and measurements.

In the present and following sections far-field radiation pattern data from simulations and measurements are presented and discussed for mobile phone antennas operating in free space. The need for studying the far-field characteristics of an antenna lies in the importance of understanding its radiation characteristics. The far-field gain pattern is one of the most important characteristics in assessing the performance of a radiating device and has significant implications in designing the wireless link. It is also essential to verify the reliability and accuracy of numerical methods against measurements. For antennas used in cellular communications, it is desirable to present omnidirectional radiation characteristics in the horizontal plane and, in particular, for the vertical (E_Θ) electric field component, since commercially used base station antennas are normally vertically polarised. Omnidirectional far-field gain patterns for the antenna allow the mobile phone to exhibit similar performance in all directions. This is because the orientation of the mobile station with respect to the base station antenna is random.

Two numerical methods have been used for far-field predictions. These are the MoM and the FDTD method. Each method uses a different computational approach to the problem as described in Chapter 2. Therefore, the processing time differs for each method. For far-field calculations the available MoM code gives results at a fraction of the time required by the FDTD but only for a single frequency at a time and for antennas made only from conductive materials. On the other hand, FDTD can excite the antenna with a Guassian waveform source, which result in far-field patterns over a wide bandwidth. Due to that, a post-processing of the data is needed and an FFT filtering method is used to produce the far-field radiation patterns. In addition, the FDTD can easily accommodate dielectric materials in the model. This is useful if the plastic cover of the handset or any other dielectric material in the proximity of the antenna is required in the numerical model like the inclusion of the user's head.

4.5.1 The monopole (whip) antenna.

The first antenna tested is the quarter wavelength monopole antenna (Fig. 4.3). The geometrical numerical models used in both methods are shown in Fig. 4.7. The 3D radiation patterns (E_Θ) at 945 MHz, as computed by the MoM and the FDTD, are presented and compared in Fig. 4.8 where good agreement can be observed. The patterns are omnidirectional in the horizontal plane and it can be said that they are similar to the $\lambda/2$ dipole radiation pattern given in [2.4]. The 3D radiation patterns, however, cannot be used for a detailed quantitative study of the far field since 3D far-field measurements can not be performed with the equipment available in the lab. For these reasons, selected 2D radiation patterns are presented in the remainder of this section obtained by the MoM and measurements.

The radiation patterns for the monopole antenna have been measured for three different orientations (Fig. 4.9) for measurements in the xy-, yz-, and xz-planes. For each orientation the E_Θ and E_Φ are measured using the VNA and the 3-antenna method described above. The E_Θ can be referred to as co-polar and E_Φ as cross-polar radiation pattern. According to Kraus [2.1] "even if the antenna is believed to be

linearly polarised, measurements of the 4 patterns plus axial ratio must be desirable to establish polarisation purity."

In Fig. 4.10 the normalised measured xy (E_Θ) radiation pattern shows good agreement with the radiation pattern obtained from the numerical simulations but this is not true for the E_Φ radiation pattern (Fig.4.11). This is a limitation associated with the MoM in general, and has been reported previously in the literature [3.1]. The accuracy of the measurements of the cross-polarised fields are also affected by the linearity of the reference antenna, which although in the simulations was assumed perfectly linearly polarised, this was not the case in the measurements. The reference antenna for the measurements (dipole) was elliptically polarised with a small electric field component in the horizontal direction. The effect of the wooden stand on the reference antenna, the antenna under test, as well as reflections from the floor and the walls added to the errors in the measured radiation pattern. Antennas and, as a consequence, electromagnetic waves used in mobile communications base stations are designed to be vertically polarised. Vertical polarisation of antenna gives better system efficiency with fewer ground losses and reflections and it has been argued that it is also more suitable for handset antennas.

Simulation and measurement graphs of the far-field radiation patterns in the yz-plane are shown in Figs. 4.12 and 4.13. Good agreement between experimental and numerical results can be seen again for the E_Θ component. On the other hand, there are significant discrepancies between the results for the horizontal plane (E_Φ) from 150° to 300°. This corresponds to the bottom side of the mobile phone. The same error has been observed in the last case, where xz-plane radiation patterns are obtained. In should be noted that for the yz- and xz-planes, E_Θ radiation pattern measurements, the reference antenna was horizontally placed relative to the ground in contrast to its vertical orientation when the xz-plane radiation patterns were measured (Fig. 4.9). This orientation change results in additional measurement error due to relatively higher reflections from the chamber ground, ceiling walls and stand, which are in the direction of the high field (see 3D radiation patterns).

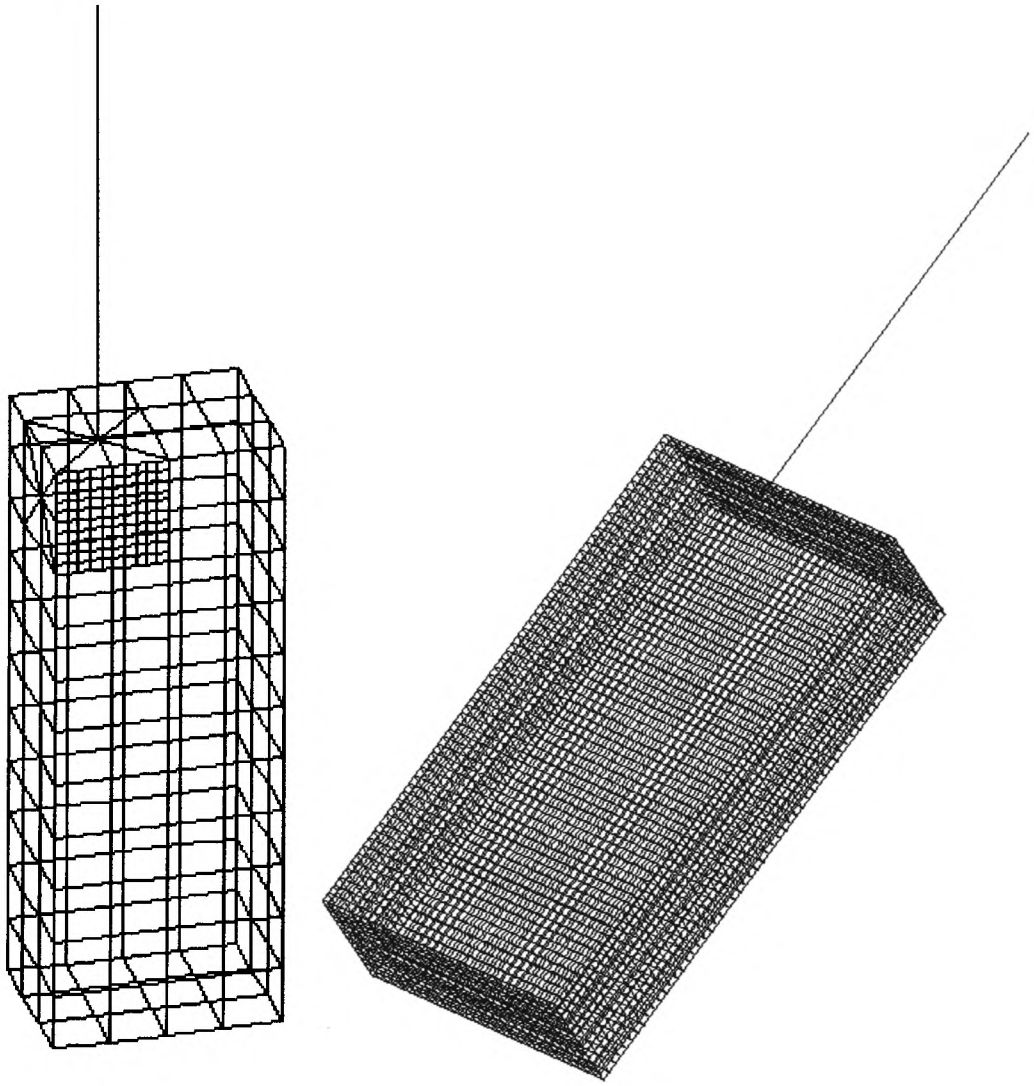

a) b)

Fig. 4.7 *Geometrically models of the whip antenna. a) MoM with wire grid segmentation, b) FDTD.*

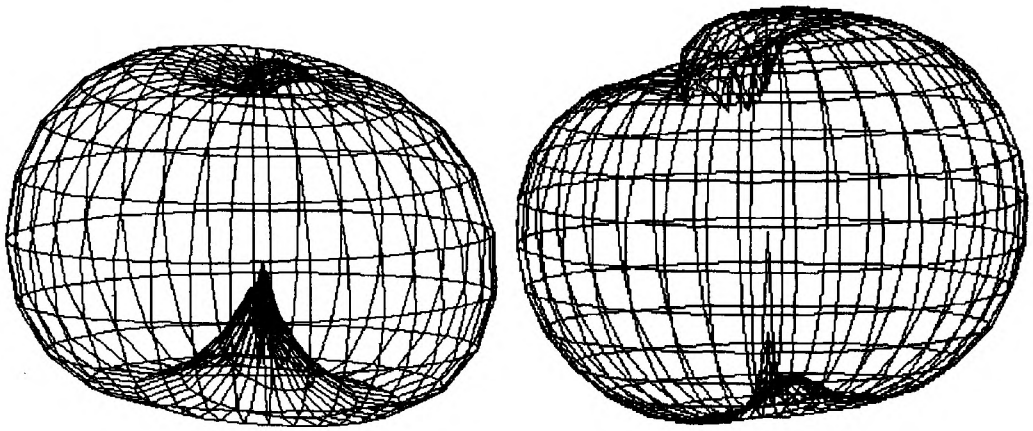

a) b)

Fig. 4.8 *3D far-field (E_Θ) radiation patterns of the whip antenna computed by: a) the MoM and b) the FDTD.*

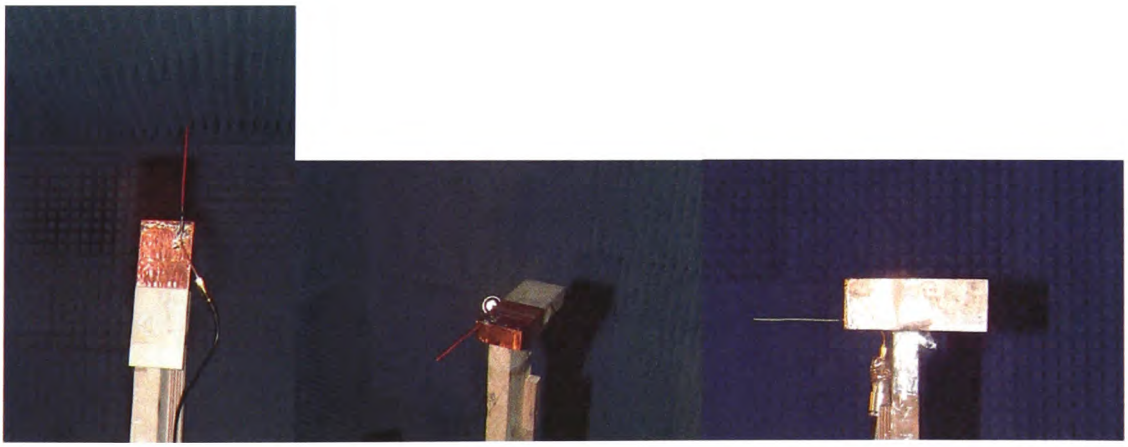

a) b) c)

Fig. 4.9 *The actual orientation of the whip antenna in the anechoic chamber: a) xy-plane, b) yz-plane, and c) xz-plane measurements.*

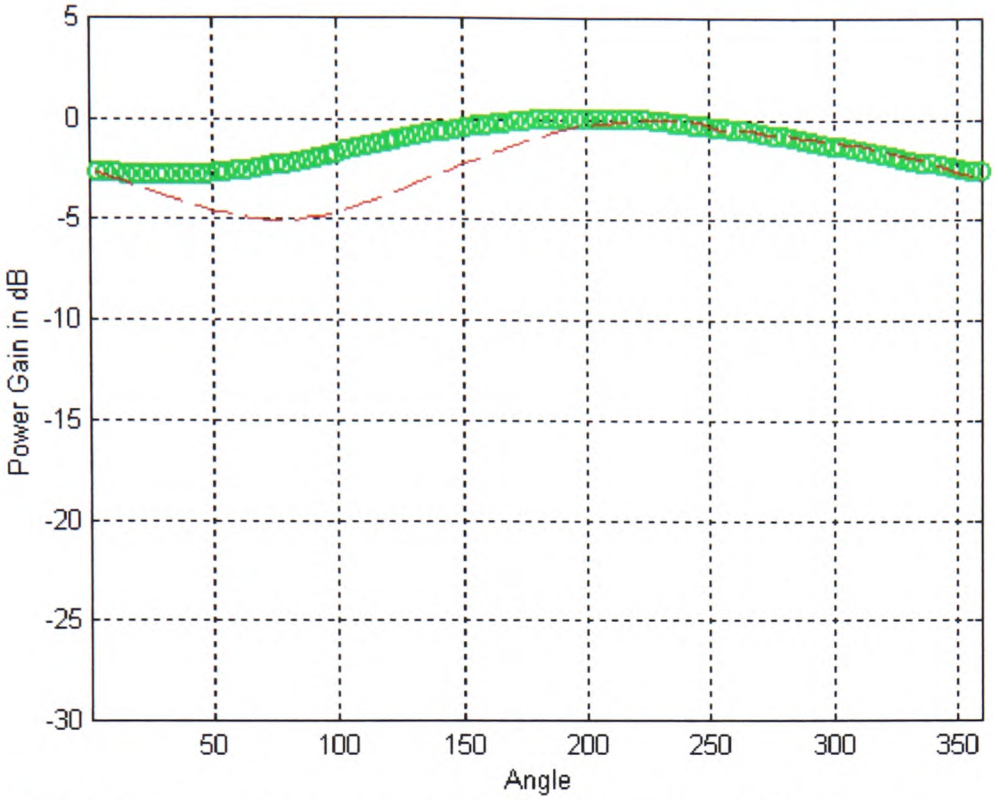

Fig. 4.10 *The normalised xy vertical (E_Θ) far-field radiation patterns of the monopole antenna: oo MoM simulation --- measurements.*

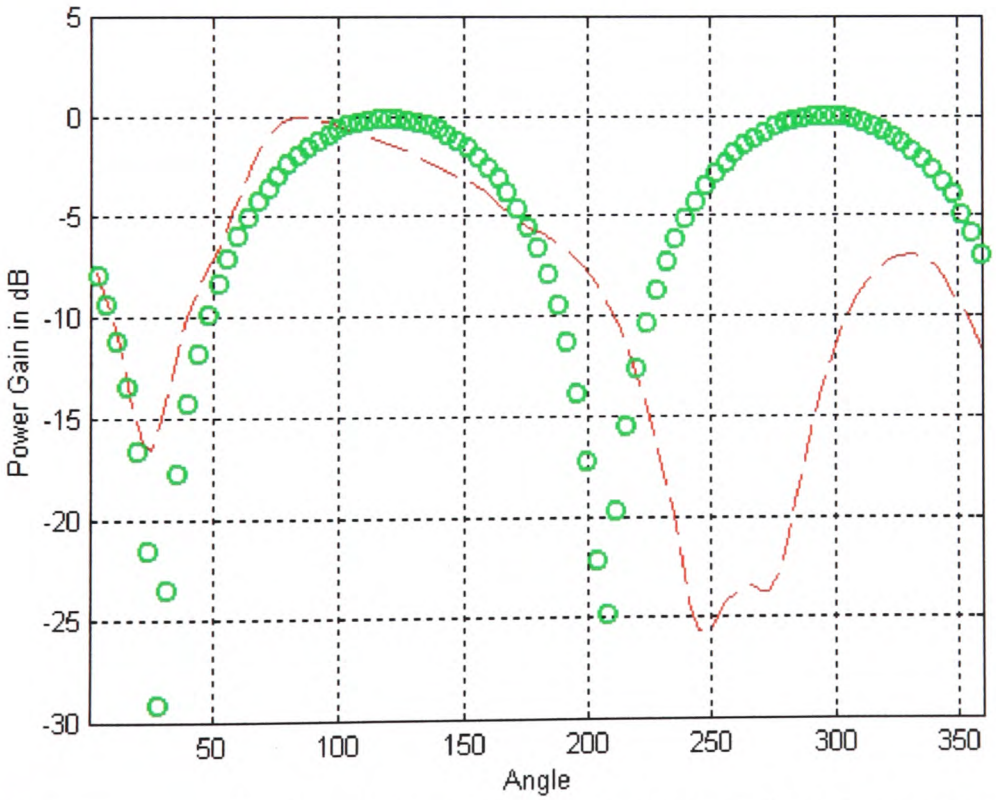

Fig. 4.11 *The normalised xy horizontal (E_Φ) far-field radiation patterns of the monopole antenna: oo MoM simulation --- measurements.*

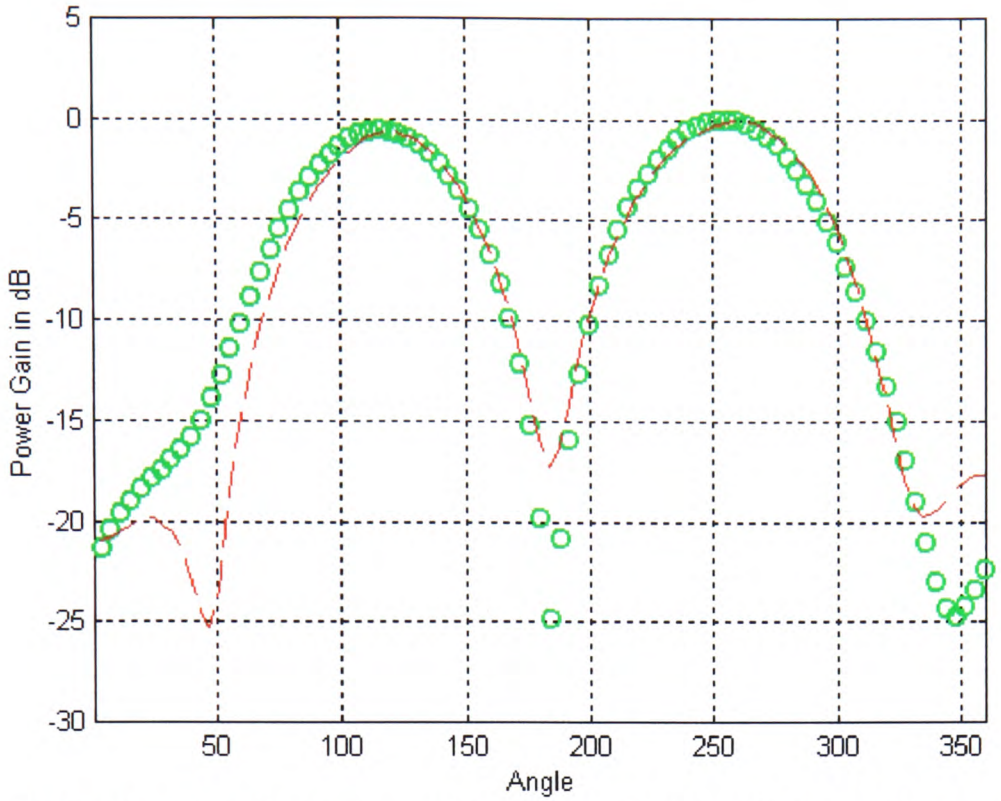

Fig. 4.12 *The normalised yz vertical (E_Θ) far-field radiation patterns of the monopole antenna: oo MoM simulation --- measurements.*

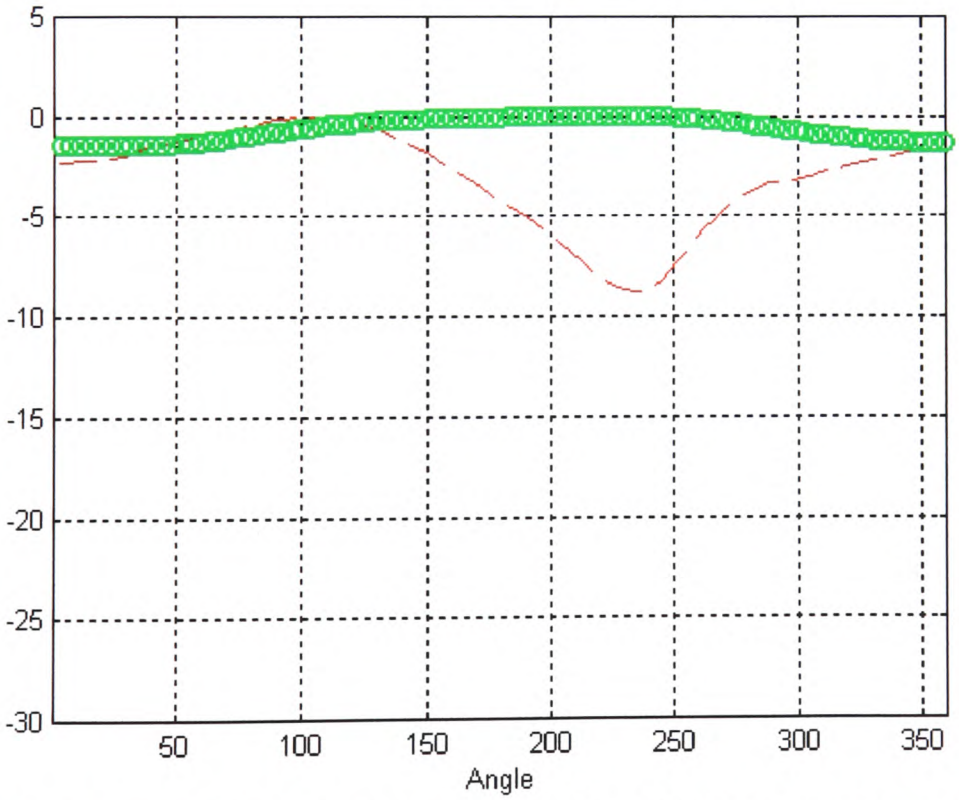

Fig. 4.13 *The normalised yz horizontal (E_Φ) far-field radiation patterns of the monopole antenna: oo MoM simulation --- measurements.*

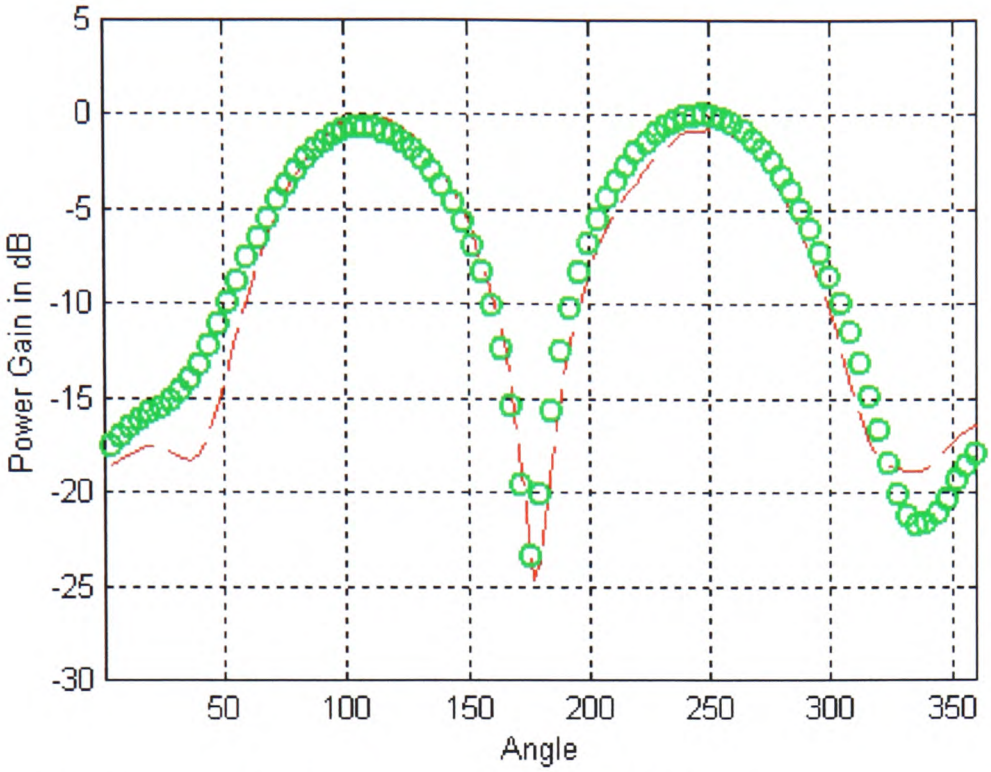

Fig. 4.14 *The normalised xz vertical (E_Θ) far-field radiation patterns of the monopole antenna: oo MoM simulation --- measurements.*

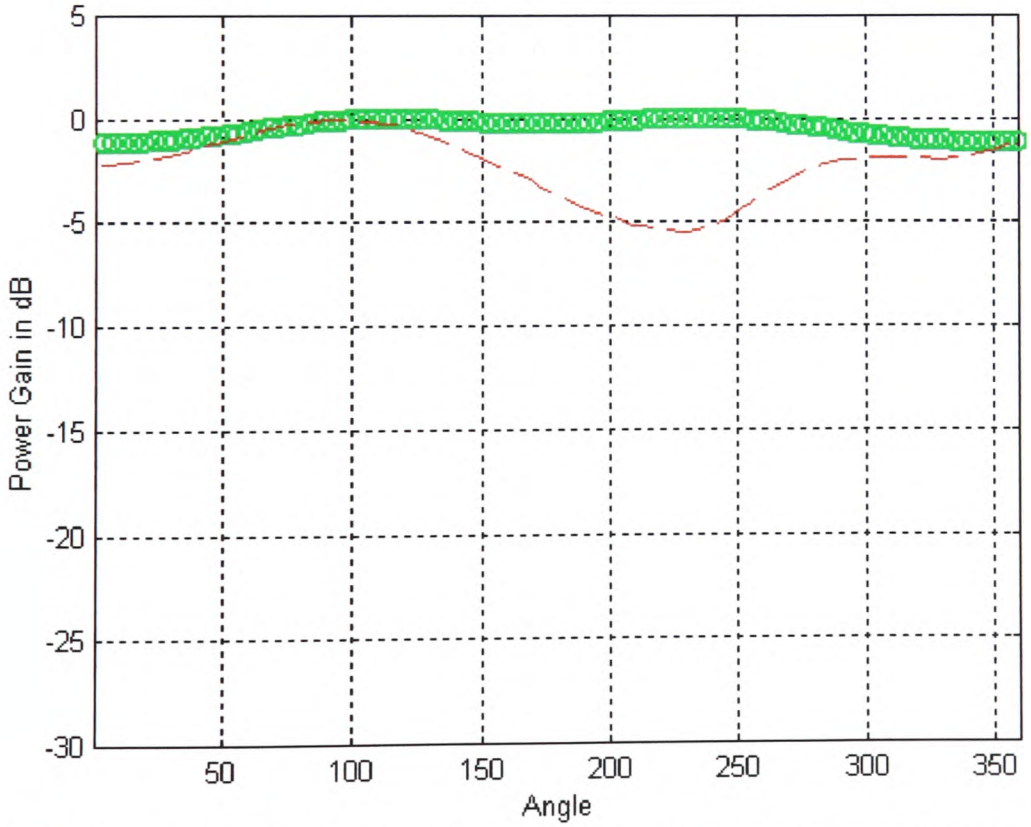

Fig.4.15 *The normalised xz horizon (E_Φ) far-field radiation patterns of the monopole antenna: oo MoM simulation --- measurements.*

4.5.2 The helix antenna.

The small helix tuned at 945MHz is the next antenna simulated and measured in anechoic conditions. The same orientations, as described before for the monopole antenna, were used for the helix antenna measurements and simulations. The antenna and its orientations in the anechoic chamber are shown in Fig. 4.16 while Fig. 4.17 displays the antenna models used in the two numerical methods. The results from the MoM and the FDTD in the 3D far-field radiation patterns are presented in Fig. 4.18 where good agreement can be seen. From the comparison of the 2D patterns obtained by simulations and measured similar conclusions can be outlined as those in section 4.5.1. All the measured E_Θ patterns have very good agreement with the predicted patterns. This is not, however, true for the E_Φ patterns, especially for the yz- and xz-planes, where significant discrepancies can be observed.

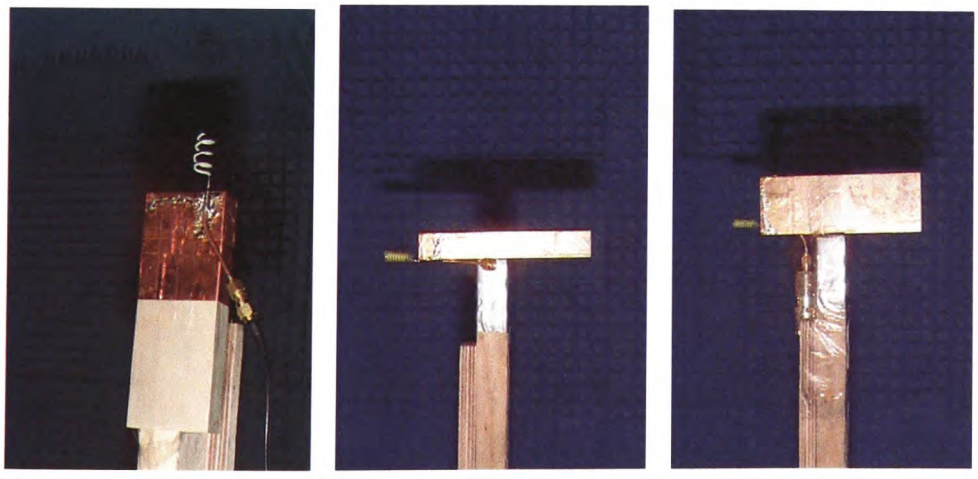

a) b) c)

Fig. 4.16 *The orientation of the helix antenna in the anechoic chamber: a) xy-plane, b) yz-plane, and c) xz-plane measurements.*

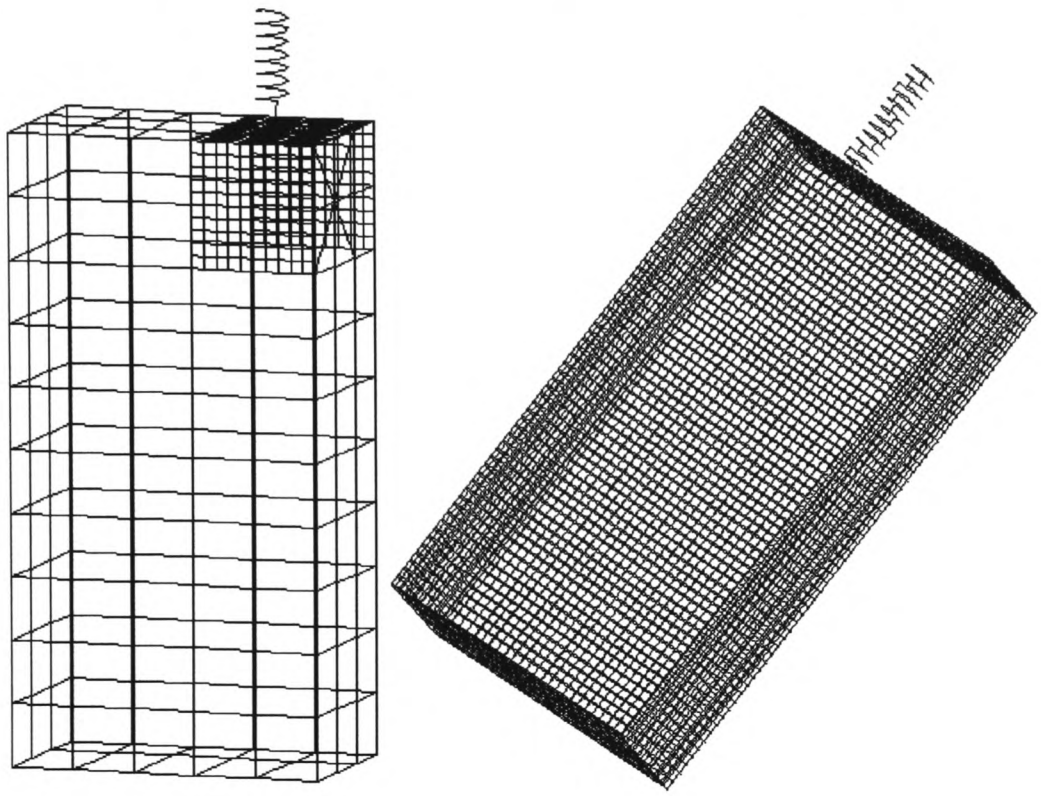

a) b)

Fig. 4.17 *Geometrically models of the helix antenna. a) MoM with wire grid segmentation, b) FDTD.*

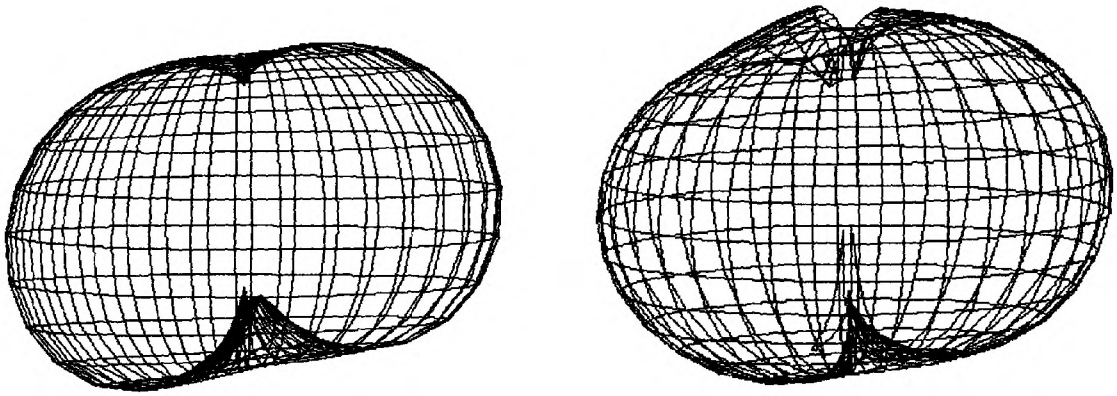

a) b)

Fig. 4.18 *3D far-field (E_Θ) radiation patterns of the helix antenna computed by: a) the MoM and b) the FDTD.*

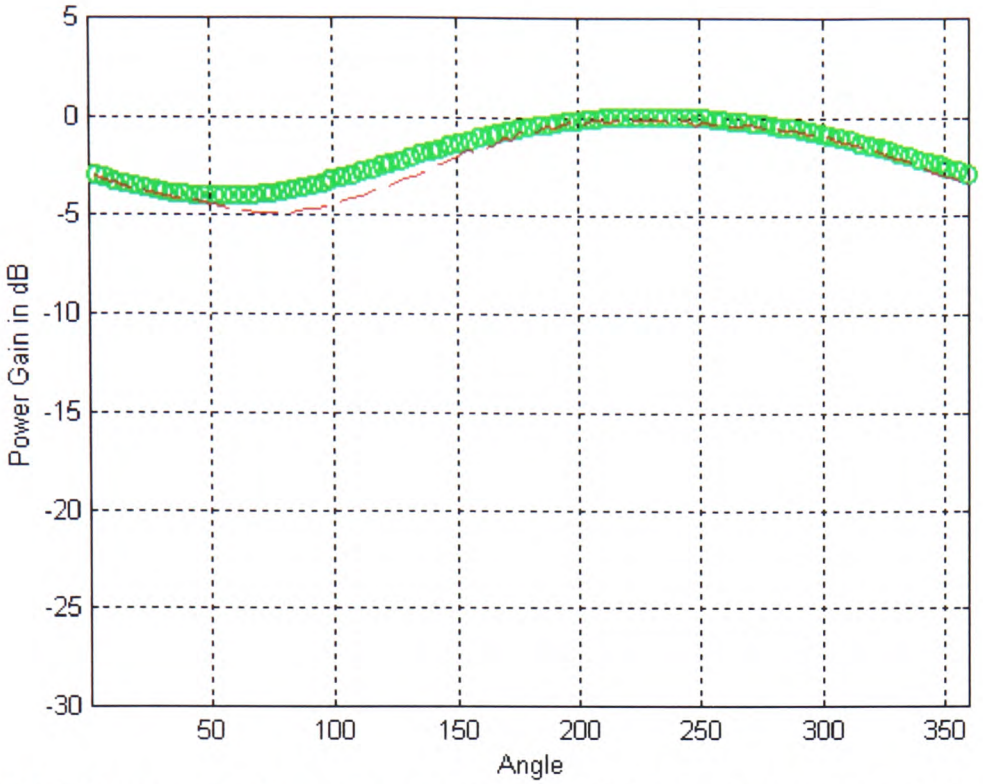

Fig.4.19 *The normalised xy vertical (E_Θ) far-field radiation patterns of the helix antenna: oo MoM simulation, --- measurements.*

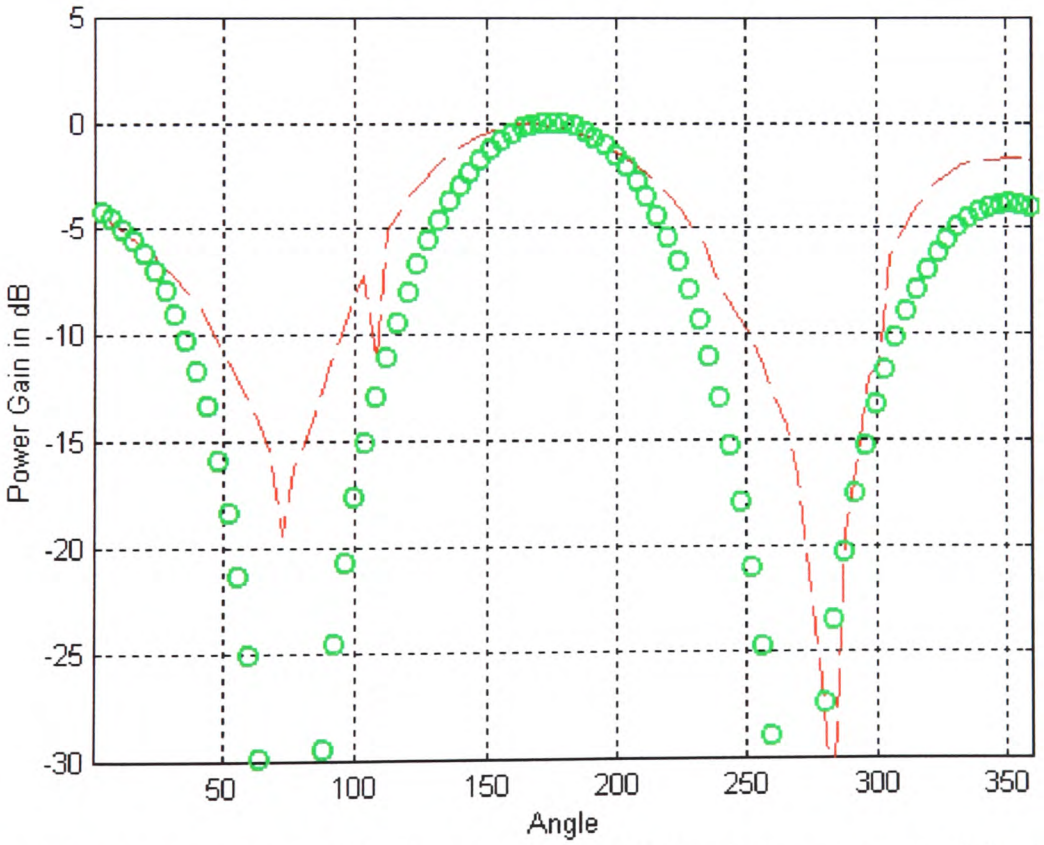

Fig. 4.20 *The normalised xy horizontal (E_Φ) far-field radiation patterns of the helix antenna: oo MoM simulation, --- measurements.*

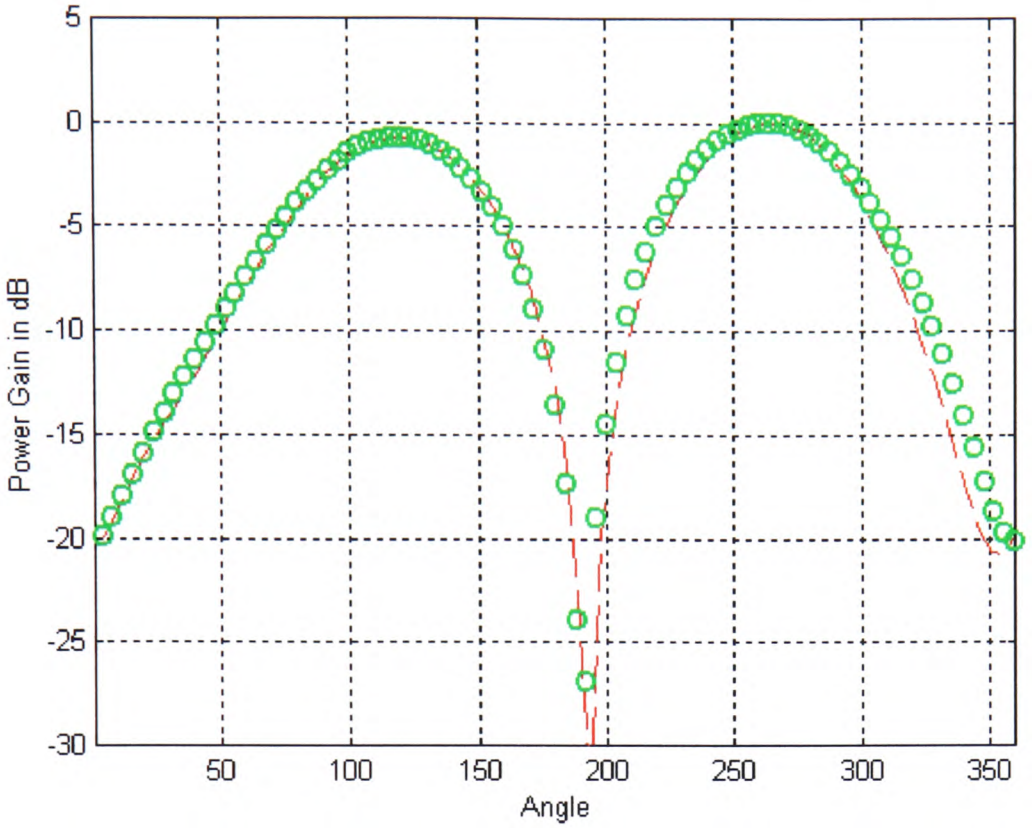

Fig. 4.21 *The normalised yz vertical (E_Θ) far-field radiation patterns of the helix antenna: oo MoM simulation, --- measurements.*

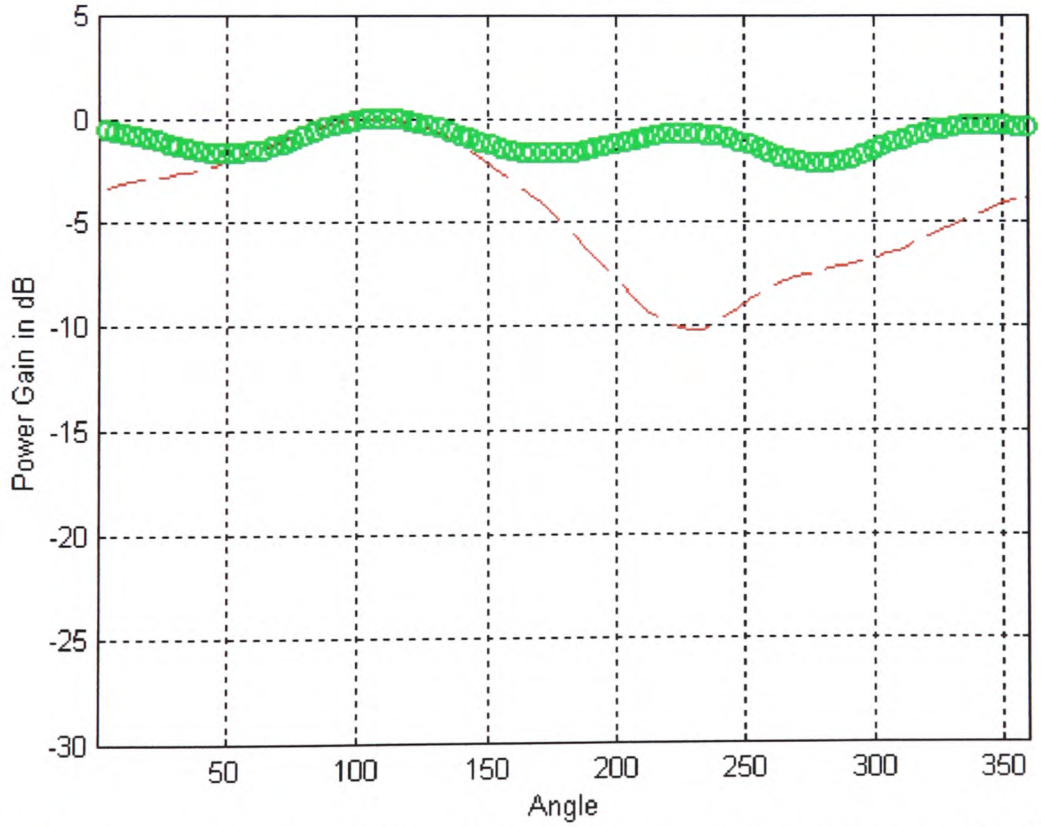

Fig.4.22 *The normalised yz horizontal (E_Θ) far-field radiation patterns of the helix antenna: oo MoM simulation, --- measurements.*

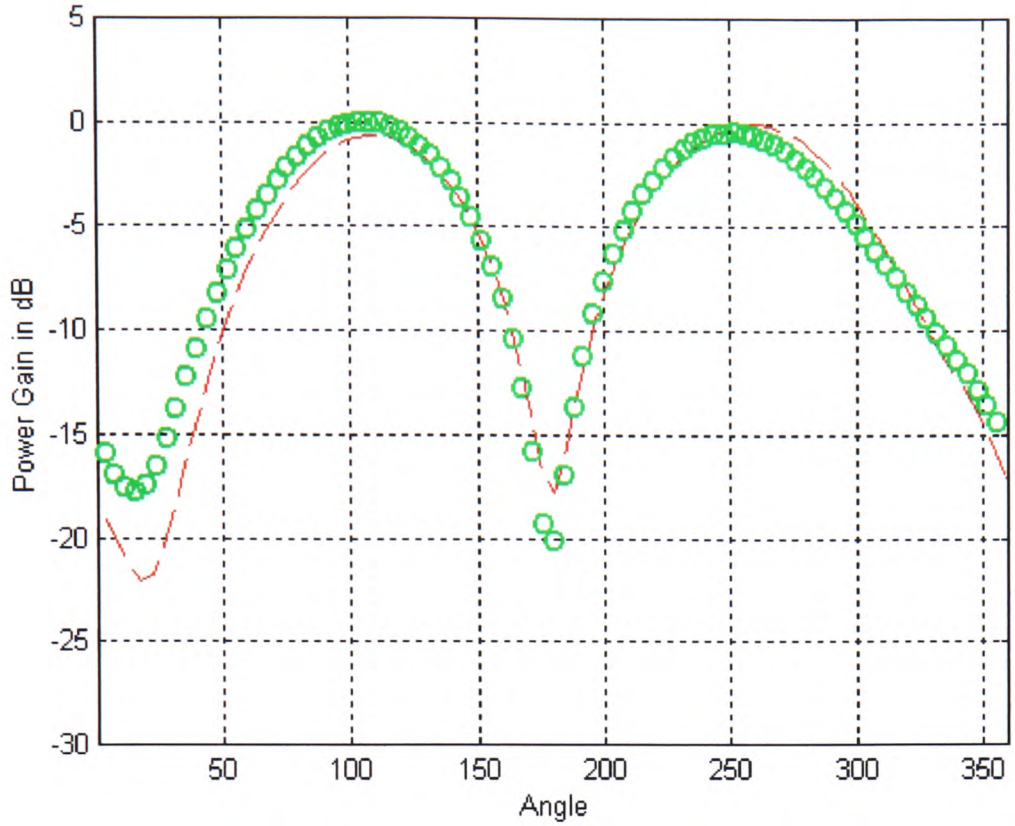

Fig. 4.23 *The normalised xz vertical (E_Θ) far-field radiation patterns of the helix antenna: oo MoM simulation, --- measurements.*

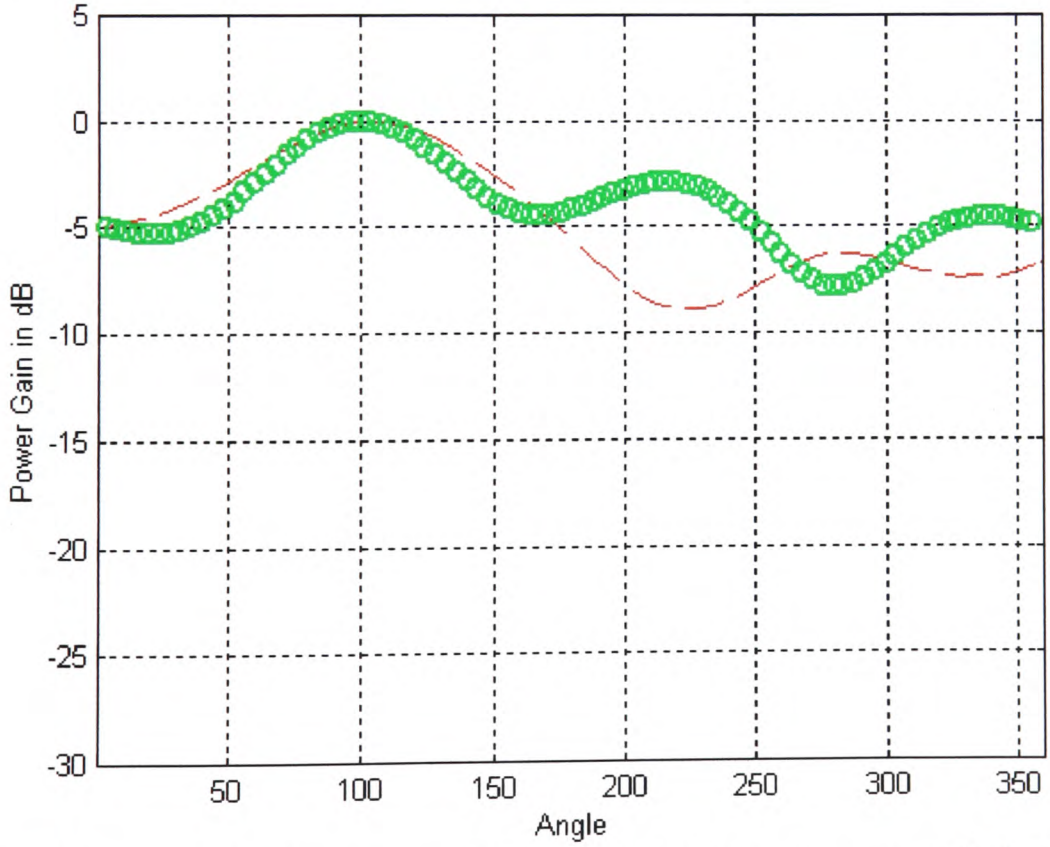

Fig. 4.24 *The normalised xz horizontal (E_Φ) far-field radiation patterns of the helix antenna: oo MoM simulation, --- measurements.*

4.5.3 The PIFA antenna.

The third antenna simulated and measured in the anechoic chamber is the PIFA (Figs. 2.25 and 2.26). In the previous sections it was shown that this antenna has a higher gain compared to the monopole, the helix and the dipole antennas. It will be shown later in this report that the efficiency of PIFA is also higher under coupling conditions and that the energy delivered to the operator is low. Three dimensional far-field radiation patterns are illustrated in Fig. 4.27. Both methods predict omnididirectional patterns in the horizontal plane similar to the monopole and helix antennas. The radiation power is degraded at the poles (where $\Theta = 0$ or $\Theta = 180$). This is more obvious in the yz-plane, and xz-plane patterns presented in Fig 4.30 and 4.32 respectively. The results from the radiation pattern measurements show good agreement with simulations. Even though the E_Θ patterns do not compare as well as in the helix case, the E_Φ patterns show better agreement compared to the previous two antennas cases reported.

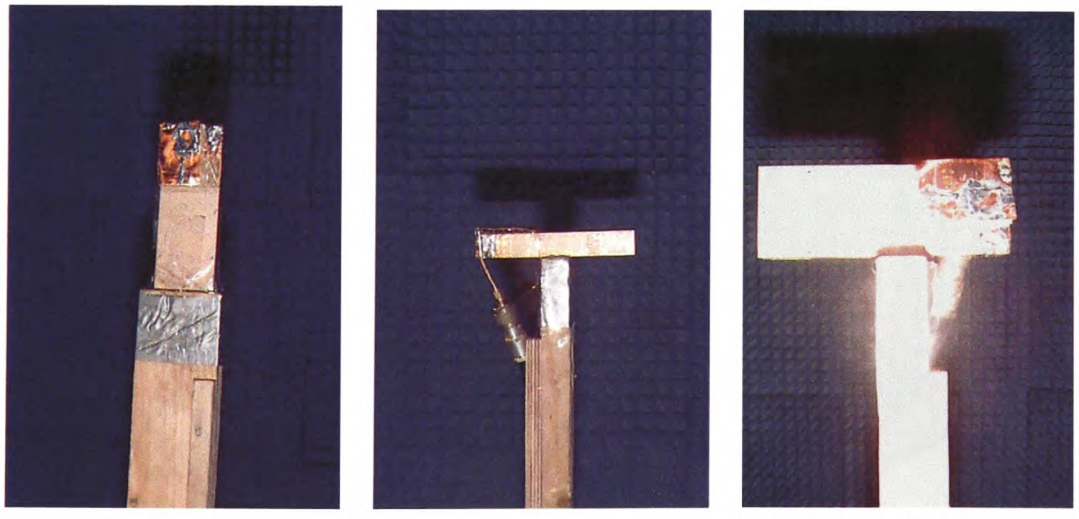

Fig. 4.25 *The measurement orientation of the PIFA in the anechoic chanber: a) xy-plane, b) yz-plane, and c) xz-plane measurements.*

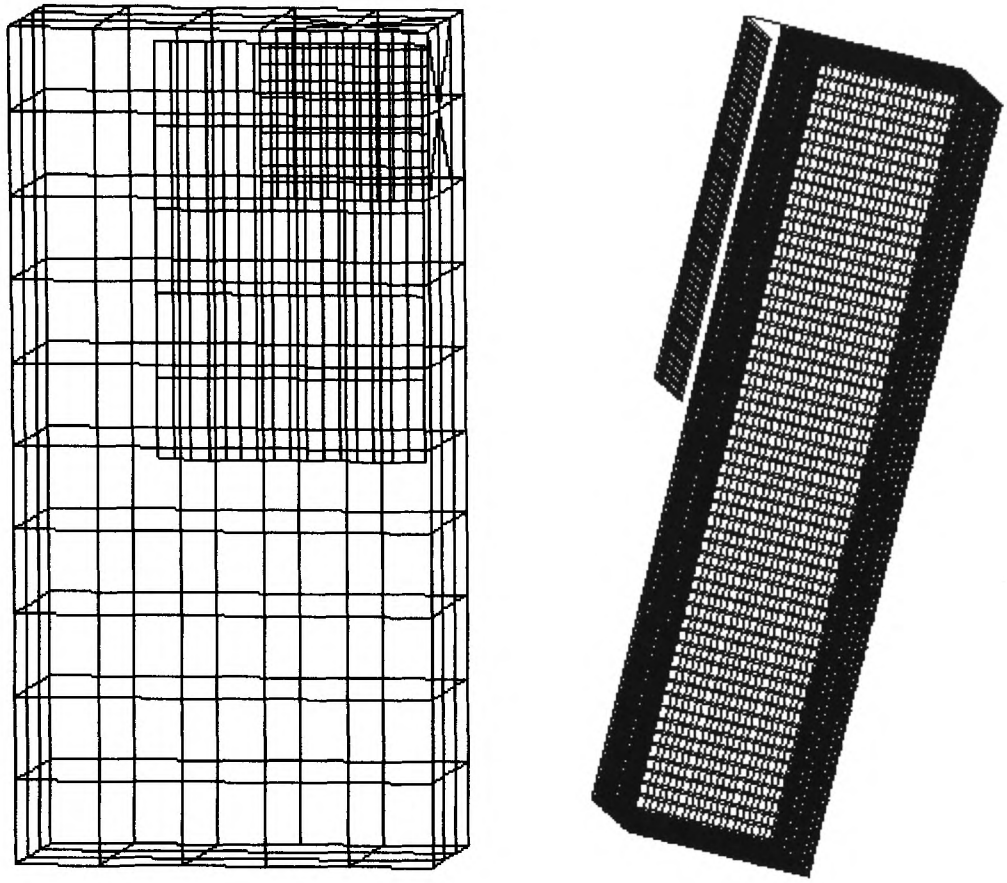

a) b)

Fig. 4.26 *Geometrically models of the PIFA antenna. a) MoM with wire grid segmentation, b) FDTD.*

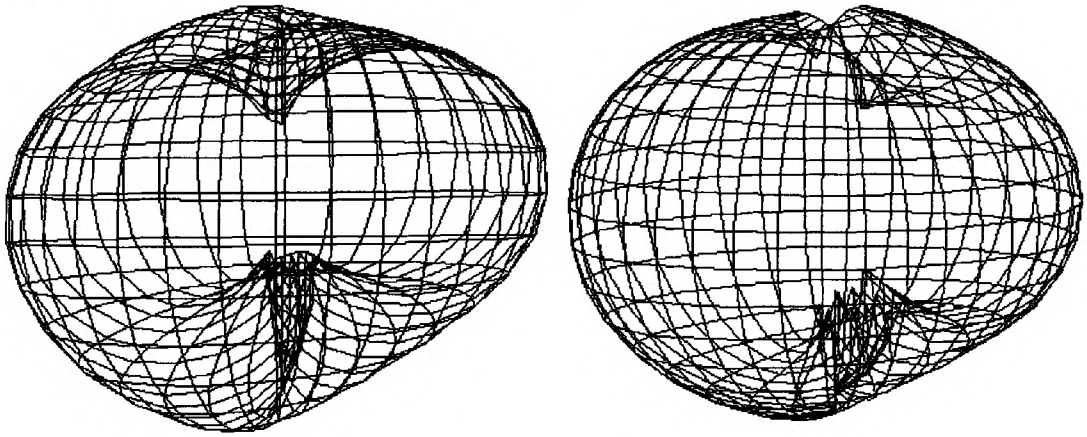

a) b)

Fig. 4.27 *3D far-field (E_Θ) radiation patterns of the PIFA antenna computed by: a) the MoM and b) the FDTD.*

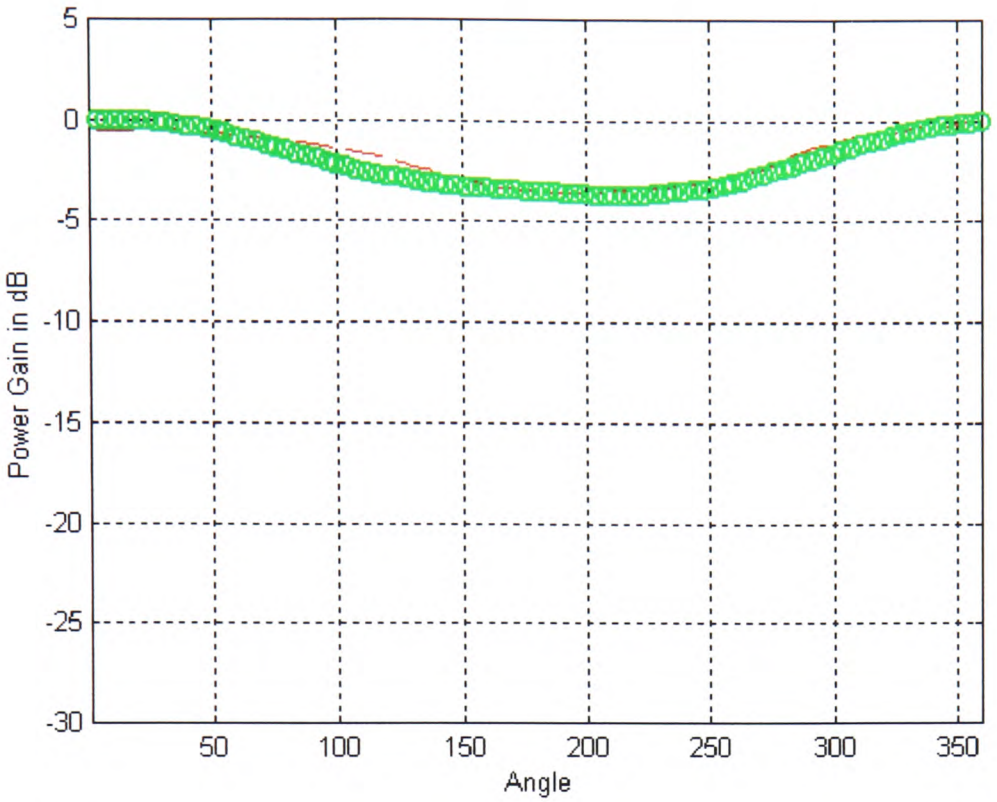

Fig. 4.28 *The normalised xy vertical (E_Θ) far-field radiation patterns of the PIFA antenna: oo MoM simulation, --- measurement.*

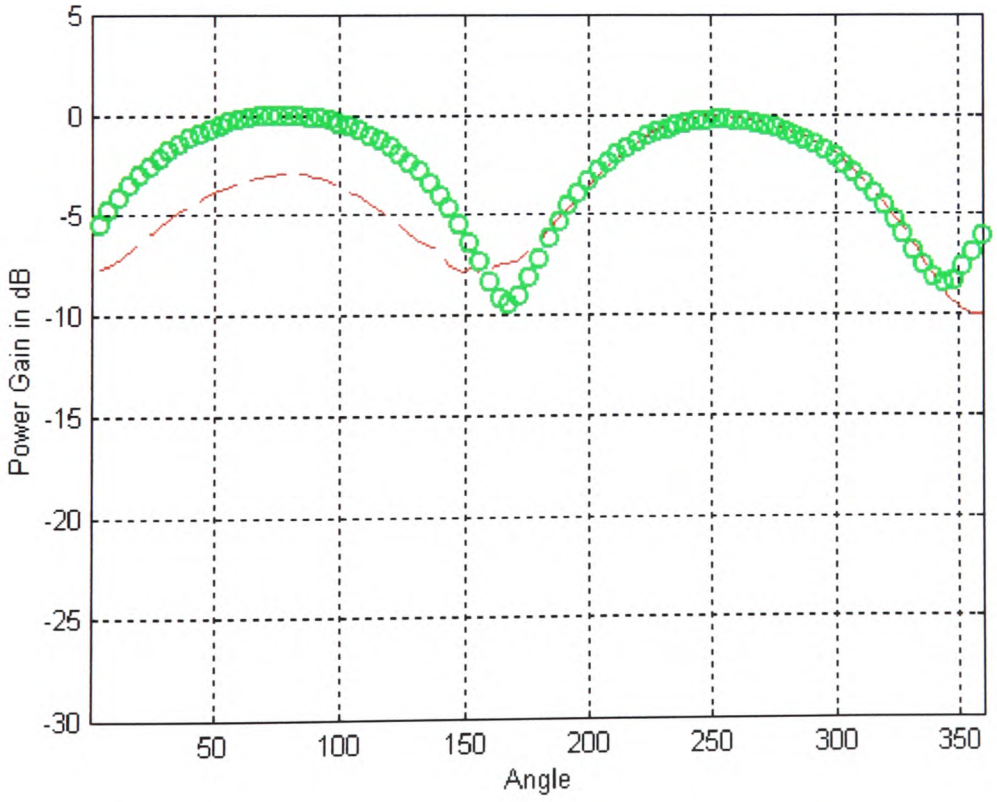

Fig. 4.29 *The normalised xy horizontal (E_Φ) far-field radiation patterns of the PIFA antenna: oo MoM simulation, --- measurement.*

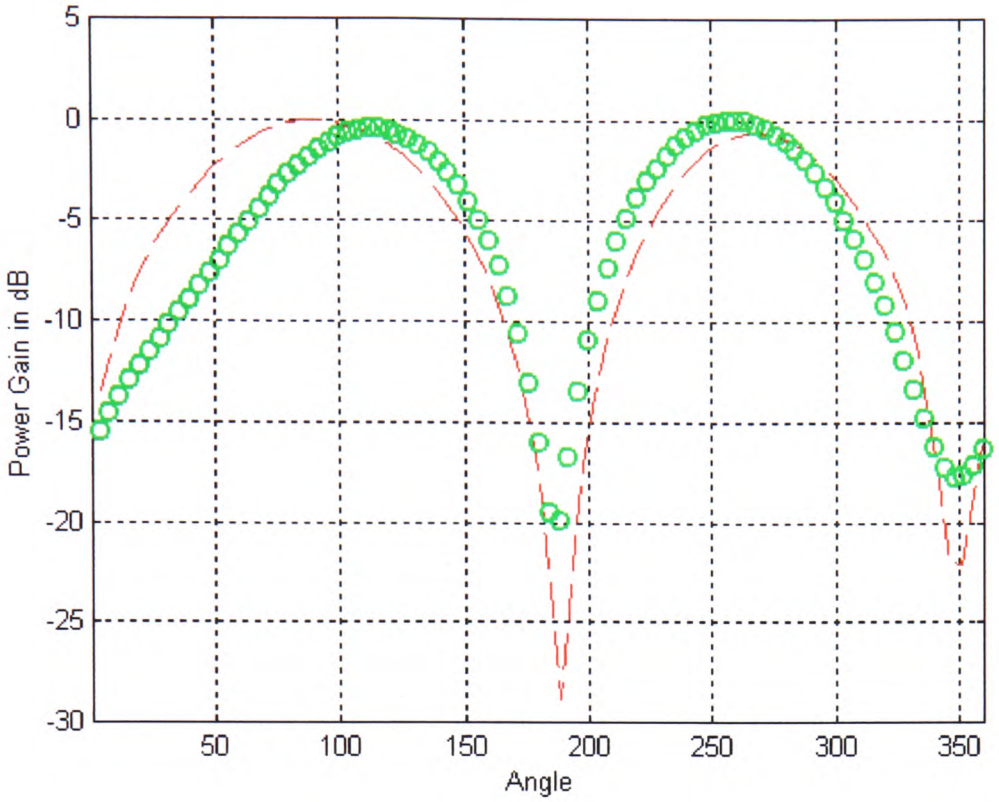

Fig.4.30 *The normalised yz vertical (E_Θ) far-field radiation patterns of the PIFA antenna: oo MoM simulation, --- measurement.*

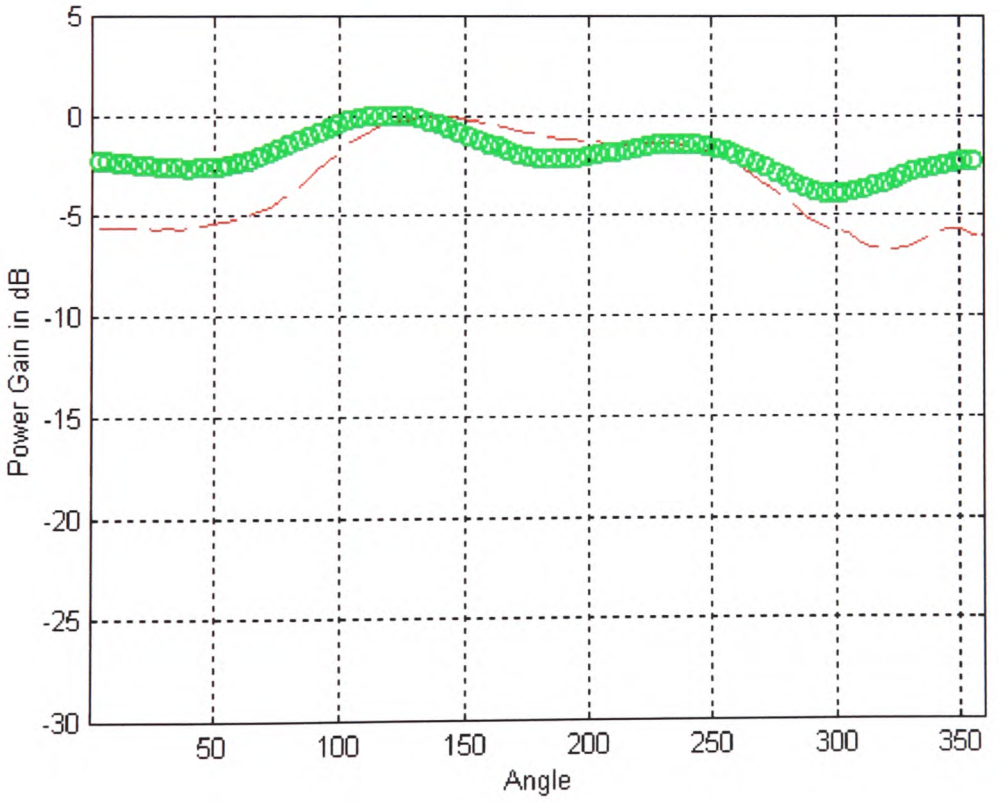

Fig. 4.31 *The normalised yz horizontal (E_Φ) far-field radiation patterns of the PIFA antenna: oo MoM simulation, --- measurement.*

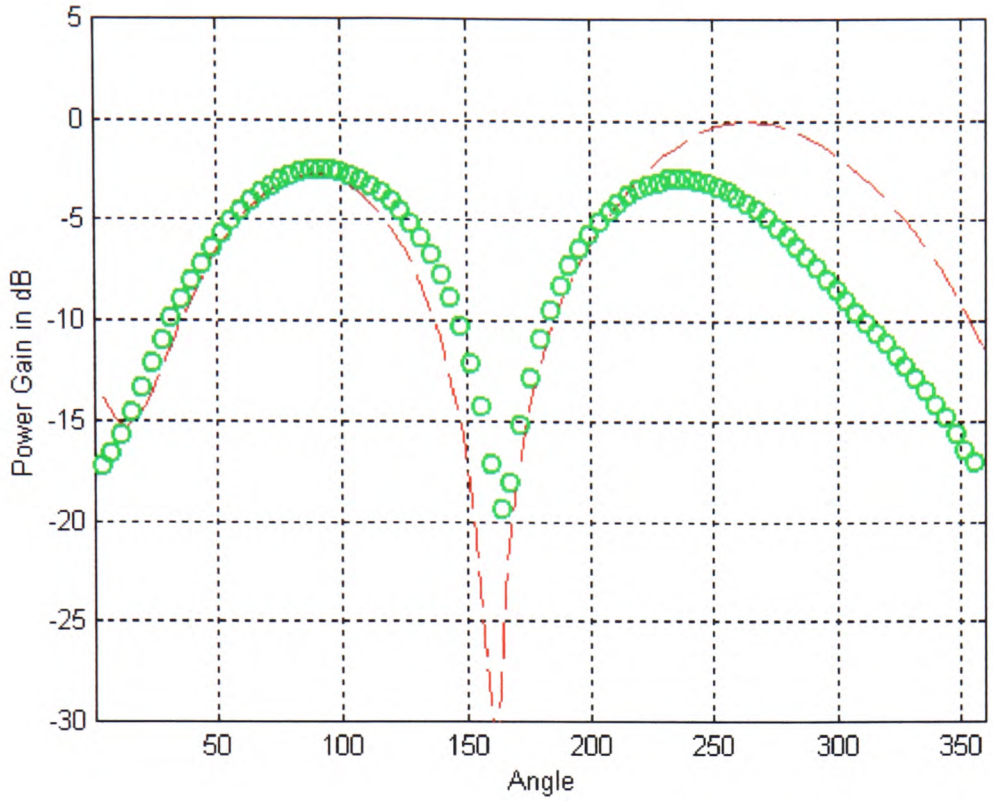

Fig. 4.32 *The normalised xz vertical (E_Θ) far-field radiation patterns of the PIFA antenna: oo MoM simulation, --- measurement.*

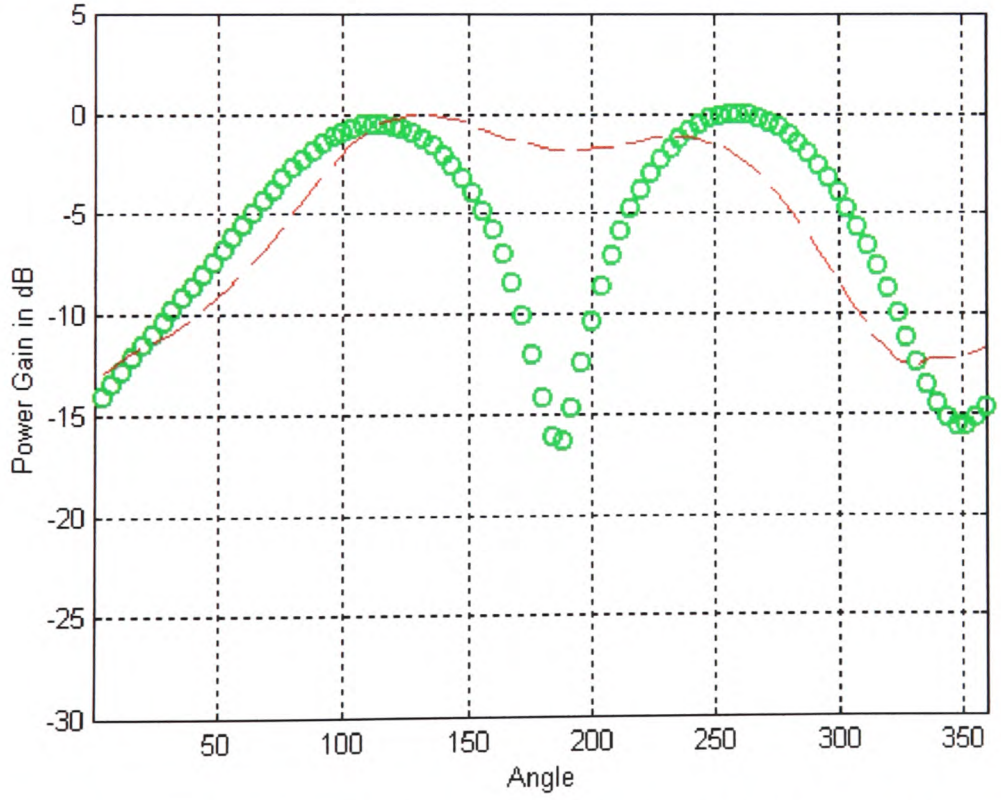

Fig. 4.33 *The normalised xz horizontal (E_Φ) far-field radiation patterns of the PIFA antenna: oo MoM simulation, --- measurement.*

4.6 Far field measurements and simulations in the presence of operator.

In Sec. 4.5 measured and predicted far-field radiation patterns of antennas operating in free space have been presented. In this section, far-field radiation patterns of antennas operating in the presence of the operator are reported. Measurements were done under anechoic conditions using volunteers. The transmitted power was set to a maximum of 10 dBm, which, however, is well below the 33 dBm maximum power radiated by a Class-4 GSM900 handset. Measurement time did not exceed 3 min with a 5 min break between measurements. This was chosen in order to keep radiation exposure by volunteers at low levels. The measurement set-up used in the anechoic chamber is shown in Fig. 4.34. The operator stood on a turntable rotating round the vertical axis. On the opposite side and at a distance of 1-m the signal was received by a half-wave dipole. Due to practical limitations, only horizontal (xy-) plane measurements could be performed. The FDTD method was used for evaluating the 3D far-field patterns and the numerical model used is shown in Fig. 4.35. The operator's hand was not been simulated. In the measurements, care was taken to position the hand at the lower end of the handset in order to eliminate its effect on the radiation patterns. More information on the hand effect is given in Chapter 7, where SAR predictions are discussed in detail.

Fig. 4.34 *Settings for radiation patterns measurements in the presence of the operator.*

Fig. 4.35 *The FDTD numerical head/shoulders model and handset used for far-field radiation pattern evaluation.*

In Fig. 4.36, 3D radiation patters of the monopole with and without the operator in the proximity of the handset are plotted in the same graph. The solid pattern represents the far-field radiation pattern of the monopole antenna when it is operating next to the operator's head. The line-grid pattern, on the other hand, is the pattern of the same antenna operating in free space. In Fig. 4.37, predicted and measured far-field data of the monopole operating in free space and next to the operator's head in polar form are shown. The antenna radiation intensity is reduced both in the direction of the head and in the opposite direction. However, in the direction of the head the reduction is greater. The radiation intensity reduction is due to the energy absorption by the head of the operator and the reflection efficiency reduction caused by the coupling between the antenna and the operator. In Fig. 4.38 – 4.41, data for the helix and the PIFA are presented and good agreement between the predicted and measured results can be obscured.

In Figs. 4.42 – 4.44 both the E_Θ and E_Φ patterns of the horizontal xy-plane normalised to the E_Θ maximum value, are shown, where good agreement between the predicted and measured data can be seen for both electric field components. The measured radiation patterns of all three antennas, when operating near the operator's head, are shown in Fig. 4.45 for comparison. A signal reduction due to coupling with

the operator is observed in Fig. 4.46. Higher field values in this graph are exhibited in the direction of the head. The helix presents the highest values in the direction of the head, with the monopole coming second. As will be discussed further later, the poor performance of the helix is due to its short vertical length, which results in the antenna been closer to the head. Table 4.1 shows pattern averaged signal values degradation due to operator proximity. From this table, PIFA gives the lowest reduction to signal level under these conditions.

Antenna Type	**Averaged received power loss**
Monopole (whip)	15.4 dB
Helix	18.9 dB
PIFA	12.6 dB

Table 4.1 *Pattern averaged loss due to the operator proximity for the three antennas tested.*

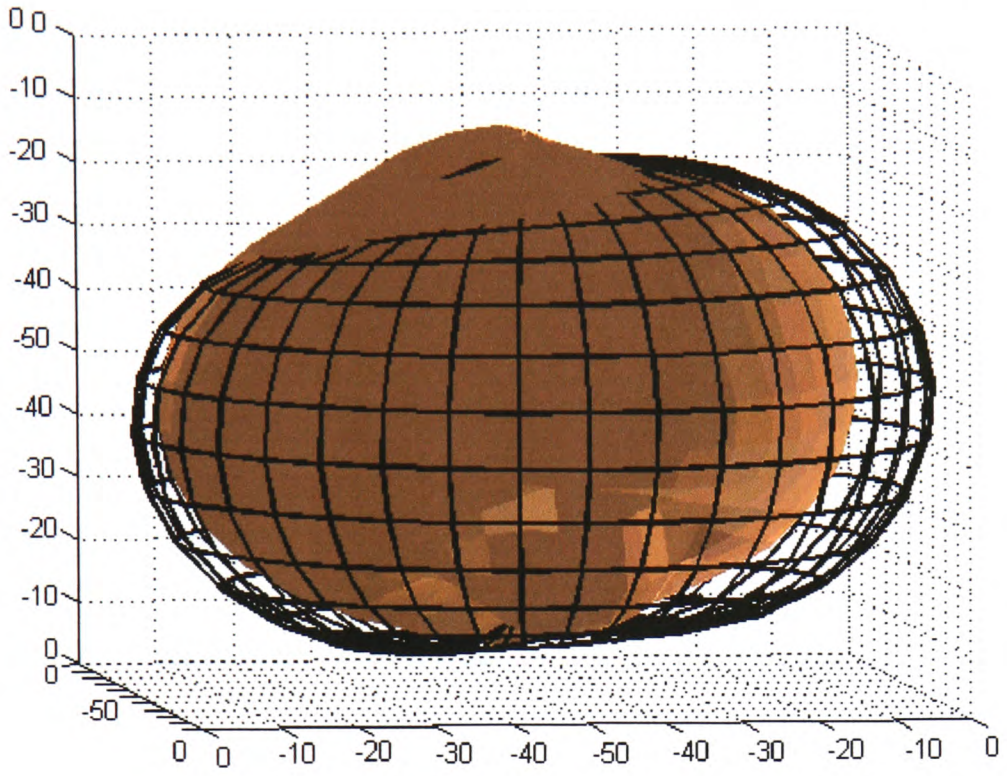

Fig. 4.36 *3D far-field radiation patterns (E_Θ) of the monopole antenna with (solid) and without (grid) the presence of the operator.*

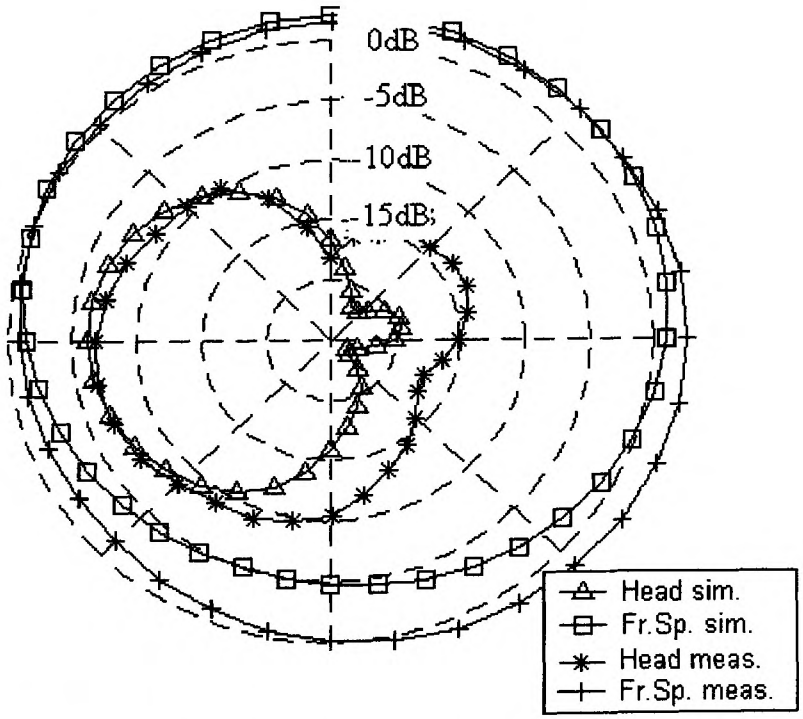

Fig. 4.37 *Predicted and measured horizontal (xy-plane) far-field radiation patterns (E_Θ) of the monopole antenna with and without the presence of the operator.*

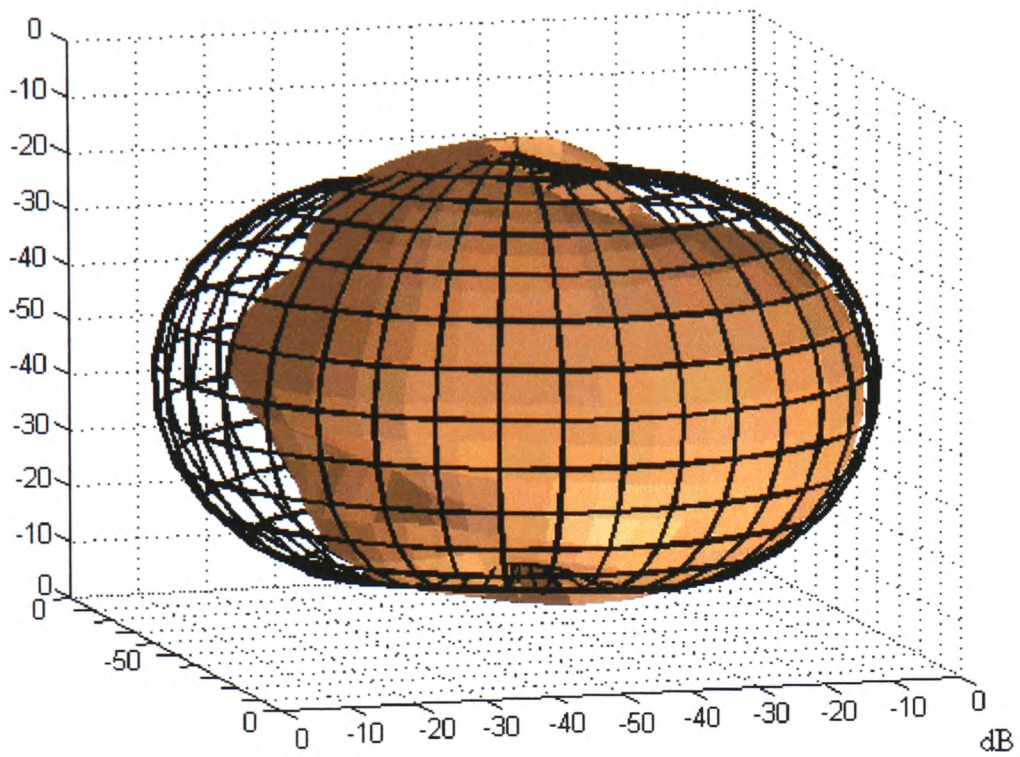

Fig. 4.38 *3D far-field radiation patterns (E_Θ) of the helix antenna with (solid) and without (grid) the presence of the operator.*

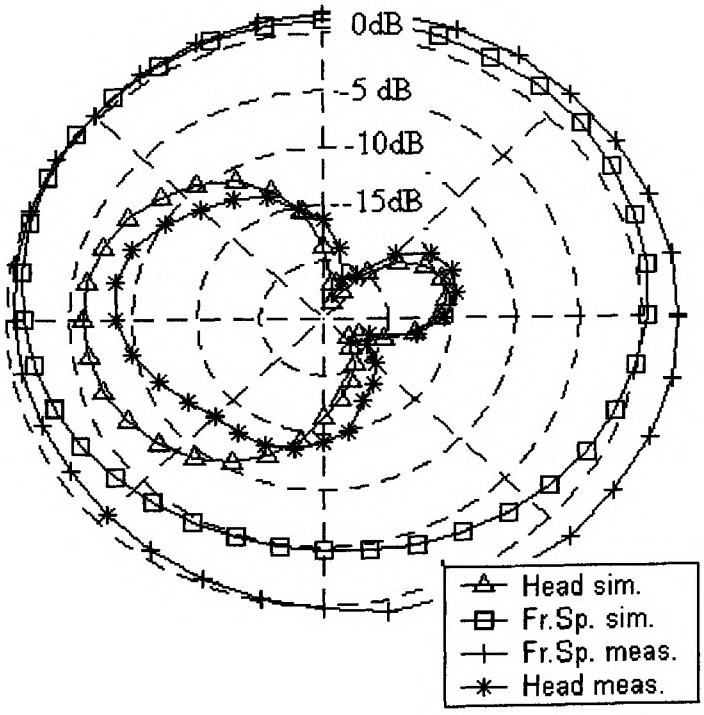

Fig. 4.39 *Predicted and measured horizontal (xy-plane) far-field radiation patterns (E_Θ) of the helix antenna with and without the presence of the operator.*

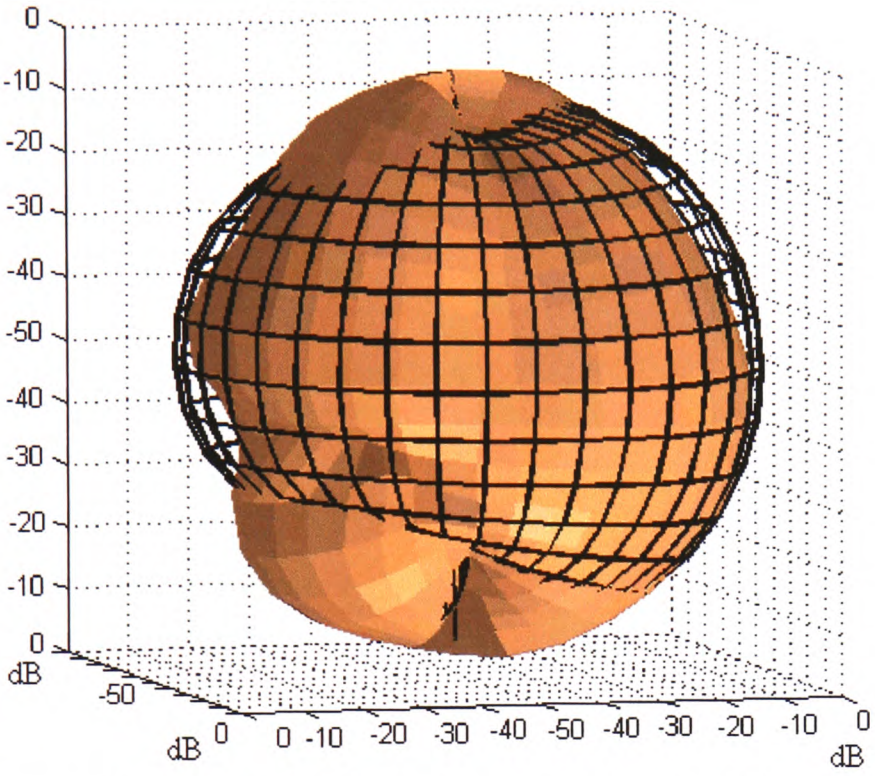

Fig. 4.40 *3D far-field radiation patterns (E_Θ) of the PIFA antenna with (solid) and without (grid) the presence of the operator.*

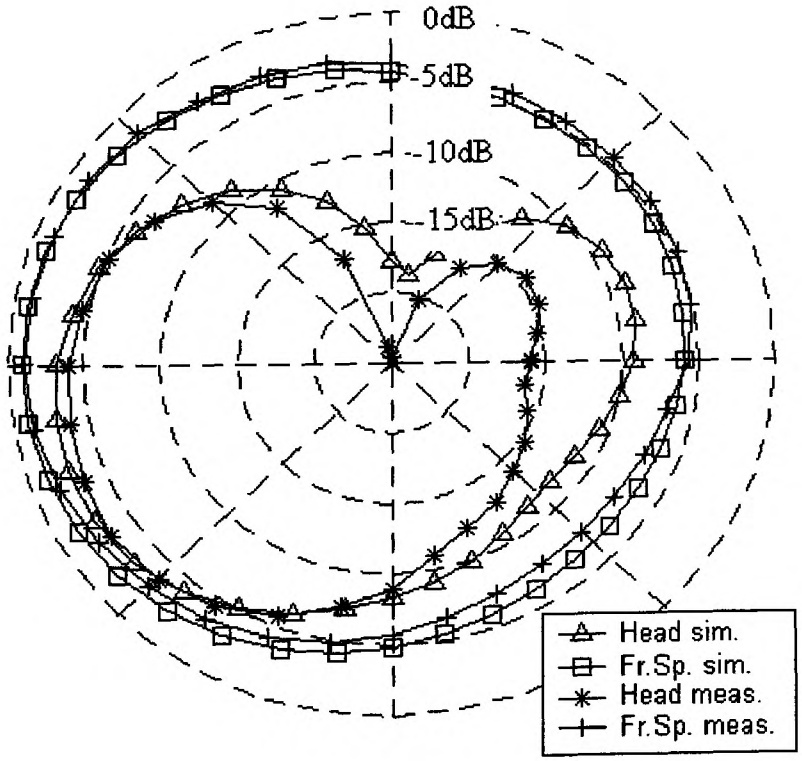

Fig. 4.41 *Predicted and measured horizontal (xy-plane) far-field radiation patterns (E_Θ) of the PIFA antenna with and without the presence of the operator.*

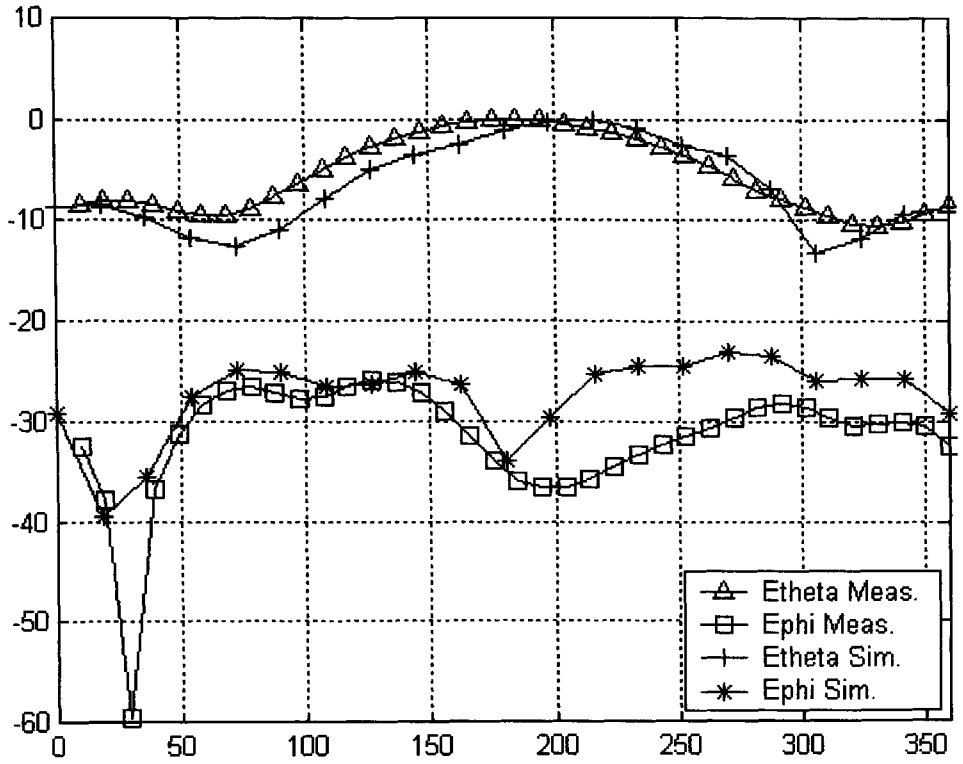

Fig. 4.42 *Predicted and measured horizontal (xy-plane) far-field radiation patterns (E_θ) and (E_ϕ) of the monopole antenna in the presence of the operator.*

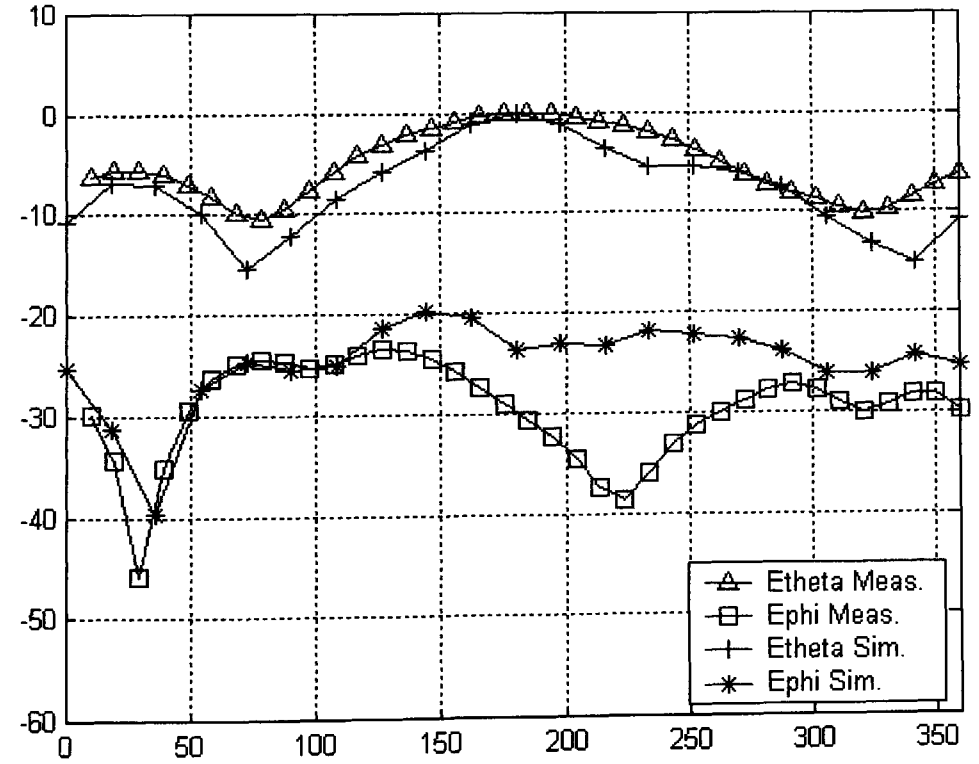

Fig. 4.43 *Predicted and measured horizontal (xy-plane) far-field radiation patterns (E_θ) and (E_ϕ) of the helix antenna in the presence of the operator.*

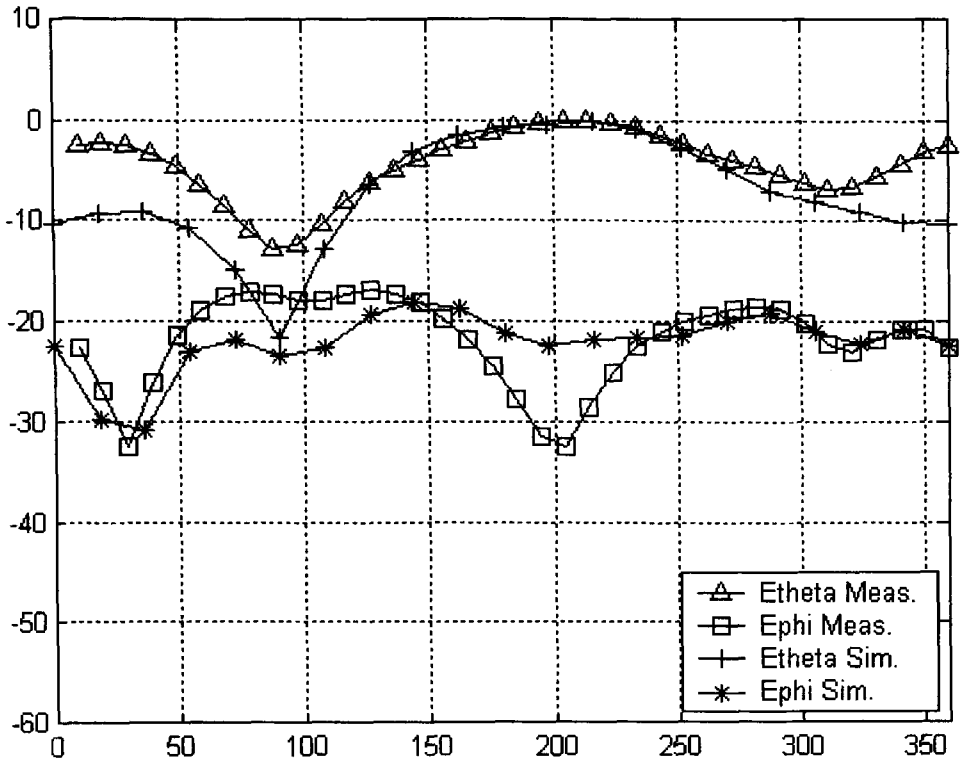

Fig. 4.44 *Predicted and measured horizontal (xy-plane) far-field radiation patterns (E_θ) and (E_ϕ) of the PIFA antenna in the presence of the operator.*

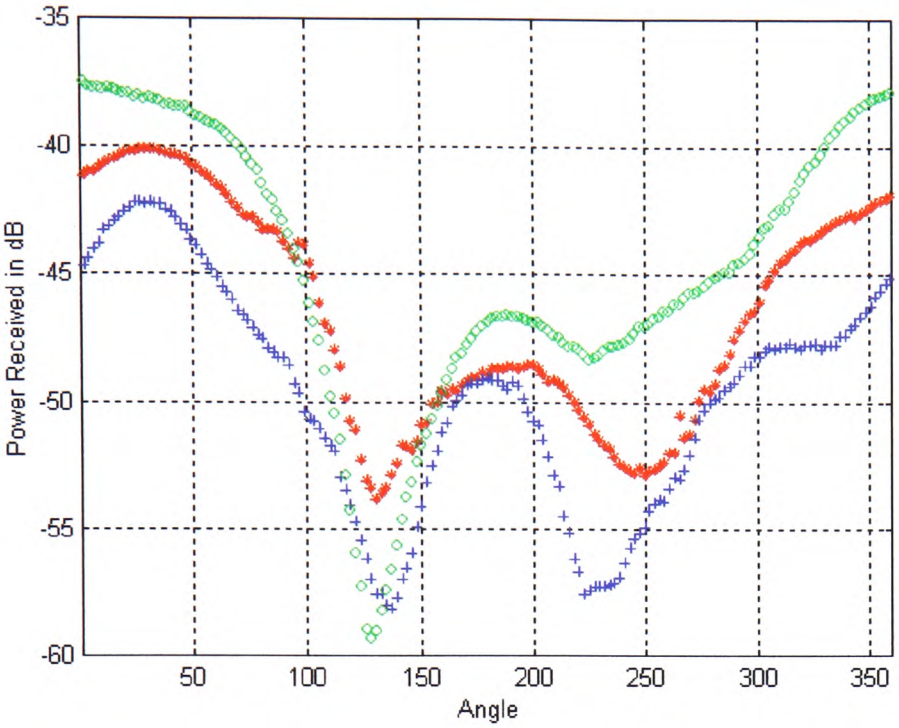

Fig. 4.45 *Measured radiation Patterns (E_Θ) of the monopole, helix, and PIFA antenna in the presence of a human operator.* ** *Monopole* ++ *Helix* oo *PIFA*

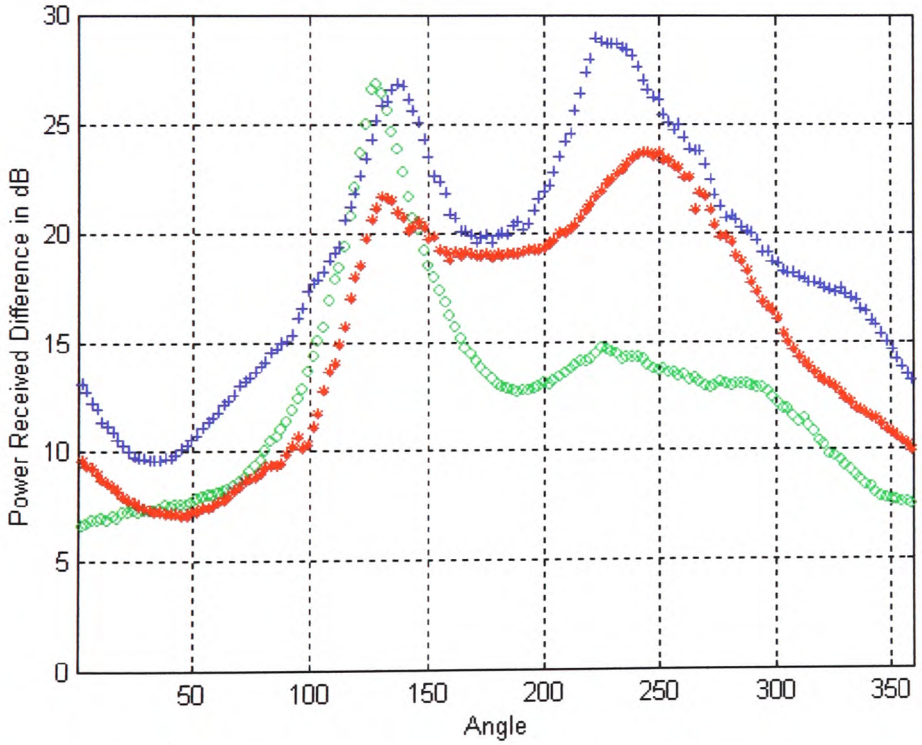

Fig. 4.46 *Change between the radiation patterns (E_Θ) caused by the presence of the operator:* ** *Monopole* ++ *Helix* oo *PIFA*

4.7 Interim conclusions.

Following a brief introduction of basic antenna parameter definitions, far-field computed and measured patterns are presented. The 3D far-field radiation patterns computed by both the MoM and FDTD show an omnidirectional radiation behaviour in the horizontal plane with the two numerical methods exhibiting good agreement. Similar agreement has been encountered between the measured and predicted E_Θ patterns. For the E_Φ radiation patterns the measured and simulated results deviate especially in the direction towards the bottom of the handset. This agrees with what has been reported in [3.1].

Investigation of the far field leads into two conclusions. Firstly, the good agreement between the two numerical methods and between the evaluated and measured results, encourage and justify further research using only numerical methods where measurements are not feasible. This is the case for the near-field patterns and SAR evaluation where conclusions are based only on simulation data. Secondly, it has been shown that PIFA has an advantage over the other two antennas when operating next to the operator's head. PIFA therefore is characterised by higher efficiency compared to wire antennas under coupling conditions and as a consequence can result in lower SAR. These advantages of PIFA encourage further work on investigating methods for increasing its bandwidth. In Chapter 5 work on the near-field patterns of the three antennas using the MoM and FDTD is reported.

5. NEAR-FIELD PATTERN EVALUATION

In this chapter near-field patterns of the three antennas introduced in Chapter 5 are presented. The data have been produced using MoM and FDTD. A wire-grid numerical model is used in the MoM model, which for the particular type of problems is a good compromise in terms of modeling versatility and computation time. The wire crossing and the segment size are 10 mm except near the feed point where this is reduced to 1 mm. Smaller grid and wire segmentation are used near the source to accurately simulate the more rapid variations in the current distribution. The MoM numerical models of the three antennas are the same as those used in far-field predictions (Figs. 4.7.a, 4.17.a and 4.26.a.)

Electrically small Perfect Electromagnetic Conductor (PEC) patches of 1.67×1.67 mm^2, which are equivalent to the Yee cell dimensions selected in this particular case, are used in the FDTD models. The FDTD numerical models for near-field predictions are shown in Figs. 4.7.b, 4.17.b and 4.26.b. The near field is computed at a distance of 1.67mm from the handset sides. In the following figures and text, we define the *rearside* of the handset as the side which is towards the operator's head, whilst *frontside* is that facing in the opposite direction. The maximum-value-normalized data are plotted on a logarithmic scale. Yellow colour represents high electric field intensity and white represents low electric field intensity over the plotted area. In addition to the vector magnitude (E_{mag}), the amplitude of the three components E_x, E_y and E_z are individually plotted for each case.

5.1 Monopole antenna operating in free space.

In Figs. 5.1-5.4, the near field of a quarter wavelength monopole antenna mounted on a conductive case operating at 945 MHz is shown. For the E_{mag} plots and for both the MoM and FDTD patterns it can be seen that high field exists along the edges of the handset. Highest values are near the top and bottom of the conductive case compared to the left and right sides. High field intensity exists also near the monopole with higher values at its top. The difference between the front and the back plots near the antenna is mainly due to the difference in the distance between the antenna and the handset sides. The antenna is located at 10 mm from the front side and at 20 mm from the rearside. Good agreement between the two numerical methods can be observed. In these plots, the wire grid in the MoM plots is visible due to the higher field that exists around the wires than in the intervening space. On the top left corner, this effect is eliminated due to the increased grid resolution.

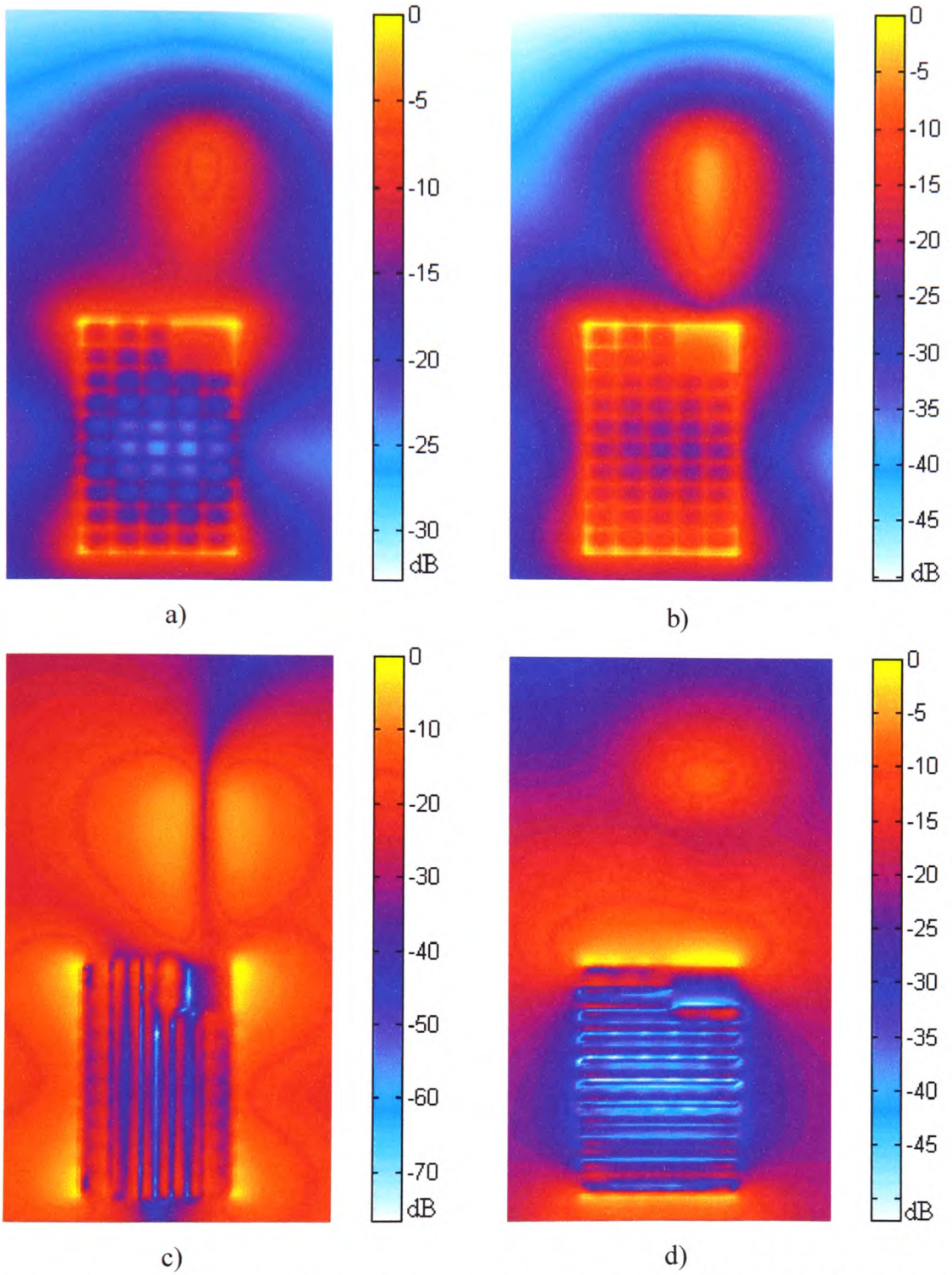

Fig. 5.1 *Normalized near-field patterns of monopole at 945 MHz (frontside) obtained from MoM simulations: a) E_{mag}, b) E_x, c) E_y and d) E_z.*

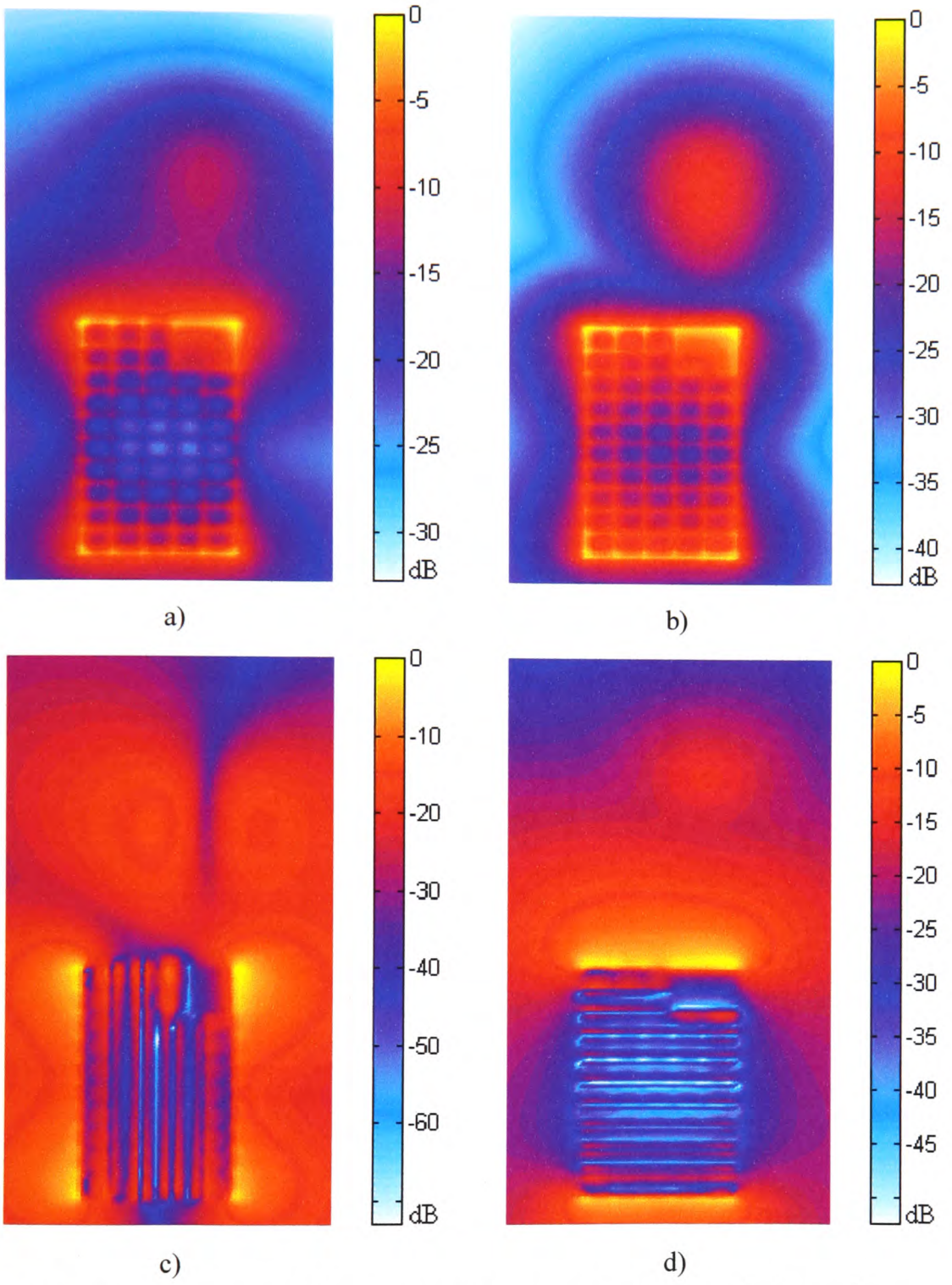

Fig. 5.2 *Normalized near-field patterns of the monopole at 945 MHz (rearside) obtained from MoM simulations: a) E_{mag}, b) E_x, c) E_y and d) E_z.*

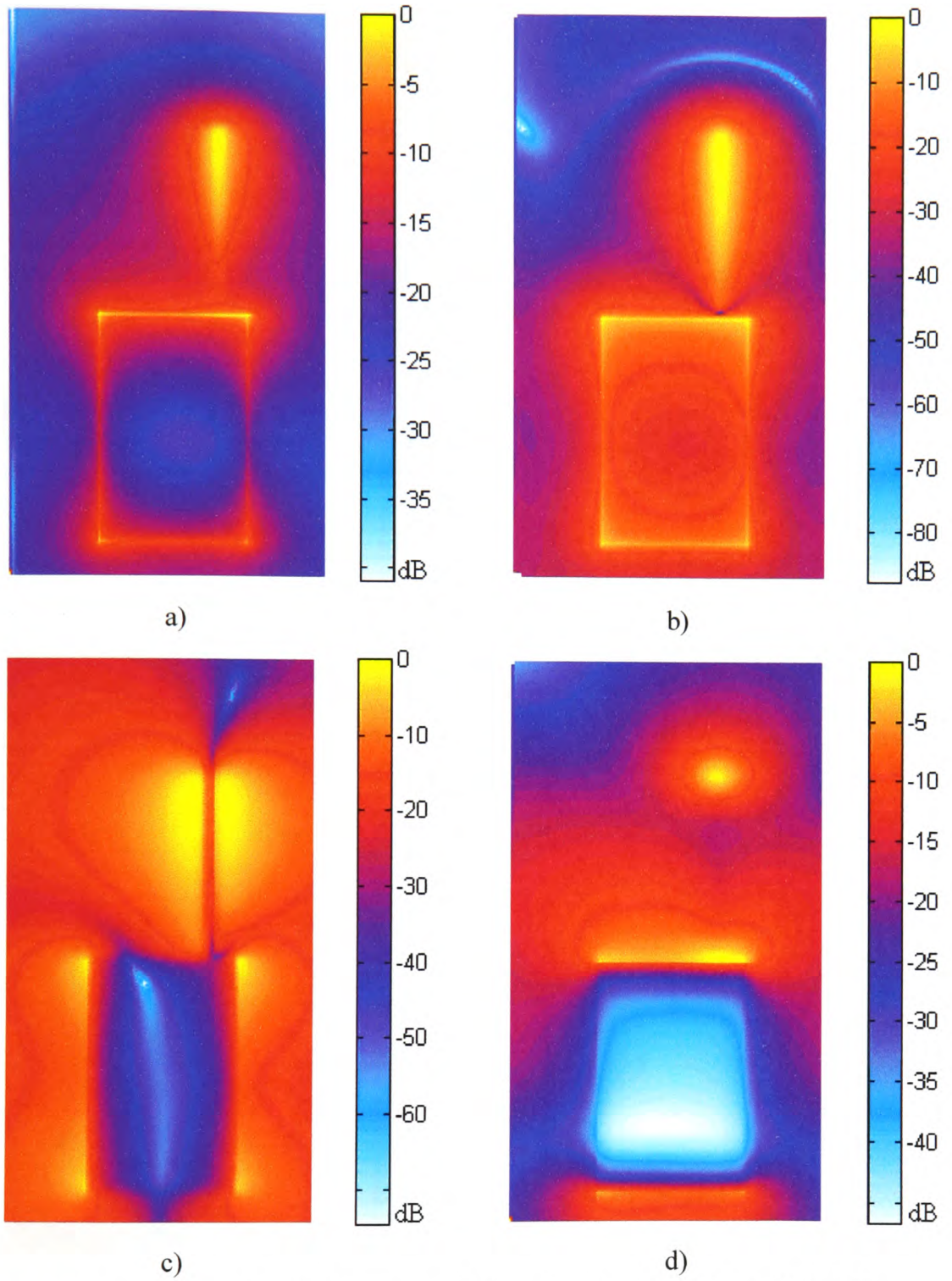

Fig. 5.3 *Normalized near-field patterns of the monopole at 945 MHz (frontside) obtained from FDTD simulations: a) E_{mag}, b) E_x, c) E_y and d) E_z.*

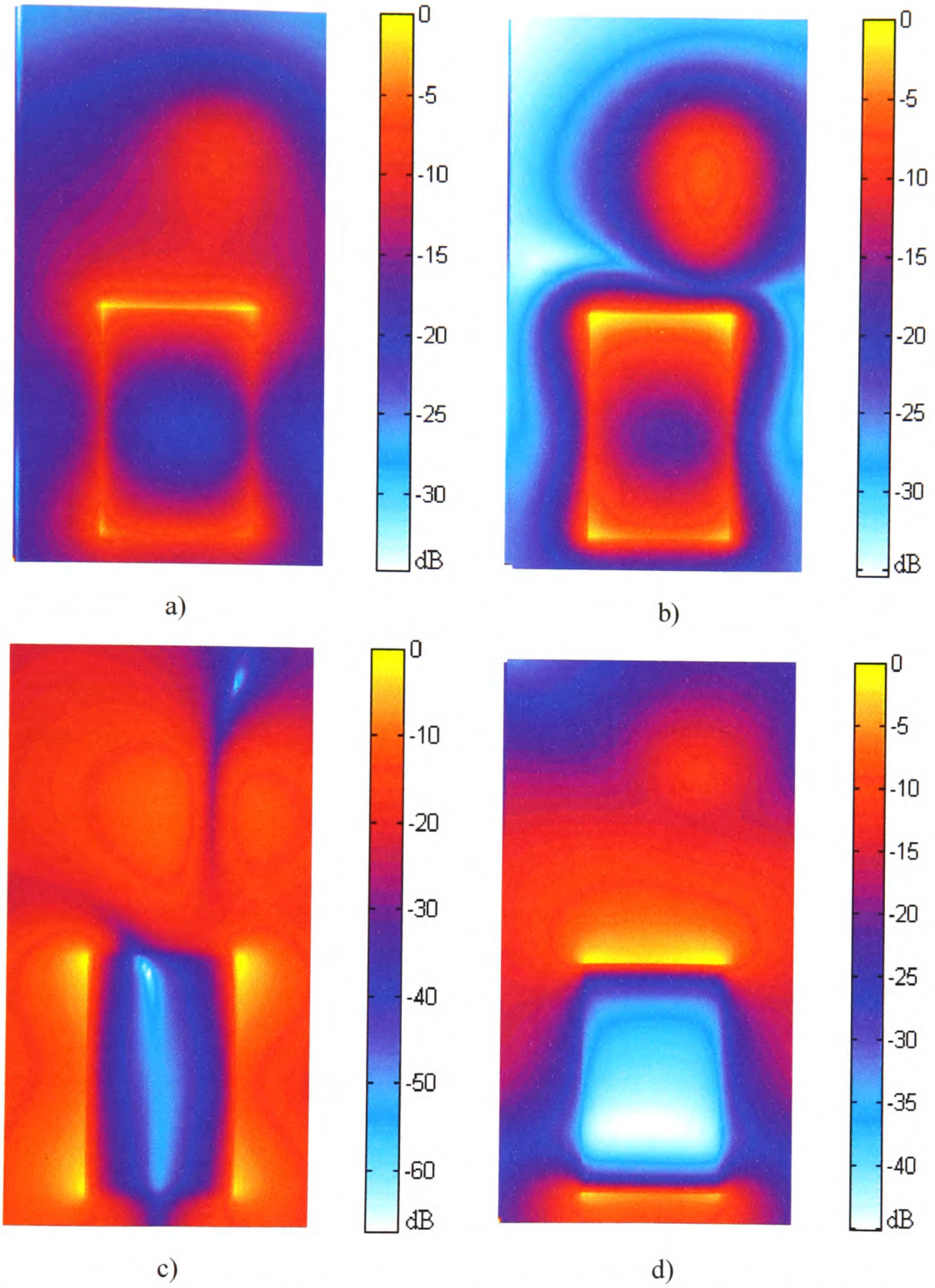

Fig. 5.4 *Normalized near-field patterns of the monopole at 945 MHz (rearside) obtained from FDTD simulations: a) E_{mag}, b) E_x, c) E_y and d) E_z.*

5.2 The small helix antenna in free space.

In this section near-field patterns of the small helix antenna are presented. For the purpose of FDTD simulation a square turn helix model has been developed, as shown in Fig. 4.17. This helix has the same length and turns as the MoM wire-grid model and that one used in measurements. Numerical evaluation of the antenna resonance frequency (f_r) has shown good agreement with the measured value. Despite differences in the MoM and FDTD numerical models, the near-field patterns do not significantly vary. Similarly to the whip antenna, high field is observed near the edges of the conductive case and the antenna. However, due to the fact that the helix is shorter in height compared with the monopole, the field along the entire antenna length and near the top end of the conductive case is higher. It must be noted that due to its larger diameter, the antenna is physically closer to the computational planes. More importantly at the rearside, the electric field is stronger near the antenna compared to values computed for the monopole. This, as will be seen later, results in higher SAR values.

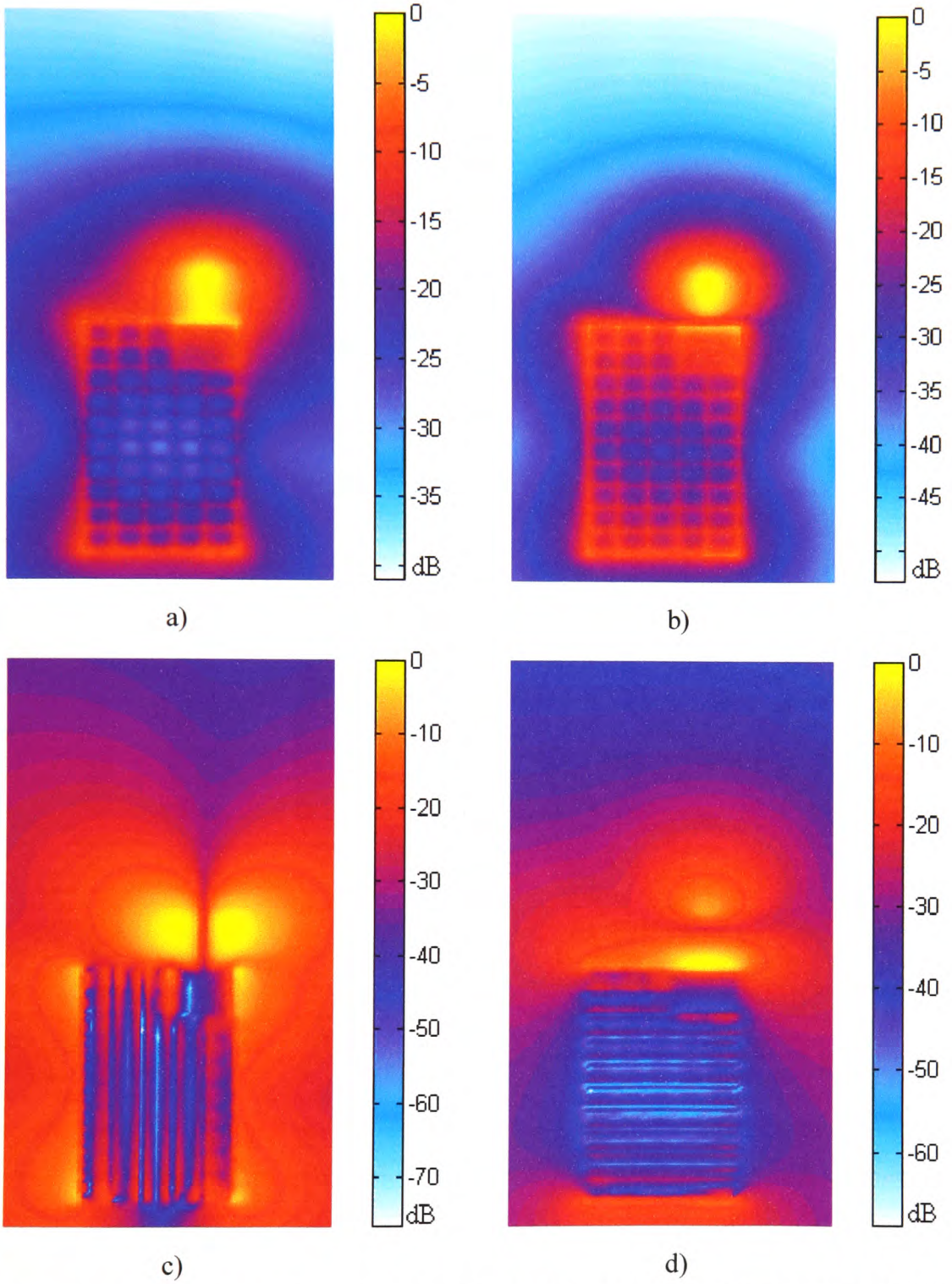

Fig. 5.5 *Normalized near-field patterns of the helix at 945 MHz (frontside) obtained from MoM simulations: a) E_{mag}, b) E_x, c) E_y and d) E_z.*

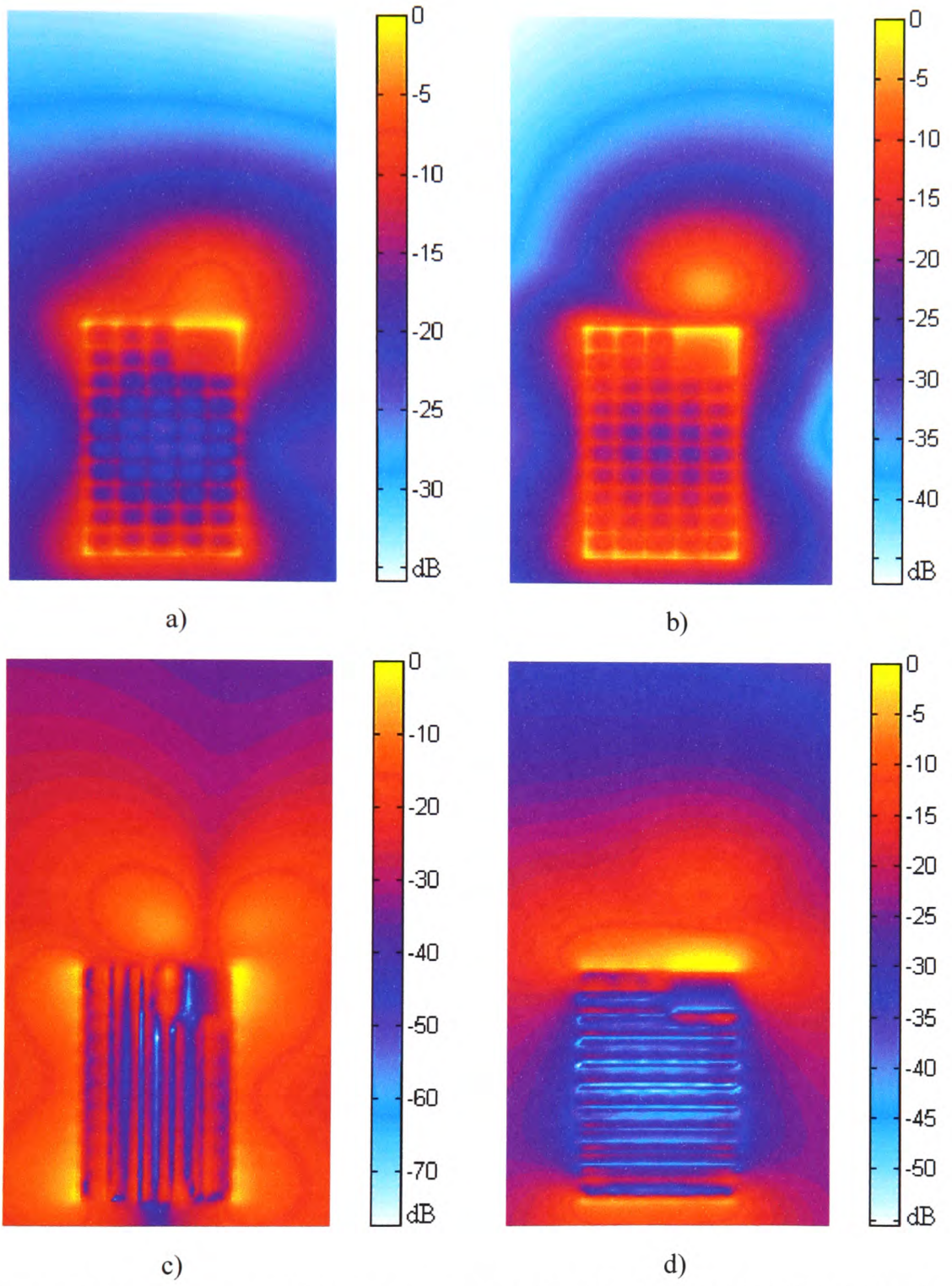

Fig. 5.6 *Normalized near-field patterns of the helix at 945 MHz (rearside) obtained from MoM simulations: a) E_{mag}, b) E_x, c) E_y and d) E_z.*

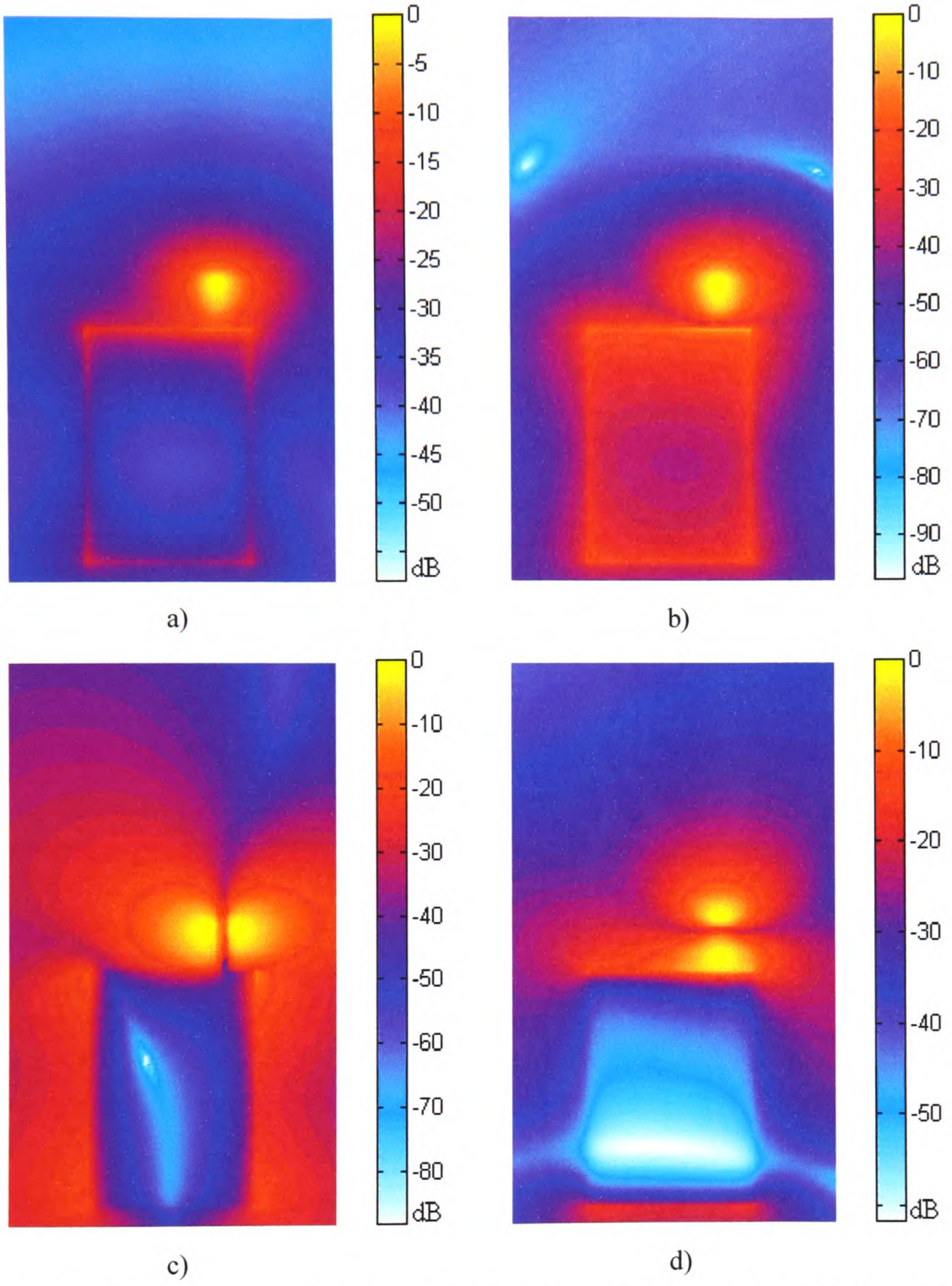

Fig. 5.7 *Normalized near-field patterns of the helix at 945 MHz (frontside) obtained from FDTD simulations: a) E_{mag}, b) E_x, c) E_y and d) E_z.*

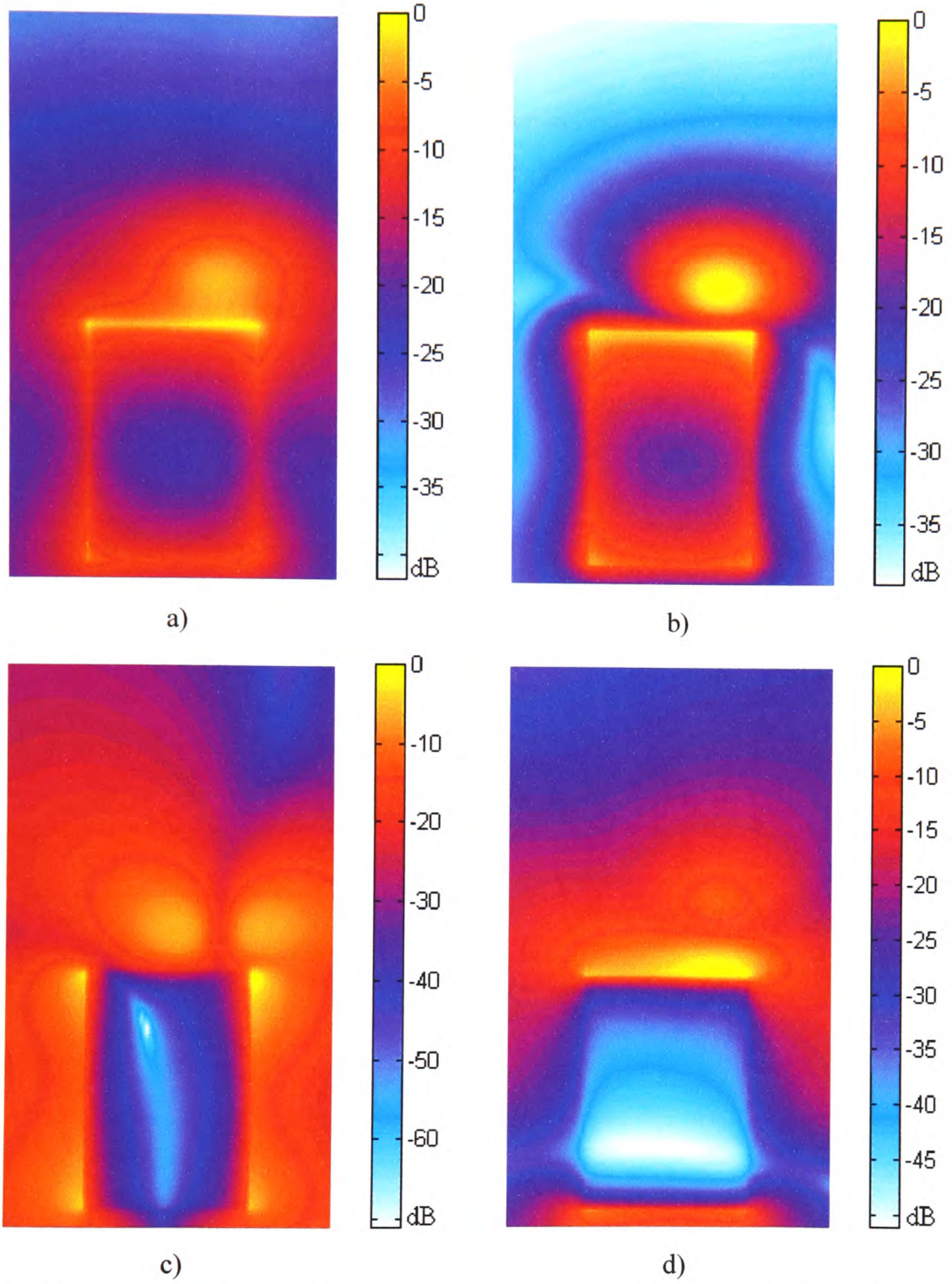

Fig. 5.8 *Normalized near-field patterns of the helix at 945 MHz (rearside) obtained from FDTD simulations: a) E_{mag}, b) E_x, c) E_y and d) E_z.*

5.3 The PIFA antenna in free space.

Near-field plots of PIFA normalized to maximum values are shown in Figs. 5.9 – 5.12. In the same manner as in the monopole and helix antennas, discussed in Sections 5.1 and 5.2, high field intensity is concentrated around the edges of the handset and near the antenna. This is not very obvious from the front-side plots presented here because the field is computed at 1.76mm from the PIFA patch, which is approximately 6 mm away from the handset. High field is also present along the edges of the patch and especially at its corners. No short pins are simulated in both the MoM and the FDTD models. MoM does not allow a short circuit near the feed point, unless a considerable amount of segments separate the short and the feed. This however requires very fine grid model, which results in increased computation time. From the FDTD simulations it was shown that the absence of short pin in the model has no significant effect on the normalized near-field plots except for a small area near the short pin where the field is reduced. Short pin affects the input impedance of the antenna and as a consequence the reflection efficiency, but not necessarily the far-field radiation pattern or the near-field characteristics of the PIFA.

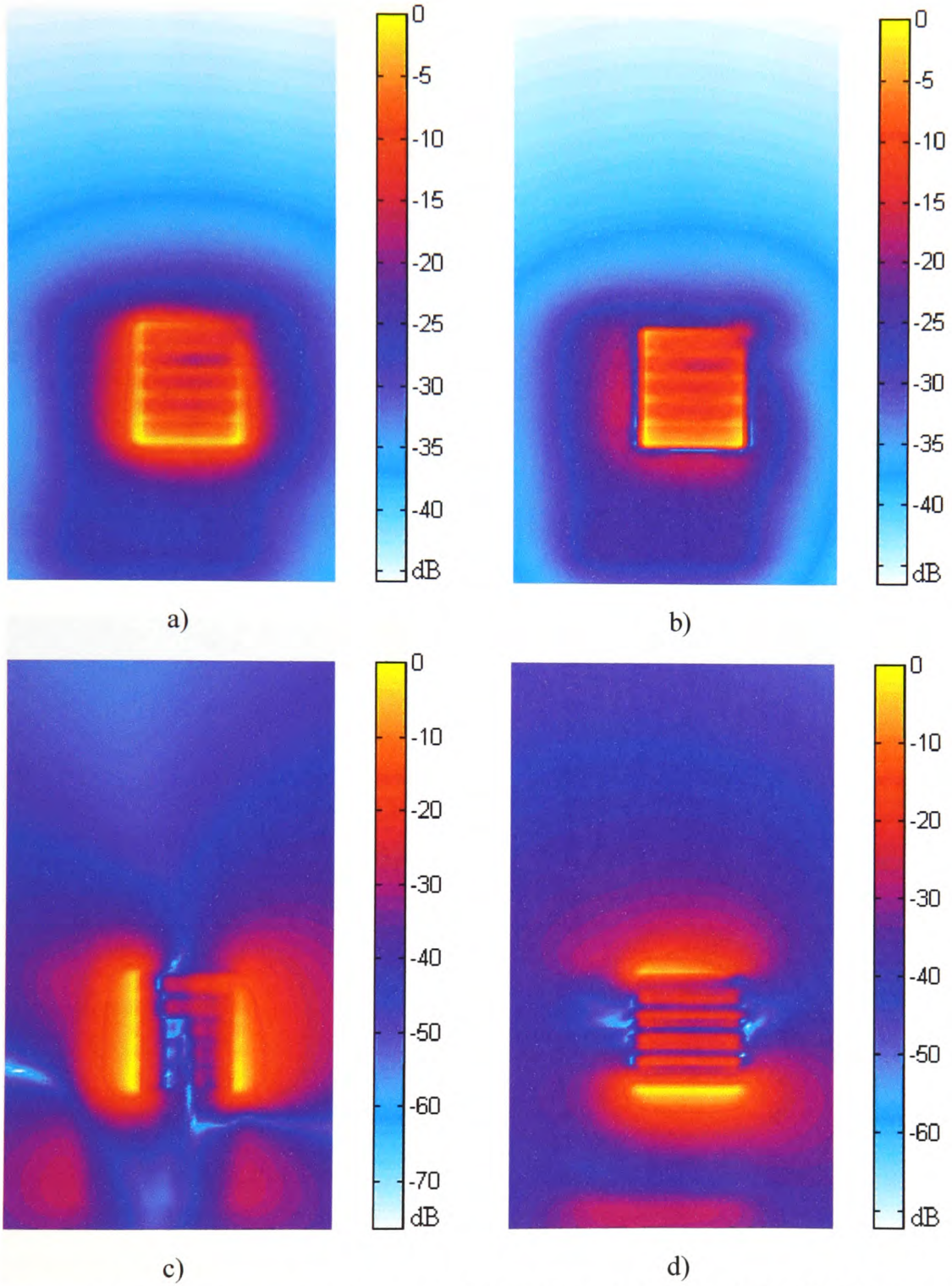

Fig. 5.9 *Normalized near-field patterns of the PIFA at 945 MHz (frontside) obtained from MoM simulations: a) E_{mag}, b) E_x, c) E_y and d) E_z.*

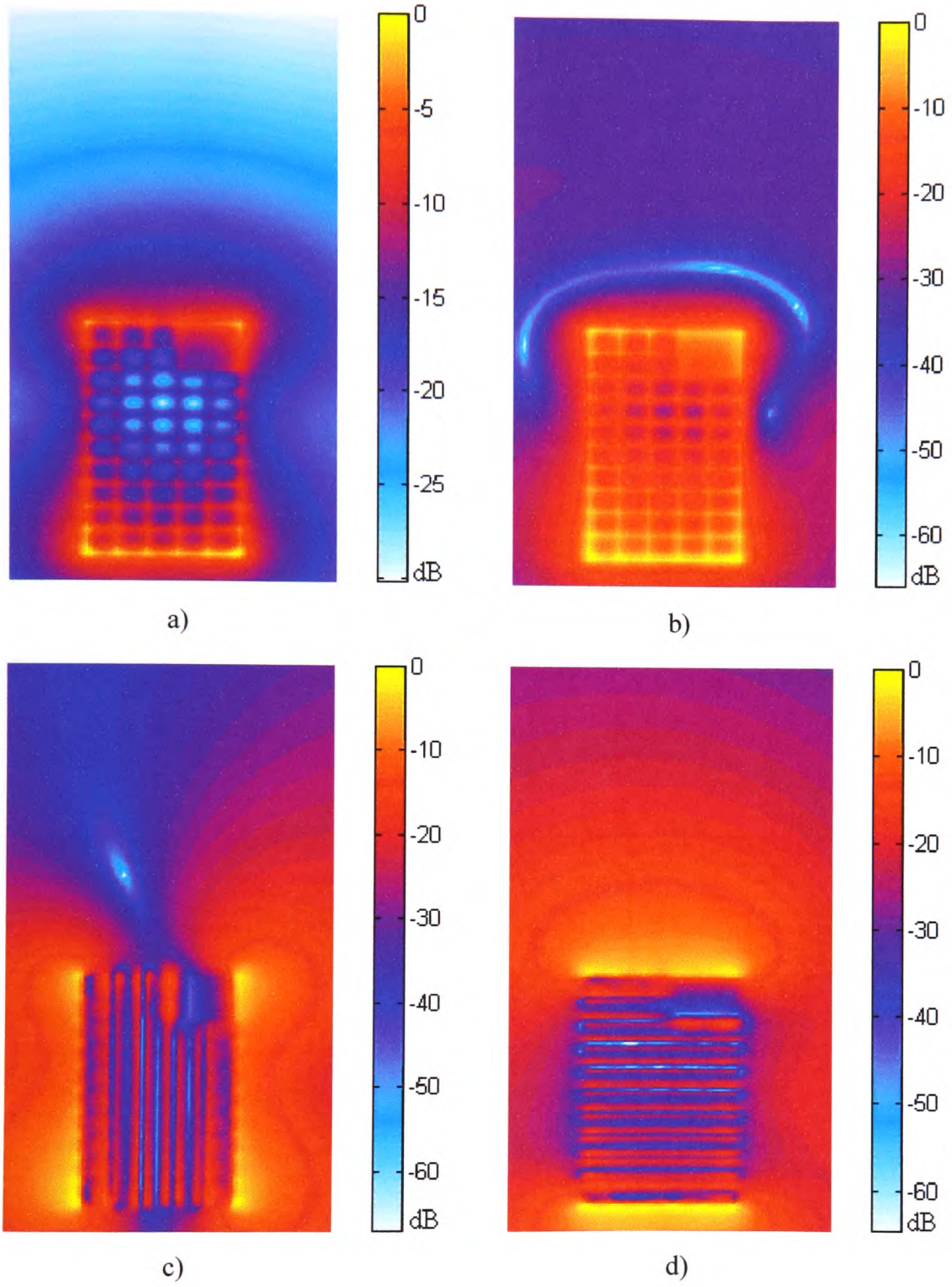

Fig. 5.10 *Normalized near-field patterns of the PIFA at 945 MHz (rearside) obtained from MoM simulations: a) E_{mag}, b) E_x, c) E_y and d) E_z.*

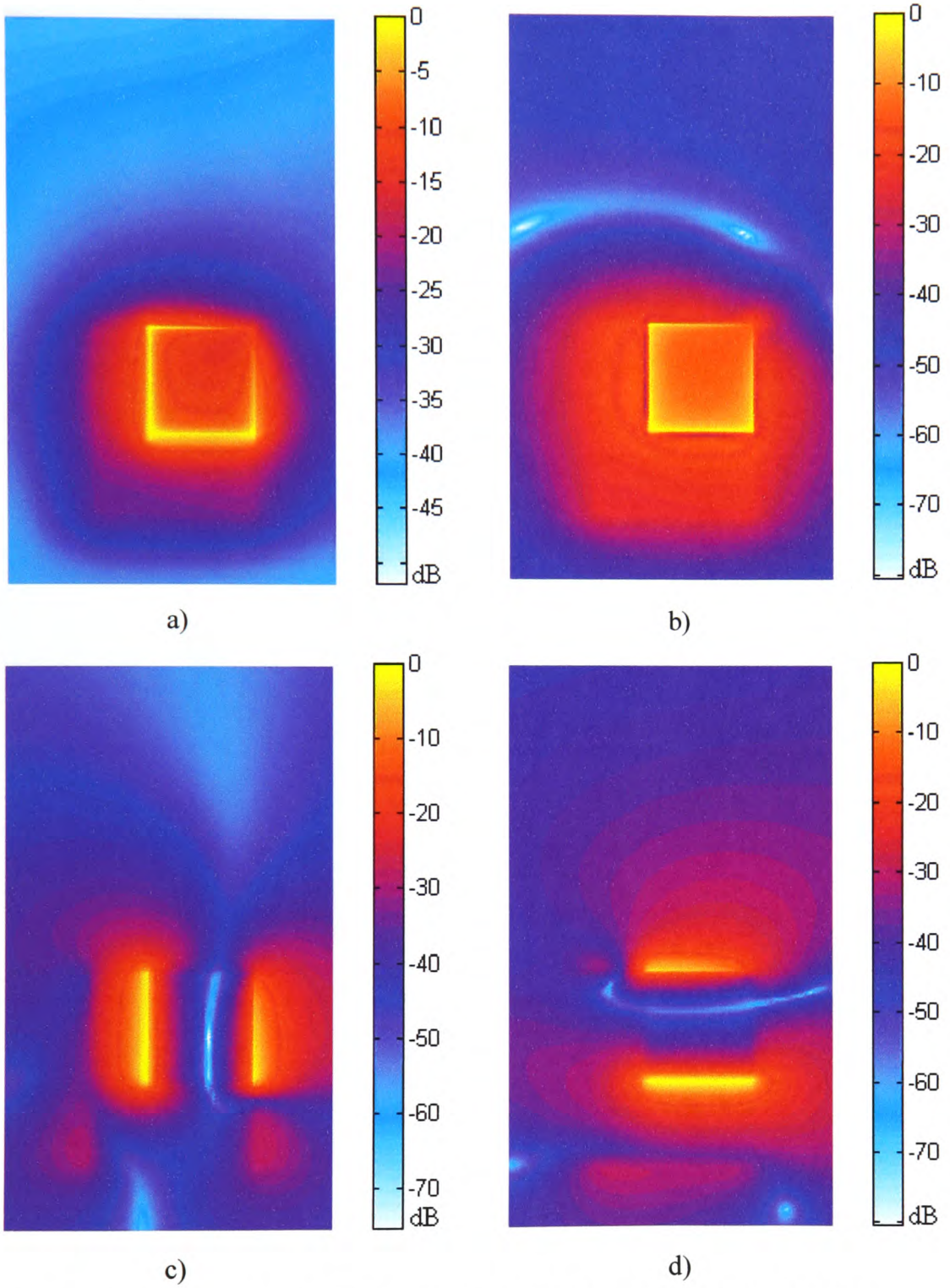

Fig. 5.11 *Normalized near-field patterns of the PIFA at 945 MHz (frontside) obtained from FDTD simulations: a) E_{mag}, b) E_x, c) E_y and d) E_z.*

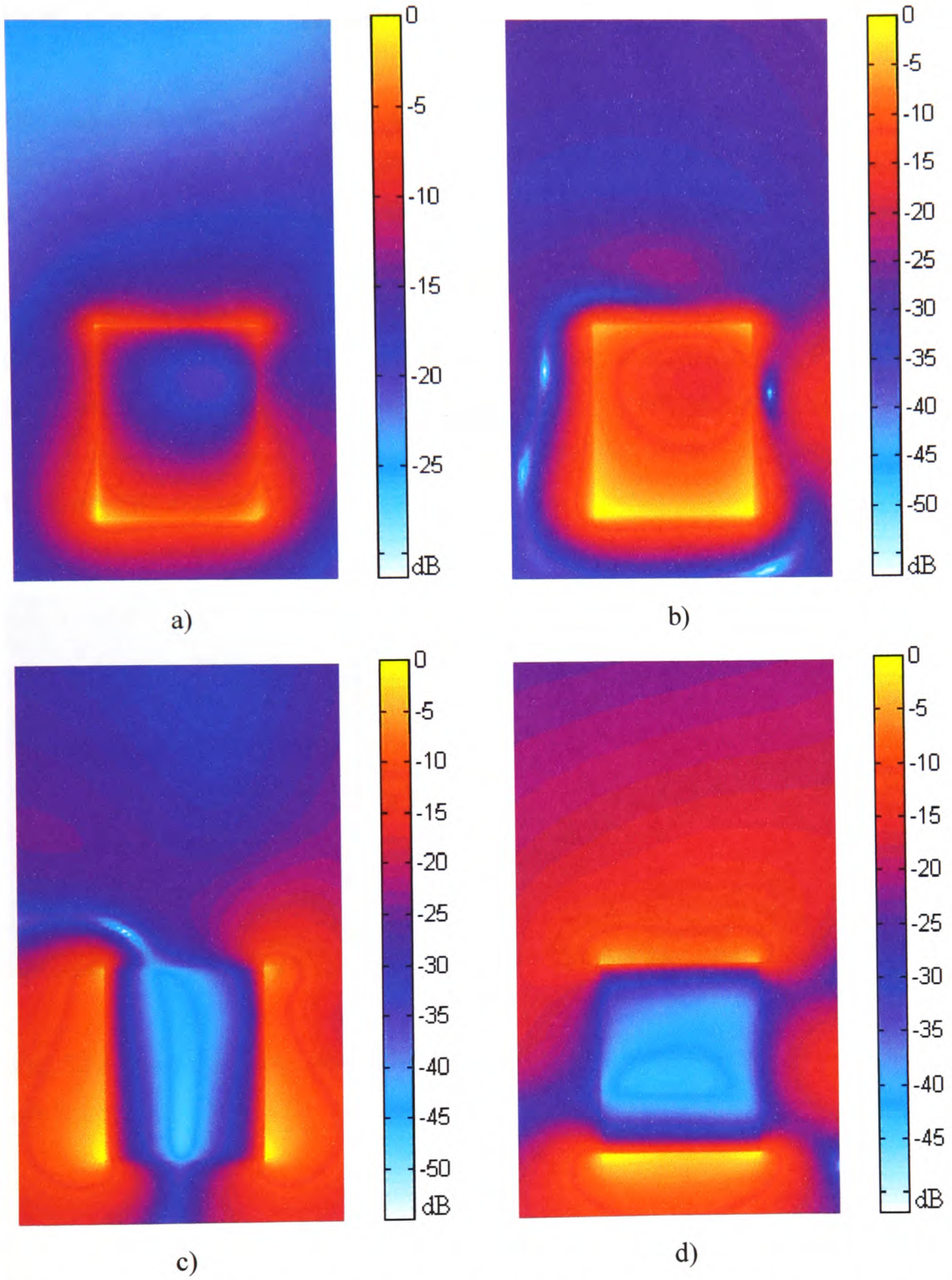

Fig. 5.12 *Normalized near-field patterns of the PIFA at 945 MHz (rearside) obtained from FDTD simulations: a) E_{mag}, b) E_x, c) E_y and d) E_z.*

5.4 Near-field patterns of the PIFA operating next to the operator's head.

The near field of a PIFA operating next to the operator's head, computed with FDTD, is shown in Fig. 5.13.a. Strong electric fields appears near the ear region which lies closest to the handset, in addition to vicinity of the edge of the handset. The effect of the handset and the antenna type on the energy absorbed by the operator is discussed in Chapter 7 where SAR evaluations are presented. When the observation plane is displaced by one cell towards the head/shoulders mesh, the near field pattern of Fig. 5.13.b is obtained. The ear and the left shoulder can be clearly seen in this figure where, due to the dielectric properties of the modelled tissues, the field becomes degraded.

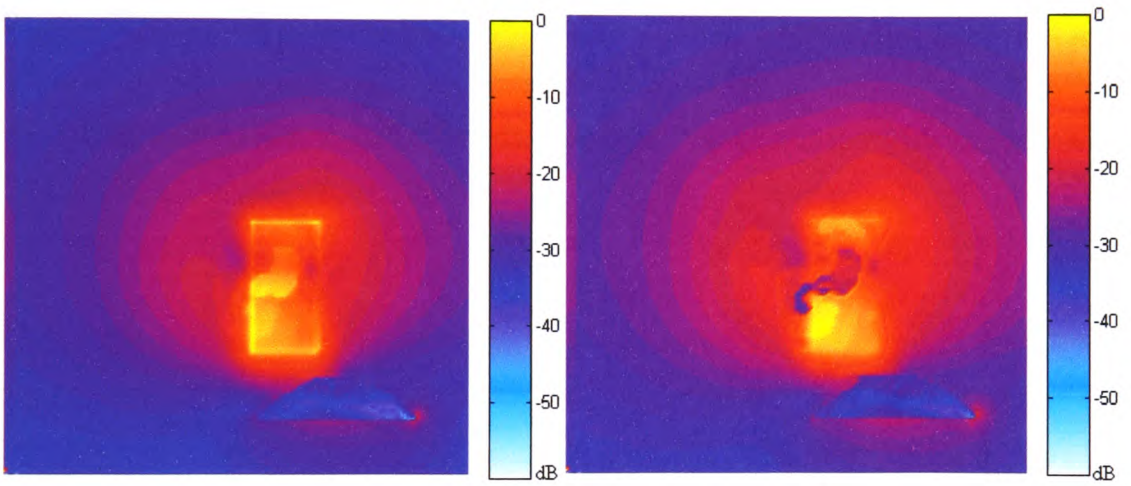

a) b)

Fig. 5.13 *Normalized near field at the back of a PIFA antenna in the presence of the operator.*

5.5 Interim conclusions.

Near-field radiation patterns evaluated by both the MoM and the FDTD have been presented. Due to the difficulty of doing measurements in the near field region of the radiator without causing considerable coupling errors because of probe proximity, only numerical evaluation methods were used. Good agreement between the two numerical methods for all electric field components is evident from the figures presented in this chapter. This is also true for the helix models, which are not identical. Higher electric field intensity around the handset edges and along the length of the antennas has been observed, as expected. This is true for antennas operating in free space as well those in coupling configurations. In the case where the antenna lies near the operator's head a high electric field is also present near the ear region. The near field, around the handset and the antenna, directly affects the SAR values. The relation between the near field with the SAR and the radiation efficiency of mobile antennas are discussed in Chapter 7 where wide band SAR and efficiency predictions are presented.

6. TUNING TECHNIQUES FOR THE PLANAR INVERTED F-ANTENNA

As pointed out in Chapter 4, the bandwidth of the planar inverted-F antenna is relatively narrow for mobile handset applications. This is a significant disadvantage of the PIFA counteracting its merits that include low SAR and high radiation efficiency under coupling conditions with human tissue. The advantages of PIFA are discussed further in the Chapter 7, where operation of portable handset antennas next to the operator's head is further considered. To extend its applicability, methods for improving the PIFA bandwidth become necessary especially if PIFA is to be applied widely in handset design. In [3.3]-[3.5] two different methods for improving the PIFAs bandwidth are proposed, as have been summarised in Chapter 3. These articles include useful results and data, especially for frequencies in the DCS1800 band. However, the effect of resonance frequency shift arising from the PIFA being next to the operator's head is not considered. This resonance frequency shift is of the order of 15 MHz in the GSM900 band, and generally is of the order of 1-2%. When the resonance frequency of a narrow band antenna is shifted by this amount, the result will be undesirably high reflections and eventually poor radiation efficiency. When the PIFA is to be used in mobile phone handsets, means are needed to correct this frequency shift in order to maintain good matching with the radio transceiver. In this chapter, methods for controlling the resonance of the PIFA having fixed patch dimensions, feed point and short pin positions are presented. Finally, prototype antennas for dual GSM900 and DCS1800 band operation with electronically controlled tuning are demonstrated.

6.I Design parameters for the PIFA.

The PIFA consists of a patch that is placed in parallel with the conductive case ground and is short-circuited near the feed point (Fig. 6.1.a). The relationship between the resonance frequency (f_r) and the dimensions of the patch for a typical PIFA, when no dielectrics are used, is given by eq. 3.2. The handset conductive case acts as a ground for the antenna and for this reason is connected to the copper shielding of the coaxial cable used. Not only the size of the patch defines the

resonance frequency of the antenna, but also the number and the position of the short pins.

In order to improve the bandwidth and gain performance of this antenna, a more extensive research on tuning techniques for PIFA has been carried out. Some of the parameters that define the value of the resonance frequency, such as the size of the patch and the position of the feed cannot be changed in a practical application. However, other parameters, such as the short pin position and its impedance, can, in principle, be adjusted during operation.

The first parameter that affects the resonance frequency and has been systematically studied is the position of the short pins. The position of the short pin is directly related to the current distribution in the antenna and as a consequence with its input impedance. For measurement reasons, the radiation patch of the PIFA has been segmented as shown in Fig. 6.1.b. The dimensions of the handset and antenna used for this case are given in Fig. 6.1.a. The size of the conductive box is chosen to be typical for mobile phone handsets. The measurements were carried out in anechoic conditions and the measured data were obtained from reflection coefficient measurements with the vector network analyzer. Fig.6.2 shows the VSWR of a typical PIFA with two short pins placed near the feed point and d = 5 mm. In this particular case, the antenna bandwidth is not greater than 10 MHz and this represents only 14% of the bandwidth required by the GSM900 system.

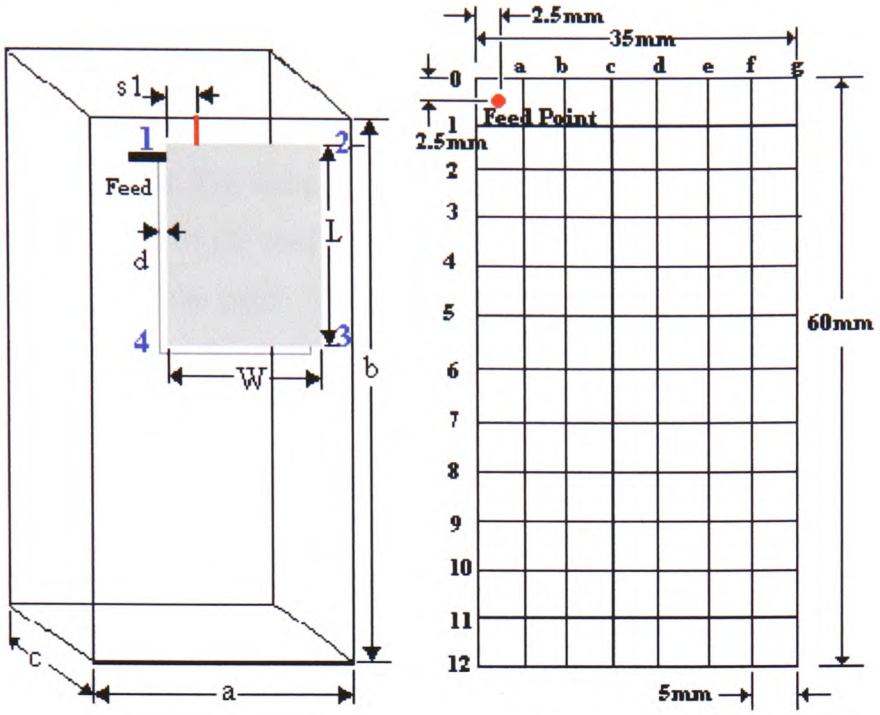

a) b)

Fig. 6.1 ***a)*** *A conventional PIFA. a: 50mm, b: 100mm, c: 25mm, d: 5mm, s1: 5mm (Short Pin), L: 60 mm, W: 35mm.* ***b)*** *Scaled PIFA patch used for measurements of VSWR (not in scale).*

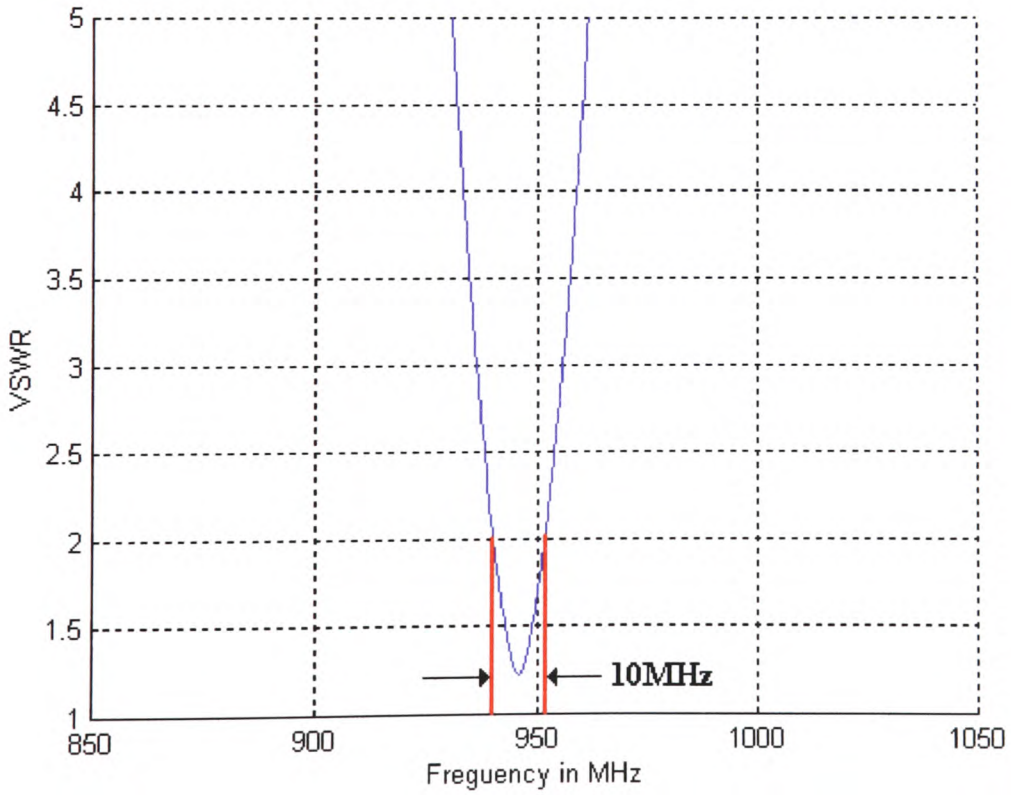

Fig. 6.2 *VSWR vs. frequency of a conventional PIFA.*

6.2 Short pin effects on resonance frequency.

The first method for PIFA tuning that has been systematically studied is the one short pin repositioning method. The radio configuration for the particular method is shown in Fig. 6.3. The position of the feed point and the dimensions of the conductive case as well as the height of the patch from the conductive case, as already pointed out, are fixed. A short pin at a fixed distance s1 = 5 mm from the top left corner is also used to add the necessary inductance to the antenna so that the VSWR near the resonance frequencies is less than 2:1. A second short pin, referred to as "*travelling pin*", is introduced to achieve fine-tuning of the PIFA. The VSWR and input impedance of the antenna are measured in steps of 5-mm, as the pin moves clockwise along the perimeter of the patch. For instance, legend "1→4" in Fig. 6.4 indicates that the short pin was moved from reference corner 1 towards reference corner 4. The resonant frequencies, for the four different cases studied, corresponding to the short pin travelling along the four patch edges, are plotted in Fig. 6.4. As the distance from the feed increases, f_r increases too, but this continues up to a point. When the short pin approaches the opposite corner, f_r starts to decrease again. Hence, the corners of the patch have a noticeable effect on f_r, whilst f_r values do not only depend on the distance of the short pin from the feed point. This is because of the current distribution on the patch that attains high values in the proximity of the patch corners. This is depicted in Figs. 5.9.a and 5.11.a where the resultant near field is stronger near the edges of the radiation patch. Despite the corners' effect on f_r, we can propose as a rule of thumb that "f_r increases as the distance of the travelling pin from the feed increases."

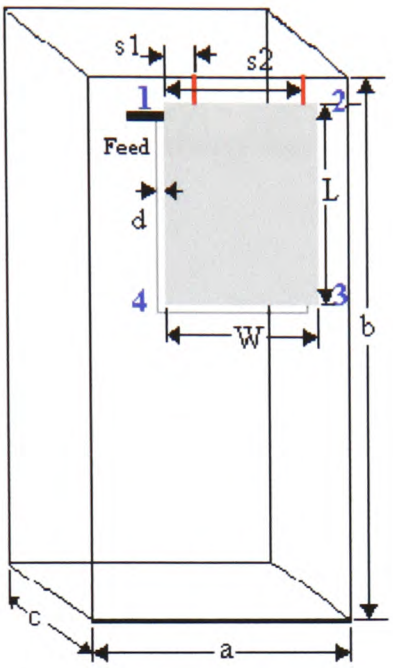

Fig. 6.3 *PIFA configuration for short pin position tuning.*

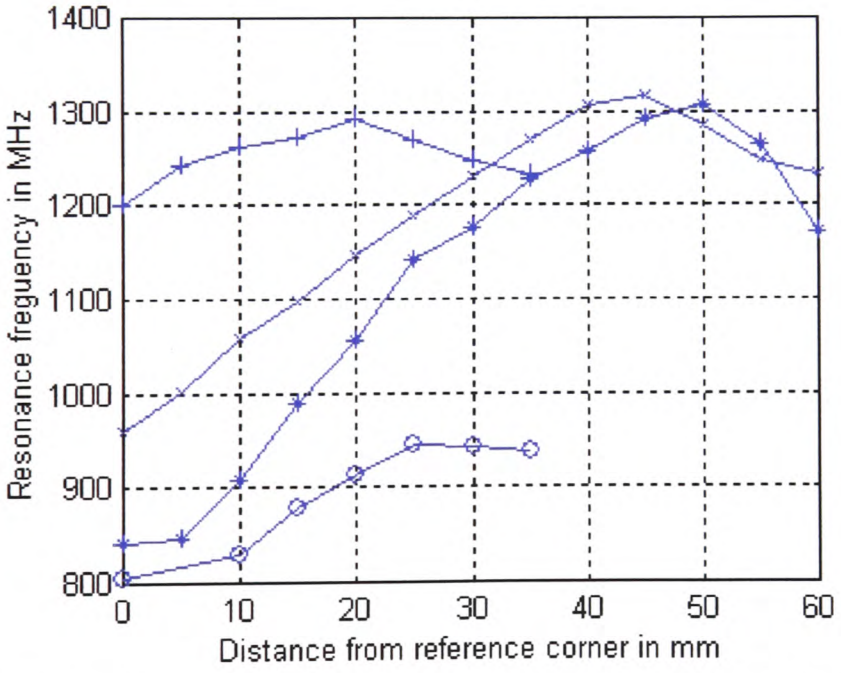

Fig. 6.4 *Resonance frequency of PIFA for various short pin positions: o Reference corner 1→2, x Reference corner 2→3, + Reference corner 3→4, *Reference corner 1 →4.*

If we define the *effective bandwidth* of an antenna as the frequency range that can be covered using a specific tuning technique, then the effective bandwidth of the antenna described above is approximately equal to 500 MHz (804 → 1306 MHz).

The effective bandwidth of the PIFA, using the short pin repositioning method can satisfy the GSM900 band requirements and is by far wider than the bandwidth of the quarter wavelength monopole and the small helix antennas. It should be further noted that the VSWR within this bandwidth is always less that 2:1 giving good reflection efficiency for the antenna.

Fig. 6.5 shows the VSWR vs. frequency and the Smith chart for two travelling pin positions and, in particular, when the travelling pin is at positions 0g or 9g as shown on the grids in Fig. 6.1.b. From the study of the Smith chart curves and for the frequencies of interest, the antenna input impedance (reactance) becomes less capacitive as the short pin is placed further from the feed point. This is due to the added inductance because of the increased distance of the feed point from the short pin. As a result, for higher frequencies, the impedance of the PIFA approaches 50Ω and consequently the resonance frequency increases. The resonance frequency is 961 MHz and 1316.4 MHz for 0g and 9g positions, respectively. For short pin positions between 0g and 9g, the curves will be similar and will fall between the two curves shown in Fig.6.5. A table of all the measurements results and related data files from VNA are given in Appendix B.

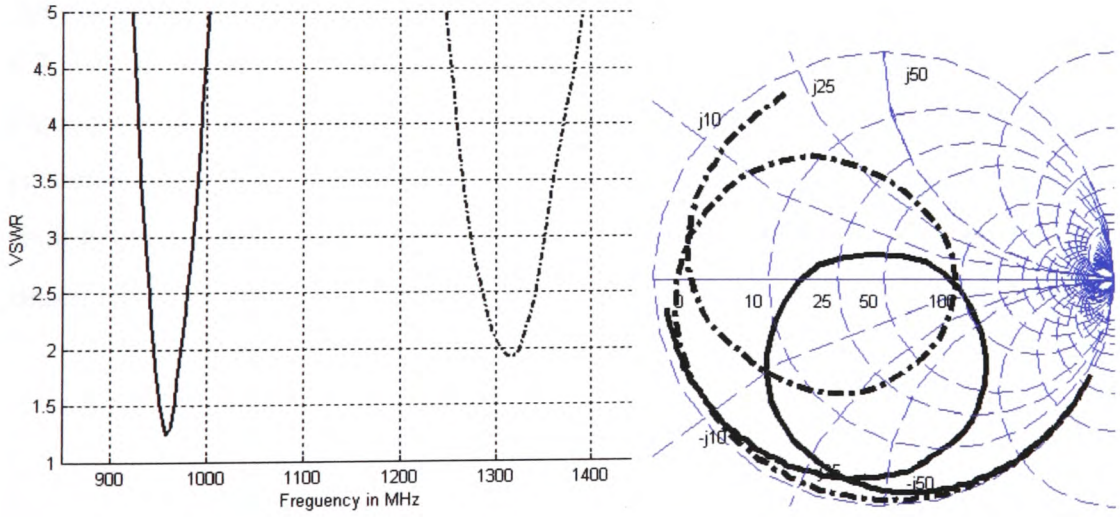

a) b)

Fig. 6.5 *VSWR and Smith chart for two different short pin positions:* ——— *0g* - - - - *9g.*

6.3 Capacitance tuned PIFA.

The travelling short pin can be replaced by a capacitor. By varying the capacitance of the pin, the input reactance of the antenna changes and, as a result, f_r changes. This is depicted in Fig. 6.7. The antenna dimensions are the same as those used in Section 6.2. The effect of the capacitance values was measured at the four reference points 1,2,3, and 4 of Fig. 6.6. The capacitors used in these measurements were miniature, multi-layer, ceramic capacitors with a tolerance of ±5% mounted on a small PCB and soldered on one side of the PIFA and to the conductive case on the other side.

Fig. 6.7, shows the f_r for capacitance values ranging from 3pF to 100pF. For low capacitance values f_r has relatively high values. As the capacitance increases, f_r decreases, but the rate of change of f_r with capacitance is reduced. For capacitance values higher than 30pF, f_r is almost constant. By using this method, the effective bandwidth that can be achieved, when the capacitor has a fixed position, is about 175 MHz. It became evident that f_r depended on the position of the capacitors. The further the capacitor from the feed, the higher the frequency bands covered.

Fig. 6.8 shows the VSWR vs Frequency and Smith chart curves for capacitor values of 3, 10 and 100pF at the reference point 2. The area of the circle formed around the frequencies of interest increases with capacitance. It can be also seen that the reactance of the PIFA is less inductive as the shorting pin capacitance increases. The result is that at lower frequencies the impedance of the antenna is closer to 50Ω and consequently the resonance frequency reduces as the short pin capacitance increases.

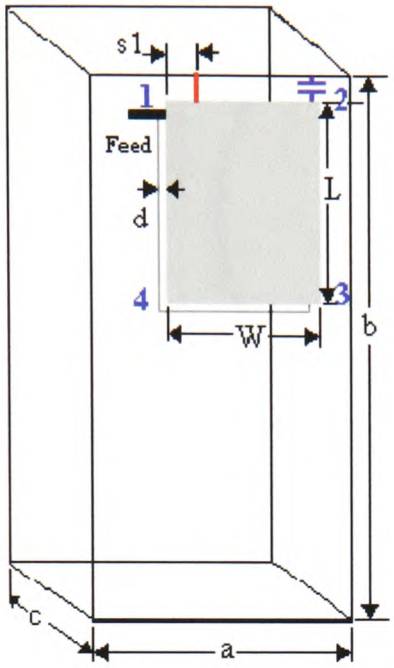

Fig. 6.6 *PIFA configuration for shorting pin capacitance tuning.*

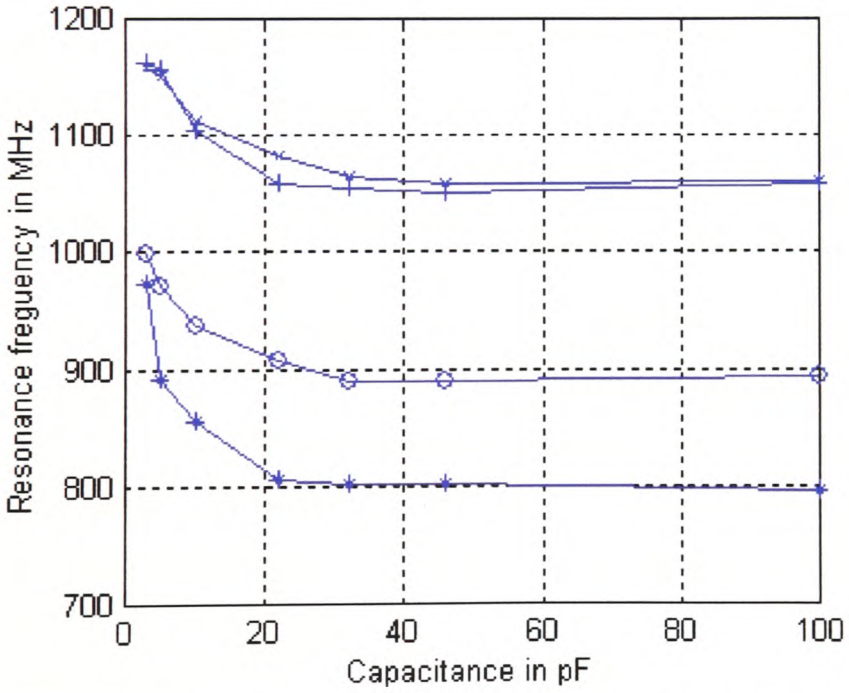

Fig. 6.7 *Resonance frequency vs pin capacitance placed at four reference points:*

** Reference point 1, o Reference point 2, x Reference point 3, + Reference point 4.*

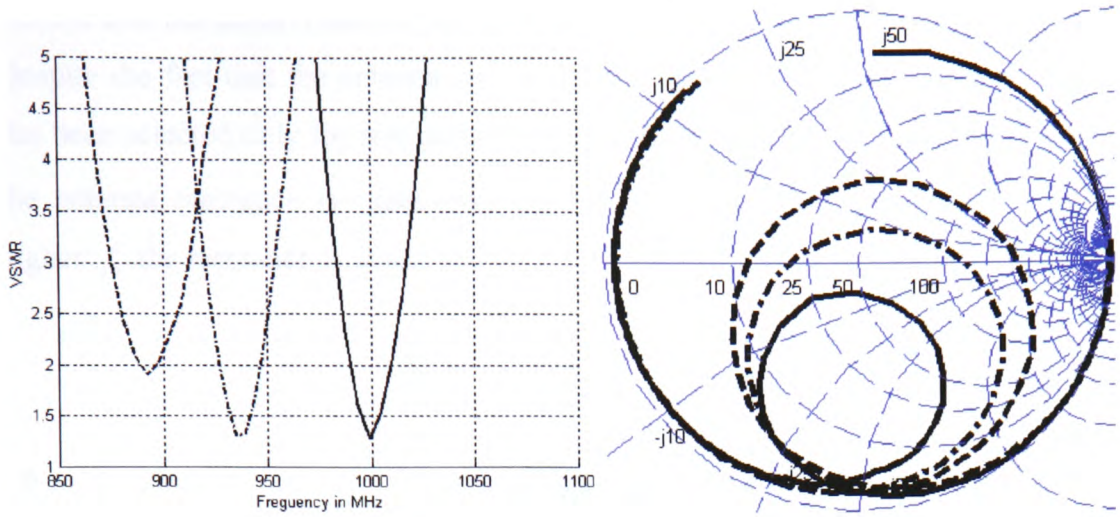

a) b)

Fig. 6.8 *VSWR and Smith chart for three capacitors values at position 2:* ——— *3pF* –·–·– *10pF* ------ *100pF*

6.4 Dual-band fine-tuned PIFA.

Using the information and knowledge gained from the measurements in Sec. 6.3, regarding the position and capacitance value of the pins, a prototype dual-band (GSM900/DCS1800) PIFA was designed. The dimensions of the antenna patch can be reduced by 33% (L=40 mm and W = 35 mm), since the frequency band covered in this case is directly related to the position and the capacitance of the pins used. The position of the fixed short pin for this antenna is again 5 mm from reference corner 1 and the height of the antenna from the conductive case is 5 mm. Two variable capacitors (1.8 – 12.5 pF) have been used. The first capacitor (c1 = 25 mm from corner 1 in Fig. 6.9) is referred to as the *calibration capacitor*, because its value is set only once during calibration of the antenna at the specific frequency band. For the particular antenna dimensions considered here, its value was measured to be approximately 7.3 pF. A second capacitor, referred to as the *tuning capacitor* (c2 in Fig. 6.9), is used to tune the antenna at any frequency channel within the two bands.

In Fig. 6.10, the VSWR and the normalised bore-sight gain of the dual-band fine tuned PIFA are shown for three tuning capacitor values. Both GSM900 (890-960MHz) and DCS1800 (1710-1880MHz) bands can be accommodated in this antenna model just by changing the tuning capacitor value from 1.8 pF to 3.0 pF. The

VSWR and the Smith chart of the antenna tuned at 890 MHz is given in Fig. 6.11. Despite the fact that the antenna has dual resonance frequency, the capacitor value has been selected only for resonance at 890 MHz. For frequencies near the lower f_r the antenna reactance is capacitive. On the other hand, for frequencies near the higher f_r the reactance is inductive.

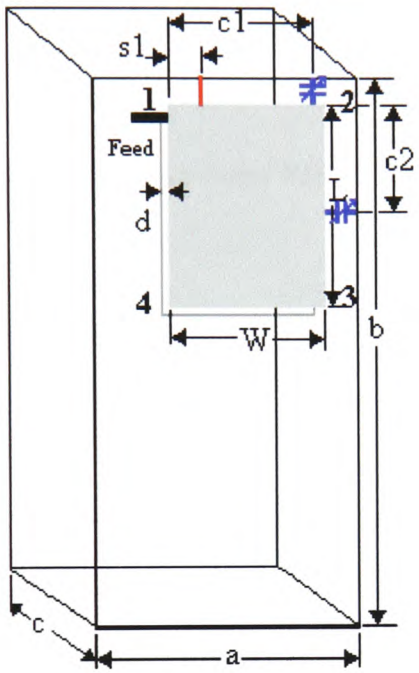

Fig. 6.9 *PIFA configuration for Dual-Band (GSM900/PCN1800) tuning.*

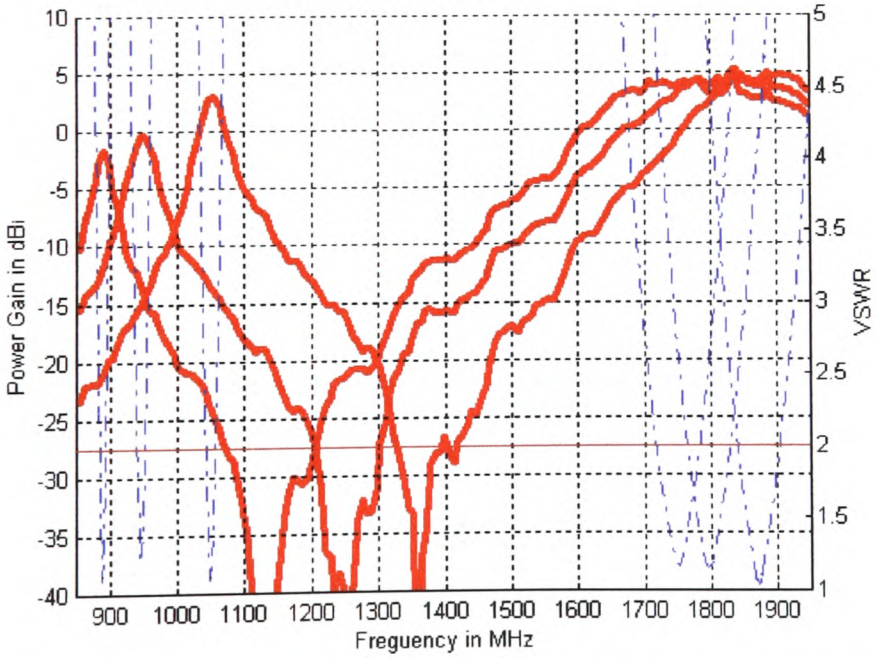

Fig. 6.10 *Bore-sight gain (dBi) and VSWR vs. frequency for the dual-band fine-tuned PIFA for three tuning capacitor values.*

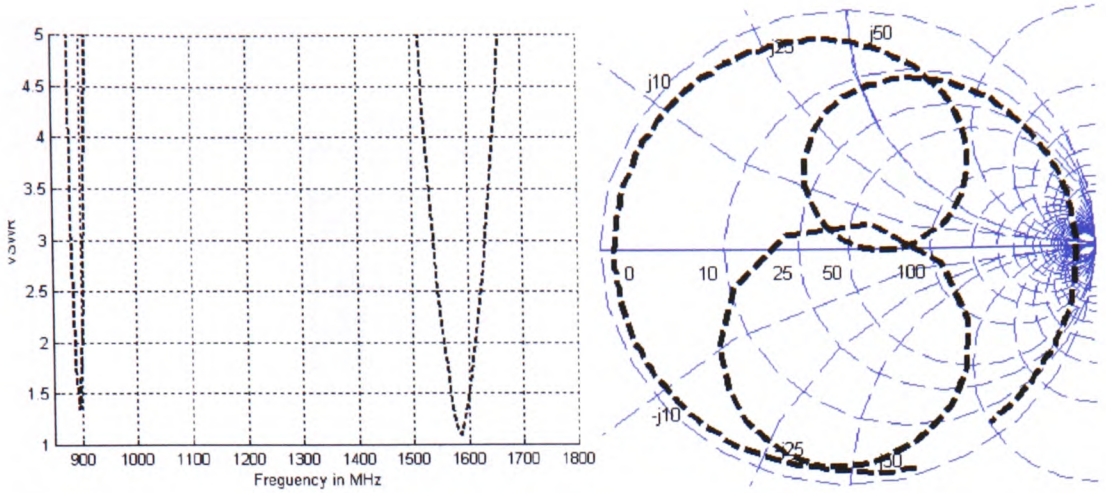

Fig. 6.11 *VSWR and Smith chart of the dual-band PIFA.*

6.5 Voltage controlled fine-tuned PIFA.

Utilising the measured data in Sec. 6.4, a voltage controlled fine tuned PIFA for the GSM900 band was designed. The antenna geometry is illustrated in Fig. 6.12. A top patch has been introduced to provide the electric isolation between the varactor and voltage-source system and the antenna, since the PIFA is connected to the ground via the short pin. It is noted that the patch can be replaced by a low value capacitor. An inductor is used to de-couple the RF signal from the voltage supply. The capacitance value of this varactor starts from approximately 37pF when the reverse voltage is 0 Volts and goes down to 3pF when the reverse bias voltage is 30 Volts.

VSWR measurements from this test antenna are presented in Fig. 6.13. It is evident that the effective bandwidth is much wider than that required by the GSM900 system. The maximum reverse voltage to satisfy the GSM900 band requirements is 15 Volts for VSWR < 2:1. It is also observed that for low reverse bias voltage values the variation of the resonance frequency is relatively small.

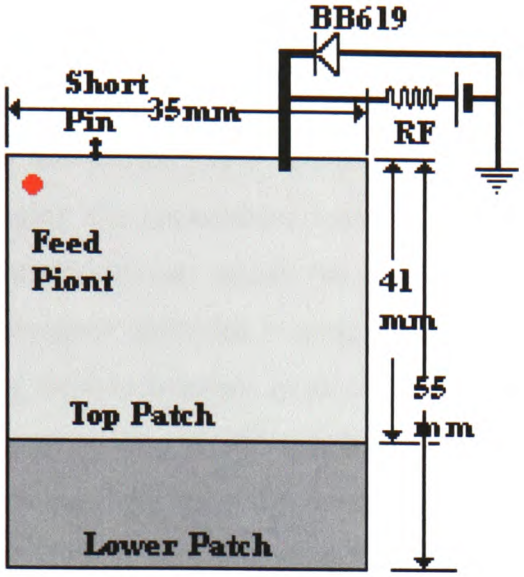

Fig. 6.12 *The varactor controlled PIFA design.*

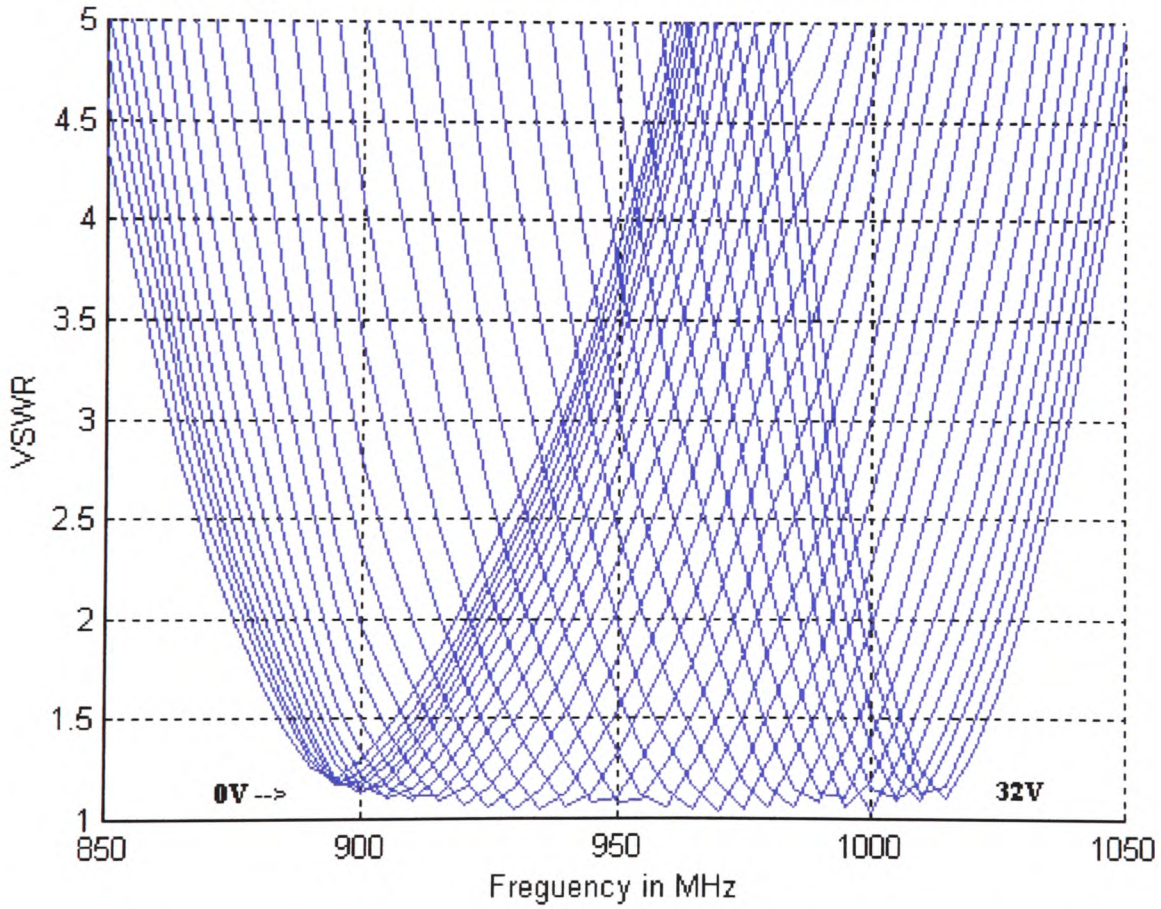

Fig. 6.13 *VSWR vs. frequency for the PIFA, of Fig. 6.12, for reverse voltage 0 to 32 Volts.*

6.6 Interim conclusions.

From the studies discussed in Secs. 6.1-6.5, it is concluded that the inherently narrow bandwidth problem of a low-profile PIFA can be effectively addressed by varying the position or by changing the capacitance value of the pins. By applying these methods, the effective bandwidth can satisfy the requirements of the mobile phone frequency bands. The frequency shift, due to coupling with the operator, can be also compensated by applying these techniques. In an electronically tuned PIFA, the short pins can be replaced by transistors or PIN diodes, and the tuneable capacitors by varactor diodes. Based on the experimental results highlighted above, a prototype of an electronically fine-tuned PIFA was built to demonstrate the practical applicability and implications of these novel tuning techniques. It may be argued that using non-linear circuit elements such as the varactor diodes in the antenna can lead to harmonics and intermodulation products. Some measurements were made covering the bandwidth of the GSM signals. Results from these measurements indicated that levels of such spurious components were insignificant.

For a commercial version of an electronically fine-tuned PIFA a feedback circuit is required which will automate the tuning procedure. This circuit can operate based on antenna reflection measurements or by implementing a look-up table. These methods are discussed further in Chapter 8.

In Chapter 7, the efficiency of the PIFA and the other wire antennas when operating next to the operator's head, as well as SAR related issues are discussed.

7. SAR, RADIATION EFFICIENCY, AND 3dB SAR VOLUME FOR HANDSET ANTENNAS

The popularity of voice mobile communications has rapidly grown since the mid 90's and after the introduction of the digital mobile communications like the GSM system. The GSM system has provided enhanced capacity and a range of services, as well as good quality of communications.

Even though the averaged power radiated by a standard hand-held device is limited to a maximum value of 250 mW, concerns about potential health risks related to the use of mobile phones have been highlighted by the public and the news media. However, there have been no clear evidences so far of any health hazards related to the extensive use of mobile phones. In order to minimise potential health risks due to the uncontrolled exposure to radiation, regulatory bodies have proposed safety standards for the level of exposure. The Specific Absorption Rate or SAR is such a parameter, which is specified in the safety regulations and constrains the maximum averaged power allowed to be absorbed per tissue mass in Watts per Kilogram (W/Kg). It is generally believed that the power absorbed is dissipated in the form of heat with not necessarily a chemical or atomic reaction in the human cells caused by this form of radiation. It is not clear from research that DNA deformation or chemical alteration of the cell molecules can result from exposure to radiation at the utilised frequencies. However, it is important to limit the exposure in order to satisfy the proposed standards by appropriate design of the antennas and handsets.

Significant work has been done on determining the exposure rates by mobile devices and for different types of antennas. Some of the most important papers published on this subject have been summarised in Chapter 3. It is evident from work done by other researchers that the type and size of the antenna used, as well as the size of the handset are important factors that not only affect the performance of the mobile phone but also the peak mass-averaged SAR values. These can determine the level of exposure to radiation energy.

In this chapter, studies on evaluating mass-averaged SAR values are reported. The FDTD method is exclusively used for determining the SAR for a range of frequencies and for different antenna types. The results are compared for three different handset dimensions in order to relate the handset size to the peak SAR values. Antenna efficiency when operating in the presence of the operator for different configurations is also presented, including simulations with the handset inclined by 30° from its original vertical position. A newly proposed concept, the 3dB SAR volume, is introduced. Finally, work on reduced size head models representing 5- and 10-years-old child users concludes the chapter.

7.1 Specifications for numerical simulations.

A number of simulations using FDTD have been conducted in order to get a better understanding of the effect antennas operating next to the operator's head have on peak mass-averaged SAR values. Regulatory bodies have assigned standard values of SAR as limits aimed at preventing excessive exposure to radiation energy by mobile phone users. In the United States and North America the maximum exposure is set at 1.6 W/kg averaged over 1g of tissue mass. In Europe this limit is 2.0 W/kg averaged over 10g of tissue mass. In the United Kingdom this limit is considerably higher and is set at 10 W/kg for data averaged over 10g of tissue.

Table 7.1 gives the basic restrictions of human exposure to electromagnetic fields (EMF) from Mobile Communication Equipment (MTE) in the frequency range 30 MHz - 6 GHz that are proposed by the European committee for electrotechnical standardisation (CELENEC) [7.1]. It is noted that the shape of the averaged mass, referred to in this table, shall be chosen as a cube of 10g-weight. In [7.1] it is stated that "the biological effects which result from such (EMF radiation) temperature increases are rather well understood and are commonly referred to as thermal effects."

	SAR averaged over any 6-min. time interval and over the hole body	**SAR averaged over any 6-min. time interval and any 10g tissue other than hands, wrists, feet, ankles**	**SAR averaged over any 6-min. time interval and any 10g tissue in the hands, wrists feet, ankles**
General Population	0.08 W/Kg	2 W/Kg	4 W/Kg
Workers	0.4 W/Kg	10W/Kg	20 W/Kg

Table 7.1 *Basic restrictions for human exposure to EMF's from mobile communication equipment in the frequency range 30 MHz - 6 GMHz [7.1].*

The modelling of the human body according to [7.1] must satisfy the following requirements:

- The SAR values assessed must never be less than the actual maximum SAR value that can be included among all users under the operational conditions.
- Parallel shift in the direction of the MTE with respect to the surface of the body shall not result in any significant increase of the SAR values assessed for a range of 1cm around the operational conditions.
- Left-hand and right-hand use of the MTE shall be appropriately simulated.
- Tests shall be conducted without simulating the hand.

CELENEC comments that the human hand is an anatomically and geometrically complex structure, which can cover an MTE in almost an infinite number of configurations. Certain ways of holding the device with the hand significantly lower the induced SAR values while others not at all. Significant increases have never been observed and consequently, non-modelling of the hand represents the worst-case scenario of those involved in holding the device.

An assessment of the errors in numerical simulations is also given in [7.1]:

- Uncertainties of each solution by appropriate selection of numerical validation tools.
- Uncertainties due to neglect of any details of the device that can not be simulated due to limitations of the software package used or because some constructional

details are not available (e.g., internal structures, the material parameters of the structure, etc.)

- Uncertainty of the chosen head phantom with respect to the phantom requirements.
- Uncertainty due to the unknown effects on the output circuit from the proximity of the phantom to the MTE.

The software used must satisfy the following requirements.

- Ability to model a phantom.
- Accurate electromagnetic modelling of the MTE in all the operational positions and conditions.
- Accurate simulation of the near-field coupling between the head and device.
- Capability of assessing the solution and modelling of uncertainties as defined above.

In the U.K. restrictions on human exposure to time varying electromagnetic fields and radiation are determined by the National Radiological Protection Board (NRPB) and reported in [7.2]. Some important points are given below:

- There is no clear evidence of adverse health effects at the EMF levels to which people are normally exposed. In particular, the epidemiological data do not provide a reliable basis for restricting human exposure to electromagnetic field and radiation.
- As the frequency increases, the depth of penetration in the body decreases and the deposition of energy becomes more superficial.
- It is estimated that an SAR between 2 and 3 W/Kg would cause a rise of approximately 1° C within 1 hour in a lightly clothed person seated in a comfortable environment.
- The FDTD method is inherently suitable for calculating the interaction of EMF's with complex 3D lossy dielectric bodies.
- To avoid excessive localised temperature, the SAR should not exceed 10 W/kg in any 10g of the head and embryo, and in any 100g of any other part of the body excluding the extremities.

The Federal Communication Commission (FCC) in the United States has similar regulations, which are summarised in [7.3]. Among others it is stated: "the use of appropriate numerical and computational techniques, such as FDTD analysis, may be accepted for demonstrating compliance with SAR values. Studies have indicated that such techniques can be used to determine energy absorption characteristics in exposed subjects. However, in order for numerical techniques to be valid the basic computational algorithm and modelling of the portable device should be validated and appropriate models of the human body should be used which will provide reasonable accurate estimates of the SAR. Accurate models of the human body exist at the present time, but developing models of devices may be more problematic. In general, numerical device and antenna models should represent the actual device under test and should be confirmed accordingly, e.g. with appropriate techniques, analytical data, published data or far-field radiation patterns." In our case the far-field radiation patterns of the antennas in the presence of the operator have been measured and predicted and the comparison of the results has given reasonable good agreement to encourage further work on SAR evaluation using only the FDTD.

For the simulations in this research, an anatomically based head/shoulders numerical model, which is based on data from the "visible human" project [7.4], has been used. The mesh consists of 3 mm cubical cells, which results in 153×118×120 or 2,166,480 cells. From those cells, only 255,333 form part of the head/shoulder geometry (Fig. 7.1). The remaining cells are allocated as free space. To reduce reflection at the simulated geometry space boundaries, a minimum of 15 free space cells should separate the head/shoulders model from geometry's boundaries. Five tissue types plus a separate skin layer are used in this head/shoulders model. The dielectric properties of each tissue type used are given in Table 7.2. These values are taken as constants over the frequency range used. This is due to a lack of precise information on dielectric properties of the materials for each frequency used, as well as the uncertainty of dielectric values assigned to tissues reported in different publications [3.11]. The dielectric properties used in the particular model comply with the FCC values given for the specific tissues at frequency range of GSM900 and DCS1800.

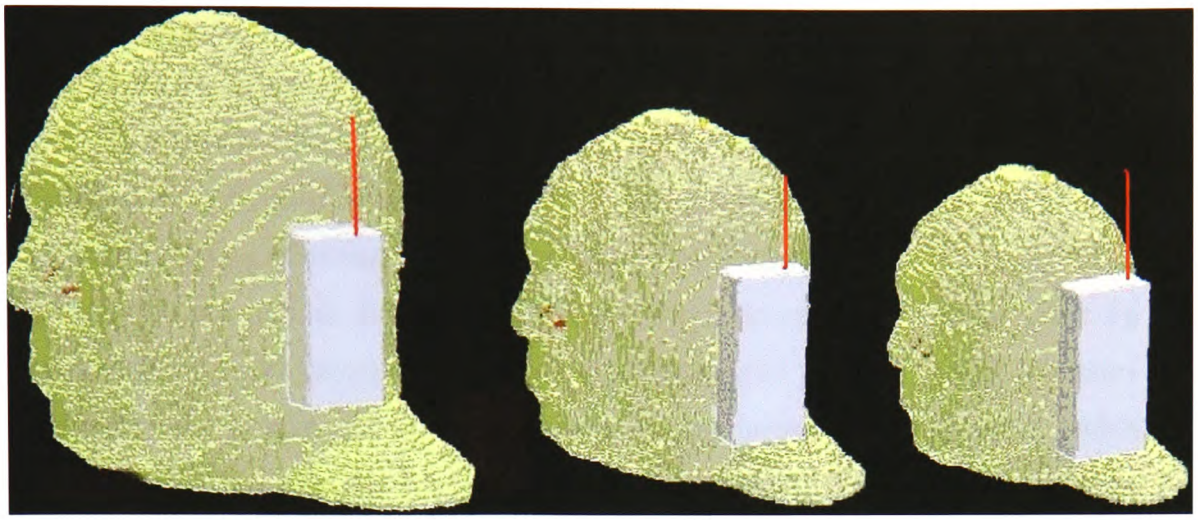

a) b) c)

Fig. 7.1 *Numerical head models for: a) adult, b) 10-year-old child, and c) 5-year-old child.*

Tissue Type	**Conductivity (σ)** ʊ/m	**Relative Permittivity (ε_r)**	**Density (ρ)** kg/m^3
Bones Joints Tissue	0.782000	42.650002	1000
Head muscle	0.969000	55.950001	1040
Eye Tissue	1.167000	55.270000	1000
Brain Tissue	0.766600	45.799999	1030
Skin Tissue	0.867000	41.400002	1000
Bone (Skull) Tissue	0.242000	17.620001	1850

Table 7.2 *Dielectric properties of tissues used in the numerical head model.*

7.2 SAR prediction for adult users.

It has been reported in [3.11] and [3.16] that reducing the size of the handset results in the increase of the localised mass-averaged peak SAR. This is, in general, due to the reduced physical distance separation of the radiating element and the radio case edges from the operator's head. The areas of high near-field intensity in the vicinity of a handset are shown in Figs. 5.1-5.12. High electric fields exist around the radiating elements (antennas) and at the edges of the handset. In [3.11, 3.16] it has been also shown that an increase in the monopole antenna size results in lower 1g mass-averaged SAR values. This can be explained again with the aid of the near-field plots and the existence of higher electric field at the top of the monopole, which are physically closer to the head if the size of the handset is smaller. Due to the increased distance of the radiating element from the operator's head and the shielding provided by the handset acting as a reflector, simulations using the PIFA have yielded lower peak SAR values compared to those arising for monopole or helix antennas operating at the same frequencies.

In Figs. 7.2 and 7.3 the peak 1g and 10g mass-averaged SAR values for various operational frequencies and conductive case dimensions, normalised to 1 W antenna input power, are plotted. The SAR for a typical GSM mobile phone may be derived from these figures by dividing the plotted values by four, since the maximum output power of the GSM transceiver is 2 Watts pulsed over 1/8 of the operation time. The three conductive cases that were used to model the handset, are 50mm wide, 25mm thick and their heights were fixed at 100mm, 88mm and 76mm. The vertical centre of the handset has been kept at a constant location during handset height reduction and at a distance of 3 mm (one Yee cell) from the left ear. No plastic coating has been used since a more general approach is studied and since no particular commercial handset model is modelled. For the monopole case, the size of the antenna is $\lambda/4$, where λ is the operational frequency wavelength. For the PIFA, on the other hand, the operating frequency has been obtained by using a Guassian input pulse as described in [3.5]. This was subsequently verified by VSWR measurements of the antenna. Table 7.3 gives the resonance frequency values for each of the patch and handset dimensions used. The size of the patch has been reduced by 3 mm for

each simulation and, for simplicity, only in the vertical direction. Fig. 7.2 shows that the value of the peak 1g mass-averaged SAR varies with frequency and with the conductive case height. In some frequencies the peak SAR is relatively higher compared to other frequencies. It can be also seen from this figure that the original curve (handset height equal to 100 mm) is shifted to the right (higher frequencies). The shift is of the order of 100 MHz, which is about 10% at the 1 GHz band and 5% at the 2 GHz band. The handset height has been reduced by approximately 20% each time. Since the results are valid for both the monopole and the PIFA antennas, it is concluded that reduced SAR values require handset height approximately equal to a quarter or half a wavelength. For these cases, peak 1g-SAR can be reduced by up to 30% compared to those predicted at other frequencies. The size reduction of the conductive case has also resulted in an overall increase of the 1g-SAR. This is due to the reduced physical distance separating the conductive case edges (top and bottom) from the operator's head, where high electric field intensity exists. The 10g mass-averaged peak SAR as a function of the operational frequency is given in Fig. 7.3 where similar conclusions can be drawn. Peak SAR values for the PIFA antenna are lower for both the 1g and 10g mass-averaged SAR values while efficiency is higher (Fig. 7.4). From the same figure, it is also observed that for the monopole antenna, efficiency improves with frequency. For the PIFA, the efficiency is at its minimum when the SAR is high, as expected.

Computations including the operator's hand in the vicinity of the handset were also performed. The head/shoulders-handset-hand configuration is shown in Fig. 7.5. These simulations have shown 1% reduction in radiation efficiency for the monopole and 11.5% for the PIFA at GSM900 frequencies, due to additional power dissipation in the hand tissue. The hand, in this model, has been assumed to consist of bone tissue covered by skin. The thumb and fingers have been simulated in a natural speaking position around the handset. Due to the physical size of the PIFA, the hand, and in particular the thumb, are very close to the radiating element. Because of this, the efficiency has been dramatically reduced and the computed peak SAR is located at the top of the thumb. Design of handsets equipped with a PIFA antenna must, therefore, consider the hand positioning during operation and prevent it from been very close to the antenna. This can be achieved with appropriate handset design. The

complexity and variety of the hand position next to the handset, as mentioned above, make it difficult for detailed results relating the hand effect on SAR and efficiency to be obtained in this study.

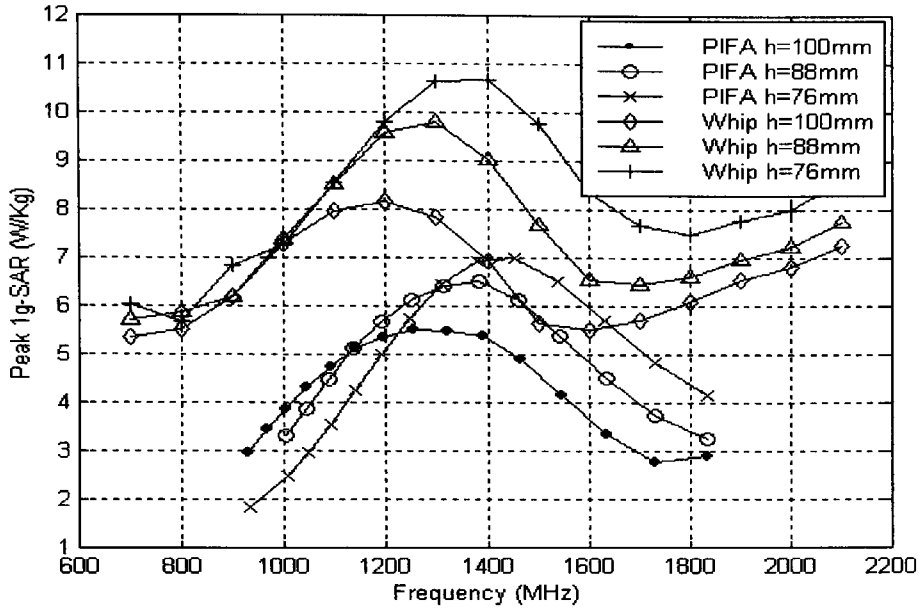

Fig. 7.2 *1g mass-averaged peak SAR for monopole and PIFA antennas.*

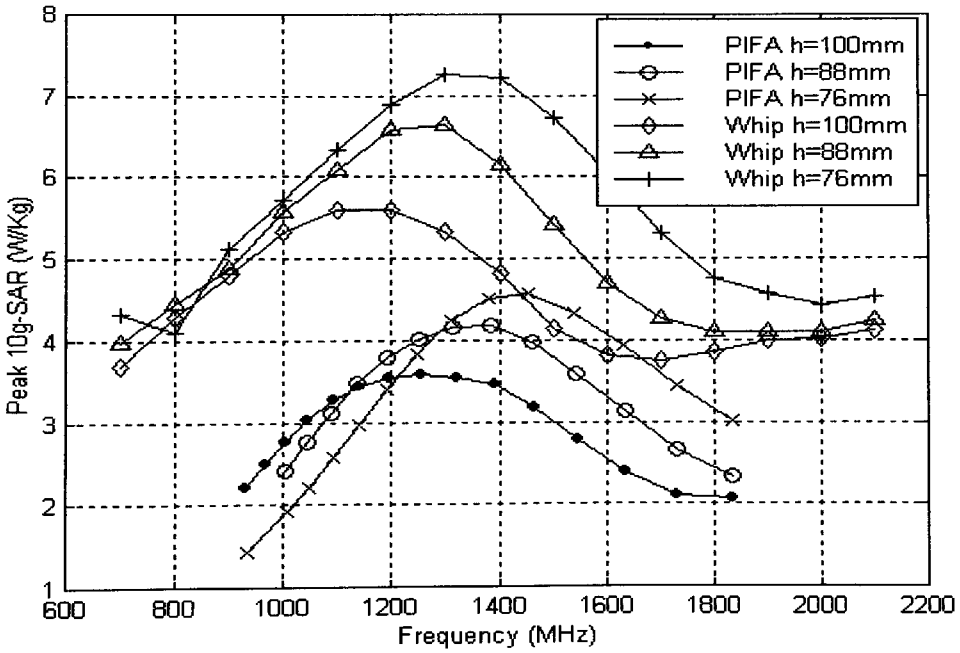

Fig. 7.3 *10g mass-averaged peak SAR for monopole and PIFA antennas.*

PIFA Dimensions (mm)	R_f Height = 100mm (MHz)	R_f Height = 88mm (MHz)	R_f Height = 76mm (MHz)
54×30	928.349	933.640	-
51×30	964.004	-	-
48×30	1002.300	1003.000	1007.300
45×30	1044.557	1043.897	1047.200
42×30	1090.777	1088.796	1139.000
39×30	1141.618	1137.656	1139.000
36×30	1197.421	1191.799	1191.100
33×30	1255.846	1250.564	1249.600
30×30	1319.893	1314.911	1310.649
27×30	1389.222	1385.260	1379.318
24×30	1463.533	1461.200	1454.589
21×30	1545.707	1544.400	1538.444
18×30	1634.845	1634.800	1630.883
15×30	1731.905	1732.600	1729.924
12×30	1837.229	1837.900	1835.569

Table 7.3 *PIFA resonance frequency as a function of patch and handset dimentions.*

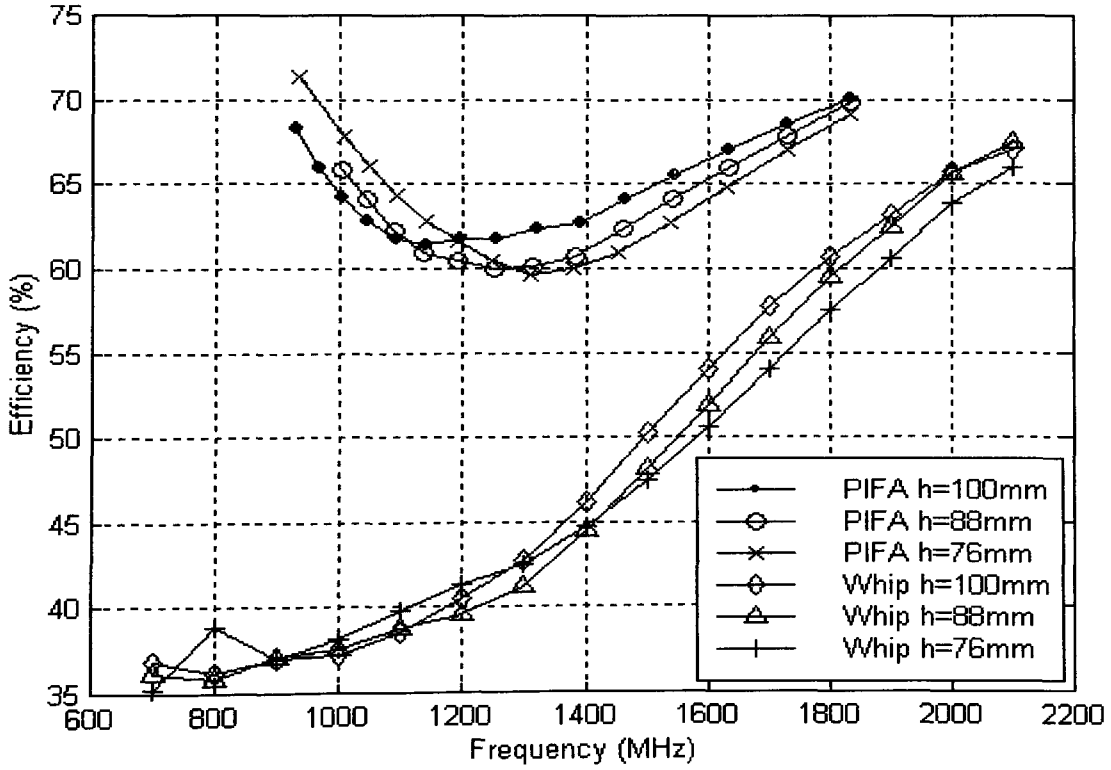

Fig. 7.4 *Radiation efficiency of monopole and PIFA antenna operating next to the operator's head and shoulders.*

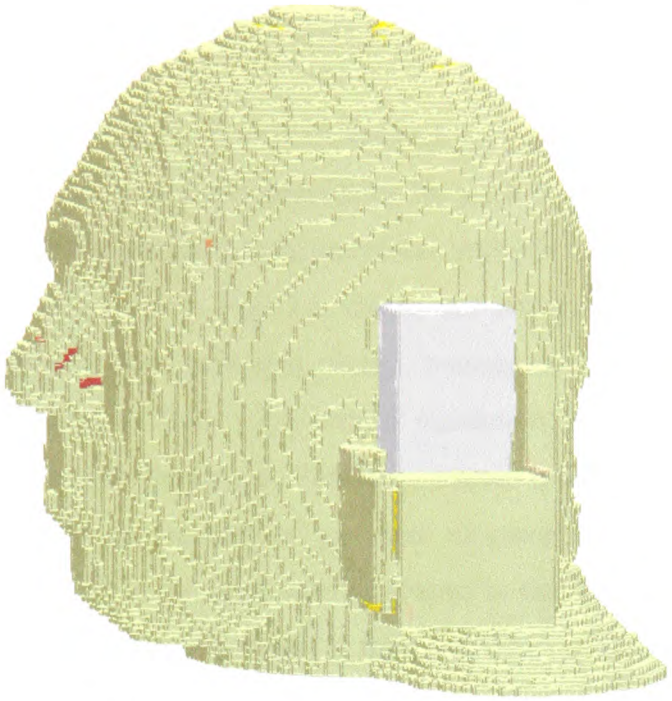

Fig. 7.5 *Head/shoulders-handset-hand configuaration.*

7.3 Antennas radiation efficiency when operating in the presence of the operator.

When a mobile handset antenna operates next to the operator's head its radiation efficiency is degraded. This can be seen in Fig. 7.4 where the radiation efficiency of the two antennas is plotted over the frequency range of interest. In FDTD the efficiency is calculated using eq. 2.66. When the antenna operates in free space the radiation efficiency is 100% since only PEC is used.

The efficiency curves of Fig. 7.4 do not show the same trend as the peak mass-averaged SAR curves of Figs. 7.2 and 7.3. This is more noticeable from the efficiency curves of the quarter-wavelength monopole, which show that efficiency is monotonically increased with frequency. For the SAR case, where the handset height is an even multiple of the operational wavelength, the peak SAR assumes low values. It is concluded that the way the absorbed energy is distributed in the head varies and does not depend entirely on the peak mass-averaged SAR values. This means that the head volume exposed to high SAR varies with frequency. The following sections provide additional insight into the distribution of the absorbed energy. This is achieved by the introduction of a new concept referred to as the "*3dB SAR volume.*"

7.4 The 3dB SAR volume concept.

Before introducing the 3dB SAR volume concept a simple approach to the problem is needed. Locating and graphically presenting the peak SAR value position in a 3D-head model is rather complicated. It is therefore desirable to introduce a 2D method of displaying this information. Fig. 7.6 shows the distribution of maximum SAR values observed in the three principal planes, namely the xy-, yz-, and xz-planes. Curve 1, for instance, in Fig. 7.7.a shows maximum SAR values observed in successive xy-planes with varying z. Similarly, curves 2 and 3 show the maximum SAR values obtained in successive yz- and xz-plane with varying x and y, respectively. Curves 1,2, and 3 have similar shapes in that they start from relatively low value reaching a maximum, which is the peak SAR value in the head volume, and end at a low value. The highest point, which has the same value for each curve, is the peak mass-averaged SAR value over the head. This value corresponds to a single point whose coordinates x, y, and z can be read from the curves 1,2, and 3, respectively, as shown in Fig. 7.6. The whole process leading to Fig. 7.6 can be repeated using the *averaged SAR values per numerical model slice* instead of the maximum values. This leads to the graphs of Fig. 7.7, which show similar curves to those in Fig. 7.6. Similar comments apply for 10g mass-averaged SAR data.

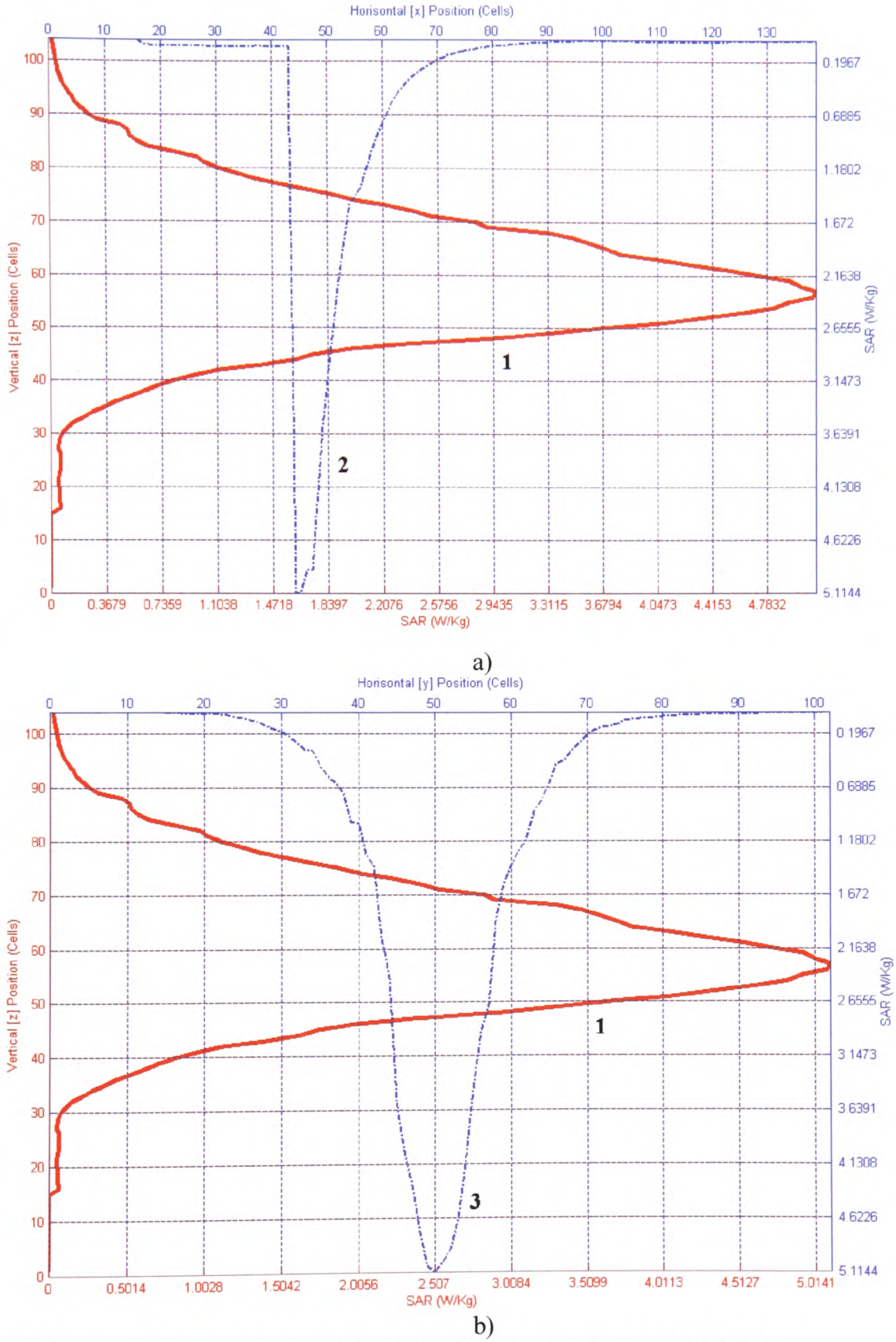

Fig. 7.6 *Maximum 1g-mass-averganed SAR values per plane at 945 MHz.*

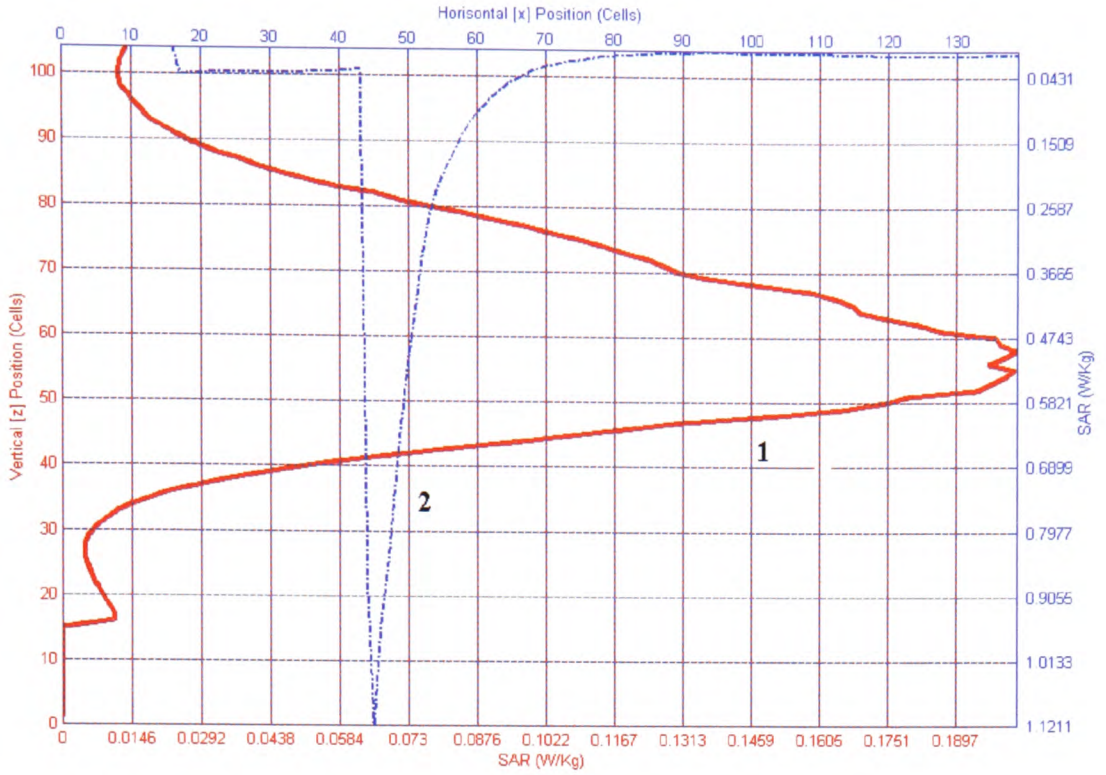

a)

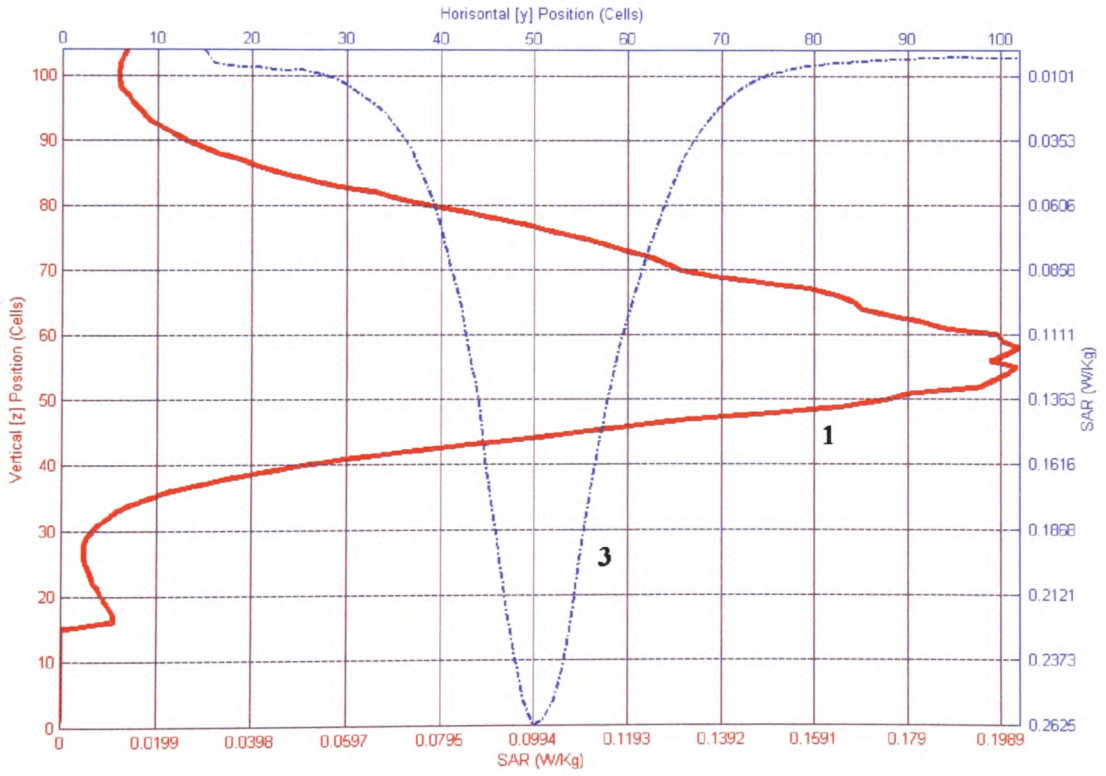

b)

Fig. 7.7 *Averaged 1g-mass-averganed SAR values per plane at 945 MHz.*

Two important remarks can be extracted from Fig. 7.6 and 7.7. First, in general high SAR exists near the ear region (Fig. 7.8) of the operator's head, which is closer to the handset. Some researchers [3.16] insist that the presence of the ear in simulations is superfluous. This is because in operating the handset, the user tends to press the device closer to the head and in the process causes it to be touching the head. Second, high SAR values do not arise in the interior of the skull as shown by the x-axis curves. The skull appears to provide good protection to the brain against EMF radiation. This is an important observation, which is noted to be valid for all the simulations performed as part of this research.

Having discussed the 2D plots, which is useful in locating the peak mass-averaged SAR value, the 3dB volume concept can be introduced. Fig. 7.9 is similar to Fig. 7.6 but data for more than one operational frequency are plotted on the same chart. Fig. 7.9 is useful in providing information on the variability of the peak SAR with frequency as well as in introducing the new measure of the 3dB SAR volume. The 3dB SAR volume concept can be introdused in two ways. The first one yields the *absolute SAR volume* (V_{abs}) that contains the actual number of contiguous and non-contiguous Yee cells where the predicted SAR value is greater than half of the peak SAR value defined above. Alternatively, we can define the *maximum SAR volume* (V_{max}), which is represented by a continuum of head volume containing cells with half or more of the peak SAR. The difference between V_{abs} and V_{max} is further described below. By definition V_{max} is given by:

$$V_{max} = x'y'z' \tag{7.1}$$

where x', y', and z' are distances along the x-, y- and z-axes, respectively, in which SAR values are within 3dB of the maximum. Computations of V_{max} and the x' and z' distances are illustrated in Fig. 7.9 that shows maximum SAR graphs at three different frequencies plotted against the vertical z-axis (L.H.S.) and similarly SAR graphs vs. the x coordinate. Taking one of these graphs, e.g. the SAR against z for the quarter-wavelength monopole, it is possible to determine z' by identifying the range of values of z over which the SAR lies within 3dB of its maximum value. This

is shown in the inset portion of Fig. 7.9. Similarly x' can be found by identifying the relevant range of x and the process is repeated once more to find y', thus yielding V_{max} for the antenna under investigation [Appendix C]. The maximum 3dB SAR volume is more informative than the absolute 3dB volume, because the latter is significantly influenced by the mobile phone position relative to the head during use.

Even though the method described above is the actual method used to calculate the 3dB volume from FDTD mass-averaged SAR data, Fig. 7.10 can be also used for better understanding of the concept. If in a single horizontal plane (slide) of the numerical head/shoulders model the cells having mass-averaged SAR values greater than half of the peak SAR in the entire head are marked with "X", then, the sum of these cells in the entire head multiplied by the volume of a single cell gives the absolute 3dB SAR volume. If instead of taking the individual cells we take the rectangular area that encompasses cells that satisfy the above criterion, and add all such areas in the slides forming the numerical model, we arrive at an estimate of the maximum 3dB SAR volume.

In Fig. 7.11, the maximum 3dB SAR volume as a percentage of the exposed subject (head and shoulders) is plotted. These data sets are obtained from the same simulations as in Fig. 7.2. At frequencies resulting in high peak SAR the 3dB SAR volume is actually reduced. On the other hand, high V_{max} has been computed for frequencies resulting in low peak SAR. This is true for both the monopole and the PIFA. Similarly, results for V_{abs} are shown in Fig. 7.12, where values are approximately 30% lower than V_{max}. Hence, when the operator is exposed to high peak SAR the absorbed energy is concentrated in a smaller volume. In contrast, when the peak SAR is low the volume exposed to relatively higher SAR values is increased, provided the same antenna is used.

The importance of the 3dB volume lies in the fact that it is a measure independent of the peak SAR value and, as a consequence, independent of the radiated power. The 3dB volume gives how much of the head is exposed to high radiation and depends only on the geometrical configuration, the antenna type, and the frequency of operation. It also relates the SAR values computed to the radiation efficiency of the

antenna. If, for instance, the absorbed energy is high (low efficiency) and the SAR is low the 3dB volume will be high. On the other hand, when we have high efficiency and high SAR then the 3dB volume will be low. The specification of maximum mass-averaged SAR can be of limited value, since peak values relate only to a single cell in the head model. This Yee cell has very small volume (even after mass averaging) and in real life, since the handset is not placed at the same identical position next to the head every time the handset is used, is not all that meaningful. It is recommended, then, that the peak SAR values are accompanied by the 3dB SAR volume when specifying absorption levels in order to give a clearer and more meaningful picture of the exposure to radiation. The importance of referring to the 3dB SAR will be further highlighted in the next sections, where simulations with smaller head models corresponding to child users, are presented.

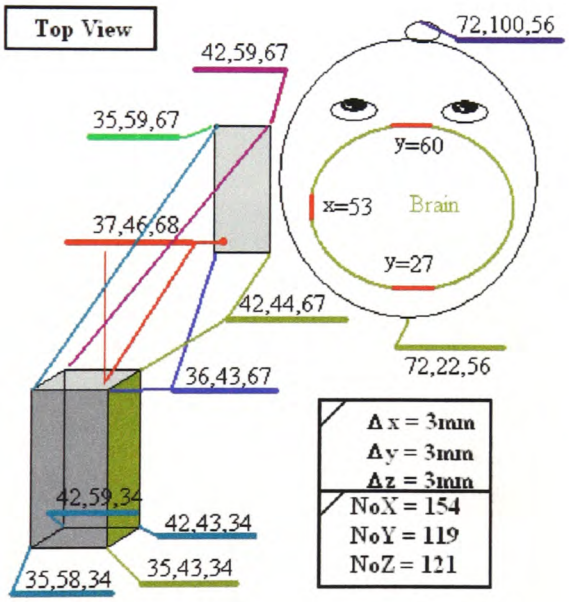

Fig. 7.8 *Numeical model diagram with dimensions (monopole antenna).*

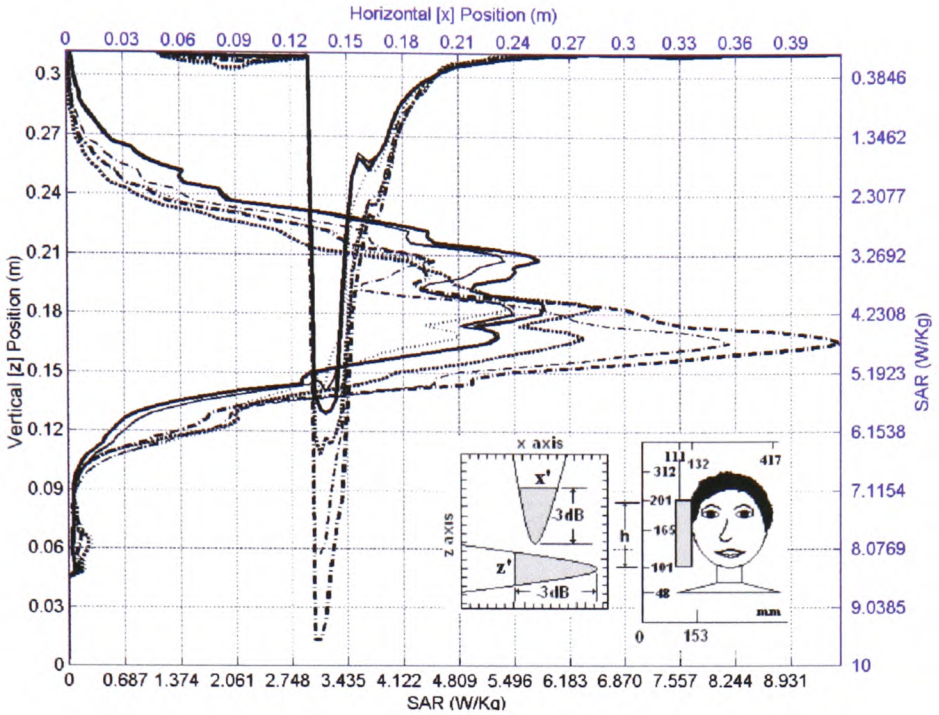

Fig. 7.9 *The distribution of peak SAR along the x- and z-axes for a quarter-wavelength monopole antenna:* —— *800Mhz* ----- *1200MHz* ····· *1600MHz. Thin line: h = 100mm, thick line: h = 88mm.*

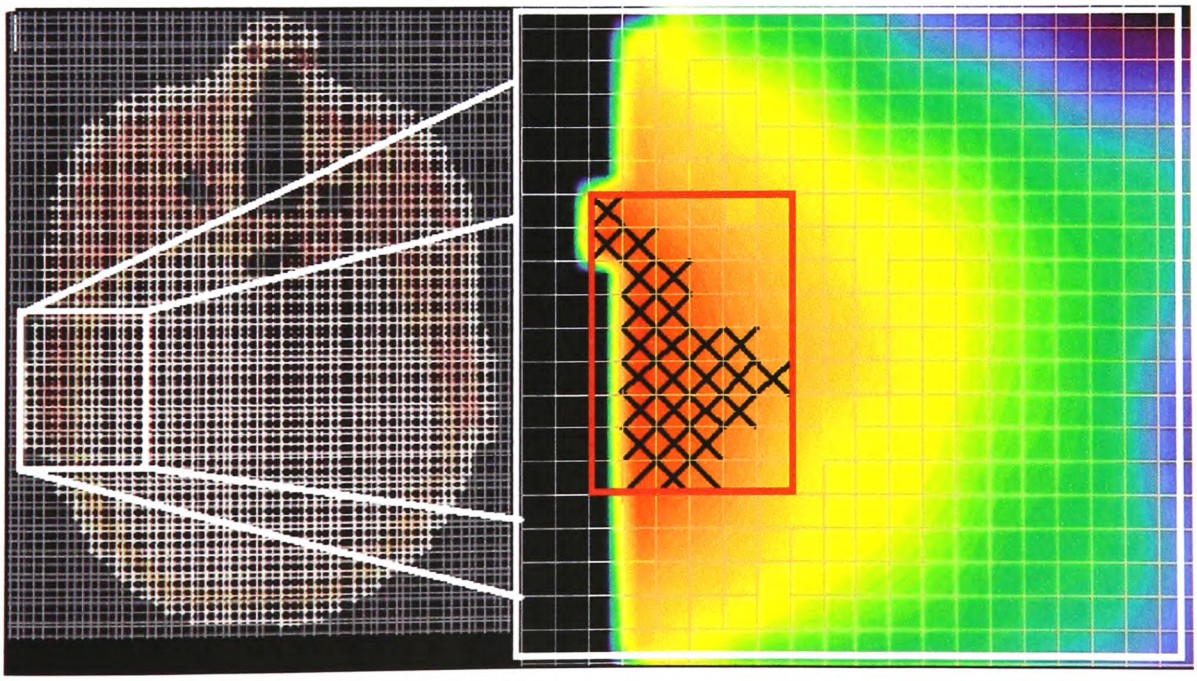

Fig. 7.10 *Single plane V_{abs} points and V_{max} area.*

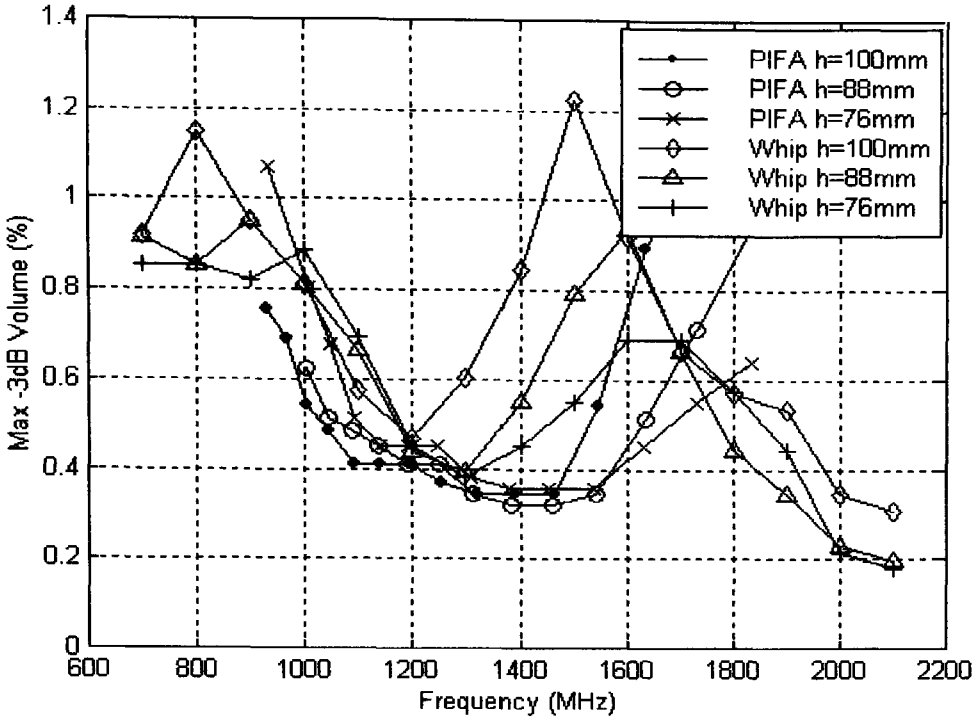

Fig. 7.11 *Percentage maximum 3dB volume V_{max} vs. frequency.*

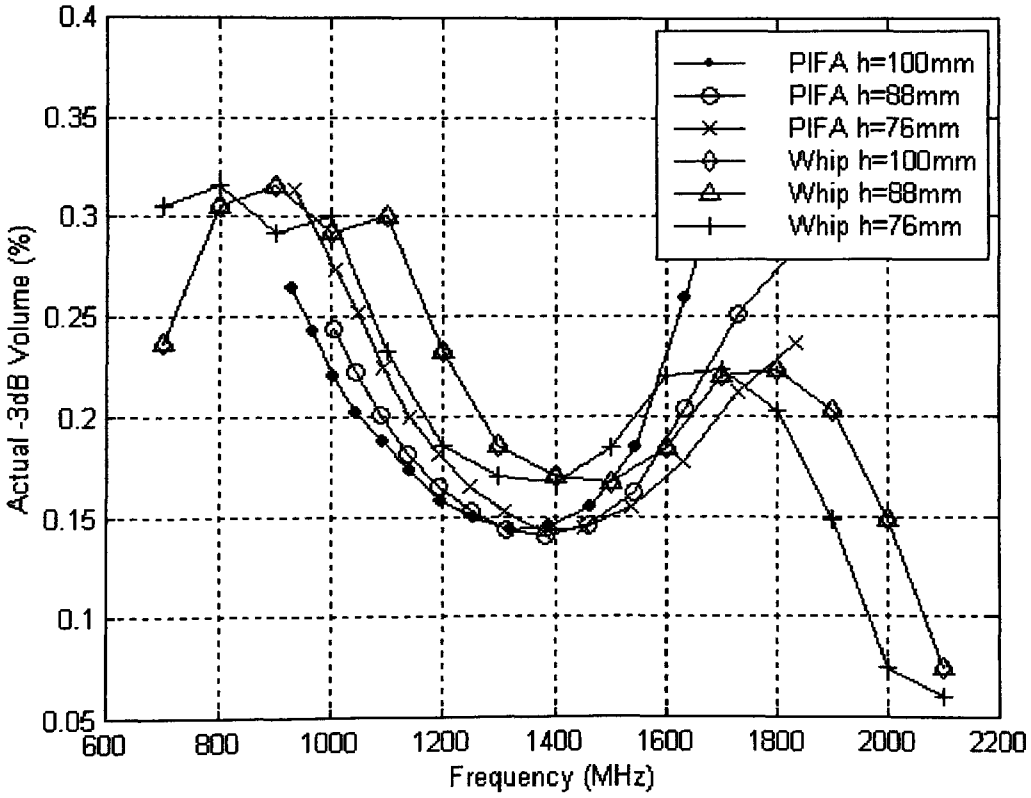

Fig. 7.12 *Percentage maximum 3dB volume V_{abs} vs. frequency.*

7.5 SAR prediction for adults and 3dB volume for handset at 30° inclination.

Simulations similar to those described in Sec. 7.2-7.4 have been carried out with the handset at 30° inclination with respect to the vertical next to the operator's head. This orientation represents a more natural-speaking position of the handset next to the head. The head/shoulders model and the new orientation of the handset are shown in Fig. 7.13. To achieve this new orientation the head, instead of the handset, has been rotated accordingly due to the Cartesian mesh of FDTD, which makes rotation of the handset box cumbersome. In order to maintain the distance from the model's boundaries, due to the head/shoulders rotation, the size of the geometry was increased. This, however, does not affect the results but only the processing time.

In order to make comparisons with the results presented in Sections 7.2-7.4 the axes scale used in Figs. 7.14 – 7.18 are the same as the axes scale of Figs. 7.2-7.4, 7.11 and 7.12. Comparing the mass-averaged SAR plots, it is evident that the shape of the curves is similar with low SAR values where the wavelength is equal to 2×h or 4×h where h is the height of the handset. The overall increase in the peak SAR curves due to the handset height reduction is less for this case. This is true for both the 1g and 10g mass-averaged SAR curves. The new computations have shown that for the h = 100mm case, the reduction in SAR between vertical and tilted handset positions is insignificant. On the other hand, when h = 76mm the reduction in the SAR between the two configurations can be as high as 3 W/kg. From this observation it can be concluded that small handsets will not significantly contribute to higher SAR, if the handset is used at an angle next to the head, compared to case in which the handset is used upright.

A small increase in the efficiency due to handset inclination is shown in Fig. 7.16. The curves have the same shape as those in Fig. 7.4. A very small increase of the order of 0.2% is shown in Figs. 7.17 and 7.18 for the maximum and absolute 3dB volumes that also have the same shape as those in Figs. 7.11 and 7.12, respectively. Reduced 3dB SAR volume values, as reported before, occur at frequencies where higher peak SAR values are also encountered.

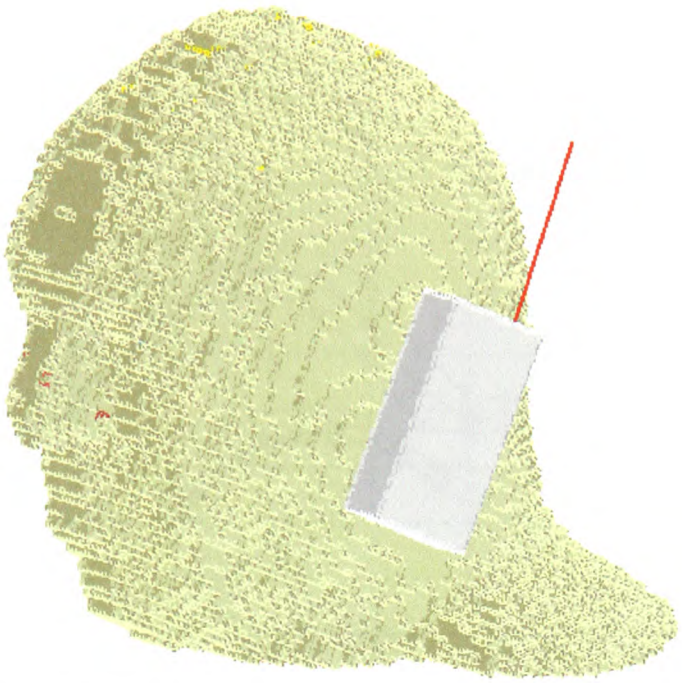

Fig. 7.13 *Numerical model of the head and handset at 30° inclination with respect to the vertical.*

PIFA dimensions (mm)	R_f (height = 100mm) (MHz)	R_f (height = 88mm) (MHz)
48×30	1003.6	1003.0
45×30	1045.9	1045.2
42×30	1092.1	1090.8
39×30	1142.9	1141.0
36×30	1197.7	1195.8
33×30	1257.2	1255.8
30×30	1321.9	1319.9
27×30	1391.9	1390.5
24×30	1467.8	1467.1
21×30	1550.3	1549.7
18×30	1640.1	1640.1
15×30	1735.9	1737.5

Table 7.4 *PIFA resonance frequency as a function of the patch and handset dimensions. The handset is inclined by 30° with respect to vertical.*

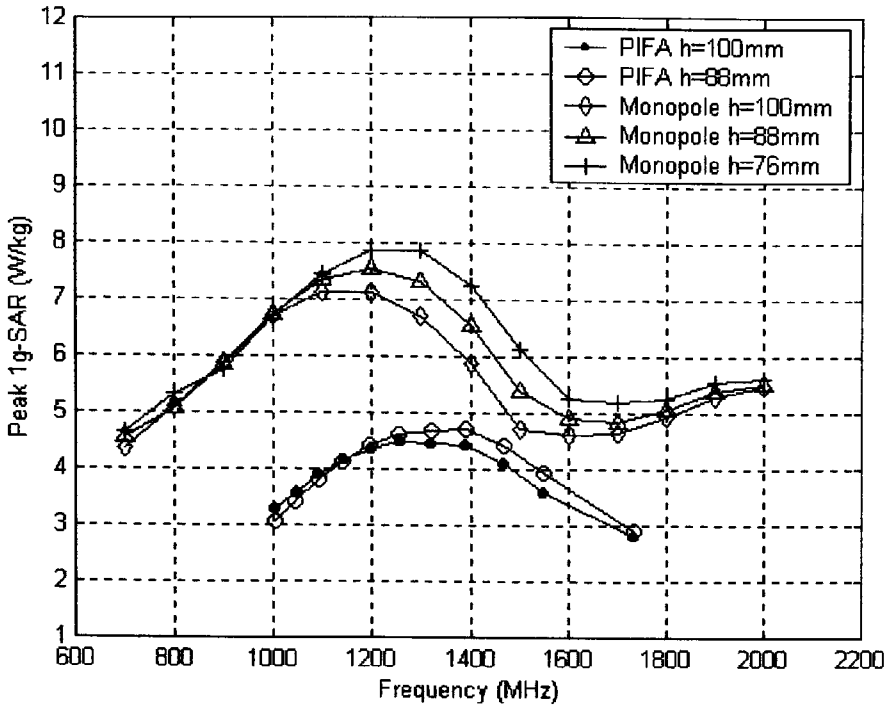

Fig. 7.14 *1-g peak SAR for the quarter-wavelength monopole and PIFA antennas.*

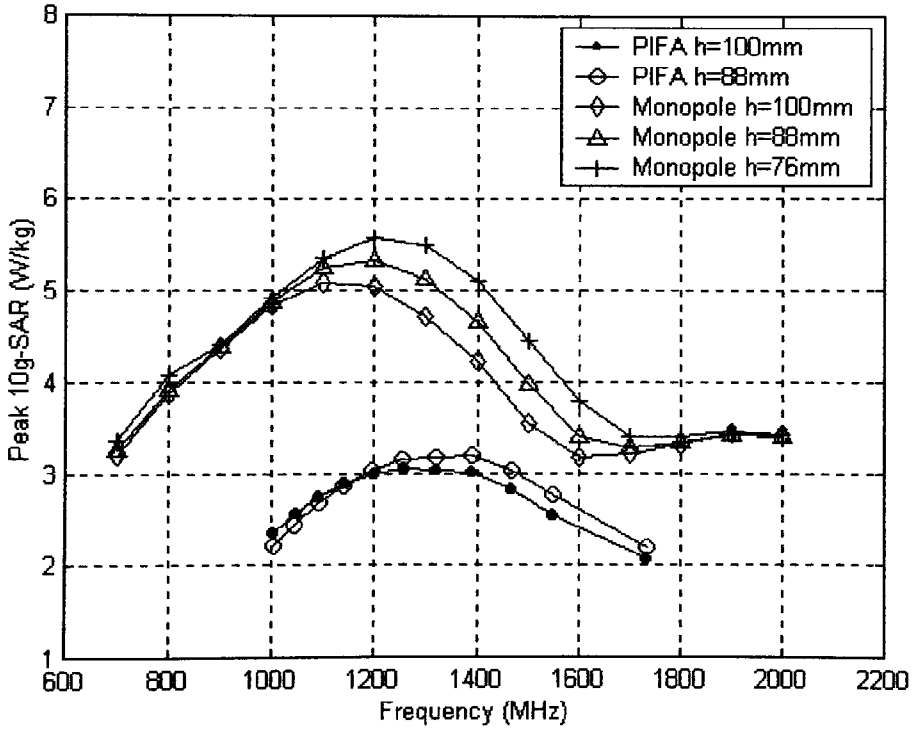

Fig. 7.15 *10-g peak SAR for the quarter-wavelength monopole and PIFA antennas.*

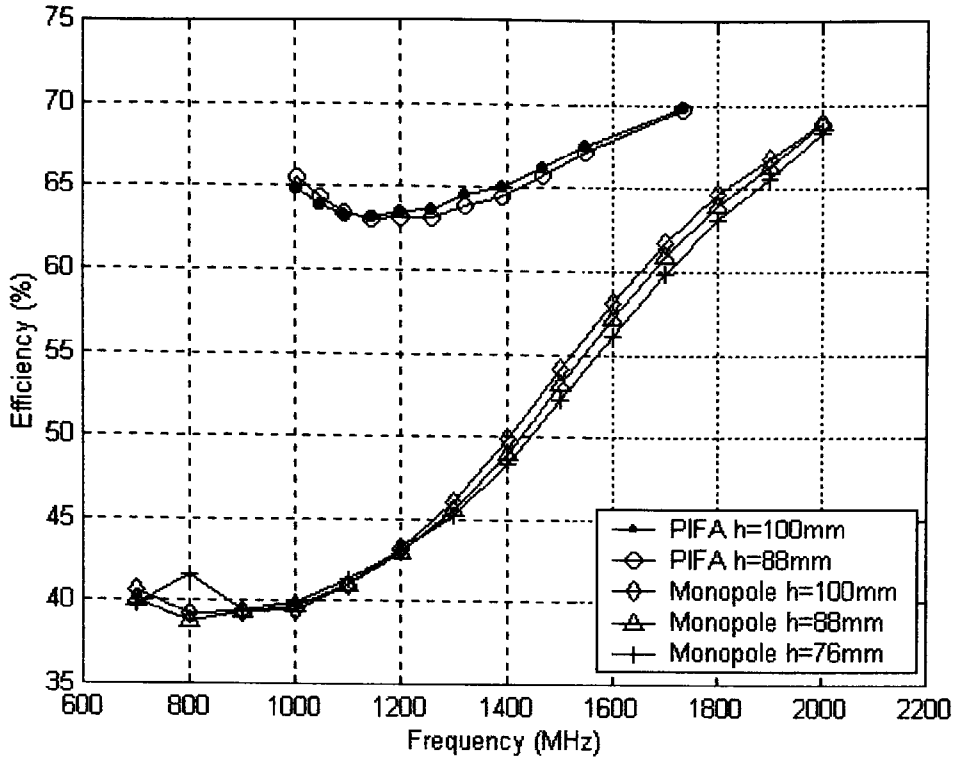

Fig. 7.16 *Radiation efficiency of the quarter-wavelength monopole and PIFA antennas.*

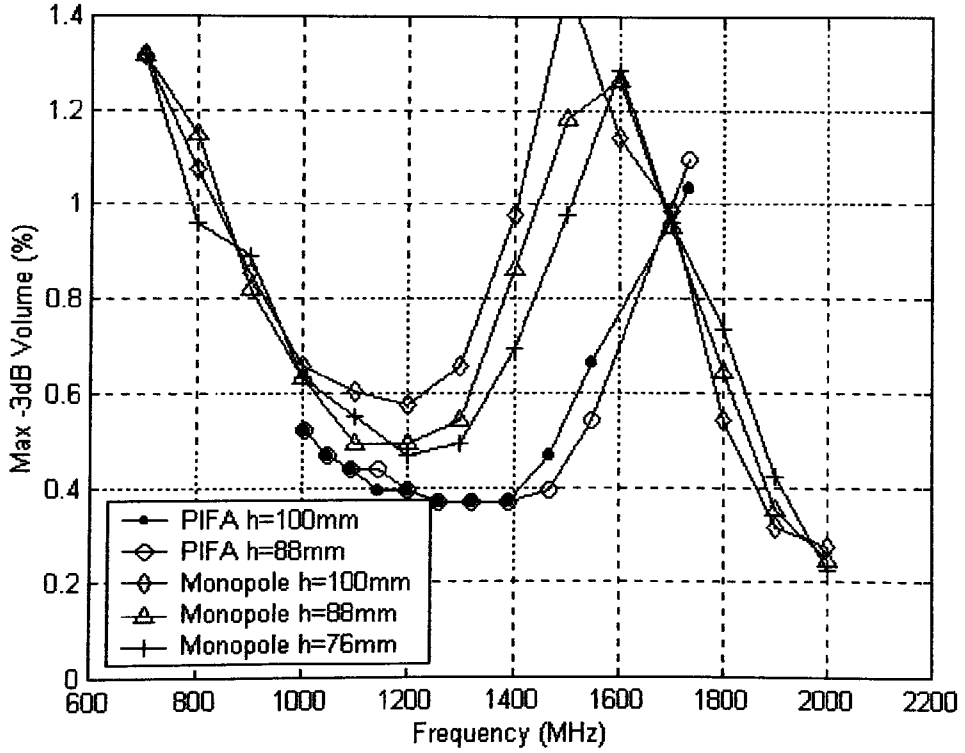

Fig. 7.17 *Percentage maximum 3dB volume (V_{max}) vs. frequency for the quarter-wavelength monopole and PIFA antennas.*

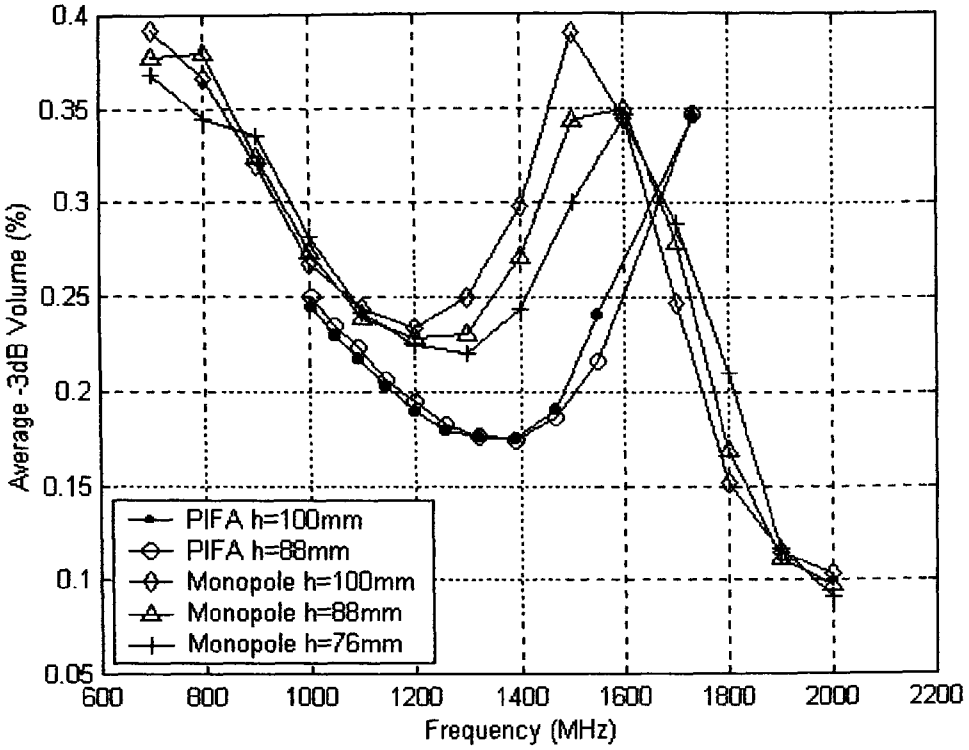

Fig. 7.18 *Percentage absolute 3dB volume (V_{abs}) vs. frequency for the quarter-wavelength monopole and PIFA antennas.*

7.6 SAR predictions for 5- and 10-years old child users.

Simulations utilising head/shoulder models representing children have been conducted in a separate study linked closely to the research. A solution to the head/shoulder model reduction in FDTD simulations is accomplished by reducing the dimensions of the Yee cells. The approach is to keep the handset dimensions fixed and see how the different parameters, like SAR, efficiency and 3dB volume, change with head size. The new head models are shown in Figs. 7.1.b and 7.1.c next to the head model of an adult (Fig. 7.1.a) for comparison. It can be seen that the size of the handset is the same but the actual handset model consists of more cells. This is also shown in Fig. 7.19 where the dimensions of the handsets for the three different head models are indicated. The new FDTD cell sizes are 2.347 mm and 1.905 mm for the 10- and 5-years old head models respectively. These dimensions represent approximately 22% and 37% reduction of the original adult model. The data for the reductions are based on statistical head size differences between adults and children at the relevant ages taken from volunteers and recommendations by experts [3.11]. In

addition to the two antenna types described and studied before, right hand side and left hand side square helix antennas as well a half-wavelength dipoles have been investigated. The resonance frequency of the helix antennas has been obtained using an impulse response input signal to the antenna model. Using post-processing that includes FFT filtering, the helix antenna input impedance vs. frequency could be found. The results have been subsequently verified by VSWR measurements on the antenna.

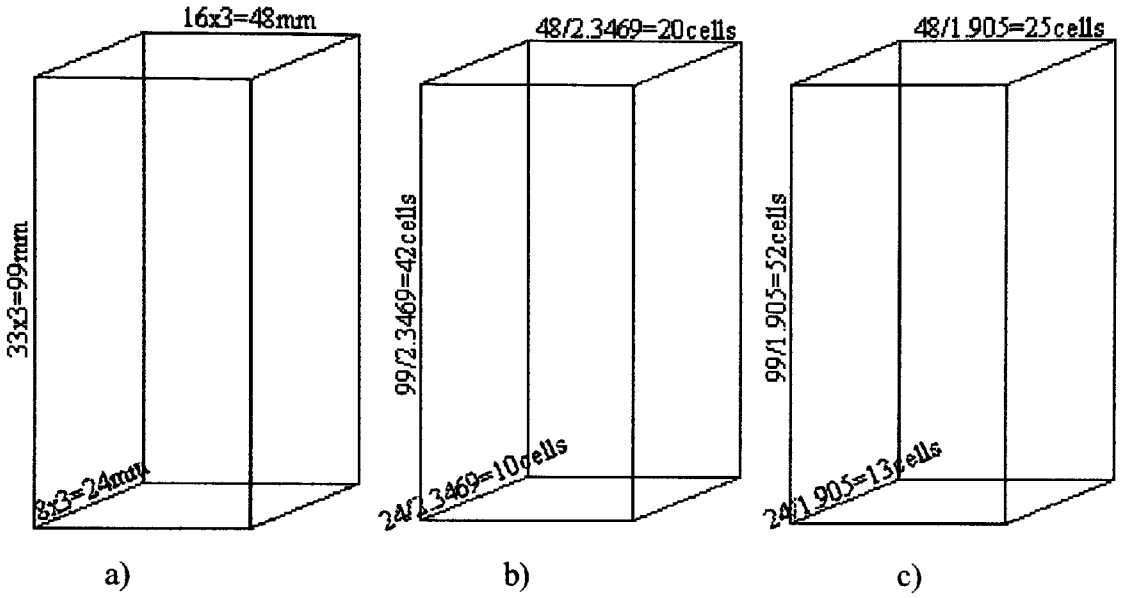

Fig. 7.19 *3D perspectives of the three boxes used. a) adult, b) 10-years-old, and c) 5-years-old models.*

Table 7.5 gives the dimensions of the PIFA antenna used for the 10-year-old child head/shoulder model and the resonance frequency for each case. Similarly table 7.6 gives data for the 5-years-old child head/shoulder model. In Fig. 7.19 the lowest horizontal plane *a* and the next plane *b* on top of *a* of the helix antenna for the 5-years-old model is shown. This is actually the method used to model the square helix. The process is repeated along the z-axis until the length of the antenna is reached. It can be seen from this figure that the helix antenna is square and not circular as those used on real handsets and prototype models in the laboratory. Even so, resonance frequencies computed with FDTD were found to be close to those measured for circular helix antennas having the same length, diameter and turns. The helix resonance frequency as a function of its length computed using FDTD for the two models studied are given in tables 7.7 and 7.8.

Size of the PIFA (Cell)	Resonance Frequencies (MHz)
13×21	968.9
13×20	999.3
13×18	1069.4
13×14	1241.6
13×10	1462.7
13×6	1747.1
13×2	2077.1

Table 7.5 *The sizes of the PIFA antenna and related resonance frequencies for the 10-year-old model.*

Size of the PIFA (Cell)	Resonance Frequencies (MHz)
16×26	957.6
16×24	1007.5
16×20	1127.1
16×14	1369.4
16×12	1472.4
16×8	1711.5
16×4	1995.4

Table 7.6 *The sizes of the PIFA antenna and related resonance frequencies for the 5-year-old model.*

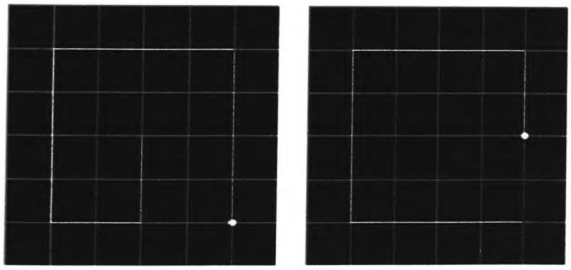

Fig. 7.20 *Top view of the helix antenna for the 5-years-old model for two consecutive horizontal (xy-) planes.*

Length of the Helix (Cells)	Helix Frequency (MHz)
97	687.9
89	736.0
81	794.2
69	894.7
62	972.3
47	1207.8
43	1289.7
33	1594.4
28	1777.5
23	2074.6
19	2379.3

Table 7.7 *Length of the helix and its resonance frequency for the 10-year-old model.*

Length of the Helix (Cells)	Helix Frequency (MHz)
146	509.5
100	680.0
90	734.1
80	809.0
70	893.2
67	930.6
40	1378.8
32	1631.5
25	2022.4

Table 7.8 *Length of the helix and its resonance frequency for the 5-year-old model.*

From the investigation of power absorption by younger users some important conclusions could be outlined. Since smaller head/shoulder models are used, it was expected that the mass-averaged SAR values would be higher. This, however, is not the case. Comparing the 1g and 10g mass-averaged peak SAR values computed for the adult model and the child models it becomes evident that the smaller the head the lower the value of the computed peak SAR. The same results for the smaller models are also true for the efficiency. From the efficiency curves it can be said that the efficiency increases considerably. The increase is about 10% for the 10-years-old child model and 15% for the 5-years-old child model. The reason for this behaviour of SAR and efficiency can be found from a closer inspection of Fig. 7.1, where the three head/shoulder models are plotted. It can be seen that the handset, which has the same physical dimensions in all three cases, is larger relatively to the smaller head. The ratio between the handset and head height is also reduced. This means that the

antenna as well as the handset "hot" points (edges) are located physically further away from the head as the head size is reduced.

Despite the lower SAR and higher efficiency values computed for the child models, the maximum and the absolute 3dB volume has increased as the head size is reduced. This means that the smaller the head the higher the percentage head volume that is exposed to high-energy absorption. Also the SAR reduction is not proportional to the efficiency increase and that high energy levels are dissipated in greater head volume. In particular the SAR reduction for the PIFA can be around 36% accompanied by an efficiency increase of the order of 10%. This result highlights once again the importance of the 3dB SAR volume measure, which gives more information describing the distribution of absorbed energy in the user's head.

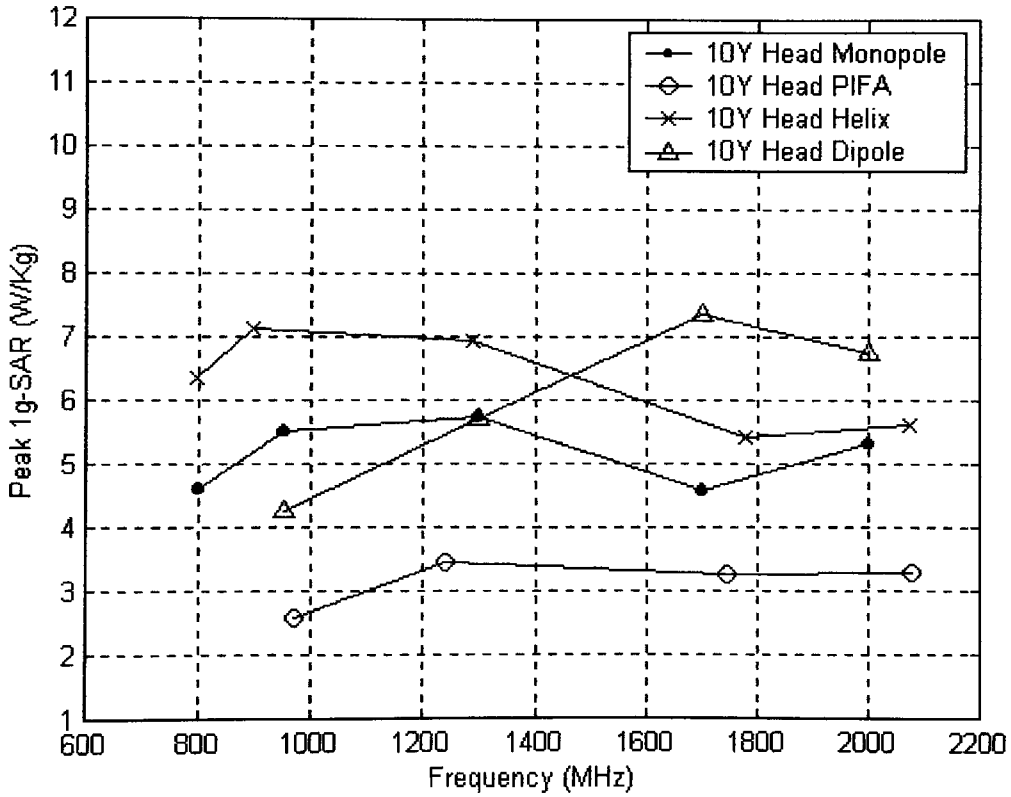

Fig. 7.21 *Peak 1g-mass-averaged SAR values vs. frequency for the 10-year-old child head/shoulders model.*

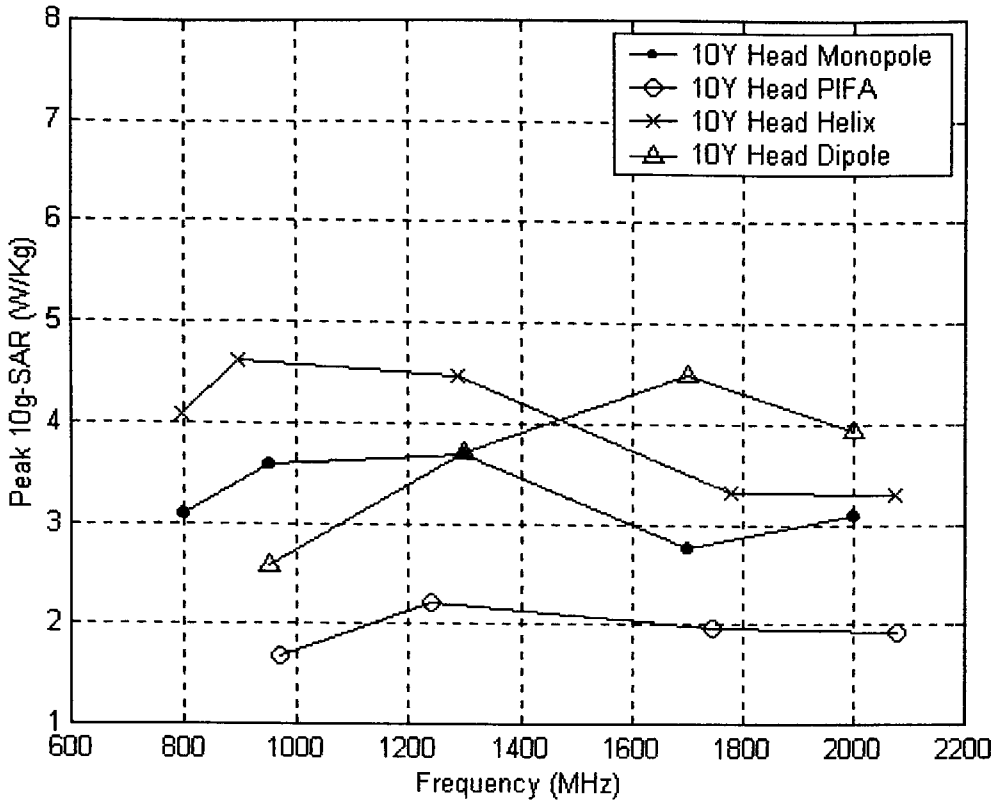

Fig. 7.22 *Peak 10g-mass-averaged SAR values vs. frequency for the 10-year-old child head/shoulders model.*

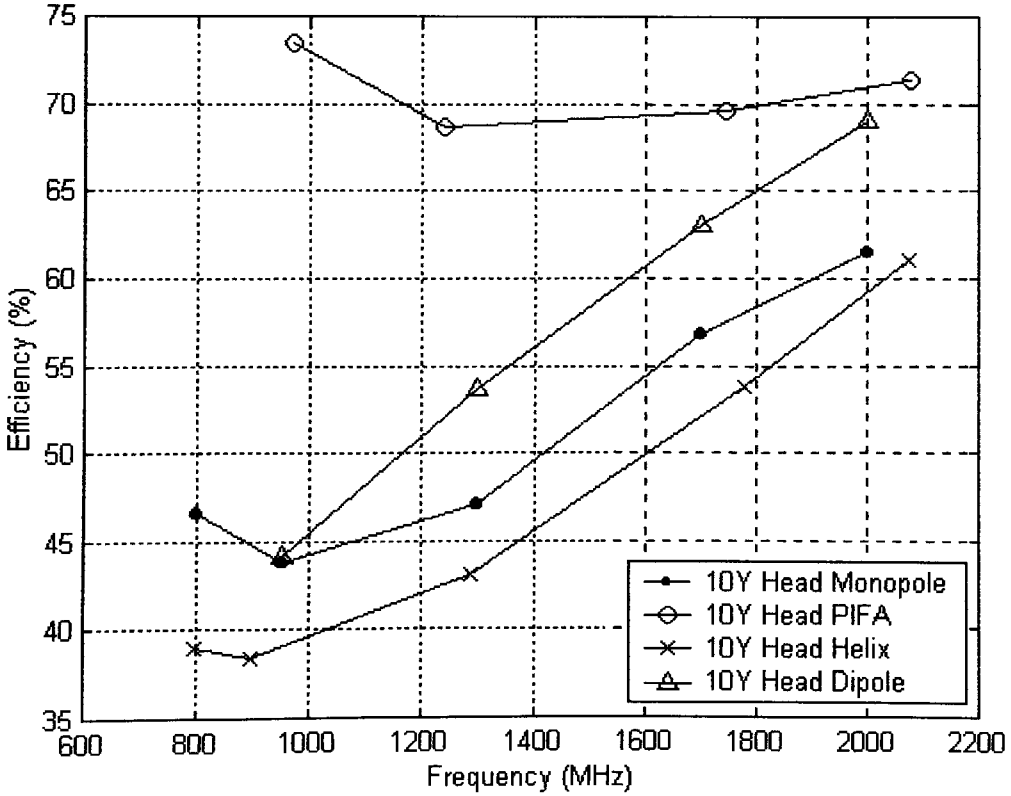

Fig. 7.23 *Efficiency curves vs. frequency for the 10-year-old child head/shoulders model.*

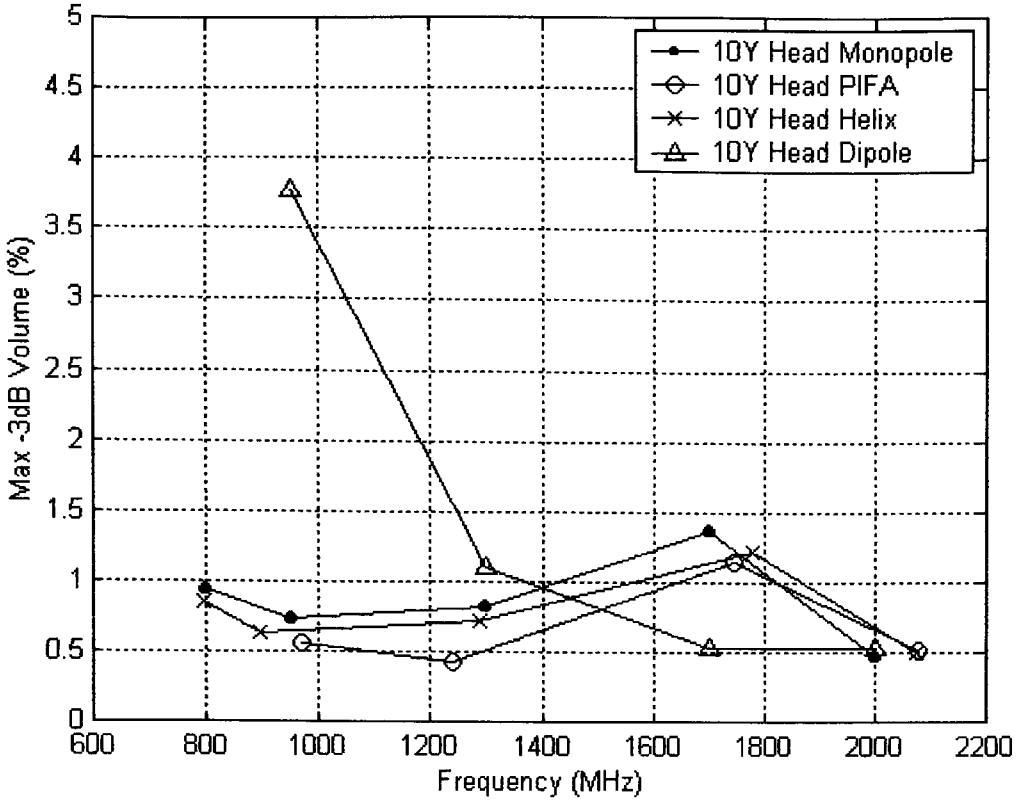

Fig. 7.24 *Maximum –3dB % volume vs. frequency for the 10-year-old child head/shoulders model.*

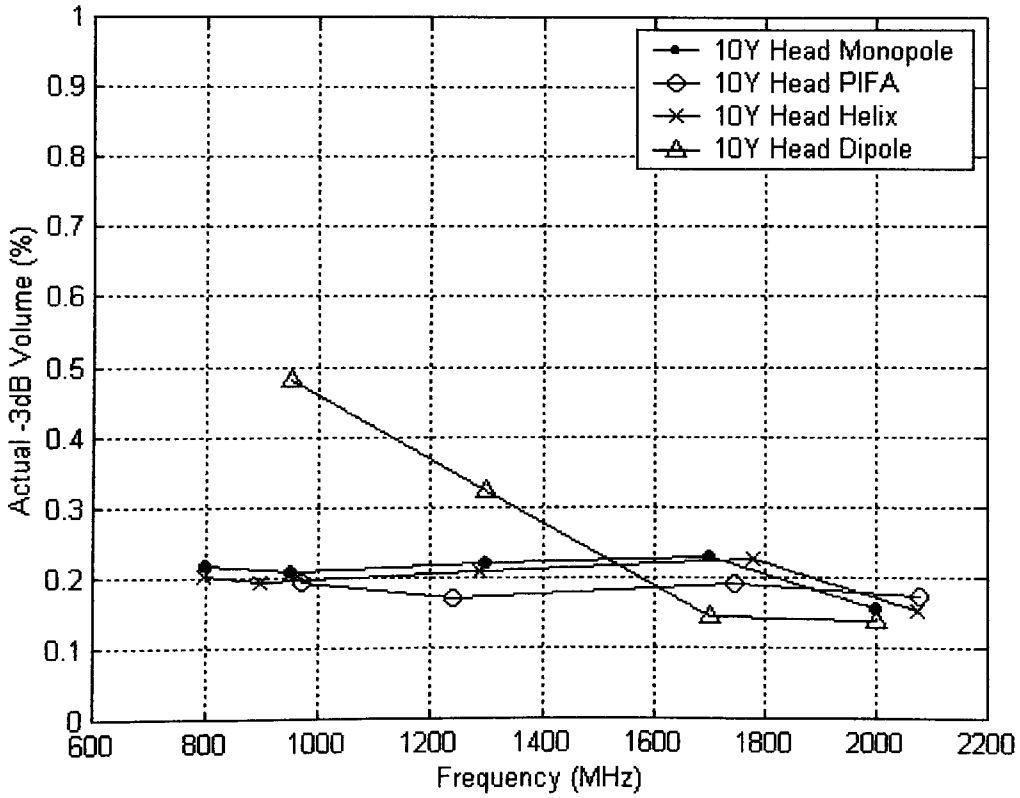

Fig. 7.25 *Actual –3dB % volume vs. frequency for the 10-year-old child head/shoulders model.*

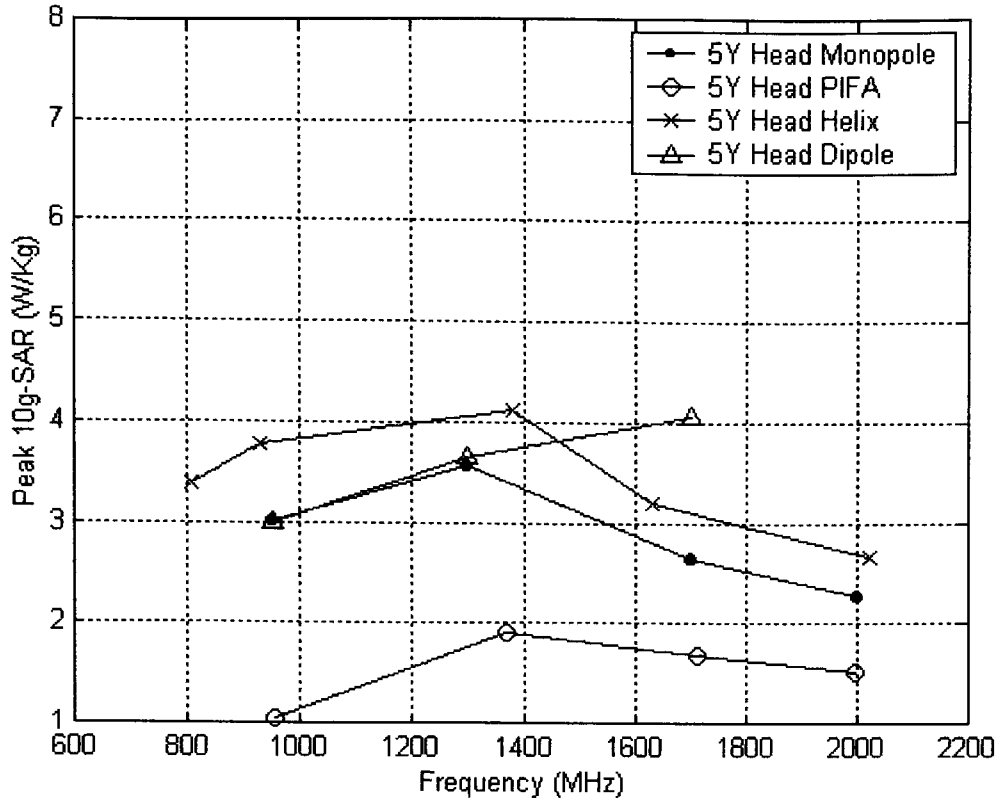

Fig. 7.26 *Peak 1g-mass-averaged SAR values vs. frequency for the 5-year-old child head/shoulders model.*

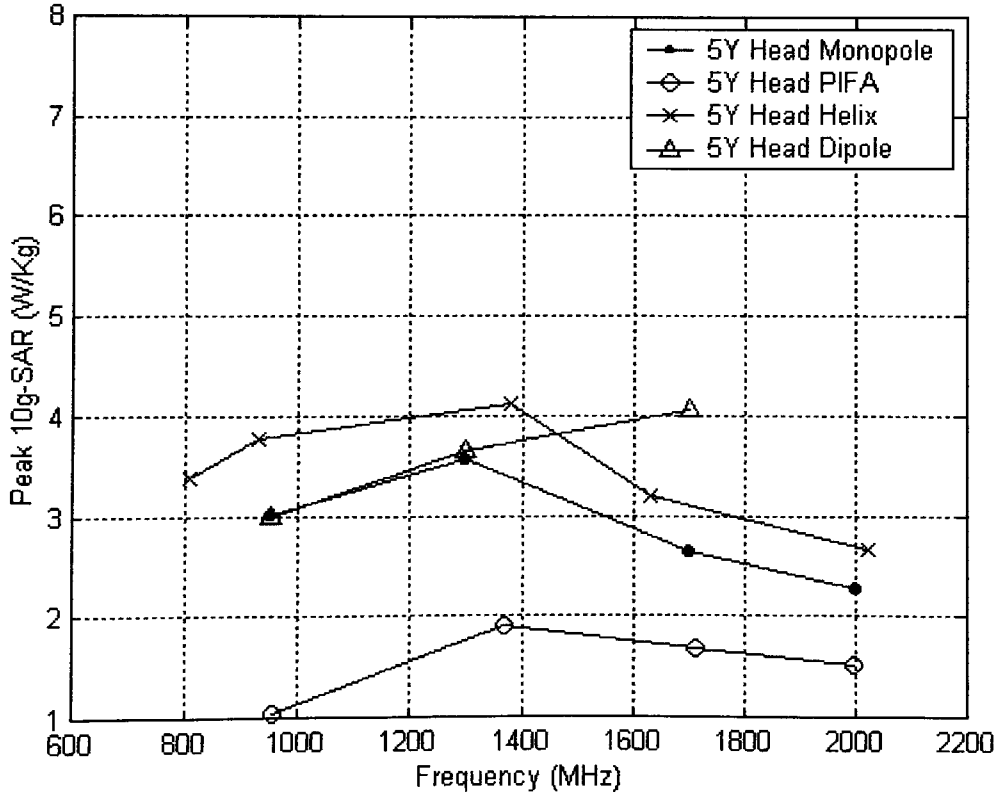

Fig. 7.27 *Peak 10g-mass-averaged SAR values vs. frequency for the 5-year-old child head/shoulders model.*

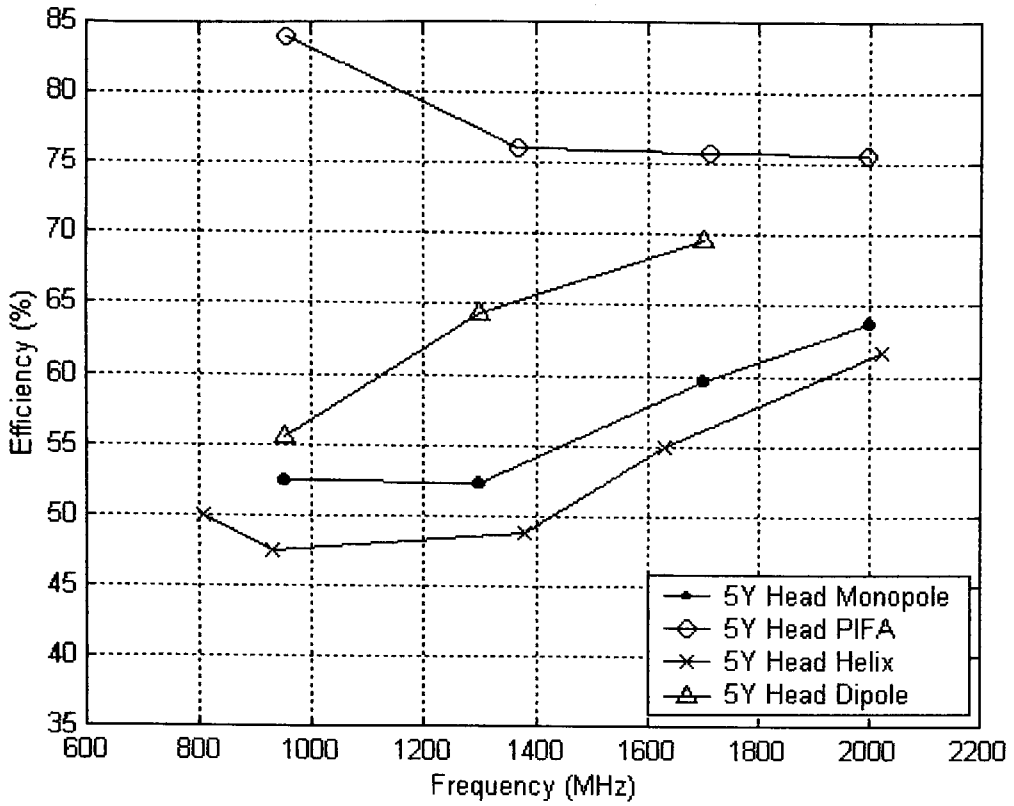

Fig. 7.28 *Efficiency curves vs. frequency for the 5-year-old child head/shoulders model.*

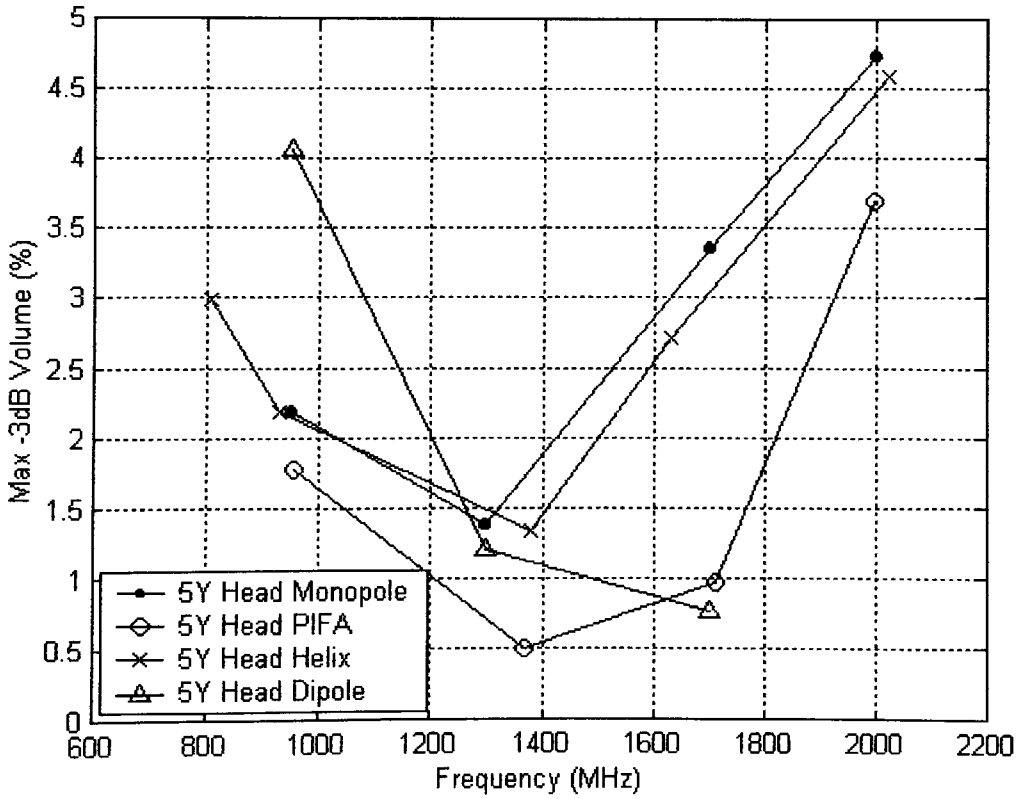

Fig. 7.29 *Maximum –3dB-percentage volume vs. frequency for the 5-year-old child head/shoulders model.*

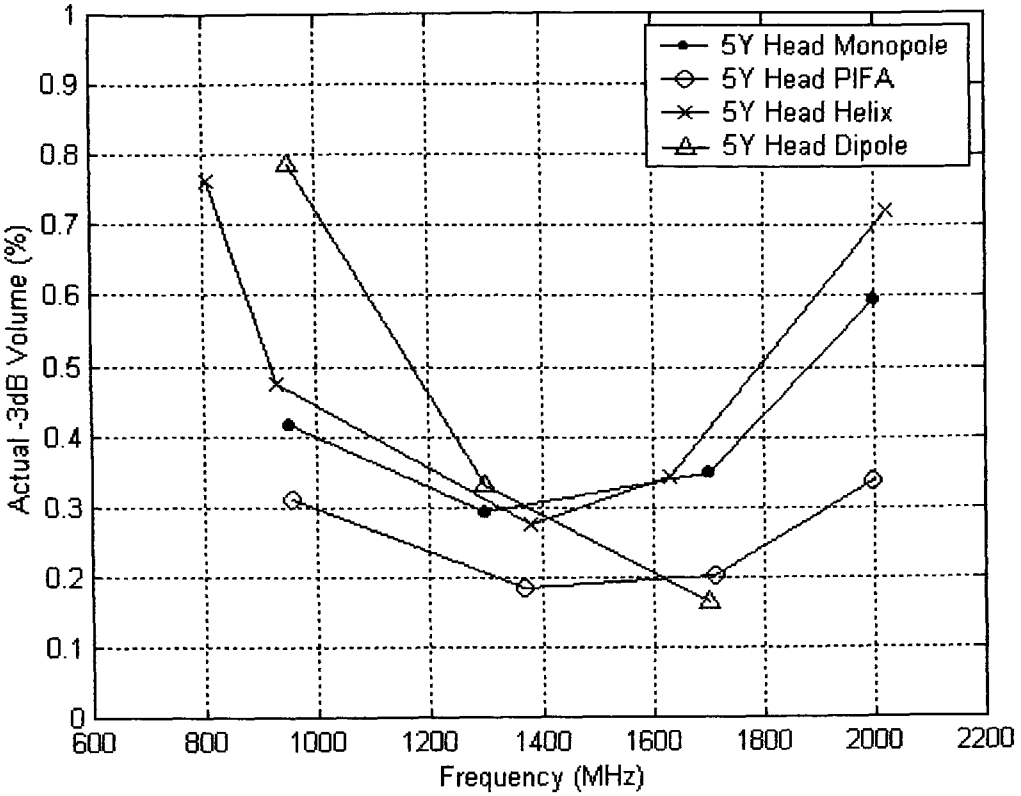

Fig. 7.30 *Actual –3dB-percentage volume vs. frequency for the 5-year-old child head/shoulders model.*

7.7 Comparison with recommended standards.

Data presented in previous sections are normalised to 1 W input power. Since the averaged power from a mobile station is only 250 mW the figures in the plotted data need to be divided by four in order to compare these results with the proposed maximum SAR. Baring in mind that a generic handset form has been used containing sharp corners and other differences that are not found in commercial handsets, the following conclusions can be drawn:

1. Mass averaged SAR values resulting from the use of the PIFA do not exceed the standards values in all the cases studied.
2. Mass averaged SAR values resulting from the use of the quarter wavelength monopole are below the standard values for the GSM900 and DCS1800 frequencies with few exceptions for the smaller handsets.
3. The use of the helix antenna can result in SAR values, which just exceed standard values.

Based on the results from the study, it can be concluded that, with an exception of few cases, the standard values of the SAR recommended are satisfied for the generic

handset form. In particular, the use of PIFA has shown that the standards are never exceeded for adult and child head models.

7.8 Interim conclusions.

In this chapter, evaluation of the SAR for a range of antenna types is reported. It has been shown that the mass-averaged SAR values are not proportional to the operational frequency, but lower values are predicted for frequencies having wavelength equal to two or four times the vertical length of the handset. The height of the handset is also responsible for the increase of SAR over the frequencies that have been studied. The smaller the handset the higher the SAR. This is true for both adult and child head models. The importance of handset height on SAR increase was shown not to be significant if the handset was inclined by an angle of 30° next to the head.

The antenna radiation efficiency has also been computed for all the different configurations. PIFA has resulted into higher efficiency compared to all the other antenna types. It has also resulted in higher efficiency, where the SAR is low. On the other hand, monopole antenna radiation efficiency is only a function of frequency. The higher the operational frequency the higher the efficiency. According to our calculations the helix antenna has the lower efficiency when operating next to the operator's head and shoulders. This is expected due to its small vertical size and increased radius, causing the antenna to be closer to the head.

The 3dB SAR volume concept has been introduced and this parameter was computed for all the configurations studied. The measure corresponding to V_{max} helps to get a better understanding of the difference seen between the SAR and efficiency curves shapes. It also helps to understand how the energy absorption is distributed in the head by giving the proportion of the head that absorbs high levels of energy. The importance of the 3dB SAR volume can be further illustrated in the comparisons between adults and children in the way they absorb radiation. The peak SAR seems to be reduced by about 35% for a child model. The efficiency, however, is improved by only 10%. Hence, the SAR reduction does not match the efficiency reduction and a question is posed on how and where the dissipated power is absorbed. The study of

the 3dB SAR volume facilitates a better understanding of the absorption by the user's head. It has further shown an increase of the head volume exposed to relatively high SAR in child head/shoulders models.

Throughout the work done on SAR and 3dB SAR volume, the advantages of PIFA in terms of efficiency and peak SAR have been highlighted. Even for the worst case, PIFA is superior compared to the monopole and the helix antennas. PIFA can be used as a low profile alternative for mobile phones. The bandwidth limitation that characterizes the PIFA, which has been addressed in the Chapter 6, has so far limited its potential for extensive application in commercial mobile phones. In addition, positioning of the operator's hand on the handset to prevent blocking of the PIFA antenna needs to be addressed by appropriate design of the handset. In Chapter 8, research studies on both the antennas and the SAR are revised and discussed. Finally, future work is proposed on both the PIFA bandwidth improvement and SAR/3dB SAR volume.

8. SUMMARY AND CONCLUSIONS

In the last decade of the 20th century we have witnessed a revolution in mobile communications. The introduction of digital technology and GSM systems have enhanced the network quality and capacity and reduced the cost of mobile voice and data communication services. The size and weight of the handset is an important factor that may affect users' choice. The size of the battery and the antenna, in particular, are among the most important factors that determine the mobile phone size and operation time. Battery technology is improving with time allowing higher capacity in more compact packaging. Efficient and wideband antenna radiation, on the other hand, is constrained by its electrical size. A monopole is thin and can be made flexible, however, its minimum resonant length is approximately $\lambda/4$. Helix antennas are shorter but they are thicker and cannot easily made flexible. In several commercial mobile phones, a combination of monopole and helix antennas is used for better radiation efficiency, under different operating conditions. Built-in antennas have been recently introduced with widely acceptable radiation characteristics, in terms of network requirements. An increasing interest is appearing, mainly driven by equipment manufacturers, in low-profile built-in antennas that can be embedded not only in the GSM phone handsets but also in other portable devices proposed for the next generation of mobile communications. Such devices that may include computers with the facility to wirelessly connect to computer networks will put additional constraints in terms of size, weight and battery life. The PIFA antenna is compact, efficient and has low manufacturing cost. PIFA is also characterized by narrow bandwidth, which so far has been a major problem for practical considerations. Research to overcome this problem and to make the PIFA operate in a dual-band mode has been reported in Chapter 5 and is summarised below.

8.1 The Planar Inverted-F antenna.

The resonance frequency of the PIFA is not only dependent on its dimensions, but also on the number and position of the short pins used. In order to understand better how the short pin position can affect the resonance frequency of the PIFA systematic measurements have been done on a fixed size antenna, mounted on a conductive box

[8.1]. Applying the short pin repositioning method it was found that the effective bandwidth of the antenna can be increased attaining values of up to 500 MHz. In practice, the short pins must be replaced by transistors or pin diodes. The relation between the short pin distance and the resonance frequency has been investigated in detail. In general, the longer the distance of the short pin from the feed the higher the resonance frequency.

An alternative method for controlling the resonance frequency of the PIFA, which has been introduced in this thesis, is by changing the pin reactance. The method was tested at four reference points on the PIFA. It has been proved that up to 175 MHz of effective bandwidth can be achieved by implementing this method and by varying the capacitance of a single pin. The lower the capacitance of the shorting pins the higher the resonance frequency. The bandwidth covered by applying this method is also affected by the distance from the feed, as it was expected from observations of the short pin positioning method.

Two variable capacitors have been used for a prototype dual-band PIFA operating at GSM900 and DCS1800 frequency bands. By changing the capacitance of only one capacitor, PIFA can resonate at all channels available for the two GSM systems. The physical size of the PIFA is reduced since the frequency band covered can be customized by appropriate capacitor positioning and value selection and not only by the size of the patch.

Having studied the different methods of tuning the PIFA, a prototype model of an electronically tuned PIFA for the GSM900 band has been built. This antenna is capable of resonating at all GSM900 channel frequencies (up-link and down-link) by varying the voltage applied to a varactor diode. A DAC circuit and a control algorithm have been developed for the measurements, which have shown good stability and quick response of the antenna.

The basic methods for addressing the bandwidth limitation of PIFA are presented. Further work, however, is required before these methods and in particular the electronically tuned PIFA can become widely applicable. Such further work may include:

- Design of a feedback circuit that will allow a computer based algorithm to control the reverse bias voltage on the varactor (Fig. 8.1). A low cost coupling mechanism should measure the reflections on the transmission line, particularly during transmission mode, and feed the information to an ADC after amplification. The information should be then input to a computing system. This computes the reverse bias voltage required to correct the antenna resonance frequency. The feedback circuit should also tune the antenna to the assigned channel frequency. For this reason the voltage on the varactor (V_{var}) should have the following value:

$$V_{var} = V_{Ch} + V_{error} \tag{8.1}$$

where V_{ch} is the voltage required to tune the varactor into the associated channel frequency and V_{error} is the voltage required to correct the resonance frequency due to antenna coupling with nearby objects like the operator's head. According to our measurements, the coupling f_r error on the PIFA due to external factors is the same during both transmission and reception. For this reason the correction voltage computed for the transmit mode can be used in reception mode too. This is required since the received signal is so weak that the reflections on the transmission line may be undetectable.

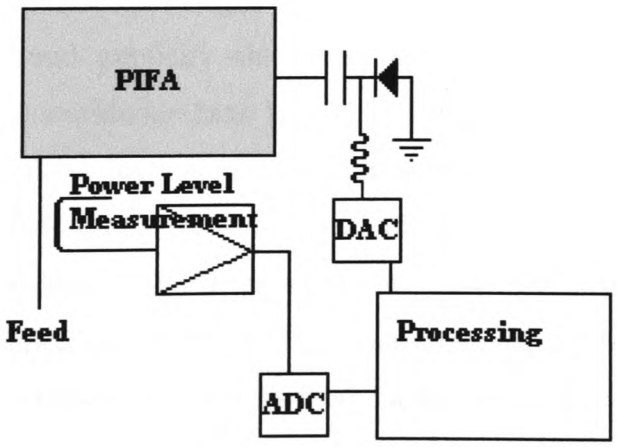

Fig. 8.1 *Block diagram of an electronically fine-tuned.*

- In a range of varactor diodes tested none were found to work at frequencies near 2 GHz. Further work is needed on the design of the varactors so that they will give similar results as those measured in the GSM900 band and with even lower reverse bias voltages. The voltage available in a GSM mobile phone is only 3 volts which is much lower compared to the 15 volts required for the prototype antenna described here.
- Different configuration can be used in utilizing the PIFA/varactor method described here. For instance two instead if one PIFA patch can be used, one for transmission and one for reception. The proposed configuration is shown in Appendix B. Using this method the reverse bias voltage of each varactor can be reduced. Alternatively, methods for dual patch PIFA based also on work reported in [3.4-3.5] for single feed can be implemented.

Despite the issues associated with the practical implementation of a low profile PIFA in mobile handsets, the predicted high efficiency and low SAR values for this antenna encourage further work as proposed above. The advantages of PIFA have been highlighted in the second part of this research where radiation absorption issues are studied.

8.2 SAR, efficiency and 3dB SAR volume predictions.

Health related concerns from prolonged use of mobile phones is a topic which has been given a widespread publicity since the wide spread use of GSM mobile telephony. Regulations worldwide have been issued in order to control the exposure by cellular phone users to high levels of electromagnetic radiation. The specific absorption rate or SAR is such a measure for which regulatory bodies have assigned maximum values in order to control the exposure. SAR can be either measured or computed using numerical methods. FDTD is an approved method for evaluating SAR. To confirm the validity of this method, in an early stage of this research, predicted far-field radiation patterns have been compared with measured patterns resulting in good agreement. A review of this work covering the monopole, helix and PIFA antennas is given in Chapter 4. Near-field patterns are also presented in Chapter 5 where good agreement between the MoM and FDTD numerical methods is

demonstrated. FDTD and an anatomically correct numerical model of the human head have been extensively used for SAR predictions [8.2]. Predicted results have been compared with published data resulting in good agreement.

It has been reported in the literature that smaller handsets in general result in higher SAR. Similar conclusions have been reported for the monopole antenna, resulting in higher absorbed power by the operator as its length reduces. In contrast to the monopole antenna, use of PIFA results in lower SAR due to the increased distance of the radiating element from the operator's head and due to the handset position between the antenna and the head. As a result the handset blocks some of the antenna-radiated power from reaching the operator. In computing the SAR for a wide bandwidth, instead for a single frequency as done by others, and modeling three different size handsets, interesting results have been revealed. It can be seen from the mass-averaged SAR plots that SAR has low values when the handset height is approximately equal to half or quarter of wavelength. This observation has been confirmed by a number of PIFA and monopole antenna simulations as well as by 30° handset inclination predictions, which have been studied, in addition to the upright positioning of the handset. This observation is also true for the child-user models predictions. In some cases the SAR reduction is of the order of 30%. From the same plots it is confirmed that the handset reduction results into higher SAR and that PIFA gives much lower SAR compared to the monopole antenna. If the handset is placed with an angle next to the operator's head model, representing a more natural operating position, similar results are produced. However, the peak SAR values are reduced compared to the previous case and the effect of the handset height reduction on the SAR increase is smaller. SAR reduction due to handset inclination was expected since the edges and the antenna are physically further from the head than when the handset is positioned vertically next to the head.

For the same simulations the radiation efficiency of the antennas has been plotted against frequency. For the monopole antenna the efficiency monotonically increases with the operational frequency. For the PIFA the efficiency curves are quite different compared to those of the monopole. Higher radiation efficiency occurs at frequencies where the SAR is low and, vice versa, efficiency is lower when the SAR is high. The PIFA efficiency curves are expected, since higher absorption due to higher SAR

should result into lower efficiency. On the other hand, efficiency data from the monopole simulations have given results that do not match these expectations. The 3dB SAR volume concept is introduced in order to explain this discrepancy.

The 3dB SAR volume values give the percentage of the head volume exposed to relatively high absorbed power during operation. It is a quantity independent of the radiation power levels but is dependent on the geometry of the handset and the user, the operational frequency and the antenna type used. It is a way of understanding how absorbed power is distributed in the head. From the simulations it has been realized that when the mass-averaged SAR has high values the 3dB volume is low and vice versa.

Having information about the SAR is not by itself sufficient for a clear understanding of the exposure level by human operators caused by radiation from mobile phone handsets. Having high SAR at a single point, and in particular when in real life the position of the handset next to the head is not always identical, is not equivalent to having the same SAR distributed over the entire head volume. Providing SAR and efficiency information is also not sufficient information, since the two quantities are not directly related. The 3dB SAR volume is an important measure in understanding the form and distribution of radiation exposure. This is clearer in the results obtained from simulations on child models. Although the mass-averaged SAR values decrease as the head size reduces and efficiency increases the factor by which the SAR is reduced is not the same as the factor by which the efficiency reduces. This is because a larger percentage of the head volume is exposed to higher levels of absorbed power. This shows that the use of mobile phones by children does not enclose fewer risks especially if we consider the higher tissues sensitivity in a child head.

For further research, it is proposed that more systematic investigation of the 3dB SAR volume should be carried out along with experimental verification. Although there is no clear evidence about health risks due to radiation at the frequencies considered here it is a responsibility of the scientific community to investigate further how to reduce the SAR and the 3dB SAR volume values to which the users are exposed by appropriate design of the handset and the antenna used. It has been demonstrated here how the height of the handset affects SAR values. Alternative

handset designs that will reduce the exposure rates should be studied. Design and evaluation work should not only concentrate on peak SAR values and their location in the head, but also on the percentage of the head volume exposed to relatively high levels of radiation.

The exposure to EM radiation will become more of a health risk problem as more as human communication needs inevitably rely on wireless links. Wireless equipment designers need to consider methods of continually minimising these risks in addition to the present requirements of aesthetic and handset system qualities.

8.3 Contribution to published literature.

Part of the work presented in this report has been published and presented in international conferences including CAR'99 and AP2000. In [8.1] tuning techniques for PIFA are described based on measured data presented in Chapter 6. This work has attracted the interest of antenna and handset manufacturers like Siemens. In [8.2] far- and near-field radiation patterns, SAR and efficiency results are reported based on evaluation data given in Chapter 7. A paper has also being submitted to "IEEE Transactions on Antennas and Propagation" entitled "SAR Prediction and Tuning Techniques for the Planar Inverted-F Antennas." A copy of both published papers is given in Appendix B.

References:

[1.1] S. M. Redl, M. K. Weber, and M. W. Oliphant, "*An Introduction to GSM*," vol. 0-89006-785-6, First ed. Boston, London: Artech House Publishers, 1995.
[1.2] UMTS Forum, "Report on UMTS/IMT-2000 Spectrum," : UMTS Forum, 1998 (Web page: http://www.umts-forum.org/index.html).
[1.3] S. Faruque, *Cellular Mobile System Engineering*, vol. 0-89006-518-7, First ed. Boston, London: Artech House Publishers, 1996.

[2.1] J. D. Kraus, *Electromagnetics*, vol. 0-07-035621-1, Fourth ed. London: McGraw-Hill International Editions, 1991.
[2.2] K. S. Kunz and R. J. Luebbers, *The Finite Difference Time Domain Method for Electromagnetics*, vol. 0-8493-8657-8: CRC Press, 1993.
[2.3] K. S. Yee, "Numerical Solution of Initial Boundary Value Prebloms Involving Maxwell's Equations in Isotropic Media," *IEEE Transactions on Antennas and Propagation*, vol. AP-14, pp. 302-307, May, 1966.
[2.4] C. A. Balanis, *Antenna Theory, Analysis and Design*, vol. 0-471-59268-4, Second ed, 1997.
[2.5] F. R. Connor, *ANTENNAS*, vol. 0-7131-3279-5, First ed. Bath: The Pitman Press, 1981.
[2.6] IEEE std-1993, "IEEE Standard Definitions of Terms for Antennas," 1993.
[2.7] J. D. Kraus, *Antennas*, vol. 0-070354227, Second ed. London: McGraw-Hill Book Company, 1988.
[2.8] G.J. Burke and A. J. Poggio, *Numerical Electromagnetic Code (NEC) – Method of Moments Part I: Program Description – Theory,* Lawrence Livermore Laboratory, January 1981.
[2.9] G.J. Burke and A. J. Poggio, *Numerical Electromagnetic Code (NEC) – Method of Moments Part II: Program Description – Code,* Lawrence Livermore Laboratory, January 1981.
[2.10] *Numerical Electromagnetic Code (NEC) – Method of Moments Part III: User's Guide,* Lawrence Livermore Laboratory, September 1996.

[3.1] T. Taga and K. Tsunekawa, "Performance Analysis of a Built-In Planar Inverted-F Antenna for 800 MHz Band Portable Radio Units," *IEEE journal on selected areas in communications*, vol. SAC-5, pp. 921-929, June 1987.
[3.2] G. F. Pedersen and J. B. Andersen, "Integrated Antennas for Hand-held Telephones with Low Absorption," *IEE Colloquium, Ref. 1997/022*, 1994.
[3.3] C. R. Rowell and R. D. Murch, "A Capacitively Loaded PIFA for Compact Mobile Telephone Handsets," *IEEE Transactions on Antennas and Propagation*, vol. 45, pp. 837-842, May 1997.
[3.4] Z. D. Liu and P. S. Hall, "Dual-Band Antenna for Hand Held Portable Telephones," *Electronics Letters*, vol. 32, pp. 609-610, 28th March 1996.
[3.5] Z. D. Liu, P. S. Hall, and D. Wake, "Dual-Frequency Planar Inverted-F antenna," *IEEE Transactions on Antennas and Propagation*, vol. 45, pp. 1451-1458, October 1997.
[3.6] C. R. Rowell and R. D. Murch, "Design of Diversity Antennas for Mobile Telephones," *International Symposium on Radio Propagation*, 1997.
[3.7] K. Ogawa and T. Uwano, "A Diversity Antenna for Very Small 800MHz Band Portable Telephones," *IEEE Transactions on Antennas and Propagation*, vol. 42, pp. 1342-1345, September 1994.

[3.8] C. R. Rowell and R. D. Murch, "A Compact PIFA Suitable for Dual-Frequency 900/1800-MHz Operation," *IEEE Transaction on Antennas and Propagation*, vol. 46, pp. 596-598, April 1998.
[3.9] J. Fuhl, P. Nowak, and E. Bonek, "Improved internal antennas for hand-held terminals," *Electronics Letters*, vol. 30, pp. 1816-1818, 27th October 1994.
[3.10] S.-G. Pan, T. Becks, A. Bahrwas, and I. Wolff, "N antenna and Their Applications in Portable Handsets," *IEEE Transactions on Antennas and Propagation*, vol. 45, pp. 1475-1483, October 1997.
[3.11] O. P. Gandhi, G. Lazzi, and C. M. Furse, "Electromagnetic Absorption in the Human Head and Neck for Mobile Telephones at 835 and 1900MHz," *IEEE Transactions on Antennas and Propagation*, vol. 44, pp. 1884-1897, October 1996.
[3.12] Jorn.Toftgard, S. N. Hornsleth, and B. Andersed, "Effect on Portable Antennas of the Presence of a Person," *IEEE Transactions on Antennas and Propagation*, vol. 41, pp. 739 - 746, June 1993.
[3.13] V. Hombach, K. Meier, M. Burkhaedt, E. Kuhn, and N. Küster, "The Dependence of EM Energy Absorption Upon Human Head Modeling at 900 MHz," *IEEE Transactions on Microwave Theory and Techniques*, vol. 44, pp. 1865-1873, October 1996.
[3.14] M. Okoniewski and M. A. Stuchly, "A Study of the Handset Antenna and Human Body Interaction," *IEEE Transaction on Microwave Theory and Techniques*, vol. 44, pp. 1855-1864, October 1996.
[3.15] S.-i. Watanabe, M. Taki, T. Nojima, and O. Fujiwara, "Characteristics of the SAR Distribution in a Head Exposed to Electromagnetic Fields Radiated by a Hand-Hand Portable Radio," *IEEE Transactions on Microwave Theory and Techniques*, vol. 44, pp. 18741883, October 1996.
[3.16] S. V. Amos, M. S. Smith, and D. Kitchener, "Modeling of Handset Antennas Interactions With The User and Sar Reduction Techniques," *NCAP1999*, vol. 461, pp. 12-15, 1999.

[7.1] CENELEC, "*Safety Considerations for Human Exposure to EMF's from Mobile communication Equipments (MTE) in the Frequency Range 30 MHz - 60 MHz*," CENELEC, 30 April 1996.
[7.2] NRPD, "Board Statement on Restrictions on Human Exposure to Static and Time Varying Electromagnetic Fields and Radiation," National Radiological Protection Board 19-Nov-1993 1993.
[7.3] "Evaluating Compliance with FCC Guidelines for Human Exposure to Radiofrequency Electromagnetic Fields," FCC, Edition 97-01, August 1997.
[7.4] Internet Site: "http://www.nlm.nih.gov/research/visible/visible_human.html"

[8.1] P. K. Panayi, M. Al-Nuaimi, and L. Ivrissimtzis, "Tuning Techniques for the Planar Inverted F-Antenna," *NCAP99*, vol. 1, pp. 259-262, April 1999.
[8.2] P. K. Panayi, M. Al-Nuaimi, and L. Ivrissimtzis, "Near/Far Field and SAR of Mobile Communication Antennas," *AP2000*, p351, April 2000.

Appendix A

A.1 Vectors and Coordinate Systems.

Despite the scalar quantity, which has only magnitude, a *vector quantity* has both magnitude and direction. In rectangular for a vector $\overline{A}$ can be analysed into three components. Each of the components of the vector may in turn be expressed as the product of a scalar magnitude and a unit vector.

$$\overline{A} = \hat{x}A_x + \hat{y}A_y + \hat{z}A_z \qquad \text{(A.1)}$$

From the theorem of Pythagoras, the *scalar magnitude* of a vector, $|\overline{A}|$, is given by

$$|\overline{A}| = \sqrt{A_x^2 + A_y^2 + A_z^2} \qquad \text{(A.2)}$$

The *dot product* $(\cdot)$ of two vectors, $\overline{A}$ and $\overline{B}$, is a scalar

$$\overline{A} \cdot \overline{B} = |\overline{A}||\overline{B}|\cos\theta = AB\cos\theta \qquad \text{(A.3)}$$

where θ is the angle between $\overline{A}$ and $\overline{B}$. Some of the dot product properties are given in Table A.1.

Property	**Comments**
$\overline{A} \cdot \overline{B} = \overline{B} \cdot \overline{A}$	commutative law
$\overline{A} \cdot \overline{B} = 0$	if $\theta = 0$
$\hat{x} \cdot \hat{y} = \hat{y} \cdot \hat{z} = \hat{z} \cdot \hat{x} = 0$	
$\hat{x} \cdot \hat{x} = \hat{y} \cdot \hat{y} = \hat{z} \cdot \hat{z} = 1$	
$\overline{A} \cdot \overline{A} = A^2$	
$\overline{F} \cdot d\overline{L} = F\cos(\theta)dL$	$d\overline{L}$ is the vector incremental length θ angle between $\overline{F}$ and $d\overline{L}$

Table A.1 *Vectors dot product properties.*

The *cross product* $(\times)$ of a vector, on the other hand, is a vector with a magnitude equal to the product of the vector magnitudes multiplied by the sine of the angles between them. The direction of the new vector is perpendicular to the plane containing the two vectors. This is given by

$$\overline{C} = \overline{A} \times \overline{B} = \hat{x}(A_x B_z - A_z B_y) + \hat{y}(A_z B_x - A_x B_z) + \hat{z}(A_x B_y - A_y B_x) = \begin{vmatrix} \hat{x} & \hat{y} & \hat{z} \\ A_x & A_y & A_z \\ B_x & B_y & B_z \end{vmatrix} \quad \text{(A.4)}$$

Some of the cross product properties are given in Table A.2.

Property	**Comments**
$\|C\| = \|A\|\|B\|\sin\theta$	magnitude if C
$\hat{x} \times \hat{y} = \hat{z}$, $\hat{z} \times \hat{x} = \hat{y}$, and $\hat{y} \times \hat{z} = \hat{x}$	unit vector cross product
$\overline{A} \times \overline{B} = \overline{C} = \hat{n}AB\sin\theta$	$\hat{n}$ is a unit vector normal to the plane containing $\overline{A}$ and $\overline{B}$

Table A.2 *Vectors cross product properties.*

A vector at a point P can be described in three coordinate systems. In the rectangular coordinate system the point P can be expressed by x, y, and z which are the distance from the origin from x-, y-, and z- axes respectively. Similarly, for the spherical r, θ, and φ are used. Table A.3 shown point transformation for rectangular and spherical coordinate systems and Table A.4 shows coordinate transformations formula for vector components.

Point transformation	
$x = r\sin\theta\cos\phi$	
$y = r\cos\theta\sin\phi$	
$z = r\cos\theta$	
$r = \sqrt{x^2 + y^2 + z^2}$	$(r \geq 0)$
$\theta = \cos^{-1}\dfrac{z}{\sqrt{x^2 + y^2 + z^2}}$	$(0 \leq \theta \leq \pi)$
$\phi = \tan^{-1}\dfrac{y}{x}$	

Table A.3 *Point transformation for rectangular and spherical coordinate systems.*

Rectangular to Cylindrical

$$A_r = A_x \frac{x}{\sqrt{x^2+y^2}} + A_y \frac{y}{\sqrt{x^2+y^2}}$$

$$A_\phi = -A_x \frac{y}{\sqrt{x^2+y^2}} + A_y \frac{x}{\sqrt{x^2+y^2}}$$

$$A_z = A_z$$

Rectangular to Sperical

$$A_r = A_x \frac{x}{\sqrt{x^2+y^2+z^2}} + A_y \frac{y}{\sqrt{x^2+y^2+z^2}} + A_z \frac{z}{\sqrt{x^2+y^2+z^2}}$$

$$A_\theta = A_x \frac{xz}{\sqrt{x^2+y^2}\sqrt{x^2+y^2+z^2}} + A_y \frac{yz}{\sqrt{x^2+y^2}\sqrt{x^2+y^2+z^2}} + A_z \frac{\sqrt{x^2+y^2}}{\sqrt{x^2+y^2+z^2}}$$

$$A_\phi = -A_x \frac{y}{\sqrt{x^2+y^2}} + A_y \frac{y}{\sqrt{x^2+y^2}}$$

Cylindrical to rectangular

$$A_x = A_r \cos\phi - A_\phi \sin\phi$$

$$A_y = A_r \sin\phi - A_\phi \cos\phi$$

$$A_z = A_z$$

Spherical to rectangular

$$A_x = A_r \sin\theta\cos\phi + A_\theta \cos\theta\cos\phi + A_\phi \sin\phi$$

$$A_y = A_r \sin\theta\sin\phi + A_\theta \cos\theta\sin\phi + A_\phi \cos\phi$$

$$A_z = A_r \cos\theta = A_\theta \sin\theta$$

Table A.4 *Coordinate Transformations.*

In engineering is useful to consider the rate of change of vectors. The differential form of vectors is expressed in mathematics with the help of the gradient, divergence, and curl. The gradient of a scalar is a vector and is given by

$$gradf = \nabla f = \hat{x}\frac{\partial f}{\partial x} + \hat{y}\frac{\partial f}{\partial y} + \hat{z}\frac{\partial f}{\partial z} \tag{A.5}$$

The divergent of a vector, on the other hand is a scalar and given by

$$div \cdot \overline{A} = \nabla \cdot \overline{A} = \frac{\partial A_x}{\partial x} + \frac{\partial A_y}{\partial y} + \frac{\partial A_z}{\partial z} \tag{A.6}$$

Finally, the curl of a vector is a vector and it is given by

$$curl \times \overline{A} = \nabla \times \overline{A} = \hat{x}(\frac{\partial A_z}{\partial y} - \frac{\partial A_y}{\partial z}) + \hat{y}(\frac{\partial A_x}{\partial z} - \frac{\partial A_z}{\partial x}) + \hat{z}(\frac{\partial A_y}{\partial x} - \frac{\partial A_x}{\partial y}) = \begin{vmatrix} \hat{x} & \hat{y} & \hat{z} \\ \partial & \partial & \partial \\ \partial x & \partial y & \partial z \\ A_x & A_y & A_z \end{vmatrix} \quad (A.7)$$

The gradient, divergence and curl for the cylindrical and spherical coordinates are given in Table A.5

Cylindrical coordinates

$$\nabla f = \hat{r}\frac{\partial f}{\partial r} + \hat{\Phi}\frac{1}{r}\frac{\partial f}{\partial \Phi} + \hat{z}\frac{\partial f}{\partial z}$$

$$\nabla \cdot \overline{A} = \frac{1}{r}\frac{\partial}{\partial r} rA_r + \frac{1}{r}\frac{\partial A_\Phi}{\partial \Phi} + \frac{\partial A_z}{\partial z}$$

$$\nabla \times \overline{A} = \hat{r}\left(\frac{1}{r}\frac{\partial A_z}{\partial \Phi} - \frac{\partial A_\Phi}{\partial z}\right) + \hat{\Phi}\left(\frac{\partial A_r}{\partial z} - \frac{\partial A_z}{\partial r}\right) + \hat{z}\frac{1}{r}\left(\frac{\partial}{\partial r} rA_\Phi - \frac{\partial A_r}{\partial \Phi}\right) = \begin{vmatrix} \hat{r}\frac{1}{r} & \hat{\Phi} & \hat{z}\frac{1}{r} \\ \partial & \partial & \partial \\ \partial r & \partial \Phi & \partial z \\ A_r & rA_\Phi & A_z \end{vmatrix}$$

Spherical coordinates

$$\nabla f = \hat{r}\frac{\partial f}{\partial r} + \hat{\Theta}\frac{1}{r}\frac{\partial f}{\partial \Theta} + \hat{\Phi}\frac{1}{r\sin\Theta}\frac{\partial f}{\partial \Phi}$$

$$\nabla \cdot \overline{A} = \frac{1}{r^2}\frac{\partial}{\partial r} r^2 A_r + \frac{1}{r\sin\Theta}\frac{\partial}{\partial \Theta}(A_\Theta \sin\Theta) + \frac{1}{r\sin(\Theta)}\frac{\partial A_\Phi}{\partial \Phi}$$

$$\nabla \times \overline{A} = \hat{r}\frac{1}{r\sin\Theta}\left(\frac{\partial}{\partial \Theta}(A_\Phi \sin\Theta) - \frac{\partial A_\Theta}{\partial \Phi}\right) + \hat{\Theta}\frac{1}{r}\left(\frac{1}{\sin\Theta}\frac{\partial A_r}{\partial \Phi} - \frac{\partial}{\partial r} rA_\Phi\right) + \hat{\Phi}\frac{1}{r}\left(\frac{\partial}{\partial r} rA_\Theta - \frac{\partial A_r}{\partial \Theta}\right)$$

Table A.5 *Gradient, divergence and curl in cylindrical and spherical Coordinates.*

A.2 Electromagnetic theory and Maxwell's equations.

A force acts on two or more bodies that have an electric charge. Unlike charges attract but like charges repel. This force is given by *Coulomd's law.*

$$F = k\frac{Q_1 Q_2}{r^2} \quad (A.8)$$

This electric force is inversely proportional to the square of the distance between the charges Q_1 and Q_A. k is the *constant of proportionality* and is given by

$$k = \frac{1}{4\pi\varepsilon} \tag{A.9}$$

where ε is the *permittivity* or dielectric constant. The permittivity of free space is $\varepsilon_0 = 8.85 \times 10^{-12} (F/m)$. In most of the cases, the permittivity of an object is referred relative to the permittivity of the vacuum.

$$\varepsilon_r = \frac{\varepsilon}{\varepsilon_0} \tag{A.10}$$

where ε_r is the *relative permittivity* of dielectric and ε is the permittivity of the dielectric. Around a charge, Q_1, there is an electric field in which forces act. The force per unit charge is defined as the *electric field intensity* $(\overline{E})$ and is given by

$$\overline{E} = \frac{Q_1}{4\pi\varepsilon_r\varepsilon_0 r^2} = \frac{\Delta\overline{F}}{\Delta Q}\left(Vm^{-1}\right) \tag{A.11}$$

If more than one charge is present then the total or resultant field at a point is the vector sum of the individual component fields at the point. The volume *charge density* at a point is defined by

$$\rho_u = \frac{Q}{u} = \lim_{\Delta Q \to 0} \frac{\Delta Q}{\Delta u} \tag{A.12}$$

the charge now can be expressed in terms of the charge density as $Q = \rho(\overline{R})du$ where $\overline{R}$ is the vector to infinitesimal charge of volume du. The work (or energy) per unit charge required to transport ΔQ a distance Δx is called the difference in *electric potential* ΔV across Δx. The work per coulomb required to bring a positive test charge from infinity to a point r_1 is called the *absolute potential* and is defined by

$$V = \frac{1}{4\pi\varepsilon_0}\frac{Q}{r_1}(Volts) \tag{A.13}$$

The *potential difference* at a field is given by the line integral

$$\Delta V = -\int_a^b \overline{E} \cdot d\overline{L} = -\int_a^b |\overline{E}| \cos\theta |d\overline{L}| \tag{A.14}$$

and for a lamellar or conservative field is zero.

$$\oint \overline{E} \cdot d\overline{L} = 0 \tag{A.15}$$

The gradiant of V is a vector with a direction along the field line. Since a potential rise occurs when moving against the electric field the direction of the gradiant is opposite to that of the field. Thus the gradiant of V is

$$\nabla V = \hat{x}\frac{\partial V}{\partial x} + \hat{y}\frac{\partial V}{\partial y} + \hat{z}\frac{\partial V}{\partial z} = -\overline{E} \qquad \text{(A.16)}$$

The gradiant of a scalar potential is a vector in the direction of the maximum rate of change of V. In an electric dipole the field lines can be replaced by tubes. If each tube represents a constant amount of *electric flux* ψ, then at any point there is a flux density D. The electric flux through any surface equals the integral of the *flux density* over the surface and in mathematics this is

$$\psi = \int_s \overline{D} \cdot d\overline{s} \qquad \text{(A.17)}$$

the electric flux density is given by

$$\overline{D} = \varepsilon \overline{E} \qquad \text{(A.18)}$$

and electric flux can be expressed as

$$\psi = \int_s \frac{Q}{4\pi r^2} ds \qquad \text{(A.19)}$$

The flux density and the electric filed intensity are vectors with the same direction. This is true for all isotropic media, i.e. media whose properties do not change with direction. *Gauss's law* states that the electric field flux through any closed surface equals the charge enclosed. This can be expressed as

$$\oint_s \overline{D} \cdot d\overline{s} = \oint_u \rho du = \oint_u \nabla \cdot \overline{D} du = Q \qquad \text{(A.20)}$$

The divergence of the flux density gives the free space charge density at a point.

$$\nabla \cdot \overline{D} = \frac{\partial D_x}{\partial x} + \frac{\partial D_y}{\partial y} + \frac{\partial D_z}{\partial z} = \rho \text{ Maxwell's divergence equation from Gauss} \qquad \text{(A.21)}$$

The divergence theorem states that the integral of the normal component of a vector function over a closed surface, s, equals the integral of the divergence of that vector throughout the volume, υ, enclosed by the surface s. The $\nabla \cdot \overline{D}$ has a value whenever charge is present.

A *capacitor* is a device for storing electric charge, and hence, electric energy. The capacitance of a capacitor is defined as

$$C = \frac{Q}{V} = \varepsilon \frac{A}{d}(F) \qquad \text{(A.22)}$$

where A is the area of a parallel plate capacitor and d is the distance between the two plates. Between the plates of a capacitor there is an electric field that is given by

E=V/d. A medium is homogeneous if its physical characteristics (mass density, molecular structure, etc.) do not very with from point to point. On the other hand, materials that do not have this property are called *inhomogeneous*, *nonhomogeneous*, or *heterogeneous*. A medium is linear with respect to an electrostatic field if the flux density $\overline{D}$ is proportional to the electric field intensity $\overline{E}$, like the case of free space. If is not, the material is called nonlinear. An isotropic material is the one whose properties are independent of direction. If the properties of the material differ with direction then the material is call *anisotropic* or *nonisotropic*. If a dielectric is placed in an electric field, although there is no migration of charges, there is a slight displacement of the negative and positive charges of the dielectric's atoms or molecules. The electric field intensity in a dielectric cannot be increased infinitely. Is a certain value is exceeded, sparking occurs and the dielectric is said to *break down*. The maximum field intensity that a dielectric can sustain without breakdown is called its *dielectric strength*. A dielectric in the influence of an electric field is polarized. This *polarization*, depending on the dielectric, can be temporary or permanent. The dielectric can change the electric flux density of a parallel plate capacitor to

$$\overline{D} = \varepsilon_0 \overline{E} + \overline{P} \tag{A.23}$$

where $\overline{P}$ is the polarization which is equal to the surface charge density

$$\rho_{sp} = \frac{Q}{A} \tag{A.24}$$

of the dielectric. For an isotropic and linear the above equation can be written as

$$\overline{D} = \varepsilon_0 \overline{E} + \overline{P} = e_r e_0 \overline{E} \tag{A.25}$$

The capacitance of a parallel plate capacitor with dielectric is now given by

$$C = \frac{\varepsilon A}{d} = \frac{\varepsilon_r \varepsilon_0 A}{d} \tag{A.26}$$

The energy stored in a capacitor, is

$$W = \frac{1}{2}\frac{Q^2}{C} = \frac{1}{2}CV^2 = \frac{1}{2}QV \tag{A.27}$$

This energy is stored in the electric field between the plates of the capacitor. No material is needed for energy to be stored by a field. Thus, energy is present even in the vacuum. Energy density is the energy divided by the volume that occupies (e.g. the volume of a capacitor) and is given by.

$$w = \frac{1}{2}(\varepsilon_0 E^2 + PE) = \frac{1}{2}\varepsilon\ E \qquad \text{(A.28)}$$

The second part in the brackets is giving the energy stored in the dielectric due to polarization of the molecules. The energy stored it can be now expressed in terms of energy density as

$$W = \int_u wdu = \frac{1}{2}\int_u \varepsilon E^2 du \qquad \text{(A.29)}$$

Electric charges in motion constitutes an *electric current*, and any current currying medium is called *conductor*. Current is defined by

$$\bar{I} = \bar{v}_d \rho A \quad \text{(Amperes)} \qquad \text{(A.30)}$$

where $\bar{v}_d$ in the *drift velocity*. The *current density* is given by

$$\bar{J} = \frac{\bar{I}}{A} = \bar{v}_d \rho \quad \text{(Amperes/meter)} \qquad \text{(A.31)}$$

Georg Simon Ohm has determined the relation between the voltage and the current. The Ohm's law states that potential difference or voltage V between the ends of a conductor is equal to the product of the *resistance* and the current and in mathematical form is given by

$$V = IR \text{ (Volts)} \qquad \text{(A.32)}$$

where R is the resistance in Ohms (Ω). Multiplying the voltage by the current yields the work per unit time, or power:

$$P = IV = I^2R = V^2/R \quad \text{(Watts)} \qquad \text{(A.33)}$$

Resistively is the resistance of a material per unit volume and has units of Ohm-meter (Ωm). Thus, resistively is independed of the dimensions of the resistor. One over the resistively gives the *conductivity* $(\sigma)$of a material in Siemens. Similar to conductivity, conductance is equal to one over the resistance of the *resistor*. Using Ohm's law it can be shown that at a point

$$\bar{J} = \sigma\bar{E} \qquad \text{(A.34)}$$

Kirchhoff's voltage law states that the algebraic sum of the electromotive forces (emfs) around a closed circuit equals the sum of the ohmic, or IR, drops around the circuit.

$$\sum V = I\sum R \qquad \text{(A.35)}$$

Kirchhoff's current law states that the algebraic sum of the currents at a junction is zero.

$$\sum I = 0 \text{ or } \oint_s \bar{J} \cdot d\bar{s} = 0 \tag{A.36}$$

The divergence of $\bar{J}$, according to the current law of Kirchhoff, is

$$\nabla \cdot \bar{J} = -\frac{\partial \rho}{\partial t} \tag{A.37}$$

For steady currents, the left part is zero. The current then is given by the rate of charge change per time.

$$i = \frac{dQ}{dt} = C\frac{dV}{dt} \tag{A.38}$$

The *motor equation*, introduced by Andrè Marie Amperè in 1820, gives the force on a wire in a magnetic field.

$$\bar{F} = (\bar{I} \times \bar{B})L \tag{A.39}$$

$$\text{or } d\bar{F} = (\bar{I} \times \bar{B})dL \tag{A.40}$$

where $\bar{F}$ is the vector indicating the force element in a conductor of L length, $\bar{I}$ is the current in the conductor and $\bar{B}$ is the flux density. Jean Baptiste Biot and Felix Savart have shown that current passing in a wire element ΔL produces a *magnetic field* given by (Biot-Savart law)

$$d\bar{B} = \frac{\mu}{4\pi}\frac{I\bar{R} \times \Delta\bar{L}}{|\bar{R}^3|} \tag{A.41}$$

$$\text{or } dB = \frac{\mu}{4\pi}\frac{IdL\sin\theta}{r^2} \text{ (Tesla)} \tag{A.42}$$

where μ is the *permeability* of medium ($\mu = \frac{L}{d}$ inductance per unit length). The permeability of vacum is $\mu_0 = 400\pi$ nHm^{-1}. The magnetic flux of a non-uniform area is given by

$$\psi_m = \iint \bar{B} \cdot d\bar{s} \tag{A.43}$$

and according to Gauss the integral of magnetic flux density over a close surface is zero.

$$\oint_s \bar{B} \cdot d\bar{s} = 0 \tag{A.44}$$

$$\text{and } \nabla \cdot \bar{B} = 0 \tag{A.45}$$

This is the Maxwell's equation from gauss's law for magnetic fields.

An *inductor* is a device to store energy in magnetic field. The *inductance* is the ratio of the total magnetic linkage (Λ) to the current I through the inductor.

$$L = \frac{N\psi_m}{I} = \frac{\Lambda}{I} = \frac{d\Lambda}{dI} \qquad \text{(A.46)}$$

Table A.6 gives the inductance for simple geometries.

Inductor	**Inductance**
Long solenoid	$L = \frac{\mu N^2 A}{l}$ A= cross-sectional l = length
Toroid	$L = \frac{\mu N^2 r^2}{2R}$ r = radius of coil R = radius of toroid

Table A.6 *Inductance of simple geometries.*

The *magnetic field* is a vector that has the same direction as the flux density and is given by

$$\overline{H} = \frac{\overline{B}}{\mu} \qquad \text{(A.47)}$$

Ampère's law states that the line integral of $\overline{H}$ around a single closed path is equal to the current enclosed.

$$\oint \overline{H} \cdot d\overline{L} = \iint_A \overline{J} \cdot d\overline{s} = I \qquad \text{Ampère's law a Maxwell equation} \qquad \text{(A.48)}$$

To get the current density at a point the curl equation is used.

$$curl\overline{H} = \nabla \times \overline{H} = \overline{J} \qquad \text{(A.49)}$$

$\nabla \times \overline{H}$ has a value whenever a current is present.

If the flux changes with time then an emf in induced. From Faraday's law this is

$$V = -\frac{d\psi_m}{dt} = \oint \overline{E} \cdot d\overline{L} - \int_s \frac{\partial \overline{B}}{\partial t} \cdot d\overline{s} \qquad \text{(A.50)}$$

and in differential form

$$\nabla \times \overline{E} = -\frac{\partial \overline{B}}{\partial t} \quad \text{Maxwell's equation from Faraday differential equation} \qquad \text{(A.51)}$$

The current through a resistor is called a *conductance current*, while the current through the capacitor is called the *displacement current*. Since the current density, the electric displacement, and the electric field intensity are actually space vectors, which all having the same direction in isotropic media there relation can be expressed as

$$\bar{J}_{diss} = \varepsilon \frac{d\bar{E}}{dt} = \frac{d\bar{D}}{dt}, \tag{A.52}$$

$$\bar{J}_{cond} = \sigma \bar{E} \tag{A.53}$$

$$\text{and } \bar{J}_{total} = \bar{J}_{cond} + \bar{J}_{disp} \tag{A.54}$$

Using the Ampère's law, which states that the line integral of $\bar{H}$ is equal to the current enclosed, we can get

$$\oint \bar{H} \cdot d\bar{L} = \iint_s \left(\bar{J} + \frac{\partial \bar{D}}{\partial t} \right) \cdot d\bar{s} \quad \text{Maxwell's equation from Ampère's law in integral form} \tag{A.55}$$

and

$$\nabla \times \bar{H} = \bar{J} + \frac{\partial \bar{D}}{\partial t} \quad \text{Maxwell's equation from Ampère's law in differential form} \tag{A.56}$$

Table A.7 is a summary of Maxwell's equations in both their integral and differential form.

No.	Integral	Differential	Description
1	$\oint_s \overline{D} \cdot d\overline{s} = \oint_u \rho du = \oint_u \nabla \cdot \overline{D} du = Q$	$\nabla \cdot \overline{D} = \rho$	**Maxwell's equation from Gauss's law for electric field.** Gauss's law states that the electric field flux D through any closed surface equals the charge enclosed.
2	$\Psi = \oint_s \overline{B} \cdot d\overline{s} = 0$	$\nabla \cdot \overline{B} = 0$	**Maxwell's equation from Gauss's law for magnetic fields.** According to Gauss the integral of magnetic flux density over a closed surface is zero.
3	$V = -\frac{d\psi_m}{dt} = \oint \overline{E} \cdot d\overline{L} = -\int_s \frac{\partial \overline{B}}{\partial t} \cdot d\overline{s}$	$\nabla \times \overline{E} = -\frac{\partial \overline{B}}{\partial t}$	**Maxwell's equation from Faraday's law.** If the magnetic flux changes with time then an emf in induced.
4	$\oint \overline{H} \cdot d\overline{L} = \oint_s \frac{\partial \overline{D}}{\partial t} \cdot d\overline{s} = I$	$\nabla \times \overline{H} = \frac{\partial \overline{D}}{\partial t}$	**Maxwell equation from Ampère's law.** Ampère's law states that the line integral of $\overline{H}$ is equal to the current enclosed.

Table A.7 *Maxwell's equations in integral and differential form for free space.*

Appendix B

The Effect of Short Pin on PIFA f_r (8-9/July/98)

	Description:	600→1400 MHz	d = 5mm	2 Short pins fix pin at 0a
Trace File Number (trace*.prn)	**Fr (MHz)**	**VSWR**	**SMITH**	**S_{11} dB**
1g	**1001.875**	818	819	820
0-4	**1055.500**	887	888	889
2g	**1057.000**	821	822	823
3g	**1096.375**	824	825	826
0-5	**1142.125**	890	891	892
4g	**1147.375**	827	828	829
0-12	**1171.938**	911	912	913
0-6	**1174.188**	873	894	895
5g	**1187.500**	830	831	832
12g – b	**1201.189**	854	855	856
0-7	**1227.062**	896	897	898
6g	**1231.000**	833	834	835
12g - a	**1232.668**	851	852	853
12-0	**1233.250**	875	876	877
12f	**1243.375**	857	858	859
11g	**1248.000**	848	849	850
12a	**1248.438**	872	875	874
0-8	**1256.875**	899	900	901
12e	**1261.375**	860	861	862
0-11	**1264.188**	908	909	910
12b	**1269.812**	869	870	871
7g	**1270.375**	836	837	838
12d	**1272.062**	863	864	865
10g	**1285.000**	847	848	849
12c	**1292.875**	866	867	868
0-9	**1292.875**	902	903	904
8g	**1306.375**	839	840	841
0-10	**1306.938**	905	906	907
9g	**1315.375**	842	843	844
0-0	**804.620**	935	936	937
0b	**829.938**	917	918	919
0-0	**840.625**	914	915	916
0-1	**847.938**	878	879	880
0c	**878.312**	920	921	922
0-2	**907.562**	881	882	883
0d	**913.750**	923	924	925
0g	**937.375**	932	933	934
0f	**942.438**	929	930	931

0e	**945.250**	926	927	928
0g	**961.000**	815	816	817
0-3	**988.562**	884	885	886

The Effect of Fixed Value Capacitor Pin on the Fr of the PIFA (10/July/98)

C pF	Ref. Corner	Fr MHz	VSWR	Smith	S_{11}dB
3	1	**972.487**	1023	1024	1025
3	2	**998.812**	1014	1015	1016
3	3	**1158.000**	1017	1018	1019
3	4	**1161.938**	1020	1021	1022
5	1	**890.625**	975	976	977
5	2	**970.250**	966	967	968
5	3	**1149.406**	989	970	971
5	4	**1155.906**	972	973	974
10	1	**856.094**	963	964	965
10	2	**936.531**	954	955	956
10	3	**1113.250**	957	958	959
10	4	**1104.719**	960	961	962
22	1	**806.438**	987	988	989
22	2	**907.125**	978	979	980
22	3	**1081.969**	981	982	983
22	4	**1058.812**	984	985	986
32	1	**801.938**	999	1000	1001
32	2	**888.562**	990	991	992
32	3	**1050.000**	993	994	995
32	4	**1053.938**	996	997	998
46	1	**801.35**	1011	1012	1013
46	2	**888.375**	1002	1003	1004
46	3	**1059.000**	1005	1006	1007
46	4	**1050.000**	1008	1009	1010
100	1	**795.750**	1035	1036	1037
100	2	**892.500**	1026	1027	1028
100	3	**1060.688**	1029	1030	1031
100	4	**1058.700**	1032	1033	1034

Dual-Band GSM900/PNC1800 PIFA Using Capacitors 850-1950MHz

Frequency (Fr) MHz	VSWR	Tx/Rx
890	939	939
945	940	941
960	942	943
1710	944	945
1795	946	947
1880	948	949
Dipole 1- Dipole2		950

Measurements of the VSWR with BB619 Varactor (22/May/1998)

VSWR	Voltage (V)	TxRx (S_{12})dB
521	0	554
522	1	555
523	2	556
524	3	557
525	4	558
526	5	559
527	6	560
528	7	561
529	8	562
530	9	563
531	10	564
532	11	565
533	12	566
534	13	567
535	14	568
536	15	569
537	16	570
538	17	571
539	18	572
540	19	573
541	20	574
542	21	575
543	22	576
544	23	577
545	24	578
546	25	579
547	26	580
548	27	581
549	28	582
550	29	583
551	30	584
552	31	585
553	32	586

Far Field Radiation patterns Measurements (14/10/1998)

Trace File Number (trace*.prn)	Description Distance: 1m Reference antenna: Dipole 2
1100	Whip XY E_Θ Vertical R.P.
1101	Whip XY E_Φ Vertical R.P.
1102	Whip YZ E_Θ Vertical R.P.
1103	Whip YZ E_Φ Vertical R.P.
1104	Whip XZ E_Θ Vertical R.P.
1105	Whip XZ E_Φ Vertical R.P.
1106	Helix XY E_Θ Vertical R.P.
1107	Helix XY E_Φ Vertical R.P.
1108	Helix YZ E_Θ Vertical R.P.
1109	Helix YZ E_Φ Vertical R.P.
1110	Helix XZ E_Θ Vertical R.P.
1111	Helix XZ E_Φ Vertical R.P.
1112	PIFA XY E_Θ Vertical R.P.
1113	PIFA XY E_Φ Vertical R.P.
1114	PIFA YZ E_Θ Vertical R.P.
1115	PIFA YZ E_Φ Vertical R.P.
1116	PIFA XZ E_Θ Vertical R.P.
1117	PIFA XZ E_Φ Vertical R.P.

Measurements on Operator's Effect on the Radiation Pattern (21/10/98)

Trace File Number (trace*.prn)	Description (**Bold** indicates data used in the report)
1118	Helix E_Θ (Vertical) Measurements with operator
1119	**Helix E_Θ (Vertical) Measurements with operator**
1120	Helix E_Θ (Vertical) Measurements with operator
1121	Helix E_Φ (Vertical) Measurements with operator
1122	Helix E_Φ (Vertical) Measurements with operator
1123	**Helix E_Φ (Vertical) Measurements with operator**
1124	Monopole E_Θ (Vertical) Measurements with operator
1125	**Monopole E_Θ (Vertical) Measurements with operator**
1126	Monopole E_Θ (Vertical) Measurements with operator
1127	**Monopole E_Φ (Vertical) Measurements with operator**
1128	Monopole E_Φ (Vertical) Measurements with operator
1129	Monopole E_Φ (Vertical) Measurements with operator
1130	PIFA E_Θ (Vertical) Measurements with operator
1131	**PIFA E_Θ (Vertical) Measurements with operator**
1132	PIFA E_Θ (Vertical) Measurements with operator
1133	PIFA E_Φ (Vertical) Measurements with operator
1134	**PIFA E_Φ (Vertical) Measurements with operator**
1135	PIFA E_Φ (Vertical) Measurements with operator

Measurements for the Absolute Gain of The Antennas

Trace File Number (trace*.prn)	Description Center: 945MHz Span: 500MHz Points: 1601
1136	Dipole 2 -- Whip
1137	Dipole 1 -- Whip
1138	Dipole 2 -- PIFA
1139	Dipole 1 -- PIFA
1140	Dipole 2 -- Helix
1141	Dipole 2 -- Helix
1142	Dipole 2 -- Dipole 1

Measuring the VSWR of The Antennas

Trace File Number (trace*.prn)	Description Center: 945MHz Span: 500MHz Points: 1601
1143	PIFA VSWR
1144	PIFA Smith Chart
1145	Helix VSWR
1146	Helix Smith Chart
1147	Whip VSWR
1148	Whip Smith Chart
1149	Dipole 2 VSWR
1150	Dipole 2 Smith Chart

Alternative dual-band PIFA (proposal).

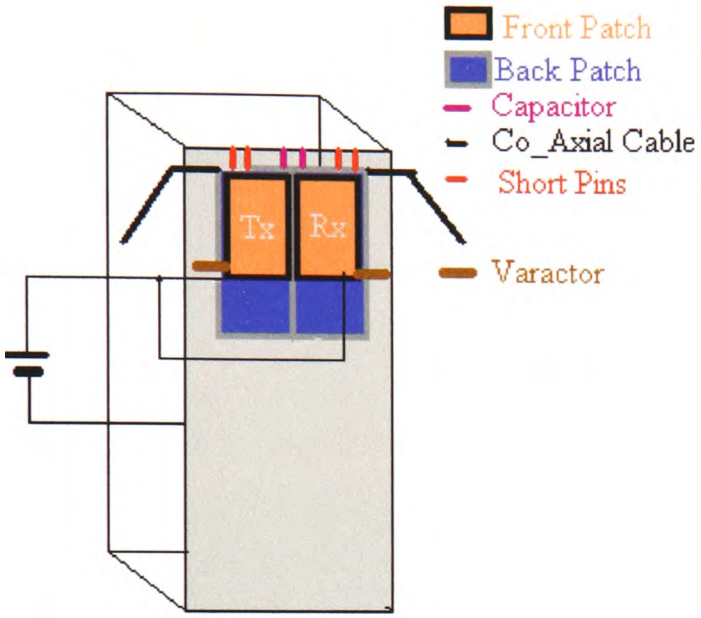

Fig. B.1 *Dual patch PIFA for GSM900.*

From Fig. B.1 it can be seen that two patches are used instead of one. The patch is approximately at a height of 5mm above the ground. There are two short pins near the feed and a variable capacitor on the opposite corner. By changing the value of this capacitor the antenna can resonate at the 890MHz (Tx) and at 935MHz (Rx).

A second patch is added on the top of the first one. The distance between the two patches is nearly zero. There is only a thin sheet of paper between them so there is no electrical (DC) connection between them. The varactor is connected at the bottom corners. The corners of the patch are preferred, because there the field strength is higher and, hence, the effect of the capacitor is enhanced. By changing the voltage across the diode its capacitance changes and the resonance frequency is increased by a maximum of 25MHz.

Dimensions of the Prototype Antenna:

Front Patch = 25 x 13 mm
Back Patch = 35 x 13 mm
Short pin 1 = 3mm from feed cornet
Short pin 2 = 6mm from feed cornet
Varactor = 25mm from the feed point
No Dielectric is used
Box = 100 x 50 x 25
Coaxial cables have the same length.

Additional Pictures.

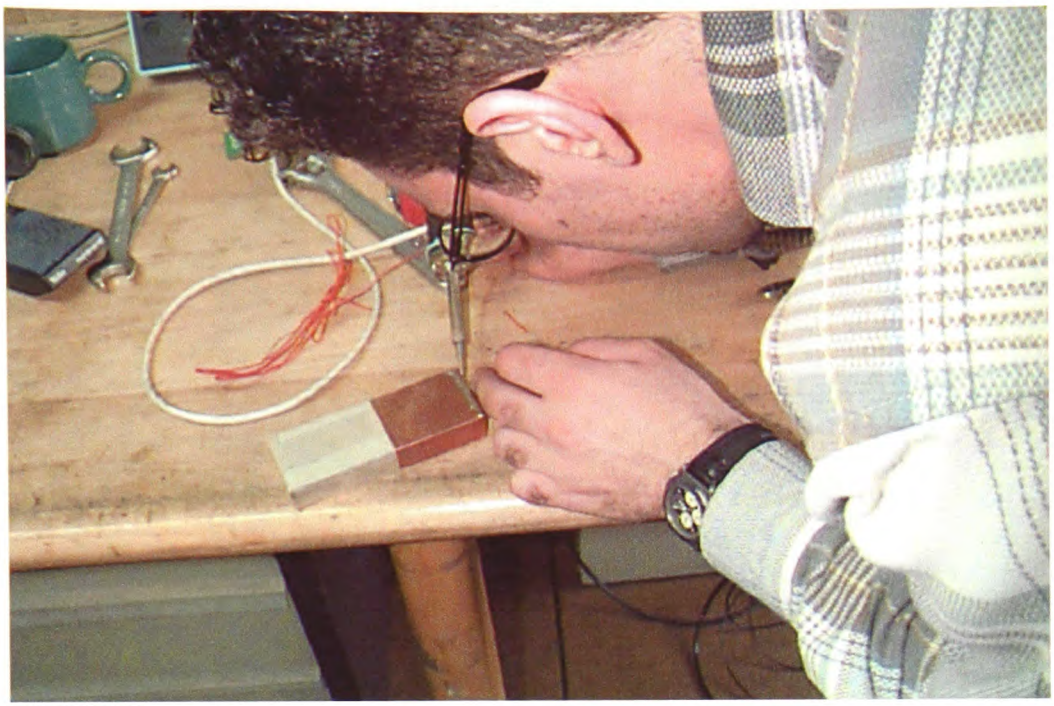

Fig. B.2 *Making of the prototype antennas.*

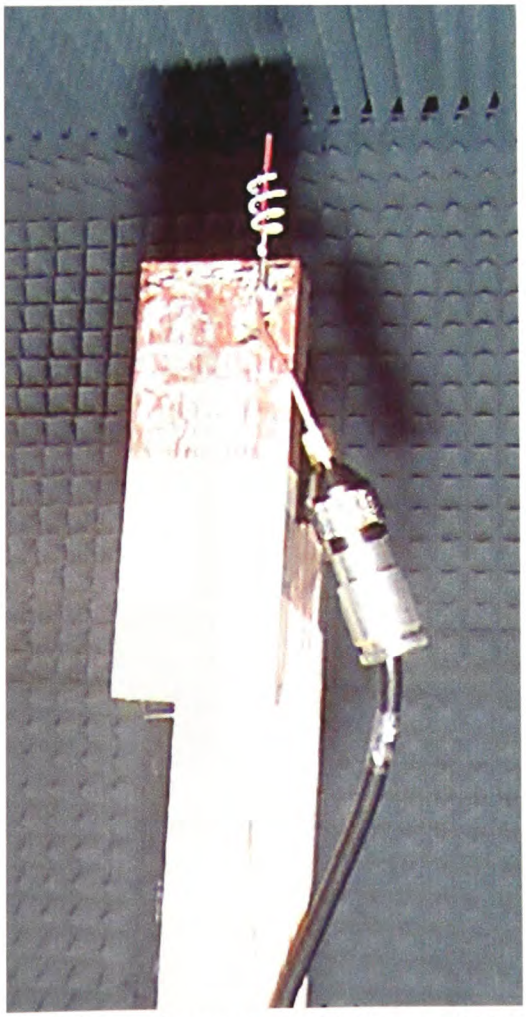

Fig. B.3 *Dual-band Helix-Monopole antenna. Helix at ~945MHz and monopole at ~1800MHz.*

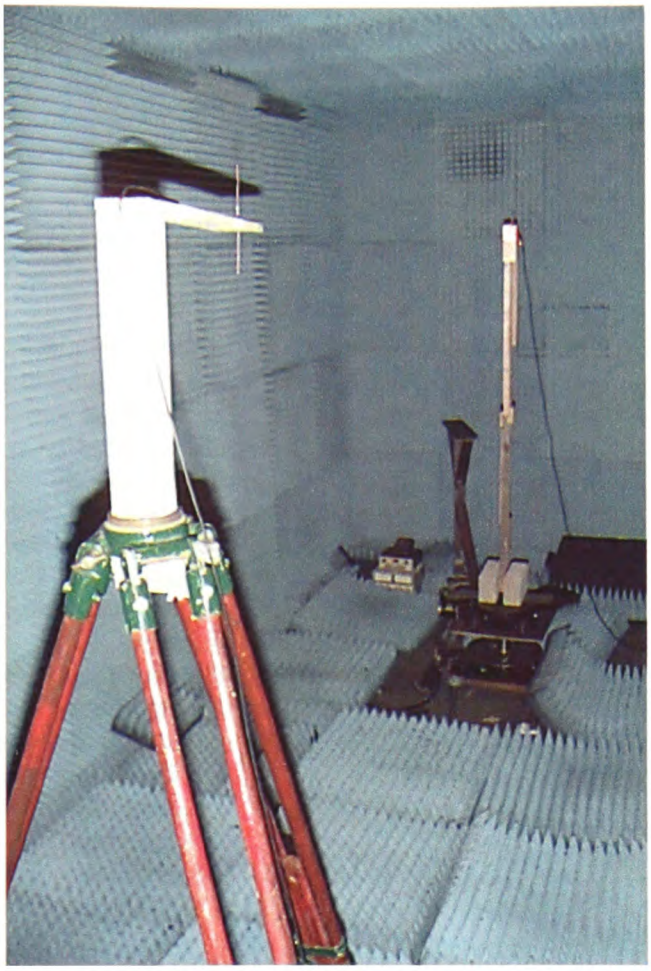

Fig. B.4 *Antenna measurements setup in the anechoic chamber.*

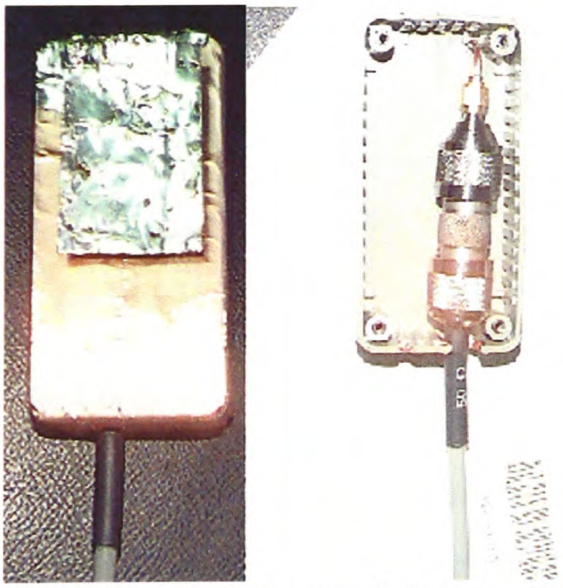

Fig. B.5 *PIFA antenna with built-in connectors designed to investigate the effect of the connector on the radiation patterns.*

TUNING TECHNIQUES FOR THE PLANAR INVERTED-F ANTENNA

P K Panayi[1], M Al-Nuaimi[2], L P Ivrissimtzis[3]

[1,2] University of Glamorgan, UK
[3] NEC Technologies (UK) LTD, UK

Abstract: - The rapid growth of mobile communications since the introduction of GSM has challenged the industry for designing terminals of reduced size, cost and power consumption. The efficiency and size trade-offs of the antenna on such terminals become an important issue. On the other hand, multi-band operation covering the existing GSM900/DCS1800 and the future UMTS bands is another significant subject of investigation in the mobile phone industry. In this paper, different methods for tuning the planar inverted-F antenna (PIFA) are discussed, in particular with regard to the positioning of the short pins and the introduction of tuning capacitors. A reduced size dual band fine tuned PIFA for the GSM900/DCS1800 bands is introduced and its performance demonstrated. Finally, a technique employing reversed biased varactors for electronically tuning the PIFA is presented.

1. INTRODUCTION

Competition in the mobile phone industry has dictated the trends for miniature and power efficient terminals. The size of future hand-held phones is expected to be further reduced, while, with the introduction of the third generation of digital cellular systems, more functions will have to be provided. However, there are two limitations to achieve these goals: firstly, the battery size and capacity and, secondly, the external antenna dimensions and efficiency.

Built-in, low profile patch antennas offer a range of new possibilities towards compact and efficient terminal design. The PIFA, which has been the subject of recent research [1]-[5], is an alternative solution, characterised by both higher efficiency (compared to a typical microstrip patch antenna) and lower profile (compared to wire antennas). The absolute directive gain of the PIFA can be as high as 6dBi if good matching can be achieved. However, the narrow reflection coefficient bandwidth which characterises the simple PIFA is one of the limitations for its commercial application in mobile hand-sets. Typical required bandwidths for a VSWR<2 at the antenna input are 7.4% and 9.5% for the GSM900 and DCS1800 bands, respectively, and such bandwidths are nominally desirable under both free space and actual operating conditions. Further, for the future UMTS system, antennas should be capable of achieving bandwidths in excess of 15% (300MHz).

In this paper, different techniques for controlling the resonance frequency (f_r) of the PIFA are studied. By controlling f_r, in order, for instance, to match the allocated channel frequency, the operational bandwidth of the antenna can be enhanced, while by achieving lower VSWR for all frequency channels, the overall antenna efficiency can be increased.

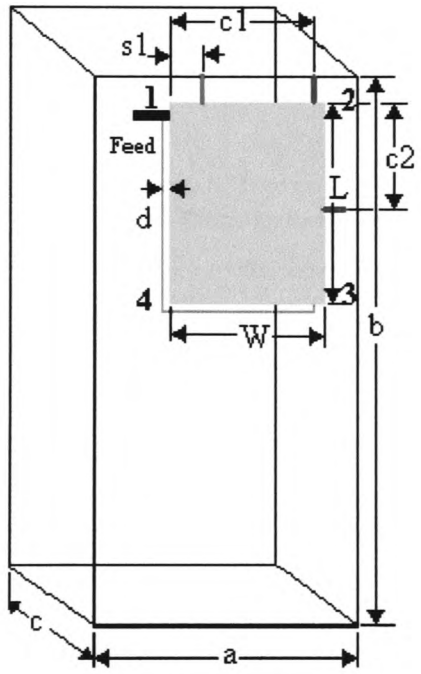

Figure 1: The dual-band fine tuned PIFA:
s1: short pin
c1: calibration variable capacitor
c2: tuning variable capacitor

2. SHORT PIN EFFECT ON RESONANCE FREQUENCY

The PIFA and radio case configuration is shown in Fig. 1. The position of the feed point and the dimensions of the conductive case and the dimensions and height of

the patch are kept constant (L = 40mm, W = 35mm, d = 5mm). A fixed short pin at a distance s1=5mm from the top left corner is introduced to add the necessary inductance to the antenna so that the VSWR at any f_r is kept less than 2. A second short pin (traveling pin) is then introduced to achieve fine tuning of the PIFA. The VSWR and input impedance of the antenna is then measured in steps of 5mm. For instance, 1→4 in Fig. 2 indicates that the short pin is moving from reference corner 1 towards reference corner 4, as shown in Fig. 1. The resonance frequency for the four different cases studied, corresponding to the short pin traveling along the four edges, are plotted in Fig. 2. As the distance from the feed increases, f_r increases too, but up to a point. When the short pin is approaching the opposite corner, f_r starts increasing again. It can be said at this point that the corners of the patch have a noticeable effect on f_r and that f_r does not only dependent on the distance of the short pin from the feed point. This is because of the high electric field intensity around the corners [5].

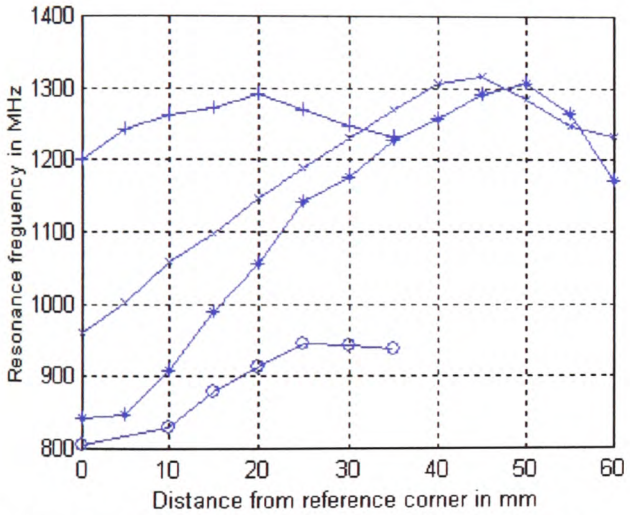

Figure 2: Resonance frequency of PIFA for various short pin positions.
o Reference corner 1→2, x Reference corner 2→3,
+ reference corner 3→4, * reference corner 1→4.

The effective bandwidth of the PIFA using this technique has been found to be as high as 502MHz (804 → 1306 MHz) and is by far wider than those associated with the whip and small helix antennas. The effective bandwidth is defined as the frequency range that can be covered by this antenna type, using one of the tuning techniques described in this paper. It should be further noted that the VSWR within this bandwidth is always less that 2. For this particular configuration, the use of the left or right side for tuning the PIFA is more suitable than the top and bottom because it gives a wider effective bandwidth.

3. CAPACITANCE SHORTED PIFA

The traveling short pin described above can be replaced by a capacitor. By varying the value of the capacitance, the reactance of the antenna changes and, as a result, f_r changes, as depicted in Fig. 3. The antenna dimensions are the same as those used in Section 2. The effect of the capacitance values have been measured at four reference points 1,2,3, and 4, as shown in Fig. 1. The capacitors used in these measurements are miniature, multi-layer, ceramic capacitors with a tolerance of ± 5%.

In Fig. 3, the results of a number of measurements are shown for capacitance values ranging from 3pF to 100pF. For low capacitance values f_r has a high value. As the capacitance decreases f_r decreases, but the rate of change of f_r with capacitance is reduced. For capacitance values higher than 30pF, f_r is almost constant. By using this method, the effective bandwidth, when the capacitor has a fixed position, is 175 MHz. From these measurements it is also evident that f_r also depends on the position of the capacitors. The further the capacitor from the feed, the higher the frequency band covered.

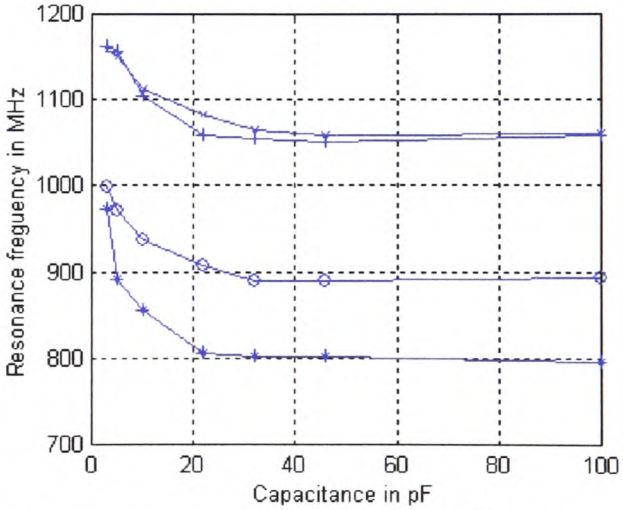

Figure 3: Resonance frequency vs pin capacitance placed at four reference points:
* Reference point 1, o Reference point 2,
x Reference point 3, + Reference point 4.

4. DUAL-BAND FINE TUNED PIFA

Based on the information from the measurements described above regarding the position and capacitance value of the pins, a dual-band (GSM900/DCS1800) PIFA has been designed. The dimensions of the antenna can be significantly reduced to L=40mm and W=35mm, since the frequency band can be controlled by the position of the pins and their capacitance value. The position of the fixed short pin for this antenna is again 5mm from reference corner 1 and the height of

the antenna from the case is d=5mm. Two variable capacitors (1.8–12.5pF) have been used. The first one (c1=25mm from corner 1) is referred to as the calibration capacitor, because its value is set once during calibration. For the particular antenna dimensions considered here, its value was measured to be 7.3pF. The second capacitor is referred to as the tuning capacitor, because it is used to tune the antenna at any frequency channel within the two bands.

In Fig. 4, the VSWR and the normalised bore-sight gain of the dual band fine tuned PIFA are shown for three tuning capacitor values. Both GSM900 (890-960MHz) and DCS1800 (1710-1880MHz) bands can be accommodated from this antenna model just by changing the tuning capacitor value from 1.8pF to 3.0pF.

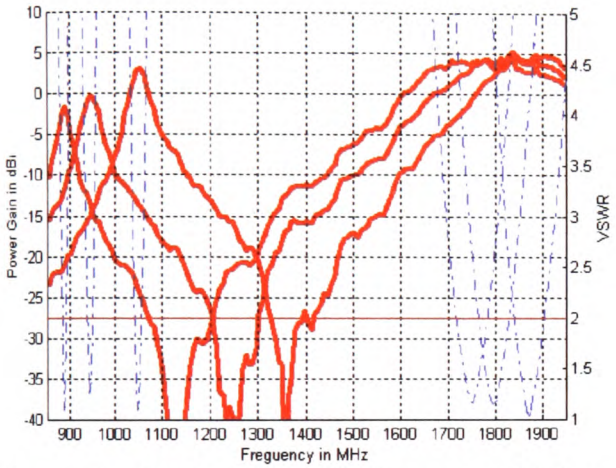

Figure 4: Bore-sight gain (dBi) and VSWR vs. frequency for the dual-band fine tuned PIFA for three tuning capacitor values.

5. VOLTAGE CONTROLLED FINE TUNED PIFA

Based on the experience gained from the experiments outlined above, a voltage controlled fine tuned PIFA for the GSM900 band has been designed. The antenna geometry is illustrated in Fig 5. A top patch has been introduced to provide the electric isolation between the varactor and voltage-source system and the antenna, since the PIFA is connected to the ground via the short pin. Note that the patch can be replaced by a low value capacitor. The inductor is used to de-couple the RF signal from the voltage supply. The BB619 varactor has been selected from a range of similar components tested. The capacitance value of this varactor starts from approximately 37pF when the reverse voltage is 0 Volts and goes down to 3pF when the reverse voltage becomes 30 Volts.

The VSWR measurements from this test antenna are presented in Fig. 6. It is evident that the effective bandwidth is much wider than that required by the GSM900 system. The maximum reverse voltage to satisfy the GSM900 band requirements is 15Volts for VSWR < 2. From Fig. 6 it can be also observed that for low reverse voltage values the variation of the resonance frequency is relatively small. Further, it should be noted that the required range of the applied reverse bias can be reduced by cascading two or more varactors in series.

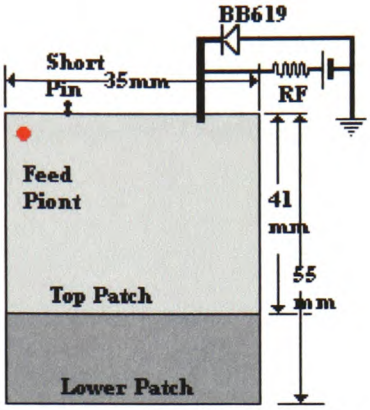

Figure 5: The varactor controlled PIFA design.

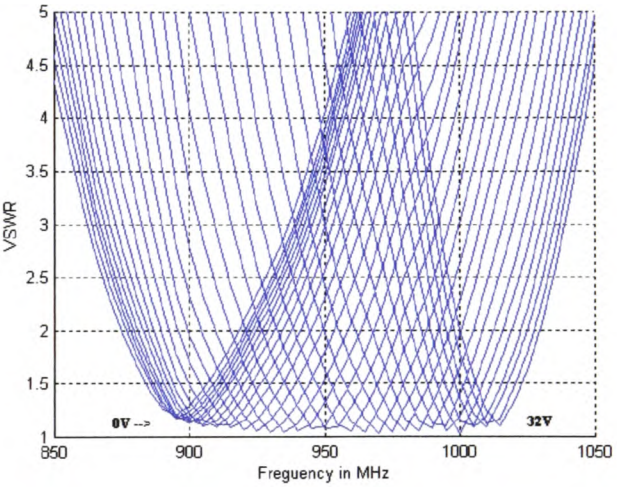

Figure 6: VSWR vs. frequency for the PIFA shown in Fig. 5 for a reverse voltage range of 0 to 32 Volts.

6. DISCUSSION

From the PIFA studies highlighted above, it is concluded that the narrow bandwidth problem can be effectively addressed by varying the position or by changing the capacitance value of the short pins. In an electronically fine-tuned PIFA the short pins can be replaced by transistors or PIN diodes, and the variable capacitors by varactor diodes. However, a number of problems are associated with these solutions.

Firstly, replacement of the short pins with transistors or the capacitors with varactors requires consideration and modeling of their characteristics at RF frequencies. In addition, for high power operation, their non-linear

behaviour must be accounted for. Secondly, the capacitance range of the varactors is limited by the maximum voltage supply range available in a mobile phone.

A closed loop circuit can be introduced that controls the tuning of the antenna either dynamically or based on a look-up table derived from an initial calibration. A generic diagram of such a control loop is shown in Fig. 7. If real-time control is implemented, the algorithm should be able to rapidly adjust the resonance frequency of the antenna under different operating scenarios, e.g. when the antenna is de-tuned due to its proximity to the user's head or hands. It has been observed, for instance, that the PIFA resonance frequency can shift by approximately 15MHz due to parasitic coupling with and absorption by the head and hands of the user in a realistic operating situation. Hence, a dynamically tuned narrow-band PIFA should provide further enhancement of the transmission efficiency and receiver sensitivity in practical applications. Nevertheless, the speed of the algorithm and the lock time and stability of the loop are issues of further concern, along with wideband phase noise and spurious emissions issues.

Despite the problems highlighted above for migrating from the manual to the electronically tuned PIFA, the low profile, the broad effective bandwidth, the low VSWR and the high efficiency that can be achieved by using these techniques, are important points that encourage further research.

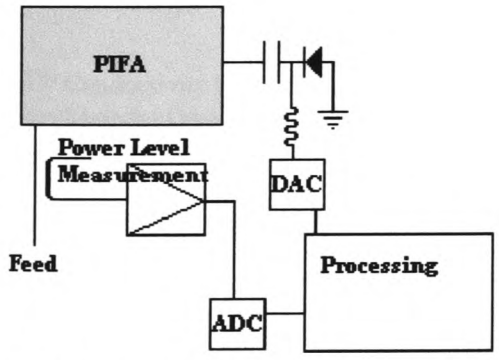

Figure 7: Block diagram of an electronically fine-tuned PIFA.

REFERENCES

[1] G. A. Kyriacou, J. N. Sahalos, " Analysis of a probe-fed short-circuited microstrip antenna," IEEE Trans. on Vehig. Techn., vol.45, pp. 427-430, Aug. 1997.

[2] C. R. Rowell, and R. D. Murch, "A capacitively loaded PIFA for compact mobile telephone handsets," IEEE Trans. Antennas Propagat., vol.45, pp. 837-842, May 1997.

[3] C. R. Rowell, and R. D. Murch, "A compact PIFA suitable for Dual-Frequency 900/1800-MHz operation," IEEE Trans. Antennas Propagat., vol.46, pp. 596-598, April 1998.

[4] Z. D. Liu, P. S. Hall, and D. Wake, "Dual-Frequency planar inverted-F antenna," IEEE Trans. Antennas Propagat., vol.45, pp.1451-1458, Oct. 1997.

[5] V. Stoiljkovic and G. Wilson, " A small planar inverted-F antenna with parasitic element for WLAN applications", ICAP, Heriot-Watt University, Edinburgh, 14-17 April 1997.

NEAR/FAR FIELD AND SAR OF MOBILE COMMUNICATION ANTENNAS.

Petros Panayi [1], M. Al-Nuaimi [1], L.P. Ivrissimtzis [2]

[1] University Of Glamorgan
School Of Electronics, Mid-Glamorgan
Pontypridd, CF37 1DL, United Kingdom
Email: ppanayi@glam.ac.uk; malnuaim@glam.ac.uk

[2] NEC Technologies
European Research and Development Centre, Imperial Way
Reading, RG2 0TD, United Kingdom
Email: leo.ivrissimtzis@nectech.co.uk

INTRODUCTION:

In cellular communications, the commercial drive for enhanced hand-held portable features and specifications, i.e. reduced size and prolonged battery life, as well as better link quality (improved coherence and lower bit error rates), prompted an interest in the study of efficient radiating elements. Antennas like the helix, the retractable monopole, and the Planer Inverted-F Antenna (PIFA) are most commonly used in today's mobile phone handsets. The near field magnitude, radiation pattern, input impedance, and radiation efficiency of the monopole antenna are descried in [1] where it was shown that the gain of the antenna in the direction of the operator's head is significantly reduced causing a "shadow effect". It has been also shown that only 4% of the dissipated energy is absorbed by the operator's hand compared to 96% absorbed by the head. The mass normalised rates of energy absorption referred as the Specific Absorption Rate (SAR) have been measured in [2] for monopole antennas and [3] for various types of antennas. In these reports the importance of the size of the monopole antenna in reducing the value of peak 1-g SAR is underlined. In [3] reduced SAR for the PIFA antenna has been also reported.
The well-established Finite Difference Time Domain (FDTD) method has been used in [1-3] and is recommended by [4] for mass averaged SAR evaluation. The method has been introduced by Yee [5] and a computer algorithm can be found in [6]. The simulated space is subdivided into small cubical cells, called Yee cells, with sides $\lambda/10$ or less where λ is the wavelength of the highest frequency used in the simulation. The number of cells used in a numerical model is limited by the processing time and computer memory requirements. This package enables post-processing facilities for 1-g and 10-g averaged SAR, which is calculated as

$$SAR = \frac{\sigma_x}{\rho_x}|Ex|^2 + \frac{\sigma_y}{\rho_y}|Ey|^2 + \frac{\sigma_z}{\rho_z}|Ez|^2 \quad \text{(W/Kg)} \qquad (1)$$

where: σ = Conductivity (S/m)
ρ = Material Density (Kg/m^3)
E = the Electric Field Intensity (V/m).

For an isotropic and homogenised materials like those used in our head model $\sigma_x=\sigma_y=\sigma_z$ and $\rho_x=\rho_y=\rho_z$.
Near, and far field radiation patterns with and without the proximity of the head and shoulders as well as 1g and 10g averaged peak SAR values, normalised to 1W input power, are presented in the following sections. Measurements of the far field radiation patterns in free space and in the proximity of the operator have been carried out in the University of Glamorgan anechoic chamber and the results have been compared with the simulations. The relation between mass averaged SAR and handset height is also discussed. Facilities limitations however, have prevented us from doing near field and SAR measurements to verify the simulations.

NEAR FIELD

The free space near field of the antennas studied has been computed using both the FDTD and the Method of Moments (MoM). Simulations of the near field with the proximity of the operator's head were obtained using only FDTD. For the FDTD free space numerical models, the Yee cubical cells used have a size of 1.67mm. On the other hand, the head/shoulder model uses 3mm cells. A wire-grid numerical model has been used with MoM. The distance between the vertical and horizontal wires is 10mm. At the top-right side of the box, however, more wires have been used to improve

the current distribution. The conductive case that is used to model the handset in both methods is 50mm wide, 25mm thick and 100mm high. The importance of the short pins to the resonant frequency for the PIFA has been highlighted in [7]. However, no shorting pins have been used in this part of our study. This is due to the MoM limitations, which do not allow short-circuits very close to the feed. The size of the patch has been obtained by measuring the reflection coefficient of the antenna. The PIFA patch has dimensions of 45×30mm. With these dimensions, the antenna resonates at 945MHz if three short pins at a distance of 1, 2, and 3mm from the feed are used. The input power has been set to 1W. Fig. 1 shows the near E-field of the PIFA. Data is normalised to the maximum value obtained by each method. It can be seen, from these graphs, that high electric field intensity exists at the corners of the handset and at the sides of the patch. Simulations with helix and monopole antennas revealed similar results for the conductive case E-field. High E-field intensity has been also computed along the length and at the ends of the wire antennas. In Figs. 1(c) and 1(d) the back side of the conductive case is shown. In the simulations including the operator's head, this side is placed next to the left ear at a vertical position. The reduced E-field is due to the distance from the antenna. From the near field simulations it can be also seen that, for the MoM, the field along the model wires has increased values. This effect fades out as the distance from the antenna increases. The near field of PIFA next to the operator's head is shown in Fig. 2. It can be seen that under coupling conditions the high E-field has increased values at the centre of the handset, and closer to the ear. The effect of the energy absorption by the operators left shoulder is shown at the bottom of Fig. 2 where the E-field intensity is significantly reduced.

FAR FIELD RADIATION

Normalised far field radiation pattern for the PIFA with and without the operator's head is shown in Fig. 3. The solid graph shows the radiation pattern with the head and on top of that, the free space 3-D pattern is superimposed for comparison. The later is similar to that computed by the MoM (not shown here). It is shown that the gain of the antenna in the direction of the head (on the left side) is reduced considerably. The gain in the bore sight is, however less affected. Increased gain due to the head proximity along the z-axis can also be observed. The computed results have been compared to the measurements in the xy-plane as presented in Fig. 4. Free space measurements and simulations have shown good agreement for the E_Θ-component in the horizontal xy-plane. The same is true for the operator proximity case where whole body measurements, including the hand, are compared to the head/shoulder simulations. Simulations and measurements with monopole and helix antennas have also shown good agreement. Careful placement of the hand must be considered in order not to block radiation from the antenna, which would cause a shift in the resonance frequency. It can be seen from this figure that in the direction of the head the E_Θ is reduced by more than 10dB compared with 1 dB in the opposite direction.

CONDUCTIVE CASE SIZE AND AVERAGED PEAK SAR

Studies of the peak 1-g averaged SAR based on the type and dimensions of the handset antennas have been carried out in the past [2,3]. In these reports, it has been shown that an increase in the size of the monopole antenna will result in lower 1-g peak SAR. PIFA has given even lower 1-g peak SAR values compared to the monopole and helix at the same operational frequencies. This is due to the increased distance of the radiating element from the operator's head and the protection provided by the handset acting as a reflector. The conductive case size, and in particular its height, can considerably affect the value of peak 1-g SAR. For the simulations of handheld portable antennas in the proximity of the operator's head and shoulders, a standard human head/shoulders biomesh has been used, in this report. This mesh uses 3mm cubical cells in space of 153×118×120 or 2,166,480 cells. Only 255,333 cell, however, are part of the head/shoulder geometry. The remaining cells are allocated for free space. At least 15 free space cells separate the head/shoulder from the model boundaries. The head and shoulders is divided into 5 tissue types plus a separate skin layer. In Fig. 4 the values of peak 1-g SAR calculated by FDTD for various operational frequencies and conductive case dimensions are plotted. The conductive case that is used to model the handset, is 50mm wide, 25mm thick and its height is 100mm, 88mm and 76mm for the three cases considered. The vertical center of the handset has been kept at a constant location and at a distance of 3mm (one Yee cell) from the left ear. The reduction of the handset has been done equally from the top and bottom. For the monopole case the size of the antenna is $\lambda/4$ where λ is the operational frequency wavelength. For the PIFA, on the other hand, the operational frequency has been obtained by using a Guassian input pulse as described in [8]. Verification has been done by measuring the antenna VSWR. Three shorting pins have been used near the feed point for this case. The size of the patch has been reduced by 3mm for each simulation and only in the vertical direction for simplicity. It can be seen in Fig. 4 that the value of the peak 1g SAR varies with frequency and with conductive case height. From these simulations, it is deduced that reduced SAR values require handset height approximately equal to a quarter or half wavelength. For these cases, 1-g peak SAR has values reduced by up to 30% compared to those experienced at other frequencies. This is true for both the monopole and the

PIFA. The size reduction of the conductive case has also resulted in an overall increase of the 1-g SAR. This is due to the reduction of the physical distance of the conductive case ends (top and bottom) from the operators head. The 10-g averaged peak SAR against frequency is given in Fig. 6 and similar conclusions can be drawn. It is noted that the 10-g SAR has lower overall values compared to that of 1g SAR. This is expected since SAR is averaged over a larger volume. PIFA has resulted into lower 1-g and 10-g SAR values and higher efficiency as shown in Fig. 7. From the same figure, it is also observed that efficiency improves with frequency. For the monopole antenna, efficiency is proportional to the operational frequency. On the other hand, for the PIFA case, the efficiency is at its minimum when the SAR is high.

CONCLUSIONS

Near and far field radiation patterns as well as mass averaged SAR for different types of handset antennas have been studied. Near field simulations using both the MoM and FDTD have shown high E field intensity at the corners of the handset and PIFA patch as well as along the length and top of wire antennas. Far field measurements and simulations have shown good agreement and reduced gain in the direction of the head. In this study, the advantages of PIFA in terms of its efficiency and SAR are also described. It has been shown, finally, that the size of the handset and in particular its height is related to 1-g and 10-g peak SAR. For handsets having height approximately equal to quarter or half wavelength, SAR can be reduced by 30%. Good selection, therefore, of the handset height can result in reduced peak mass averaged SAR values and thus reduced exposure to microwave radiation.

REFERENCES:

[1] Jorn.Toftgard, S. N. Hornsleth, and B. Andersed, "Effect on Portable Antennas of the Presence of a Person," *IEEE Transactions on Antennas and Propagation*, vol. 41, pp. 739 - 746, June 1993.

[2] O. P. Gandhi, G. Lazzi, and C. M. Furse, " Electromagnetic Absorption in the Human Head and Neck for Mobile Telephones at 835 and 1900MHz," *IEEE Transactions on Antennas and Propagation*, vol. 44, pp. 1884-1897, 1996.

[3] S. V. Amos, M. S. Smith, and D. Kitchener, "Modelling of Handset Antennas Interactions With The User and SAR Reduction Techniques," *NCAP1999*, vol. 461, pp. 12-15, 1999.

[4] J. Robert F. Cleveland, D. M. Sylvar, and J. L. Ulcek, "*Evaluating Compliance with FCC Guidelines for Human Exposure to Radiofrequency Electromagnetic Fields*," 97-01 ed. Washington, D.C.: Federal Communication Commission Office of Engineering & Technology, pp.42, August 1997.

[5]K. S. Yee, "Numerical solution of initial boundary value problems involving Maxwell's equations in isotropic media," IEEE Trans. Antennas Propagat. Vol. AP-14,pp. 302-307, May 1966.

[6] K. S. Kunz and R. J. Luebbers, "*The Finite Difference Time Domain Method for Electromagnetics*," vol. 0-8493-8657-8: CRC Press, 1993.

[7] P. K. Panayi, M. Al-Nuaimi and L. P. Ivrissimtzis, "Tuning Techniques for the Planar Inverted F-Antenna," *NCAP99*, vol. 1, pp. 259-262, April 1999.

[8] Z. D. Liu, P. S. Hall, and D. Wake, "Dual-Frequency planar inverted-F antenna," IEEE Trans. Antennas Propagat., vol.45, pp.1451-1458, Oct. 1997.

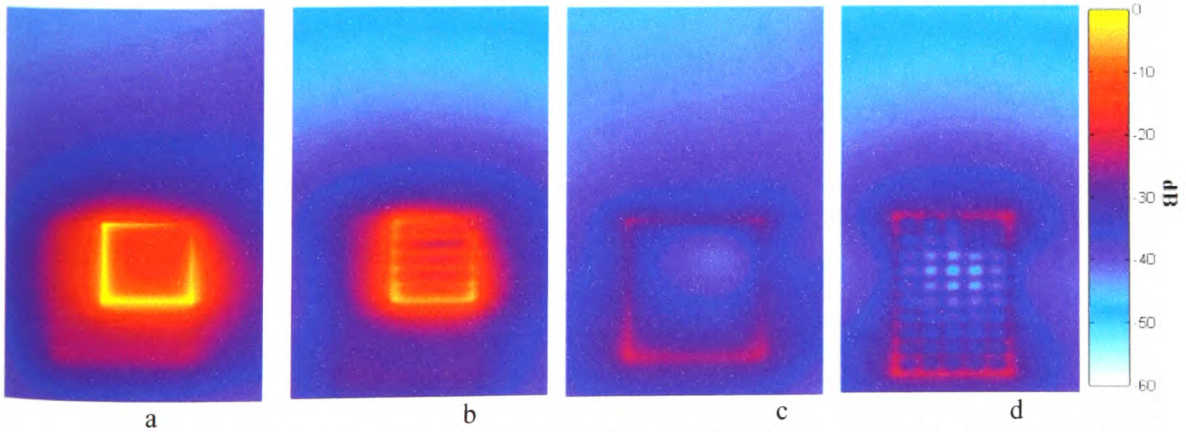

Fig. 1 Normalised near E field patterns of the PIFA antenna simulated using FDTD (a,c) and MoM (b,d). a, and b are for the handset side toward radiation and c and d are for the handset side toward the operator's head.

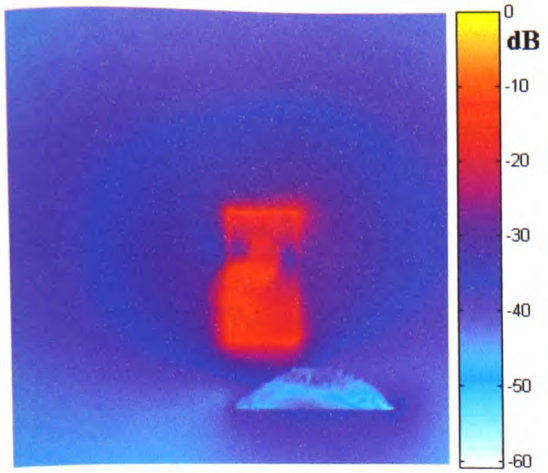

Fig.2 Normalised E field of PIFA with the proximity of the Hear.

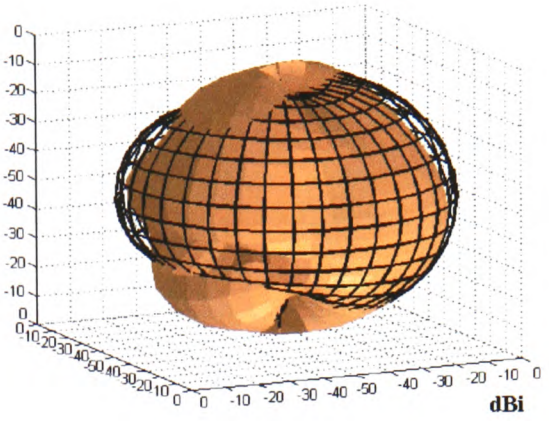

Fig. 3 Radiation Pattern of PIFA with and without the operator's head at 945MHz computed using FDTD

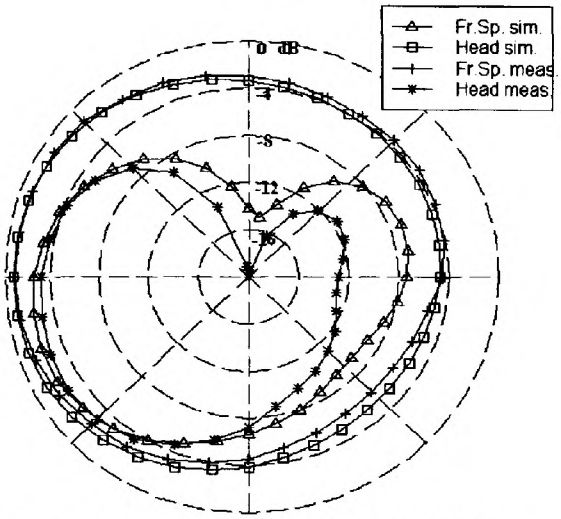

Fig. 4. Measured and Computed far-field (E_Θ) radiation patterns of PIFA with and without the operator.

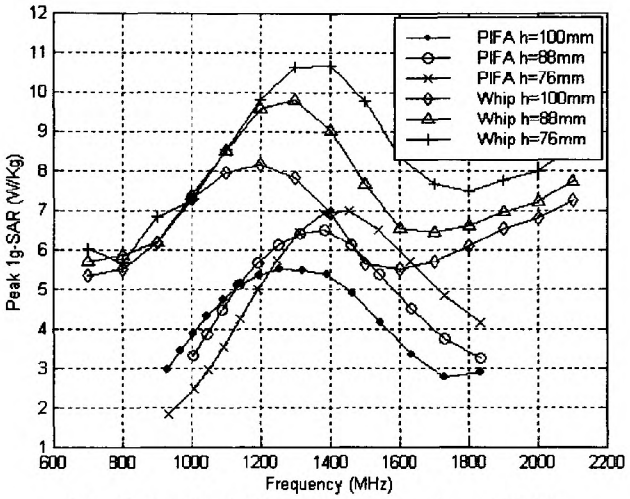

Fig. 5. 1-g Peak SAR for monopole and PIFA antennas

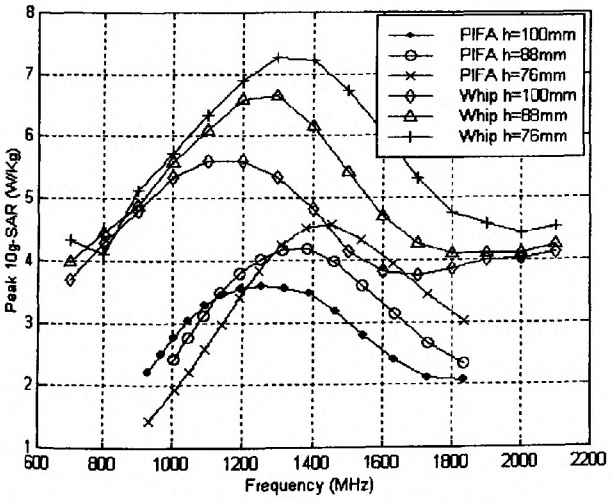

Fig. 6. 10-g Peak SAR for monopole and PIFA antennas

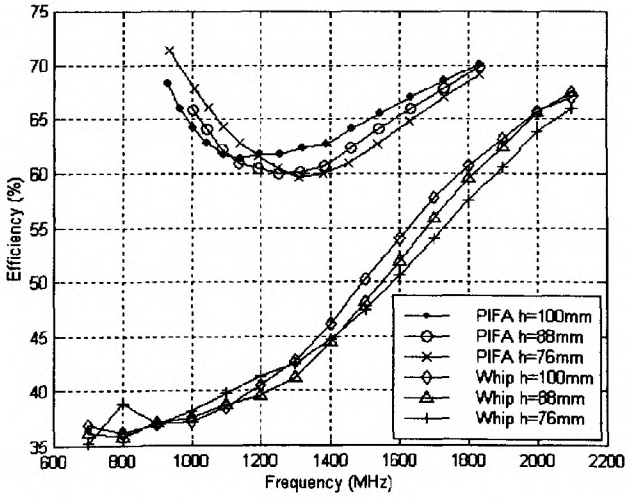

Fig. 7. Radiation efficiency of monopole and PIFA antenna operating next to the operator's head and shoulders.

Appendix C

```
function A=FDTDHEADSARAll()
% FDTDHEARSARAll Calculate and Plot of Max and Average
% SAR data from a sequence of FDTD Files
% In the source code / indicate end of commands block
% (like HTML coding)
%FDTDHEARSARAll()

clear all;
SARm3dB = 10000;

%=============================================================
% External FOR loop. Six different planes (slides)
% analyzed
%=============================================================

for Extloop=1:6

% Dimensions of the Head/shoulders Model
HeadBottom   = 50;   %16
HeadTop      = 140;  %104
HeadLeft     = 17;   %17
HeadRigth    = 139;  %139
Headfront    = 22;   %16
HeadBack     = 122;  %102

%=============================================================
% File Name
%=============================================================
%Define Constants
%================
pi = 3.141592654;

%Define Working path %CHECK !!!!!!!!
%====================================
cd d:\head30Deg\head30oMonopoleNewNew\MonopoleSARall\;
%=============================================================

%+++++++++++++++++++++++++++++++++++++++++++++++++++++++++++++
% Define the filename                          %CHECK
!!!!!!!!
File1 = 'Head30oMonopoleNewNew2100MHz';    %USE
ReplaceAll
%+++++++++++++++++++++++++++++++++++++++++++++++++++++++++++++

% Select extension based on the plane and averaging
method
%=============================================================
if Extloop == 1   | Extloop == 4
```

```
    flag = 2;           % Flag = 2 indicates that this plane
                        % is analyzed twice (to get peak SAR)
    Ext1 = '.xy';
elseif Extloop == 2 | Extloop == 5
    Ext1 = '.yz';
    flag = 1;
elseif Extloop == 3 |  Extloop == 6
    Ext1 = '.xz';
    flag = 1;
end

if Extloop == 1  | Extloop == 2 | Extloop == 3
   Ext2 = '.1gsar';
elseif Extloop == 4  | Extloop == 5 | Extloop == 6
    Ext2 = '.10gsar';
End

Ext3 = '.ssout';
%=================================================================
%  /Define the filename
%=================================================================

%============================
% Set start and stop planes
%============================
if Ext1 == '.xy'
    Start = HeadBottom;
    Stop = HeadTop;
elseif Ext1 == '.yz'
    Start = HeadLeft;
    Stop = HeadRigth;
elseif Ext1 == '.xz'
    Start = Headfront;
    Stop = HeadBack;
End
%============================
% /Set start and stop planes
%============================

%============================
% Find the Radiatied Power
%============================
% Open the *.ssout file
filename = [File1 Ext3]
fid=fopen(filename,'r');
[a,count]=fscanf(fid,'%c');
status=fclose('all');
find_start=findstr(char(10),a);

% Feed Point Impedance
```

```
FeedPointImpedance =
str2num(a(find_start(1):find_start(2)));
FeedPointImpedanceReal(Extloop) = FeedPointImpedance(1);
FeedPointImpedanceImaginary(Extloop) =
FeedPointImpedance(2);

% The Power from the antenna
InputPower = str2num(a(find_start(2):find_start(3)));
InputPowerArray(Extloop) = InputPower;

RadiatedPower =str2num(a(find_start(3):find_start(4)));
RadiatedPowerArray(Extloop) = RadiatedPower;

AntennaEfficiency
=str2num(a(find_start(4):find_start(5)));
AntennaEfficiencyArray(Extloop) = AntennaEfficiency;
clear a;clear count;
%============================
% /Find the Radiatied Power
%============================

%=============================================
% Flag Loop to prevent error on the first run
%=============================================
for iFlag= 1:flag

   TotalNoOfHeadCell = 0; %All the cells having SAR values
   TotalSARValue = 0;     %Sum of SAR in head/shoulders
   Cellm3dB = 0;          %Number of Cells that have SAR
                          %higher than -3dB of the Peak
SAR
   TotalSARinm3dBCells = 0; %The sum of SAR is all the
                            %-3dB cells

%=============================================================
% Series
%=============================================================

% Start the Loop for all planes
%==============================
for FileCount = Start : Stop

% Make the Data File Name
filename = [File1 Ext1 num2str(FileCount) Ext2]

% Open the file and read the data
fid=fopen(filename,'r');
[a,count]=fscanf(fid,'%c');
status=fclose('all');
find_start=findstr(char(10),a);
No =str2num(a(find_start(3):find_start(4)));
```

```
NoX = No(1);
NoY = No(2);
NoZ = No(3);
DD =str2num(a(find_start(4):find_start(5)));
DX = DD(1);
DY = DD(2);
DZ = DD(3);

% Average SAR values over 1 Watt input power
SARData =str2num(a(find_start(5):count))/InputPower;

if Ext1 == '.xy'
   No1 = NoX;
   No2 = NoY;
elseif Ext1 == '.yz'
   No1 = NoY;
   No2 = NoZ;
elseif Ext1 == '.xz'
   No1 = NoX;
   No2 = NoZ;
end


% Define Constants
FreeSpace = 376.7;
   %=============================================================
   % Plane
   %=============================================================
SARTotal = 0;      %The Sum of SAR in this plane
TotalCount = 0;    %Number of Cells in each plane
% Form the Z matrix for data plotting
%=====================================
for i = 1:No1 %Loop No1
   for j=1:No2 %Loop No2
      if (SARData(No1*(j-1)+i)) ~= 0;
         % Used for the whole Head DATA
         TotalNoOfHeadCell = TotalNoOfHeadCell + 1;
         TotalSARValue = TotalSARValue + SARData(No1*(j-
1)+i);

        % Find the Average for this plane
        SARTotal = SARTotal + SARData(No1*(j-1)+i);
        TotalCount = TotalCount + 1;

           if (SARData(No1*(j-1)+i)) >= SARm3dB ;
                Cellm3dB = Cellm3dB + 1;
                TotalSARinm3dBCells = TotalSARinm3dBCells
+ SARData(No1*(j-1)+i);
           end
        end
    end
```

```
 end
% Save the Averaged SAR value for this plane
SARAver(FileCount) = SARTotal/TotalCount;
% Save the maximum SAR value for this plane
SARMax(FileCount) = max(SARData);
PlotHelp(FileCount) = FileCount;

   %=============================================================
   % /Plane
   %=============================================================
% end for the Loop for all planes
%==================================
end
%=============================================================
% /Series
%=============================================================


%=============================================================
% Data for THE HEAD/SHOULDERS
%=============================================================
maxSARarray(Extloop) = max(SARMax);   % Peak SAR Value
SARm3dB = max(SARMax)/2;              % (Peak SAR
Value)/2
TotalCellArray(Extloop) = TotalNoOfHeadCell;  % Number of
                          Cells in the Head send to an Array
AverageOverTheHeadSAR(Extloop) =
TotalSARValue/TotalNoOfHeadCell;      %Head Averaged SAR

end
%=============================================================
% /Flag Loop to prevent error on the first values
%=============================================================

%=============================================================
% Plot
%=============================================================
     for xx = 1:Start-1
        SARAver(xx) = 0;
        SARMax(xx) = 0;
        PlotHelp(xx) = xx;
     end
figure;
subplot(1,2,1)
plot(SARAver,PlotHelp);
if Extloop == 1
   title('Average SAR over a xy cuts of the Head 1grm');
elseif Extloop == 2
   title('Average SAR over a yz cuts of the Head 1grm');
elseif Extloop == 3
   title('Average SAR over a xz cuts of the Head 1grm');
```

```
elseif Extloop == 4
   title('Average SAR over a xy cuts of the Head 10grm');
elseif Extloop == 5
   title('Average SAR over a yz cuts of the Head 10grm');
elseif Extloop == 6
   title('Average SAR over a xz cuts of the Head 10grm');
end
xlabel('SAR (w/Kg)');
ylabel('Vertical Position (cell)');
ax1 = gca;
grid on;
subplot(1,2,2)
plot(SARMax,PlotHelp);
ax1 = gca;
grid on;
if Extloop == 1
   title('Peak SAR over a xy cuts of the Head 1grm');
elseif Extloop == 2
   title('Peak SAR over a yz cuts of the Head 1grm');
elseif Extloop == 3
   title('Peak SAR over a xz cuts of the Head 1grm');
elseif Extloop == 4
   title('Peak SAR over a xy cuts of the Head 10grm');
elseif Extloop == 5
   title('Peak SAR over a yz cuts of the Head 10grm');
elseif Extloop == 6
   title('Peak SAR over a xz cuts of the Head 10grm');
end
xlabel('SAR (w/Kg)');
ylabel('Vertical Position (cell)');
%=============================================================
% /Plot
%=============================================================

%=============================================================
% Save Series DATA
%=============================================================
if Extloop == 1
   save Head30oMonopoleNewNew2100MHz_xy_1grmsar SARAver
SARMax;   %CHECK !!!!!!!!
elseif Extloop == 2
   save Head30oMonopoleNewNew2100MHz_yz_1grmsar SARAver
SARMax;   %CHECK !!!!!!!!
elseif Extloop == 3
   save Head30oMonopoleNewNew2100MHz_xz_1grmsar SARAver
SARMax;   %CHECK !!!!!!!!
elseif Extloop == 4
   save Head30oMonopoleNewNew2100MHz_xy_10grmsar SARAver
SARMax; %CHECK !!!!!!!!
elseif Extloop == 5
```

```
   save Head30oMonopoleNewNew2100MHz_yz_10grmsar SARAver
SARMax; %CHECK !!!!!!!!
elseif Extloop == 6
   save Head30oMonopoleNewNew2100MHz_xz_10grmsar SARAver
SARMax; %CHECK !!!!!!!!
end
%=============================================================
% /Save Series DATA
%=============================================================


%=============================================================
% Series Data
%=============================================================
% Find the -3dB size      |
%=========================
      Seriesm3dBsize = 0;
      for i = 1:length(SARMax);
         if SARMax(i) >= SARm3dB
       Seriesm3dBsize = Seriesm3dBsize + 1;
         end
      end
% Save the Length of the -3dB
Seriesm3dBsizeArray(Extloop) = Seriesm3dBsize;
% Save the number of Yee cells having >= (peak SAR)/2
Cellm3dBarray(Extloop) = Cellm3dB;
   if Cellm3dB ~= 0
       AverageSAROverm3dBVolume(Extloop) =
TotalSARinm3dBCells/Cellm3dB;
   end

clear SARAver;clear SARData;
clear SARMax;clear SARTotal;clear PlotHelp;
end
%=============================================================
% /Series Data
%=============================================================

% Display Data on Matlab Window
%==============================
%Feed Point Impedance
FeedPointImpedanceReal
FeedPointImpedanceImaginary
% The Radiated Power from the Antenna
InputPowerArray
% The Radiated Power from the Antenna
RadiatedPowerArray
% The Efficiency of the Antenna
AntennaEfficiencyArray

% Total Number of Cells in the head
```

```
TotalCellArray
% Max SAR
maxSARarray
% Averaged over the Head SAR
AverageOverTheHeadSAR

% Actual number of Cells within the -3dB Volume.
Cellm3dBarray
% Actual averaged SAR in the volume given above.
AverageSAROverm3dBVolume

% Length of the -3dB
Seriesm3dBsizeArray
% Save all the data in the ***_All file
%=========================================
save Head30oMonopoleNewNew2100MHz_All...%CHECK !!!!!!!!
FeedPointImpedanceReal FeedPointImpedanceImaginary ...
InputPowerArray RadiatedPowerArray
AntennaEfficiencyArray...
TotalCellArray maxSARarray AverageOverTheHeadSAR
Cellm3dBarray...
AverageSAROverm3dBVolume Seriesm3dBsizeArray;

A = 1;
```